Human-Based Multiscale Modelling and Simulation to Investigate Arrhythmias and Treatments in Ischemic Heart Disease

Leto Luana Riebel

Green Templeton College



Computational Cardiovascular Sciences Group

Department of Computer Science

University of Oxford

This thesis was submitted to the Department of Computer Science at the University of Oxford for the degree of Doctor of Philosophy in October 2024.

Acknowledgements

First of all, I want to thank my supervisors, Blanca Rodriguez, Jenny Wang, Hector Martinez-Navarro, and Cristian Trovato for their continuous support. Thank you, Blanca, for sharing your wisdom and knowledge with me and for always pushing for preciseness, clarity, and impact. Thank you, Jenny, for brainstorming sessions, for patiently listening to my ideas, and for sharing puppy pictures to brighten up long office days. Thank you, Hector, for your help with computing resources and collaborations and for reminding me not to burn out. Thank you, Cristian, for Friday coffee chats during COVID, for discussions of science and life, and for making my industry placements possible.

Next, I would like to thank the Computational Cardiovascular Science Team. Thank you, Hannah, for movie evenings and for sanity-checks after paper feedback. Thank you, Albert, for figuring out MonoAlg3D together and for being my PhD-office buddy. Thank you, Julia, for involving me in projects, for tricking me into lunch breaks by bringing board games to the office, and for lending an open ear, whenever needed. Thank you, Elisa, for your support and positivity, even during late-night pre-deadline writing sessions. Thank you, Lucas, for bug fixing and for making a 5-star Purkinje model. Thank you, Ruben, for the ParaView and Blender crash courses and for staying positive, even when the cycle path has flooded again. Thank you, Xin, Maxx, and Ambre, for sharing your knowledge with me and for giving me feedback with papers and presentations. Thank you, Milda, for going on a spontaneous 4-hour bus trip with me so I could see a Viking church in the middle of Norway.

To my housemates, thank you, Miles, Ali, Benny, Sarah, Jessie, and Giorgia, for sharing this journey, for family dinners, and TV evenings together. Very importantly, thank you, Tom, for listening to me talk about the heart, for keeping the chocolate cupboard stocked to fuel me writing up, and for all the happy moments. Finally, I would like to thank my mother – for a lot of things, but I will keep it brief – for teaching me to be thorough, to stay curious, and to never forget to have a laugh.

Publications

This list outlines publications that have or are planned to emerge from this DPhil:

a. Riebel, L. L., Passini, E., Margara, F., Paci, M., Biasetti, J., & Rodriguez, B. (2021). *In Silico* Identification of the Key Ionic Currents Modulating Human Pluripotent Stem Cell-Derived Cardiomyocytes Towards an Adult Phenotype. *2021 Computing in Cardiology (CinC)*. https://doi.org/10.23919/CinC53138.2021.9662683

b. Riebel, L. L., Wang, Z. J., Martinez-Navarro, H., Trovato, C., Biasetti, J., Sachetto Oliveira, R., Weber dos Santos, R., & Rodriguez, B. (2022). Modelling and Simulation Reveals Density-Dependent Re-Entry Risk in the Infarcted Ventricles after Stem Cell-Derived Cardiomyocyte Delivery. *2022 Computing in Cardiology (CinC)*. https://doi.org/10.22489/CinC.2022.392

c. Riebel, L. L., Wang, Z. J., Martinez-Navarro, H., Trovato, C., Camps, J., Berg, L. A., Zhou, X., Doste, R., Sachetto Oliveira, R., Weber dos Santos, R., Biasetti, J., & Rodriguez, B. (2024). *In silico* evaluation of cell therapy in acute versus chronic infarction: role of automaticity, heterogeneity and Purkinje in human. *Scientific Reports*, *14*, 21584. https://doi.org/10.1038/s41598-024-67951-5

d. Riebel, L. L., Wang, Z. J., Martinez-Navarro, H., Dasi, A., Trovato C., Rodriguez B. (2024). Upregulation of the sodium potassium pump current suppresses ectopic activity after stem cell delivery in the human-based heart after myocardial infarction. *Indexed Abstract from the ESC Congress* 2024, *European Heart Journal, 45*(Supplement_1). https://doi.org/10.1093/eurheartj/ehae666.3738

e. Riebel, L. L., ..., Rodriguez, B. *In Silico* Optimisation of Regenerative Cell Therapy in the Infarcted Human Ventricles to Mitigate Arrhythmic Burden. [Manuscript in Preparation]

f. Riebel, L. L., ..., Rodriguez, B., Levin, M. *In silico* identification of arrhythmic risk markers in small, paediatric-like ischemic ventricles. [Manuscript in Preparation]

Presentations

The following list outlines oral talks and poster presentations as well as associated achievements resulting from this DPhil.

Oral Talks:

- AstraZeneca BBSRC Student Symposium 2024
- Safety Pharmacology Society's Annual Meeting 2023
- Gordon Research Seminar and Conference of Arrhythmia Mechanisms 2023
- Oxford Symposium of the Computational Cardiovascular Science Group 2022
- BHF CRE Symposium Oxford 2022

Poster Presentations:

- European Society of Cardiology Congress 2024
- STEM for Britain Competition at the Houses of Parliament 2024
- Safety Pharmacology Society's Annual Meeting 2023
- Gordon Research Seminar and Conference of Arrhythmia Mechanisms 2023
- Computing in Cardiology 2022
- BHF CRE Symposium Oxford 2022
- AstraZeneca BBSRC Student Symposium 2022
- Computing in Cardiology 2021

Achievements:

- STEM for Britain Finalist in the Biological and Biomedical Sciences Category 2024
- Junior Investigator Travel Award at Safety Pharmacology Society's Annual Meeting 2023

Contents

ABBREVIATIONS 1

LIST OF FIGURES 3

LIST OF TABLES 5

ABSTRACT 6

1 Introduction 7

1.1 Thesis goals 9

1.2 Thesis outline 11

2 Physiological background of cardiac function 15

2.1 Cardiac anatomy 15

2.2 Cellular electrophysiology 17

2.3 Tissue propagation 22

2.4 The healthy human electrocardiogram 23

3 Literature review of ischemic heart disease burden and treatment 26

3.1 Causes and prevalence of ischemic heart disease in young and old 26

3.2 Clinical manifestation – the ischemic and infarcted electrocardiogram 29

3.3 Arrhythmogenicity of ischemic heart disease 30

3.3.1 Trigger for ventricular arrhythmias 31

3.3.2 Substrate for ventricular arrhythmias 32

3.4 Clinical management of ischemic heart disease 33

3.5 Experimental treatments - regenerative cell therapy 34

3.5.1 Delivery of regenerative cells into the human heart 36

3.5.2 Clinical trials of cardiac regenerative therapy 37

3.5.3 Advantages and limitations of regenerative therapy for the heart 39

4 Analysis of computational tools to simulate cardiac electrophysiology 41

4.1 Fundamentals in mathematical modelling of cellular electrophysiology 41

4.2 Single cell computer models of cardiac electrophysiology....46
4.3 Mathematical models of electrical propagation in tissue....50
4.4 Computational model solvers for 3D tissue simulations....51
4.5 Modelling and simulation to augment clinical trials and risk predictions....55
4.6 Verification, validation, and uncertainty quantification principles....61
5 Human ventricular electrophysiological modelling and simulation of ischemic heart disease for risk stratification and treatment optimisation....64
5.1 Multiscale modelling and simulation of healthy human ventricular electrophysiology....64
5.1.1 Modelling human ventricular and Purkinje cellular electrophysiology....64
5.1.2 Simulating electrical propagation in the human ventricles....65
5.2 Modelling functional and structural changes in ischemic heart disease....67
5.2.1 Modelling electrophysiological changes induced by ischemia and infarction....68
5.2.2 Creating physiological geometries of ischemic heart disease injury....71
5.2.3 Structural remodelling of the ventricles after myocardial infarction....73
5.3 Modelling and simulation of therapies for ischemic heart disease....73
5.3.1 Simulating regenerative cell therapy....74
5.3.2 Simulating ionic current agonists and antagonists....78
5.4 Simulation protocols....80
5.4.1 Simulating sinus rhythm....80
5.4.2 Stimulation protocol to assess arrhythmic burden....80
5.5 Simulation tools and software....83
5.5.1 Custom 3D model solver functions....85
5.6 Verification, validation, and uncertainty quantification....87
6 Identifying arrhythmic risk markers in small ischemic ventricles to aid clinical risk prediction in paediatric patients....91

6.1 Introduction 91
6.2 Methods 93
6.2.1 Simulating ischemia in two action potential phenotypes 93
6.2.2 Simulation and arrhythmia induction protocols 96
6.3 Results 96
6.3.1 The effect of growing ventricular size on the electrocardiogram 96
6.3.2 Arrhythmic risk increases with increasing ischemia severity 98
6.3.3 Steep-restitution action potentials facilitate ventricular fibrillation-like arrhythmias 101
6.3.4 Arrhythmic risk is substantially reduced in small but only slightly in medium-sized ischemic regions 102
6.4 Discussion 104
6.5 Conclusions 108
7 Uncovering arrhythmia mechanisms of regenerative cell therapy in the infarcted adult human ventricles 109
7.1 Introduction 109
7.2 Methods 111
7.2.1 Modelling and simulating cell delivery into the infarcted human ventricles 111
7.2.2 Simulation and arrhythmia quantification protocol 113
7.3 Results 114
7.3.1 Establishing credibility - simulations produce physiological electrocardiograms in acute, healing, and chronic myocardial infarction 114
7.3.2 Injected cells increase arrhythmia vulnerability by enabling re-entrant wavefront conduction through scar cores 117
7.3.3 Slow heart rates, chronic myocardial infarction, and heterogeneous injected cell populations facilitate spontaneous beats in the ventricles 121

7.3.4 Impaired Purkinje-myocyte coupling increases re-entrant arrhythmia susceptibility following spontaneous stem cell beats 126
7.4 Discussion 128
7.5 Conclusions 131
8 Designing anti-arrhythmic treatments to mitigate safety concerns of cell injection in the chronically infarcted human ventricles 133
8.1 Introduction 133
8.2 Methods 135
8.2.1 Experimentally informed *in silico* maturation of injected cells 135
8.2.2 Identifying anti-arrhythmic targets and optimising Ca^{2+} transients of injected cells 138
8.2.3 Simulation and arrhythmia quantification protocol 140
8.3 Results 141
8.3.1 Establishing credibility – simulations of cell therapy in the infarcted ventricles capture experimentally observed surge in tachycardia arrhythmias 141
8.3.2 Targeting the Na^{+}-K^{+} pump to suppress spontaneous beating 144
8.3.3 Ionic targes to suppress spontaneous beats, modulate pro-arrhythmic action potential duration, and maintain physiological Ca^{2+} transients 148
8.4 Discussion 154
8.5 Conclusions 158
9 Conclusions 160
9.1 Limitations and future directions 162
REFERENCES 167

ABBREVIATIONS

AP	Action potential
APD	Action potential duration
APD_x	Action potential duration at x% repolarisation
ATP	Adenosine triphosphate
bpm	Beats per minute
BZ	Border zone
CaMK	Ca^{2+}/calmodulin-dependent protein kinase II
CaT	Ca^{2+} transient
C_m	Membrane capacitance
D0	Day 0
D14	Day 14
DAD	Delayed afterdepolarisation
DDR	Diastolic depolarisation rate
dV/dt_{max}	Maximum action potential upstroke velocity
EAD	Early afterdepolarisation
ECG	Electrocardiogram
EF	Ejection fraction
f_{KATP}	Scaling factor for the fraction of open I_{KATP} channels
GPU	Graphical processing unit
G_x	Conductance of ion channel x
hPSC-CM	Human pluripotent stem cell-derived cardiomyocyte
I_{KATP}	ATP-sensitive K^+ current
I_{CaL}	L-type Ca^{2+} current
I_{CaT}	T-type Ca^{2+} current
I_{ClCa}	Ca^{2+}-activated Cl^- current
I_{K1}	Inward rectifier K^+ current
I_{Kb}	Background K^+ current
I_{KCa}	Ca^{2+}-activated K^+ current
I_{Kr}	Rapid delayed outward rectifier K^+ current
I_{Ks}	Slow delayed outward rectifier K^+ current

I_{NaF}	Fast Na^+ current
I_{NaCa}	Na^+-Ca^{2+} exchanger current
I_{NaK}	Na^+-K^+ pump current
I_{NaL}	Late Na^+ current
I_{rel}	Ca^{2+}-release current through ryanodine receptors
I_{to}	Transient outward K^+ current
I_{up}	SERCA pump current
k_{NaCa}	I_{NaCa} scaling factor
IZ	Injury zone
LAD	Left anterior descending artery
LV	Left ventricle
MDP	Maximum diastolic potential
MI	Myocardial infarction
MRI	Magnetic resonance imaging
ODE	Ordinary differential equation
PDE	Partial differential equation
PMJ	Purkinje-myocyte junction
p_{NaK}	Maximum I_{NaK}
P_s	Permeability to ion species s
RV	Right ventricle
RyR	Ryanodine receptor
RZ	Remote zone
SERCA	Sarcoendoplasmic reticulum Ca^{2+}-ATPase
SR	Sarcoplasmic reticulum
tau_s or τ_s	Time constant of ion channel s
VF	Ventricular fibrillation
V_m	Membrane potential
$V_{m,peak}$	Maximum action potential peak
VT	Ventricular tachycardia
V_w	Wilson's terminal
VW	Vulnerable window

LIST OF FIGURES

Figure 1. Cardiac anatomy 16

Figure 2. AP and key contributing ionic currents of ventricular cardiomyocytes 21

Figure 3. The healthy ECG signal 24

Figure 4. Re-entry circuit mechanisms 31

Figure 5. Evolution of computational AP models 47

Figure 6. In silico trials pipeline 63

Figure 7. Torso and biventricular geometry with Purkinje network and ECG 65

Figure 8. Electrical activation in the healthy biventricular model 66

Figure 9. Modelling and simulating ischemic heart disease 71

Figure 10. Simulated APs of ventricular-like, atrial-like, and nodal-like hPSC-CMs ... 74

Figure 11. Modelling and simulating spatial distribution of hPSC-CMs 77

Figure 12. Ectopic stimulus locations in three different transmural injuries 82

Figure 13. Convergence and run time analyses 89

Figure 14. ECG traces to quantify uncertainty of spatial hPSC-CM distribution 89

Figure 15. ECG traces with and without retrograde Purkinje propagation 90

Figure 16. ECG traces to assess uncertainty in hPSC-CM CV 90

Figure 17. Modelling and simulating ischemia 93

Figure 18. ECGs in a healthy control case with two different AP models 95

Figure 19. Effects of ventricular size on the ECG 98

Figure 20. VWs for a moderate and a severe large ischemic injury 99

Figure 21. VWs in a large ischemic injury for two different AP models 102

Figure 22. VWs in a small, medium, and large ischemic injury 103

Figure 23. Modelling and simulating MI 112

Figure 24. Activation and repolarisation of the healthy and infarcted ventricles 115

Figure 25. Comparison of simulated and clinical ECGs post MI and cell therapy ... 116

Figure 26. VWs in the small, medium, and large chronic scar 118

Figure 27. Activation and repolarisation time maps before and after cell delivery .. 120

Figure 28. Mechanisms of spontaneous beats after hPSC-CM delivery..... 123

Figure 29. Impact of infarct stage and size on delivered hPSC-CMs 124

Figure 30. hPSC-CM AP and ionic current traces under differrent pacing rates 125

Figure 31. Arrhythmic risk after spontaneous hPSC-CM beats 127

Figure 32. Arrhythmia complexity across all infarct stages and sizes 128

Figure 33. Pipeline to simulate injection of D0, D14, and rapid D14 hPSC-CMs 137

Figure 34. VT ECGs after hPSC-CM delivery in a small, medium, and large scar..... 143

Figure 35. Sensitivities of hPSC-CM biomarkers when scaling ionic currents 145

Figure 36. AP and ionic current traces of paced and unpaced hPSC-CMs 146

Figure 37. The effects of p_{NaK} modulation on hPSC-CM AP 147

Figure 38. Safety-Efficacy score of hPSC-CMs with a target APD_{90} of 330 ms..... 150

Figure 39. VWs for D0 and modified hPSC-CMs 151

Figure 40. Safety-Efficacy score of hPSC-CMs with a target APD_{90} of 150 ms..... 152

Figure 41. VWs for D0 and optimised hPSC-CMs..... 153

LIST OF TABLES

Table 1. Typical intra and extracellular ionic concentrations 43

Table 2. Scaling factors to produce transmural and apicobasal gradients 67

Table 3. Modelling ischemic and post-MI infarct, border, and remote zone 69

Table 4. CV for each infarct stage and zone 73

Table 5. Experimental and simulated spontaneous hPSC-CM AP biomarkers 75

Table 6. Current scalings to produce ventricular, atrial, and nodal-like hPSC-CMs ... 75

Table 7. Calibrated parameters for spatial hPSC-CM distribution 78

Table 8. General input parameters for MonoAlg3D 84

Table 9. Cell type encoding in the mesh files for MonoAlg3D 85

Table 10. Grid element fields for myocardial cells 86

Table 11. Scaling parameters to create the steep restitution curve model 94

Table 12. Current scalings to model D14, rapid beating, and I_{NaCa}-KO hPSC-CMs ... 136

Table 13. AP biomarkers of the D0, rapid D0, D14, and rapid D14 hPSC-CMs 137

ABSTRACT

Ischemic heart disease is a major cause of death worldwide presenting a large burden to affected patients and the health care system. Patients with a history of myocardial ischemia are at an increased risk of sudden cardiac death and heart failure. Current treatments restore myocardial blood supply and manage symptoms but often involve strenuous therapies and fail to regenerate the heart's function. New ways to identify disease mechanisms, augment clinical risk predictions, and inform the development of new therapies are needed. Computer simulations offer a cost and time effective route to test new technologies under regular and extreme conditions and allow for detailed investigations into the role of individual parameters.

My aim for this thesis was to design and conduct human-based modelling and simulation studies to uncover arrhythmia mechanisms and test the safety of new treatments in ischemic heart disease of the human ventricles. For this, I developed human ventricular electrophysiological modelling and simulation techniques by integrating state-of-the-art computational models into an established high-performance open-source GPU-based software. To demonstrate trust in this modelling and simulation framework, I carried out comparison with experimental and clinical data. Next, I devised and ran simulation studies to investigate 1) the risk of ventricular tachycardia and fibrillation in small, paediatric-like ischemic ventricles, 2) pro-arrhythmic pathways in regenerative cell therapy after myocardial infarction, and 3) anti-arrhythmic treatments to mitigate safety concerns of cell injection.

To conclude, for this thesis, I have carried out credible human-based modelling and simulation studies to unravel arrhythmia mechanisms and optimise therapies in ischemic heart disease.

1 Introduction

Every five minutes a patient is admitted with a heart attack to hospitals in the United Kingdom alone (British Heart Foundation, 2024b). Cardiovascular disease is not only a huge burden to the affected patients, whose quality of life may be severely impacted, but also to their families, carers, and the health care system. In fact, coronary heart disease, which describes an impaired blood supply to the heart's tissue due to obstruction within the coronary arteries, costs the United Kingdom's National Health Service (NHS) over £1,500,000,000 every year (British Heart Foundation, 2021, Table 4.9; Wilkins et al., 2017, Table 13.3). One of the major clinical concerns following ischemia and subsequent infarction is arrhythmogenicity, the disturbance of the regular heartbeat. The impaired blood supply causes remodelling in the injured area and may enable arrhythmias by preventing the heart's uniform electrical activation. Such arrhythmias need to be terminated quickly, as they prevent efficient contraction of the heart and therefore may cause insufficient blood and oxygen supply in other organs. Therapies to reduce arrhythmic burden in ischemic heart disease are limited and may involve substantial intervention, such as implanting pacemakers or defibrillators.

Therefore, new treatments to improve cardiac function after injury and reduce arrhythmic risk are urgently needed, but their development is not straightforward. First, disease mechanisms need to be understood in detail to identify possible targets. However, investigating the living human heart often involves invasive methods, such as catheter

mapping, and even non-invasive techniques, such as magnetic resonance imaging (MRI) or stress-tests, can be strenuous and costly. Second, once disease mechanisms have been established, targets to act on them need to be identified. This is complicated as diseases present and progress differently in every patient. Hence, finding the right treatment for the right patient at the right time often involves trial and error. Finally, how, when, and how much of a treatment is delivered needs to be determined and, again, may vary from patient to patient. To gain confidence in risk predictions and administration of treatments, large scale clinical trials are required. However, even clinical testing in thousands of patients may still not cover the response of everyone in our population. *In silico*, i.e. computational, technologies may aid to overcome these challenges in developing and testing new treatments.

Simulation studies are routinely used to test new technologies, such as cars and airplanes, and can simulate their performance in everyday use as well as extreme conditions. Such simulation studies enable large scale testing under thousands of scenarios, where each parameter can be precisely controlled and monitored. Therefore, computational tools are considered crucial in practices such as engineering and complement the real-world tests that can be performed in the lab. Recent years have shown the potential of *in silico* tools also for biomedical research to study physiologies and pathologies of different organs including the heart. Recent work has brought forward new human-based tools to create multiscale biophysically detailed human models that pave the way for large scale simulation studies (Aronis et al., 2020; Campos et al., 2018; Camps et al., 2024; Mendonca Costa et al., 2019; Myklebust et al., 2024; Strocchi et al., 2020, 2023; Sung et al., 2020; Tomek et al., 2019; Wang et al., 2021). Furthermore, advanced high-performance graphical processing unit (GPU)-based open-source

modelling and simulation software now enables large scale computational investigations at fine temporal and spatial resolutions (Sachetto Oliveira et al., 2018).

1.1 Thesis goals

The overall aim of my thesis was to design and conduct human-based modelling and simulation studies to investigate arrhythmias and treatments in ischemic heart disease. To achieve this, I addressed the following goals:

I. Integrate state-of-the-art human ventricular electrophysiological modelling and simulation tools and establish their credibility to conduct physiological simulations of ischemia, infarction, and scarring.
II. Design, perform, and analyse simulations of ischemia in small, paediatric-like ventricles to identify arrhythmia mechanisms in rare congenital diseases, with a focus on the role of action potential (AP) variability and ischemia severity to facilitate ventricular fibrillation (VF).
III. Design, perform, and analyse simulations to identify arrhythmia mechanisms of cell injection in the infarcted human ventricles and to investigate the effects of injected cell population heterogeneity, infarct progression, and size on the therapy's safety.
IV. Design, perform, and analyse simulations to mitigate pro-arrhythmic concerns of cell therapy in the human ventricles after myocardial infarction (MI), specifically, to identify ionic targets that suppress automaticity and reduce arrhythmia susceptibility following cell injection.

To achieve the first goal, I integrated established multiscale human electrophysiological modelling and simulation tools (Sachetto Oliveira et al., 2018; Tomek et al., 2019), state-

of-the-art Purkinje networks (Berg et al., 2023; Trovato et al., 2020), personalisation of the biventricular activation to the patient's electrocardiogram (ECG) (Camps et al., 2024), and remodelling induced by ischemic heart disease (Martinez-Navarro et al., 2024; Wang et al., 2021; Zhou et al., 2024). To establish trust in this human ventricular electrophysiological modelling and simulation framework to investigate ischemic heart disease and treatment, I considered verification, validation, and uncertainty quantification principles; this involved comparison of simulated biomarkers against clinical data and carrying out sensitivity and convergence analyses.

To address the second goal, I performed a simulation study of arrhythmic risk during ischemia in small, paediatric-like ventricles. The aim of this study was to improve clinical risk stratification for rare cardiac arrhythmias in congenital diseases by identifying the pro-arrhythmic effects of ischemia-induced electrophysiological remodelling severity, size of the ischemic area, and AP phenotype. As it may determine anti-arrhythmic treatment strategy and risk of sudden cardiac death, I paid particular attention to the morphology of induced arrhythmias and whether they resembled ventricular tachycardia (VT) or VF. Aiming to improve transferability of the results to a paediatric cohort, for which new ethical technologies are even more needed, I conducted the study in small ventricles.

For the third goal, I investigated the safety of regenerative cell therapy by modelling and simulating the electrical activity of the infarcted adult human ventricles following cell injection. The aim of this study was to identify how cell delivery modulates arrhythmic risk in the human ventricles post-MI and whether spontaneous beating of injected cells is necessary to facilitate arrhythmias. First, I assessed the arrhythmic risk after cell injection in chronic infarction without the delivered cells beating spontaneously, instead,

arrhythmic triggers arose from the infarct border zone. Second, I studied how variability in heart rate, Purkinje-myocyte coupling, injected cell population heterogeneity, infarct size, and disease progression from acute to chronic MI may enable automaticity of injected cells. The second part of this study resulted in a journal paper, of which I am the first author of, and which was published recently in Riebel et al. (2024) with DOI: 10.1038/s41598-024-67951-5.

For the fourth goal, to protect against the arrhythmia mechanisms found in the previous study, I systematically modulated the cellular characteristics of injected cells to identify anti-arrhythmic ionic targets. First, I discovered ionic targets that block spontaneous activity in experimentally reported slow and rapid beating cells at day 0 and day 14 after injection. I then used multiscale modelling and simulation to identify and optimise a combination of ionic targets that reduces the cells' long pro-arrhythmic AP duration (APD) whilst maintaining a physiological Ca^{2+} transient (CaT). The latter is crucial for efficient contraction and may hence impact the therapy's efficacy.

To conduct the above simulation studies, I designed, executed, and analysed over 3,000 simulations amounting to approximately 25,000 computational hours.

1.2 Thesis outline

In this section, I provide a summary of each chapter.

In chapter 1, I summarise my thesis' motivation and goals and give an overview of its structure.

In chapter 2, I outline the structure and function of the healthy human heart. Specifically, I give an overview on how the heartbeat emerges and propagates through tissue and how the electrical activity of the heart can be measured in the ECG.

In chapter 3, I review relevant literature to outline the prevalence, presentation, and clinical management of ischemic heart disease. I first outline the causes and long-term effects of ischemia and MI. Next, I discuss how the disease affects the ECG and the mechanisms through which it may induce ventricular arrhythmias. Finally, I consider current and experimental treatments of ischemic heart disease with a focus on regenerative cell therapy.

In chapter 4, I analyse fundamentals as well as advancements in cardiovascular modelling and simulation. I start by introducing the biophysical equations that govern cardiomyocyte excitation and relaxation. Then, I compare different available computational cell models. Next, I outline established mathematical formulations of tissue propagation and three-dimensional (3D) computational modelling and simulation software. This is followed by a discussion on the potential of modelling and simulation to augment clinical risk stratification and the development of new therapies. Finally, I highlight the relevance of verification, validation, and uncertainty quantification.

In chapter 5, I give a detailed overview of the employed modelling and simulation framework and justify computational design choices. I start by outlining the components of modelling and simulating electrical activity of the healthy human ventricles. Next, I present how, based on state-of-the-art techniques, I included functional and structural remodelling induced by myocardial ischemia and infarction. Then, I detail how I modelled and simulated treatment application, such as ionic current block and regenerative cell

therapy. Afterwards, I describe the simulation protocols I designed and the software I utilised, including any customised algorithms. Finally, I demonstrate credibility of modelling and simulation of the human ventricles after ischemic heart disease by considering verification, validation, and uncertainty quantification techniques. Throughout the chapter, I outline experimental and clinical data that was consulted.

In chapter 6, I simulate ischemia in small ventricles with the aim to identify pro-arrhythmic markers and augment clinical risk stratification in paediatric patients. After introduction and review of relevant literature, any additional methods are outlined. Next, I investigate the effects of variability in ventricular size on the ECG and the arrhythmic implications of ischemia severity, AP phenotype, and size of the ischemic region. I then summarise that ventricular size is crucial but that further components need to be introduced to capture all characteristics of paediatric hearts. Furthermore, I conclude that severity of ischemia-induced electrophysiological remodelling and size of the ischemic region modulate arrhythmia inducibility, while AP phenotype is the main determinant of VF over VT-like arrhythmia morphology.

In chapter 7, I motivate the relevance of computational investigations into the safety of regenerative cell therapy and outline any necessary method extensions. I then present my simulations of arrhythmias after cell injection and highlight that delivered cells may introduce pro-arrhythmic substrates with or without the cells spontaneously beating. I further show that arrhythmic risk increased from before to after cell injection and that it was highest in the large investigated scar. I then proceed to determine the arrhythmogenicity of autonomous beating of delivered cells and conclude that atrial-like and nodal-like cells are needed to spontaneously depolarise the ventricles. Finally, I

highlight that chronic infarction and slow sinus beating encourage autonomous beating of injected cells and that impaired Purkinje-myocyte coupling, large scars, and acute infarction promote subsequent arrhythmia-inducibility.

In chapter 8, I build on the arrhythmia mechanisms I identified in Chapter 7. I describe how pre-clinically reported slow and rapid beating spontaneous cell types can be simulated and how their spontaneous beating may act as a trigger for VT. I further outline how experimentally reported maturation of injected cells can be modelled and simulated to study arrhythmic risk longitudinally. Finally, I present and discuss how my simulations enable identifying and optimising ionic targets to reduce arrhythmic burden and preserve calcium dynamics of injected cells.

In chapter 9, I summarise the modelling and simulation studies I carried out throughout this thesis, highlight my work's main contributions, and discuss future directions.

2 Physiological background of cardiac function

In this chapter, I describe the anatomy and function of the healthy human heart. After introducing the heart's main components, I provide detail on its function from single cell to tissue. Finally, I review the ECG as a crucial non-invasive clinical tool.

2.1 Cardiac anatomy

The human heart is positioned in the thoracic cavity in the middle of the chest between the ribs and lungs and embedded in the pericardial sac. Its purpose is to circulate blood through the body, and it does so in two main streams – an oxygen-rich one that enters the heart from the lungs through the pulmonary veins and an oxygen-poor one that comes from the rest of the body through the superior and inferior vena cava. For this, the heart is made up of four main cavities: two upper chambers, the 'atria', and two lower chambers, the 'ventricles', as shown in Figure 1. These are organised into a left and right side; the left atrium and ventricle (LA and LV) are responsible for circulating the oxygenated blood to the other organs through the aorta, whilst the right atrium and ventricle (RA and RV) are to transport the oxygen-poor blood into the lungs using the pulmonary arteries. The left and right side of the heart are separated by the septum. Blood flow between the LA and LV as well as between the RA and RV is guarded by atrioventricular valves, the mitral and tricuspid valve, respectively. Accordingly, blood flow through the body is arranged in a circular, one-way manner as first established by William Harvey in the 17th century, as summarised by Ribatti (2009).

To efficiently distribute blood through the body, the heart is constructed like a pump. The pressure and volume changes in the atria, ventricles, and aorta are often visualised using Wiggers' diagram (Herring & Paterson, 2018, Figure 2.5; Wiggers, 1921, Figure 2). In detail, at rest, i.e. during early diastole, the myocardium is relaxed and blood flows passively through the atria into the respective ventricle. Later during diastole, atrial contraction actively propels further blood into the ventricles until the ventricular pressure rises above the atrial pressure and the atrioventricular valves shut. The ventricles then start their isovolumetric contraction, during which the aortic and pulmonary outflow valves remain shut leading the ventricular pressure to build up further. Once the LV and RV pressure exceed that of the aorta and pulmonary artery, respectively, the outflow valves open and blood is ejected out of the heart. Finally, the outflow valves close, and the atrioventricular valves re-open, and the heart undergoes isovolumetric relaxation, ready for the next cycle.

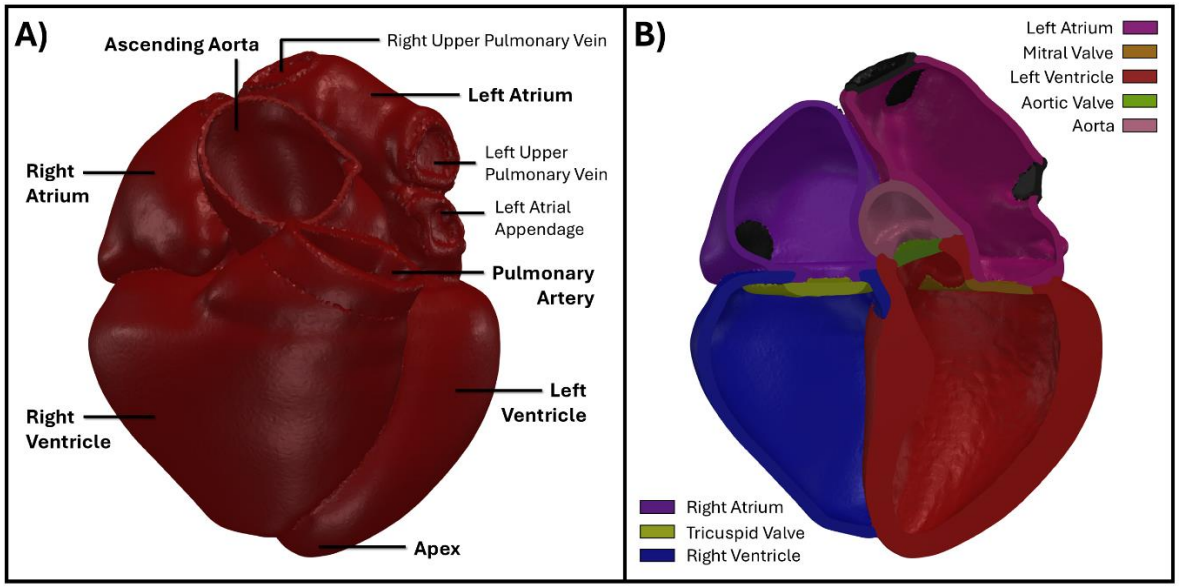


Figure 1. A) Cardiac anatomy from the anterior view and B) cross-sectional view. Important anatomical features are highlighted. Note, in the cross-sectional view, black openings indicate the inferior vena cava in the right atrium and three of the four pulmonary veins in the left atrium. Heart geometry obtained from (Rodero et al., 2021).

The human heart beats about once every second. But during the day, our body's demand for oxygen and nutrients changes. Accordingly, our heartbeat may drop when we sleep but increase during exercise when our muscles need oxygen to function. The heart also

changes as we age. During foetal development, the heart starts as a single tube which twists around itself to form the different chambers (Sherwood, 2001, p. 288). *In utero*, the RV and LV work in parallel rather than in series, pumping blood to different parts of the body (Freed, 2006). After birth, both ventricles quickly adapt to the change in function. The adaptation is especially stressful for the LV as the RV performs most of the pumping work *in utero* (Freed, 2006). This also causes left-sided defects, which may have gone unnoticed *in utero*, to, generally, be more problematic after birth than right sided defects (Freed, 2006). Whilst the heart's mass increases during childhood and adolescence (Joyce et al., 2004; Krupickova et al., 2021; van der Ven et al., 2020), heart rate decreases. Infants typically present with a heart rate of 130 beats per minute (bpm), which decreases over 85 bpm in primary school-aged children to 65 bpm in young adults (Saarel et al., 2018). The heart also changes in advanced age; specifically, the number of cardiomyocytes decreases, the LV becomes hypertrophic, and the vasculature stiffens (Singam et al., 2020). As summarised by Singam et al. (2020), common resulting complications include hypertension, atrial fibrillation, and MI and involve remodelling not only at the tissue but also at the cellular level. Cardiomyocyte excitation and relaxation, which forms the basis for cardiac contraction, is explained in the following section.

2.2 Cellular electrophysiology

The cardiomyocyte is composed of a cytosolic space with a cell nucleus and a sarcoplasmic reticulum (SR), amongst other components, and is surrounded by the cell membrane. The cell membrane is formed by a bilayer of lipids, which have a hydrophobic tail and a hydrophilic head. This makes the cell membrane largely impermeable to ions and proteins. At rest, large amounts of K^+ are available inside the cell, whilst outside the

cell, Cl^-, Ca^{2+}, and Na^+ concentrations are high. This causes electrochemical gradients across the cell membrane which depend, on one hand, on the overall charge inside and outside the cell and, on the other hand, on the diffusive drive of ionic concentrations to balance out.

Cardiac contraction is elicited by the shortening of individual cardiomyocytes. Here, sarcomeres, which are organised into chains inside muscle cells, and Ca^{2+} are key elements (Ebashi & Endo, 1968; Ringer, 1883). Ca^{2+} inside the cell binds to troponin-C, which enables the formation of cross-bridges between thick and thin filaments (Hanson & Huxley, 1953; A. F. Huxley, 1957; H. E. Huxley, 2004). This results in a power stroke that produces contractile force. To allow cardiomyocytes to relax between contractions, Ca^{2+} is transiently flowing in and out of the cell and the SR. This occurs as part of the cell's AP, the change in its membrane potential. An AP is elicited through an electrical stimulus and features not only in cardiac cells but across the body, such as in neurons.

To allow ions such as Ca^{2+} to pass into the cell, the membrane contains transport proteins, such as ion channels, pumps, and exchangers, which are specific to different ion species. Ion channels let ions pass along their electrochemical gradient and may be voltage dependent, meaning that channel opening, closing, and recovery depend on the membrane potential. Ion pumps can transport ions against their electrochemical gradient by using adenosine triphosphate (ATP) (Stys et al., 1995), which is known as primary active transport. Ion exchangers typically use the energy from transporting one ion species along its electrochemical gradient to move another one, potentially against its electrochemical gradient (Alberts et al., 2008, Chapter 11), often referred to as secondary active transport. The following paragraph will introduce key ionic currents that

flow through these channels, pumps, and exchangers, as illustrated on a ventricular AP in Figure 2, and which can be grouped depending on the part of the AP they contribute to.

Upstroke (Phase 1)

- The fast Na^+ current (I_{NaF}), which was identified as crucial for AP initiation by Hodgkin & Huxley (1952) and is encoded by the SCN5A gene: Channels open rapidly when an electrical stimulus depolarises the membrane potential but also swiftly inactivate, causing the sharp spike-like shape of I_{NaF}.

Initial Repolarisation (Phase 2)

- The transient outward K^+ current (I_{to}), encoded by KCND genes (Campbell et al., 1993; Wickenden et al., 1999): The depolarisation of the membrane potential causes K^+ channels to open with the aim to drive the membrane potential back to rest.

Plateau (Phase 3)

- The L-type Ca^{2+} current (I_{CaL}), first suggested by the results of Fatt & Katz (1953) and encoded by the CACNA1C gene: Channels open once the membrane potential has been substantially depolarised and cause an influx of Ca^{2+} into the cell. Increased levels of cytosolic Ca^{2+} cause the ryanodine receptors (RyR) of the SR to open and release further Ca^{2+} into the cell through the release current I_{rel}; this is known as Ca^{2+}-induced Ca^{2+} release.
- The Na^+-Ca^{2+} exchanger current (I_{NaCa}), encoded by the SLC8A1 gene (Baker et al., 1969; Philipson et al., 1988): This current flows throughout the AP but is most active during phase three and four. The exchanger transports three Na^+ for one Ca^{2+} and can reverse its direction depending on the electrochemical gradients of Ca^{2+}

and Na^+. During phase one, it is in 'reverse' mode, causing an influx of Ca^{2+}. For the rest of the AP, it is largely in 'forward' mode, extruding Ca^{2+} from the cell.

- The sarcoendoplasmic reticulum Ca^{2+} ATPase (SERCA) current (I_{up}) (Ebashi & Lipmann, 1962; Hasselbach & Makinose, 1962), encoded by ATP2A genes: This pump restores the Ca^{2+} storage levels within the SR throughout the AP.

Repolarisation (Phase 4)

- The rapid and slow delayed outward rectifier K^+ currents (I_{Kr} and I_{Ks}), encoded by the KCNH2 and KCNQ1 gene, respectively (Noble & Tsien, 1969; Warmke & Ganetzky, 1994): These K^+ channels open slowly and drive the membrane potential back to rest.

Rest (Phase 5)

- The inward rectifier K^+ current (I_{K1}), encoded by the KCNJ2 gene (Noble, 1965; Raab-Graham et al., 1994): This current is usually an outward current that transports K^+ out of the cell to stabilise the membrane potential, especially during repolarisation and rest. However, when the cell is hyperpolarised, it allows K^+ to flow into the cell.
- The Na^+-K^+ pump current (I_{NaK}), discovered by Skou (1957) and encoded mainly by ATP1A and ATP1B genes: The pump is active throughout the whole AP, transporting three Na^+ out of the cell and two K^+ into the cell. While it is most active during phase one to four, it serves a crucial role during rest by restoring K^+ levels inside the cell.

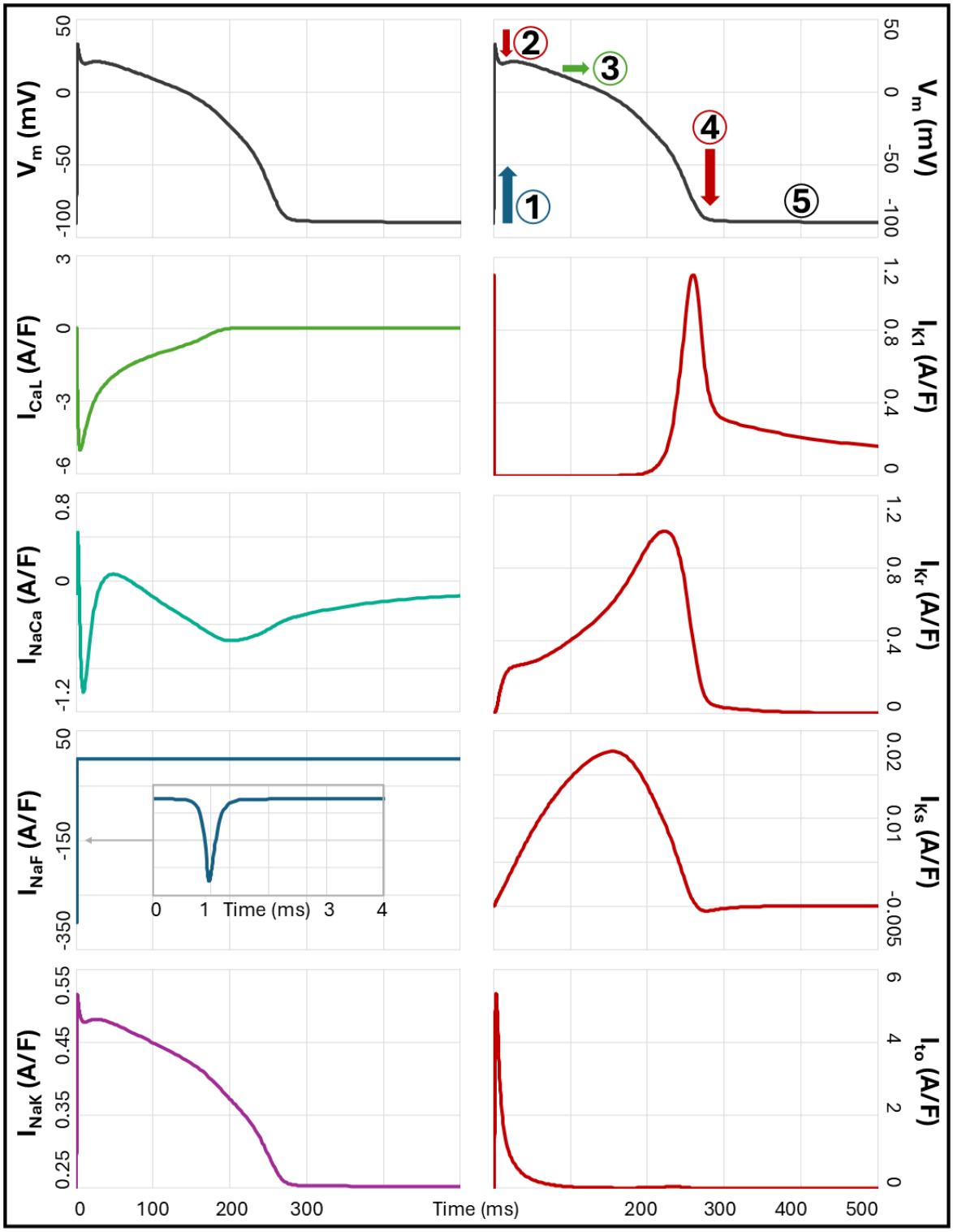


Figure 2. Simulated AP of ventricular cardiomyocytes (top row, using the ToR-ORd model (Tomek et al., 2019)) and key contributing ionic currents (bottom four rows). AP phases 1-5, i.e. upstroke, initial repolarisation, plateau, repolarisation, and rest, are indicated in the colour of the most contributing ionic currents: Ca^{2+} currents in green, Na^{+} currents in blue, and K^{+} currents in red.

Following the AP, ion channels such as I_{NaF} and I_{CaL} are inactivated. Hence, the cell is 'refractory' and cannot be excited again immediately. After stimulation, the ventricular myocardium is fully refractory for about 250 ms; this is followed by a relative refractory

period during which a strong stimulus may be required to re-excite the cell and only a diminished, shorter AP may be produced (Herring & Paterson, 2018, p. 40).

The heart contains different types of cells, which, depending on their location and function, may exhibit different AP morphologies. Specifically, endocardial and epicardial cells within the ventricular wall have been shown to express slightly different APs (Boukens et al., 2015; Franz et al., 1987). A distinct mid-myocardial AP phenotype within the subendocardium has also been reported, although its existence is subject of an ongoing debate (Nattel et al., 2011). AP differences also exist between the top (the 'base') and the bottom (the 'apex') of the ventricles (Burdon-Sanderson & Page, 1880; Okada et al., 2011; Szentadrassy et al., 2005) as well as across the atria (Aslanidi et al., 2008; Feng et al., 1998). At the top of the RA, the sinoatrial node is located. Sinoatrial nodal cells express the funny channel, which opens during diastole and gives rise to the 'funny' or 'pacemaker' current (I_f), encoded by the HCN4 gene (Brown et al., 1979; DiFrancesco, 2010). I_f in combination with an intrinsic Ca^{2+}-clock, which is enabled by spontaneous Ca^{2+} release from the SR and also depends on I_{NaCa} (Bogdanov et al., 2001; Rubenstein & Lipsius, 1989), allows the sinoatrial nodal cells to spontaneously create APs, without prior electrical excitation. These spontaneous depolarisations drive the normal heartbeat, which propagates from the sinoatrial node through the heart, as described in the next section.

2.3 Tissue propagation

Individual cardiomyocytes are linked together via gap junctions, a connection that forms between two cells through protein structures that act as small tunnels, called connexons (Brightman & Reese, 1969; Sherwood, 2001, p. 56). In the human ventricles, connexin 43

is most abundantly expressed, whereas in the atria, connexins 40 and 45 may also be found (Vozzi et al., 1999). Gap junctions are crucial in cardiomyocytes because they enable cell-to-cell communication and coordinated contraction (Weidmann, 1952). To enable efficient contraction of the whole heart, cardiomyocytes are organised in fibres and sheets. The number of connexons within and between fibres and sheets varies, with the conduction speed being highest in the fibre direction (Caldwell et al., 2009; Taggart et al., 2000). Cardiac fibres are arranged spirally around the heart to allow for a 'wringing' motion upon contraction that encourages blood flow out of the ventricles, into the aorta, and through the pulmonary arteries (Sherwood, 2001, p. 289).

The signal from the spontaneously beating sinoatrial node propagates through the atria to the atrioventricular node. It then travels along the bundle of His, through the left and right bundle branches, across the rapidly conducting Purkinje fibres, and finally, into the Purkinje junctions, which in human hearts are coupled to the ventricular endocardium. While conduction speed in the ventricular myocardium is around 50 cm/s, it can reach 200 cm/s in the Purkinje fibres (Durrer et al., 1970). Although Purkinje cells – discovered by Jan Evangelista Purkyne in the 19th century, as summarised by Cavero et al. (2017) – make up only a small fraction of the ventricular tissue, they are of high importance for uniform cardiac excitation and may also be involved in arrhythmogenesis (Haissaguerre et al., 2016).

2.4 The healthy human electrocardiogram

The ECG – pioneered by Willem Einthoven, who was awarded the Nobel Prize in 1924 – allows for observing the spread of excitation across the heart on the body surface (Einthoven, 1895; Waller, 1887). Usually, three limb electrodes are placed on the left arm,

right arm, and left leg (forming Eindhoven's triangle) and six chest electrodes are placed on the torso as shown in Figure 3.

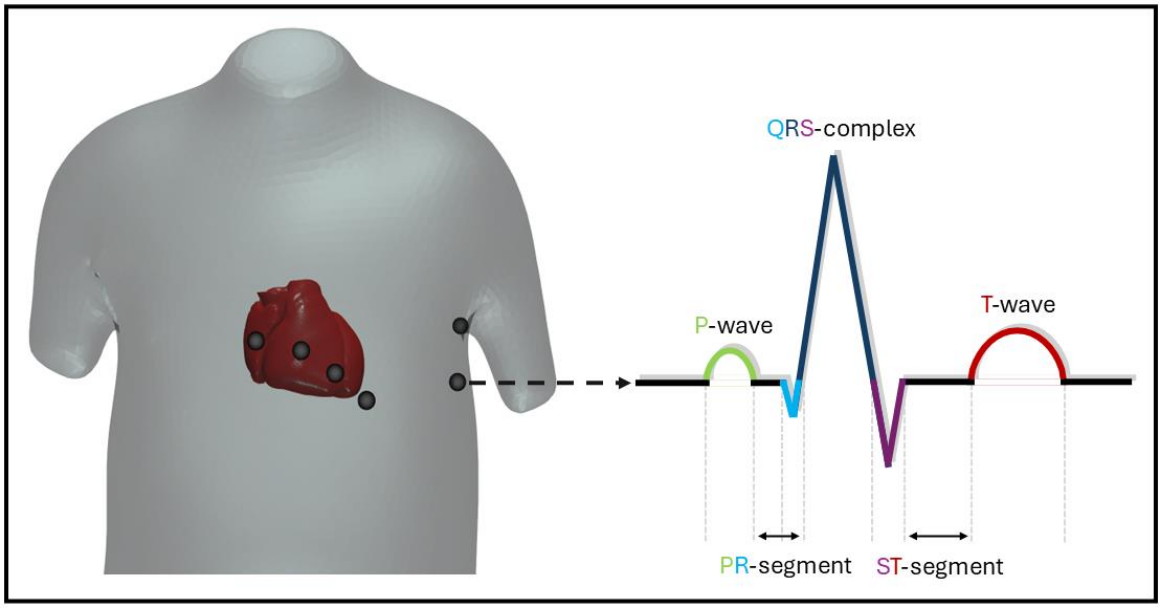


Figure 3. The healthy ECG signal. Left: heart (Rodero et al., 2021) within the torso (Mincholé et al., 2019) with precordial lead electrodes indicated. Right: illustrative ECG signal with P, Q, R, S, and T waves indicated in green, light blue, dark blue, purple, and red, respectively.

From these ten electrodes and using the Wilson's terminal (V_w), which is the average of the voltages measured at the left arm, right arm, and left leg (Wilson et al., 1934), twelve ECG 'leads' are calculated as follows:

- $I : left\ arm\ -\ right\ arm$
- $II : left\ leg\ -\ right\ arm$
- $III : left\ leg\ -\ left\ arm$
- $aVR : right\ arm\ -\ \frac{left\ arm + left\ leg}{2}$
- $aVL : left\ arm\ -\ \frac{right\ arm + left\ leg}{2}$
- $aVF : left\ leg\ -\ \frac{left\ arm + right\ arm}{2}$
- $V1\ to\ V6 :\ V_i - V_w$

These leads measure the electrical wave as it travels through the heart from different angles. Depending on the orientation of the electrode, electrical activity of different areas will be in focus. Specifically, leads V1 and V2 are known as the septal leads, leads V3 and

V4 are called anterior leads, leads I, aVL, V5, and V6 are oriented towards the lateral wall, and leads II, III, and aVF are known as inferior leads.

An ECG signal typical for leads V4 to V6 is shown in Figure 3. The healthy ECG exhibits five main waves, which may not be visible in all leads: the P, Q, R, S, and T waves. The P-wave indicates the activation of the atria, whilst the QRS complex is caused by ventricular excitation. Finally, the T-wave shows repolarisation of the ventricles. The ECG contains detailed information about the heart rate and how the electrical excitation spreads across the heart. It is a key clinical tool to identify abnormal heart rhythms, i.e. arrhythmias, and impaired conduction, e.g. resulting from infarction (Sherwood, 2001, p. 300). MI and ischemic heart disease in general are the subject of the next chapter.

3 Literature review of ischemic heart disease burden and treatment

Whilst in the previous chapter I focused on the structure and function of the healthy human heart, in the following I will review the prevalence, presentation, and treatment of cardiac disease, specifically ischemic heart disease.

3.1 Causes and prevalence of ischemic heart disease in young and old

Despite increased survival rates, cardiovascular disease remains the leading cause of death worldwide, attributing to around 30% of deaths (World Health Organization, 2021). Often, the underlying cause is related to ischemic heart disease; ischemia is defined as an insufficient blood, and therefore oxygen, supply. This may be the result of plagues rupturing in the coronary arteries (referred to as type 1 ischemia) or of an otherwise caused imbalance of oxygen demand and output (known as type 2 ischemia), the latter may be due to coronary microvascular dysfunction, sustained tachyarrhythmias, or anaemia (Thygesen et al., 2019). If this lack of oxygen prevails, it may cause necrosis of the affected tissue and ultimately MI, or more commonly known as a heart attack. After a prolonged ischemic period, acute infarction can occur, usually lasting hours to days (Antman et al., 2000). Succeeding phases are referred to as healing (days to weeks) and healed or chronic (months) (Antman et al., 2000).

Throughout ischemia and infarction, a range of structural and functional remodelling has been observed. Specifically, during ischemia, the interrupted blood supply has three main effects on the myocardium: Hypoxia, hyperkalaemia, and acidosis (Kodama et al.,

1984; Moréna et al., 1980), which usually reverse once blood supply is restored. Hypoxia denotes the lack of oxygen, which impacts the cells' abilities to metabolise ATP from glucose (Flood et al., 2023; Heerlein et al., 2005). In cardiomyocytes, this results in an activation of the ATP-sensitive K^+ current (I_{KATP}) (Noma, 1983; Weiss et al., 1992), and may further impact the function of I_{NaK} (Cross et al., 1995; Winston et al., 1990), I_{up} (Ronkainen et al., 2011), and mitochondrial Ca^{2+} buffering (Griffiths et al., 1998; Nayler et al., 1979; Shen & Jennings, 1972). Hyperkalaemia describes elevated extracellular K^+ concentrations due to limited wash-out (Harris et al., 1954; Weiss & Shine, 1982). Finally, acidosis occurs when the blood becomes too acidic causing a reduced conductance of I_{NaF} and I_{CaL} in the heart (Sato et al., 1985; Yatani et al., 1984). Together, these result in a decreased APD and elevated maximum diastolic membrane potential (MDP) in the injured area and may also affect the border zone surrounding it. In turn, these electrophysiological changes introduce repolarisation abnormalities into the tissue and may promote arrhythmias as discussed in a recent review by Oknińska et al. (2022). Indeed, arrhythmogenicity has been observed to be highest in the first 10 minutes after ischemia onset (Moréna et al., 1980) and arrhythmic episodes are often grouped into stage Ia (first 10-15 minutes) and Ib (first 15-30 minutes) (Janse & Wit, 1989; Kaplinsky et al., 1979). Distinct arrhythmia mechanisms have been suspected to be responsible for the surge in arrhythmias during stage Ia versus Ib and have also been linked to an increase in conduction failure as the cells become necrotic (Janse & Wit, 1989; Rodríguez et al., 2004; Russell et al., 1984).

Hyperkalaemia has also been reported during acute MI and was linked to an increased mortality rate (Grodzinsky et al., 2016). Reduced I_{CaL} and I_{NaF} appear to persist in the injury from early ischemia until chronic MI, and, additionally, diminished conductance of K^+

currents, such as of I_{to}, I_{Kr}, and I_{Ks}, have been observed from early infarction onwards as summarised by Pinto & Boyden (1999). Reduced I_{NaF}, which is crucial in enabling the AP upstroke and hence quick electrical propagation, and increasing necrosis cause a reduced and eventually failing conduction within the infarct. Furthermore, as infarction progresses, the ability to restore Ca^{2+} deposits within the SR through I_{up} has been reported to decrease (Høydal et al., 2018; M. T. Jiang et al., 2002). Similar to ischemia, these changes, particularly the loss of conduction in the infarct, give rise to activation and repolarisation heterogeneities within the heart and may facilitate post-MI arrhythmias. Ventricular arrhythmias may be more prevalent in patients who receive late treatment or have had previous MI (Podolecki et al., 2018).

Cardiomyocyte necrosis not only affects the injured myocardium but also implies increased loading conditions for the heart overall; as summarised by Sutton & Sharpe (2000), intracellular signalling triggers reparative processes such as dilation, hypertrophy, and scarring. This remodelling in the infarct as well as the remote non-infarcted tissue may cause reduced ejection fraction (EF), increased tissue stiffness, and overall, ventricular dysfunction, as highlighted in a review by Garza et al. (2015). Accordingly, an increased risk of heart failure has been identified in patients with ischemic heart disease (Cahill & Kharbanda, 2017; Gerber et al., 2016; Roger, 2013). 83% of UK deaths associated with coronary heart disease, including MI, occur in patients aged 65 and over, although younger people, especially men, are affected too (British Heart Foundation, 2024a, Analysis of official UK mortality data, Table 1.1).

The proportion of people over 60 is estimated to almost double from 12% in 2015 to 22% in 2050 (World Health Organization, 2024). Improved treatments and advancements in

clinical interventions have resulted in a lower mortality rate of cardiovascular disease; however, most patients are of older age, which, because of the overall aging population, causes a rise in cardiovascular disease morbidity (Kelly, 1997). As previously mentioned, old age is often associated with adverse cardiac remodelling, such as increased vascular stiffness, hypertrophy, and hypertension, as well as an elevated risk of MI.

Myocardial ischemia in younger people is rare and often linked to congenital heart disease, such as coronary artery anomalies or chromosomal abnormalities, such as Williams-Beuren syndrome (Bird et al., 1996; Carmona et al., 2013; Pober et al., 2008; Salzillo et al., 2024; Takahashi, 2010). Whilst rare, sudden cardiac death in children is commonly associated with such congenital heart diseases or inherited structural and electrical arrhythmic syndromes and, as discussed in Gajewski & Saul (2010), may occur quickly within minutes after symptoms start. Being uncommon, the mechanisms behind myocardial ischemia in children are less well understood than in adults. Furthermore, the heart develops rapidly during childhood, making accurate risk prognosis difficult. Most importantly, ethical concerns and small numbers of patients limit drug trials for paediatric diseases, as pointed out by Ahmed et al. (2023).

To summarise, myocardial ischemia and subsequent infarction are a common cause of heart failure and sudden cardiac death. Novel tools to better understand underlying mechanisms and identify new treatments are urgently needed, particularly in young patients with rare congenital heart diseases.

3.2 Clinical manifestation – the ischemic and infarcted electrocardiogram

Clinically, myocardial ischemia and infarction are often identified through ECG abnormalities. During acute ischemia, hyperacute T-waves and elevated or depressed ST-

segments are commonly observed (Nable & Brady, 2009). As described in the previous section, during ischemia, hypoxia and hyperkalaemia may lead to shorter APDs and elevated MDPs. Accordingly, transmural ischemia leads to transmurally disturbed activation and repolarisation, which often manifests as ST-segment elevation MI, referred to as 'STEMI'; non-ST-segment elevation MI may indicate that only some parts of the myocardial wall are ischemic (Vogel et al., 2019). As MI develops, fragmented QRS-complexes, which are associated with adverse LV remodelling (Chew et al., 2018), and pathological Q waves, which may also be indicative of transmural MI, can occur (Antman et al., 2000; Raffel & White, 2007, p. 261). Whilst inverted T-waves are common in early stages, they may normalise in chronic MI (Nable & Brady, 2009).

As introduced in Section 2.4, the different ECG leads allow for 'viewing' the heart's electrical activity from different angles. Hence, MI location and the affected coronary artery may be inferred from the lead in which the abnormalities manifest. Specifically, abnormalities in leads I, aVL, V5, and V6 suggest a lateral infarct, which is usually caused by obstruction of the left circumflex artery. Changes in leads II, III, and aVF may indicate an inferior infarct and occlusion of the right coronary artery. A block in the left anterior descending artery (LAD), which supplies the septal and anterior walls, commonly manifests in leads V1 to V4. Anterior infarction has been shown by Stone et al. (1988) to result in an increase of adverse outcomes, such as larger infarct size and likelihood to develop heart failure.

3.3 Arrhythmogenicity of ischemic heart disease

As described in Section 3.1, the electrophysiological and structural remodelling induced by ischemia and MI is associated with an increased risk of ventricular arrhythmias, as

summarised in a review by Ghuran & Camm (2001). Re-entry has been suggested as a fundamental mechanism underlying a large proportion of such cardiac arrhythmias (Janse et al., 1980; Mines, 1913; Paterson, 2013; Wit & Cranefield, 1978). As shown in Figure 4, re-entry requires a trigger and a substrate. If the trigger, i.e. an ectopic electrical signal, meets unidirectional conduction block at the substrate, i.e. an area of heterogeneous activation or repolarisation, it cannot uniformly excite the ventricles. Instead, the wavefront travels around the refractory area and, should this be re-excitable by the time the ectopic signal has reached the other end, re-enters. The following sections will describe the role of myocardial ischemia and infarction to provide re-entry triggers as well as substrates.

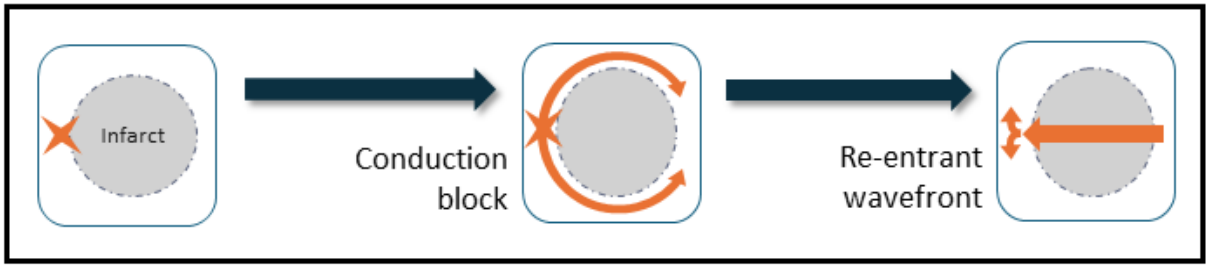


Figure 4. Re-entrant circuit mechanisms as demonstrated in Mines (1913) and Janse et al. (1980).

3.3.1 Trigger for ventricular arrhythmias

Different triggers for ventricular arrhythmias have been suggested in ischemic heart disease. They may be caused by automaticity or by repolarisation abnormalities and may clinically present as premature ventricular complexes (Marcus, 2020). Automaticity in the ventricles may be the result of Purkinje cells (Friedman et al., 1973; Szumowski et al., 2004), which can produce spontaneous beats but, in the healthy heart, are suppressed by the sinus rhythm. Following ischemia, ionic currents, particularly I_{CaL} and the T-type Ca^{2+} current (I_{CaT}), may be remodelled in Purkinje cells and cause changes in their repolarisation and automaticity (Boyden & Pinto, 1994; Ideker et al., 2009). Ectopy after

ischemia may also be caused by the 'injury current'. Injury currents flow from the injury into the surrounding border zone and vice-versa and are caused by heterogeneous APs in the two regions (Coronel et al., 1991; Janse et al., 1980; Picard et al., 1999). In detail, on one hand, the ischemic core at rest may present with an elevated MDP, as previously described, and hence may depolarise the border zone. On the other hand, due to its shortened APD, the injury may be depolarised by the surrounding, still repolarising cells. Other causes for ectopic beats are early after depolarisations (EADs) and delayed after depolarisations (DADs). EADs may form when APs are prolonged and Ca^{2+} channels are reactivated (January et al., 1991; Zeng & Rudy, 1995), while DADs are often the result of Ca^{2+} overload and Ca^{2+}-induced Ca^{2+} release (Fink et al., 2011; Marban et al., 1986). Overall, premature ventricular complexes have been shown to commonly arise in post-MI border zones (Amoni et al., 2021; Marrouche et al., 2004) but may also occur in healthy patients, including children (Cohen, 2019).

3.3.2 Substrate for ventricular arrhythmias

Remodelling during ischemia and following MI introduces structural and functional heterogeneities into the heart. Particularly, hypoxia, which causes I_{KATP} channels to open, and hyperkalaemia may cause an elevated MDP and shorter APD during ischemia (Kodama et al., 1984; Moréna et al., 1980). This may lead to ectopic beats propagating in the ischemic area while the surrounding tissue is still refractory.

Conversely, post-MI remodelling often causes an increase in the border zone and infarct zone APD (Srinivasan et al., 2019; Wickenden et al., 1998). Hence, ectopic beats originating in the border zone may meet unidirectional conduction block at the infarct core, facilitate propagation around the refractory obstacle, and enable a re-entrant

wavefront. Unidirectional conduction block may be encouraged by scarring of the affected area, which leads to a slowed conductivity within the infarct (Aronis et al., 2020; Jamil-Copley et al., 2015).

3.4 Clinical management of ischemic heart disease

Over 64% and 38% of MI patients with and without previous MI, respectively, have been estimated as 'silent', meaning they occur without chest-pain (Burgess et al., 2010; Lu et al., 2015; Valensi et al., 2011). Other symptoms include abnormal heart rate, fatigue, and shortness of breath and may be misinterpreted as other conditions. To minimise damage caused to the myocardium after MI, immediate hospitalisation is essential but often delayed, especially in silent MI. Therapy outcomes and number of adverse events have been shown to improve if treatment is administered within the first couple of hours after MI (Boersma et al., 1996). However, Zijlstra et al. (2002) highlighted that patient characteristics, such as sex and age, may also be a crucial factor, as they influence symptom presentation, treatment delay, and overall therapy outcome.

As outlined in the guidelines of the European Society of Cardiology (Byrne et al., 2023), immediate treatments often include antiplatelet drugs, such as aspirin and $P2Y_{12}$ receptor antagonists, and cholesterol-lowering medication, such as statins, to reduce the risk of further blood clots. Through injection of contrast agents, angiography may be performed to image the coronary arteries and identify the occluded vessel (Byrne et al., 2023; Proudfit et al., 1966). Finally, reperfusion or revascularisation therapy, such as percutaneous coronary intervention, which may use coronary balloon angioplasty and stents, can be used to restore blood flow through the affected arteries (Byrne et al., 2023; Grüntzig, 1978; Lu et al., 2015).

Long term management of MI includes continued prescription of statins and in heart failure patients may also involve angiotensin-converting enzyme (ACE) inhibitors, mineralocorticoid receptor antagonists (MRA), or angiotensin receptor/neprilysin inhibitors (ARNI) (Byrne et al., 2023). Cardiac rehabilitation and exercise training have also been shown beneficial (Garza et al., 2015). Clinical management post-MI focuses not only on restoration of cardiac function but also on reduction of arrhythmic events, which, as described in the previous section, are commonly observed during and after ischemia. Current guidelines recommend amiodarone, catheter ablation, and, where the LVEF is below 40%, beta-blockers for recurrent ventricular arrhythmias (Byrne et al., 2023; Zeppenfeld et al., 2022). In heart failure patients with a LVEF below 35% or those with ventricular arrhythmias persisting for at least 6 weeks after revascularisation, cardiac resynchronisation therapy, e.g. implanting a pacemaker or defibrillator, may also be considered (Byrne et al., 2023; Zeppenfeld et al., 2022).

Despite rehabilitation therapies, damage and remodelling in the myocardium are currently irreversible. Although the heart is capable of self-renewal, this happens at a slow rate. Bergmann et al. (2009) showed that only approximately 1% of cardiomyocytes renew every year in 25-year-olds with the number decreasing to 0.45% in people aged 75. Novel treatments to restore viable myocardium are hence needed.

3.5 Experimental treatments - regenerative cell therapy

The human heart does not sufficiently regenerate on its own and renewing the damaged myocardium is currently not clinically feasible. Organ transplantation often remains the only option for end stage heart failure patients but is limited by available and suitable donor organs (Martesanz, 2012). Tissue and cell transplantation for regenerative

medicine is hoped to achieve similar success whilst offering greater availability. Cell therapy can be exploited not only to halt the effects of ageing but also for a wide variety of conditions, such as neurological disorders (Ul Hassan et al., 2009), fractured bones (Iaquinta et al., 2019), and cardiovascular disease (Braunwald, 2018).

Scientists aim to establish cardioprotective therapies, i.e. prevent pathological remodelling shortly after infarction, as well as cardiorestorative therapies, such as reversal of remodelling and improvement of contractility throughout later post infarct stages (Terzic & Behfar, 2014). Different cell types and delivery methods have been explored in search of the safest and most efficient approach. Multipotent cells are often considered because they can differentiate into several cell types of the same lineage, e.g. stem cells of the mesoderm germ layer can produce heart, muscle, blood, and bone vessel cells (Sanchez et al., 2012, pp. 90–91). Progenitor cells are specialised multipotent cells and can give rise to cells of the same tissue or organ. Multipotent stem cells may be beneficial when introduced into damaged tissue due to paracrine signalling and differentiation into new vital cardiomyocytes (Ferraris, 2016).

Injection of *ex vivo* cultured stem cells and human stem cell-derived cardiomyocytes (hPSC-CMs) is hoped to introduce vital new tissue into the heart to restore its function and reduce the risk of heart failure. Pre-clinical studies have proposed a range of suitable cell types, culturing protocols, and delivery techniques and indeed shown beneficial effects such as improvements in EF (Foo et al., 2018; Liu et al., 2018; Querdel et al., 2021; Shiba et al., 2016; Zimmermann et al., 2006). For example, studies found that ventricular progenitors derived from embryonic stem cells form tissue patches *in vivo* and improve EF in mice post MI (Bu et al., 2009; Foo et al., 2018). Other groups have studied the

delivery of *in vitro* cultured hPSC-CMs, which are derived by differentiating induced or embryonic stem cells into mesoderm progenitors which are further differentiated over cardiac mesoderm cells, into heart field specific progenitors, and finally into cardiomyocytes (Mummery et al., 2012).

3.5.1 Delivery of regenerative cells into the human heart

Delivery of cells with regenerative potential into the heart has been achieved by injection or by embedding a tissue patch. Different injection methods, such as intravenous, intracoronary, and intramyocardial (Dib et al., 2010, 2011), have been investigated but all struggle to achieve controlled retention of the injected cells. Intramyocardial cell delivery can be administered epicardially through minimally invasive open-heart surgery and may be more reliable, whilst catheter-based transendocardial injection, during which the cells are injected from inside the heart via a catheter into the endocardium, can be used as a less invasive and more easily repeatable alternative, as summarised by Dib et al. (2011). Intracoronary injection may use delivery via a catheter and may be beneficial for acute MI (Dib et al., 2010, 2011). Intravenous injection however has been reported to result in entrapment of cells in the lungs (Barbash et al., 2003). The choice of method depends on the patient's condition and disease presentation. For example, while intramyocardial injection is less dependent on cell migration, it does not allow for access to all areas of the heart and may complicate treatment for some scar locations.

Poor retention of injected cardiomyocytes is a major hurdle; Hong et al. (2013) showed over 90% of cells injected into the mouse heart to disappear within the first day. To direct migration towards the infarct and increase cell survival and efficiency, different strategies have been explored. Laflamme et al. (2007) developed a pro-survival cocktail that

substantially increased graft size after infarction in rat models. Another study employed magnetic targeting to direct cells towards the ischemic zone, which resulted in improved cell retention and engraftment (K. Cheng et al., 2010). Engineered tissue patches, hydrogels, and scaffolds were studied to improve poor retention and reviewed by Garbern & Lee (2013). As discussed by Jawad et al. (2007), cardiac tissue engineering aims to create 3D scaffolds using meshes, patches, or foams, which are cultured with cells. Cardiac tissue engineering and supporting biomaterials aim to mimic the cardiac microenvironment to increase adhesion, control cell growth, and direct migration (Davis et al., 2005). However, this provides challenges because patches above 400 µm thick may be difficult to vascularise sufficiently as suggested by Riegler et al. (2014), whilst much thinner patches may fail to provide the necessary mechanical strength to support diastole as well as systole (Mancuso et al., 2020; Reis et al., 2016).

3.5.2 Clinical trials of cardiac regenerative therapy

A series of trials investigated the safety and efficacy of cell therapy. For example, the C-CURE trial intramyocardially injected mesenchymal stem cell-derived cardiac cells after ischemic heart failure and conducted cell therapy in 21 patients with a reduced LVEF of 15% to 40% (Bartunek et al., 2013). Bartunek et al. (2013) concluded an improved LVEF, reduced LV end-systolic volume, increased 6-minute walk distance, and overall safety of the method. C-CURE was followed by the larger CHART-1 trial, which administered cardiopoietic cells in 120 patients with chronic ischemic heart failure (Bartunek et al., 2017). The primary end point for the trial was neutral and only showed significant improvements for patients with severe heart enlargement, defined by a LV end-diastolic volume between 200 and 370 mL (Bartunek et al., 2017, 2020; Yamada et al., 2024).

Another study, the ESCORT trial, showed benefits of delivering fibrin patches with an area of 20 cm^2 and loaded with embryonic stem cell-derived cardiac progenitors into human hearts (Menasché et al., 2018). Menasche et al. (2018) recruited six patients with severe LV dysfunction and a history of MI older than 6 months. None of the patients exhibited sustained ventricular arrhythmias during the follow-up period, no teratomas were detected, and, where necessary, only low doses of immunosuppressants were administered (Menasché et al., 2018). The ESCORT trial showed an overall improvement in NYHA functional class from III to I/II and an increase in LVEF from 26% to 38.5% at one-year follow-up (Menasché et al., 2018).

In 2020, the first patients received hPSC-CMs through early phase clinical trials, as discussed by Mallapaty (2020). For example, the HEAL-CHF trial aims to inject around 100 million hPSC-CMs during coronary-artery bypass surgery (Zhang et al., 2022). Another trial focused on the delivery of hPSC-CM sheets, but, so far, the treatment has not shown beneficial and instead, adverse events were reported, as discussed by Cyranoski (2018) and Cyranoski et al. (2023). Cell sheet transplantation, although in pre-clinical studies indicating better cell retention, involves more invasive delivery and hence may not be suitable for patients in critical conditions, where cell injection may be more beneficial (Mallapaty, 2020).

Although cell injection may involve multiple injections rather than a single surgery, cell therapy delivery methods are generally less invasive than organ transplantation. Considering eligible patients are severely unwell, often with heart failure, strenuous surgery can be an additional risk factor. Organ transplantation proposes the risk of adverse immune reactions, which could lead to diminished therapy success and even

life-threatening events. As reviewed by Herberts et al. (2011), adverse immune reactions may also occur after cell therapy. Furthermore, as mentioned previously, most cells after delivery have been observed to not engraft long-term. This raises the question of how long beneficial effects of cell therapy last. Additionally, it is currently unclear if cell therapy needs to be repeated and how often it is safe to be repeated on the same individual.

In conclusion, many clinical studies on regenerative cell therapies are still in early phases. While some of the discussed trials indicate safety and beneficial effects, optimal delivery method may vary between patients.

3.5.3 Advantages and limitations of regenerative therapy for the heart

Translation of cell therapy into routine clinical practice is limited by uncertainty regarding the therapy's safety and optimal delivery. Specifically, the mechanisms that guide cell migration remain largely unclear, which makes reliability and consistency of therapy success difficult to predict and raises further safety concerns because cells could potentially form grafts in remote tissue, as discussed by Herberts et al. (2011). Next, while efficiency to generate large numbers of hPSC-CMs has been increased over the years, maturation within a reasonable timeframe as well as exact purification remains challenging (Ban et al., 2017; Yang et al., 2014). Poor purification of cultured cell populations can lead to a mix of cell types, including non-differentiated stem cells, non-cardiomyocytes, or nodal-like cells. Different cell types and ratios of ventricular-like, atrial-like, and nodal-like cells can be targeted by specific differentiation and purification protocols, as highlighted in several reviews (Ban et al., 2017; Devalla & Passier, 2018; B. Jiang et al., 2020). As discussed by B. Jiang et al. (2020), impure cell populations containing also undifferentiated stem cells can furthermore increase the risk of teratoma,

a kind of tumour which is composed of different cell types. Cell population heterogeneity may also have crucial pro-arrhythmic implications, which need to be assessed before clinically deploying cell therapy (Selvakumar et al., 2024).

Alongside the above safety concerns, which apply to most cell therapies, there are further apprehensions on cell therapy in the heart. Specifically, hPSC-CMs have a mostly immature structure and function compared to adult cardiomyocytes (Machiraju & Greenway, 2019). They may exhibit an immature contractile function (Ribeiro et al., 2015), round morphology (Machiraju & Greenway, 2019), and uniformly rather than anisotropically distributed connexin 43 expression (Filice et al., 2020). Furthermore, as summarised by Feric & Radisic (2016), hPSC-CMs are smaller than adult cardiomyocytes and may present with reduced electrical excitability. Additionally, hPSC-CMs express foetal-like characteristics such as slow maximum upstroke velocity (dV/dt_{max}), a depolarised MDP, low AP amplitude, and spontaneous beating behaviour (Ma et al., 2011). Overall, these immature characteristics give concern for arrhythmias when the cells are introduced into the adult heart. Indeed, experimental studies have observed a range of tachyarrhythmias following cell delivery, which have been largely attributed to the cells' spontaneous beating activity (Chong et al., 2014; Liu et al., 2018; Marchiano et al., 2023; Romagnuolo et al., 2019). It has also been pointed out that studies using smaller animal models have observed few arrhythmia incidents and that therefore arrhythmic risk after cell therapy might be linked to heart size and rate (Chong et al., 2014). Automaticity in hPSC-CMs, which has been reported in the range of about 30 to 80 bpm, has been accredited to the presence of I_f (Chauveau et al., 2017) as well as the Ca^{2+}-clock in combination with I_{NaCa} (Kim et al., 2015).

4 Analysis of computational tools to simulate cardiac electrophysiology

In this chapter, I will provide a review and analysis of state-of-the-art computational techniques to simulate cardiac electrophysiology. Specifically, I describe fundamental mathematical equations and discuss available tools.

4.1 Fundamentals in mathematical modelling of cellular electrophysiology

As discussed in Section 2.2, the cardiac AP is mainly enabled by Na^+, K^+, Cl^-, and Ca^{2+} ions crossing the cell membrane through ion channels, pumps, and exchangers. For an ion s, its flux ($\boldsymbol{\Phi_s}$) is driven, firstly, by the concentration gradient of s between the intracellular *(i)* and extracellular *(e)* spaces and, secondly, as ions contain an electrical charge, by an electrical gradient.

The diffusion flux $\boldsymbol{\Phi_{d,s}}$ is derived from Fick's first law, where D_s is the diffusion coefficient and ∇C_s denotes the concentration gradient for a particular ion:

$$\boldsymbol{\Phi_{d,s}} = -D_s * \nabla C_s \tag{1}$$

An ion's electrical flux ($\boldsymbol{\Phi_{e,s}}$) generated by an electrical field ($\boldsymbol{E} = -\nabla V$) is given as described by Maexa (2022):

$$\boldsymbol{\Phi_{e,s}} = \mu_s * Z_s * C_s * e * \boldsymbol{E} \tag{2}$$

Here, μ_s denotes the ion's mobility, Z_s the valence of the ion, and e the unit charge. Using the Einstein relation $\mu_s = \frac{D_s}{k_B * T}$ (with $k_B :=$ Boltzmann constant and $T :=$ temperature)

and that $\frac{k_B T}{e} = \frac{RT}{F}$ (where $R :=$ gas constant and $F :=$ Faraday's constant), Equation (2) becomes:

$$\boldsymbol{\Phi_{e,s}} = -\frac{FD_s}{RT} * Z_s * C_s * \nabla V \tag{3}$$

Combing Equations (1) and (3) yields the Nernst-Planck equation:

$$\boldsymbol{\Phi_s} = -D_s * (\nabla C_s + \frac{FZ_s C_s}{RT} * \nabla V) \tag{4}$$

At equilibrium $\boldsymbol{\Phi_s} = 0$, the two fluxes balance each other out and result in:

$$\nabla V = -\frac{RT}{FZ_s}\frac{\nabla C_s}{C_s} \tag{5}$$

Considering a membrane between the intracellular and extracellular space and assuming the flux of ion s occurs in one direction orthogonal to this cell membrane, Equation (5) gives the Nernst or equilibrium potential E_s as summarised by Fall & Keizer (2002, p. 25):

$$E_s = V_i - V_e = \frac{RT}{FZ_s} \ln \frac{[C_{e,s}]}{[C_{i,s}]} \tag{6}$$

Here, V_i and V_e denote the potential inside and outside of the cell, and $C_{i,s}$ and $C_{e,s}$ are the intracellular and extracellular concentrations of ion s. Ionic concentrations vary across the body and fluctuate over time, with typical values in human cells shown in Table 1. At a temperature of 310.0 K (≈37 °C), as in the human body, these result in the following equilibrium potentials: $E_{Na^+} \approx 70\ mV$, $E_{Ca^{2+}} \approx 130\ mV$, $E_{K^+} \approx -90\ mV$, and $E_{Cl^-} \approx 35\ mV$.

Table 1. Typical intra and extracellular ionic concentrations of mammalian cells (Alberts et al., 2008, Table 11-1; Herring & Paterson, 2018, Table 3.1).

Ion s	$C_{i,s}$ (mM)	$C_{e,s}$ (mM)
Na^+	10	140
Ca^{2+}	0.0001	1.5
K^+	140	5
Cl^-	30	120

To derive the resting membrane potential (E_m), the membrane's permeability (P_s) at rest for each ion s and the Goldmann-Hodgkin-Katz equation can be used, giving (Goldman, 1943; Hodgkin & Katz, 1949):

$$E_m = \frac{RT}{F} \ln \frac{\left(P_{Na^+}\left[C_{e,Na^+}\right] + P_{Ca^{2+}}\left[C_{e,Ca^{2+}}\right] + P_{K^+}\left[C_{e,K^+}\right] + P_{Cl^-}\left[C_{i,Cl^-}\right]\right)}{\left(P_{Na^+}\left[C_{i,Na^+}\right] + P_{Ca^{2+}}\left[C_{i,Ca^{2+}}\right] + P_{K^+}\left[C_{i,K^+}\right] + P_{Cl^-}\left[C_{e,Cl^-}\right]\right)} \quad (7)$$

P_s depends on the cell type, but most mammalian cells at rest are impermeable to Ca^{2+} (hence it is rarely included in Equation (7)), and significantly more permeable to K^+ than to Cl^- and Na^+, resulting in resting membrane potentials of between -60 and -90 mV (Chrysafides et al., 2023; Herring & Paterson, 2018, p. 36; Szedlak et al., 2023).

To model the excitation of cells, Hodgkin & Huxley (1952) developed the first mathematical model of an AP, specifically for squid axons. The authors described the cell membrane as an electrical circuit, in which the total current across the cell membrane is the sum of the capacitive current ($C_m * \frac{dV_m}{dt}$) and the ionic currents (I_{ion}). Here, C_m denotes the membrane capacitance, V_m the membrane potential, and t the time. It follows (Krogh-Madsen & Christini, 2020, p. 1-11):

$$\frac{dV_m}{dt} = -\frac{I_{ion}}{C_m} \quad (8)$$

To measure I_{ion}, Hodgkin & Huxley (1952) carried out voltage clamp experiments, in which they kept the membrane potential constant, maintaining $\frac{dV_m}{dt} = 0$. By altering the

ionic concentrations in the cells' medium, they were able to identify the contribution of a Na^+ current (I_{Na}), a K^+ current (I_K), and a leak current (I_{leak}) to I_{ion}, resulting in (Hodgkin & Huxley, 1952):

$$I_{ion} = I_{Na} + I_K + I_{leak} \tag{9}$$

Using Ohm's law, and with g_s being the conductance of ion s depending on voltage and time, and $V_m - E_s$ being the driving force, each ionic current I_s can be described as summarised by Krogh-Madsen & Christini (2020, p. 1-12):

$$I_s = g_s(V_m, t) * (V_m - E_s) \tag{10}$$

Hodgkin & Huxley (1952) further established that the conductance g_s depends on the maximum conductance $\bar{g}_s$ and that its dynamics over time could be described using 'gating variables'. These gating variables take a value between 0 and 1 and describe a channel's state with regards to it being either active or inactive (see Section 2.2). After calibration to their experimental data, Hodgkin & Huxley (1952) derived three activation gates m and one inactivation gate h for Na^+ and four activation gates n for K^+. Their final model consisted of the following system of four ordinary differential equations (ODEs), where α and β denote the channel's opening and closing rates, respectively, and also considering an applied stimulus current (I_{stim}) (Hodgkin & Huxley, 1952):

$$C_m \frac{dV_m}{dt} =$$

$$-\left(\bar{g}_{Na} m^3 h * (V_m - E_{Na})\right) - \left(\bar{g}_K n^4 * (V_m - E_K)\right) - \left(g_{leak} * (V_m - E_{leak})\right) + I_{stim} \tag{11}$$

$$\frac{dm}{dt} = \alpha_m(V_m) * (1 - m) - \beta_m(V_m) * m \tag{12}$$

$$\frac{dh}{dt} = \alpha_h(V_m) * (1 - h) - \beta_h(V_m) * h \tag{13}$$

$$\frac{dn}{dt} = \alpha_n(V_m) * (1 - n) - \beta_n(V_m) * n \tag{14}$$

α and β can be determined experimentally, e.g. during voltage clamp experiments, in which the voltage is held constant. For simplification, a steady-state gating variable, e.g. m_∞ for the gating variable m, and a time constant, e.g. τ_m, can be introduced as summarised by Krogh-Madsen & Christini (2020, p. 1.14):

$$m_\infty(V_m) = \frac{\alpha_m(V_m)}{\alpha_m(V_m) + \beta_m(V_m)} \tag{15}$$

$$\tau_m(V_m) = \frac{1}{\alpha_m(V_m) + \beta_m(V_m)} \tag{16}$$

Derivatives of gating variables, such as Equation (12), can then be written in the form:

$$\frac{dm}{dt} = \frac{m_\infty(V_m) - m}{\tau_m(V_m)} \tag{17}$$

Instead of using gating variables, ion channels can also be modelled stochastically with Markov models as discussed in Linaro & Giugliano (2022). For a simple two-state ion channel, a transition-state diagram can be constructed, as summarised by G. D. Smith (2002, p. 286):

$$C \underset{k^-}{\overset{k^+}{\rightleftarrows}} O \tag{18}$$

Considering a random variable $p \in \{C, O\}$, the probability for the ion channel to be in the open (O) or closed (C) state at time t are given by $P_c(t)$ and $P_O(t)$. With these, a new system of ODEs can be derived (G. D. Smith, 2002, p. 288):

$$\frac{dP_C}{dt} = -k^+ P_C + k^- P_O \quad (19)$$

$$\frac{dP_O}{dt} = +k^+ P_C - k^- P_O \quad (20)$$

While stochastic ion channel gating models bring the advantage of incorporating complex dependencies of state activation and inactivation, they usually come at a higher computational cost (Fink & Noble, 2009).

4.2 Single cell computer models of cardiac electrophysiology

In the past 70 years, Hodgkin and Huxley's work has inspired a great variety of models for many different types of cardiac cells (see Figure 5). The first model of the cardiac AP was developed by Noble (1960). In the nineties and early two-thousands, several ventricular cardiomyocyte models for various species arose, such as the Luo & Rudy (1991) model of mammalian cardiomyocytes and the TenTusscher model for human cardiomyocytes (Ten Tusscher et al., 2004; Ten Tusscher & Panfilov, 2006). Compared to previous models, one of the advancements of the TenTusscher model was its capability to capture APD restitution. A few years later, the Grandi et al. (2010) model improved CaT behaviour under different pacing conditions and the effects of I_{Ks} and I_{Kr} block. The Carro et al. (2011) model further advanced human ventricular cardiomyocyte modelling by improving S1-S2 restitution slope and APD_{90} rate adaptation. In the same year, O'Hara et al. (2011) published a model of human cardiomyocytes, called the ORd model, which was based on recordings in over 100 human hearts and overcame the limited capabilities of the TenTusscher and Grandi models to capture early after depolarisations (EADs). Recently, Tomek et al. (2019) improved I_{CaL} and I_{Kr} formulations in the ORd model, thereby resulting in the human ventricular ToR-ORd model with improved AP shape. They further

established a set of validation criteria to confirm the biophysical accuracy of their work and future models (Tomek et al., 2019).

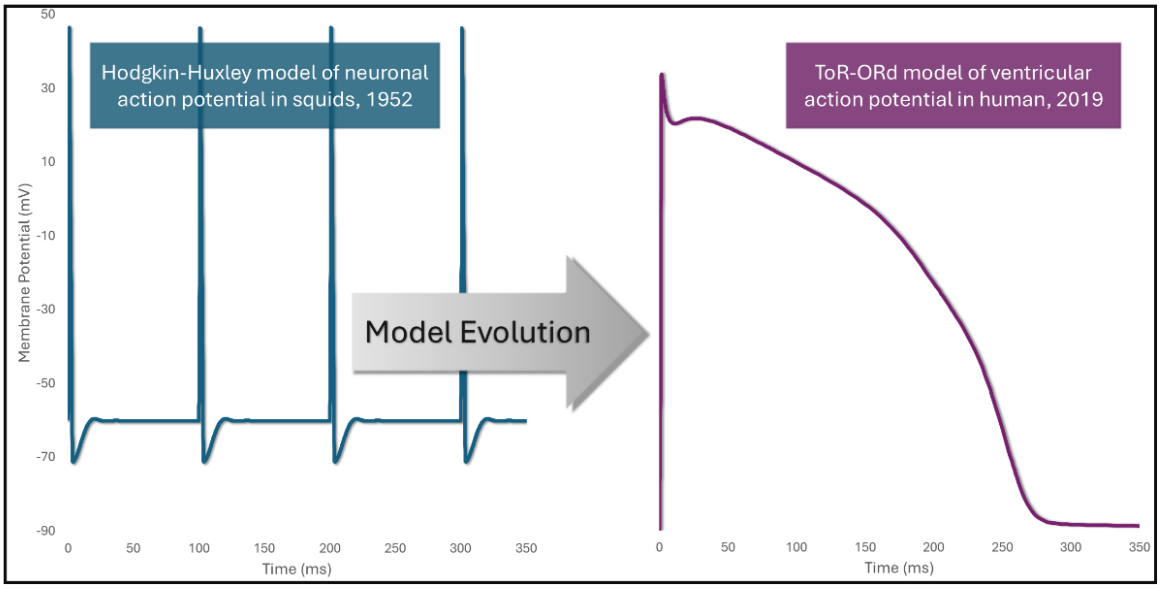


Figure 5. Evolution from the first AP model in squid neurons (Hodgkin & Huxley, 1952) to the most recent model of the ventricular AP (Tomek et al., 2019).

To design an informative and biophysically accurate simulation study of ventricular arrhythmias, the Purkinje network is essential. In fact, a model of Purkinje fibre and pace-maker APs was one of the first applications of the Hodgkin and Huxley model to a cardiac context (Noble, 1962). Since then, several other models of Purkinje cells have been developed. In 2008, a novel model of human Purkinje cells was developed and employed to a 3D setting of the ventricles to investigate bundle branch block and mechanisms of cardiac conduction (Ten Tusscher & Panfilov, 2008). Ten Tusscher & Panfilov (2008) highlighted the longer APD and higher AP upstroke velocity as key properties of Purkinje cells, as captured in their model. Stewart et al. (2009) followed with a human Purkinje cell model; the authors compared their model against experimental data and were able to reproduce experimentally observed Purkinje cell automaticity. However, the authors themselves noted that limited data on healthy Purkinje cells resulted in inherited formulations from the TenTusscher model of ventricular cardiomyocytes and the absence

of some relevant currents (Stewart et al., 2009). Sampson et al. (2010) aimed to resolve these issues by including further currents and improving ion channel kinetics using Markov models. The recently published Trovato2020 model further advanced on previous models by capturing key Purkinje AP characteristics, such as the formation of EADs and DADs under different pacing protocols and drug block (Trovato et al., 2020).

As discussed in Section 3.5.1, hPSC-CMs, which are widely employed for pre-clinical drug testing, have been explored for regenerative cell therapy. One of the first models to capture the behaviour of hPSC-CMs computationally was the Paci2012 model of human embryonic stem cell-derived cardiomyocytes (Paci et al., 2012). The hPSC-CM Paci2012 model was based on the human adult ventricular cardiomyocyte TenTusscher model and allows for modelling early and late stage hPSC-CMs. Building on the Paci2012 model, the Paci2013 model of atrial- and ventricular-like human induced pluripotent stem cell-derived cardiomyocytes was developed (Paci et al., 2013). The following Paci2015 model was constructed and able to reproduce the phenotype of long QT syndrome and predict the effects of antiarrhythmic drugs (Paci et al., 2017). Finally, the ventricular-like hPSC-CM Paci2020 model was derived and further demonstrated powerful for *in silico* drug trials (Paci et al., 2020). The Koivumäki model (Koivumäki et al., 2018) and the Kernik model (Kernik et al., 2019) are two other hPSC-CM models; the Koivumäki model used experimental hPSC-CM data to represent the cells' immature ion dynamics, while the Kernik model makes use of data from multiple groups to reproduce variability observed amongst hPSC-CMs. A recent study compared the Koivumäki, Kernik, and Paci hPSC-CM models with regards to their output characteristics and response to 15 drugs (Paci et al., 2021). The comparison showed different AP morphologies, current densities, and spontaneous beating frequencies; furthermore, due to differences in complexity, the Paci

and Kernik models were found to run 100 times faster than the Koivumäki model (Paci et al., 2021). These *in silico* drug trials demonstrated drug-induced EADs and DADs in the Koivumäki model, which were absent in the Kernik and Paci models, and found the Kernik model largely insensitive to drug-induced inhibition of automaticity in contrast to the Koivumäki and Paci models, which were built with different calcium handling and I_{NaCa} formulations (Paci et al., 2021).

Mathematical models have been written not only for electrophysiology but also for contraction, including crossbridge formation and myofilament activity, as reviewed by Trayanova & Rice (2011). Recently, Land et al. (2017) published new contractile data from human cardiomyocytes together with a detailed model of cardiac contraction, including representations of active tension, tension length-dependence, and crossbridge dynamics. Emerging from this work, the human ventricular electrophysiological ToR-ORd model was coupled with the mechanical Land-Niederer model, thereby resulting in the electromechanical ToR-ORd-Land model (Margara, Wang, et al., 2021). The capabilities of this new electromechanical model were shown through investigations of Mavacamten efficacy for hypertrophic cardiomyopathy (Margara, Rodriguez, et al., 2021). Electromechanical models have also been derived for hPSC-CMs. Forouzandehmehr et al. (2020) coupled the ventricular-like hPSC-CM Paci2020 model to two different contractile models, namely the Negroni et al. (2015) and Rice et al. (2008) models, which both produced APs and CaTs largely consistent with experimental data. Similarly to the human adult ventricular cardiomyocyte ToR-ORd-Land model, Folkmanaite et al. (2021) combined the hPSC-CM Paci2020 model and the Land-Niederer model, with the resulting Paci-Land model recalibrated to reproduce hPSC-CM-like active tension.

Due to their biophysiological detail and rigorous comparison with experimental data, I used the human adult ventricular cardiomyocyte ToR-ORd model, the human Purkinje Trovato2020 model, and the ventricular-like hPSC-CM Paci2020 model in this work. The next section will outline how cellular models such as these can be coupled in tissue to simulate electrophysiological activity of the ventricles.

4.3 Mathematical models of electrical propagation in tissue

In Equation (8) of Section 4.1, it was established that the current through a membrane (I_m) is the sum of the capacitive current and the ionic currents.

Considering a series of coupled cells with a surface area-to-volume ratio β, the conductivity tensors $\boldsymbol{G_i}$ and $\boldsymbol{G_e}$, and using $\boldsymbol{E} = -\nabla V$, the current densities in the intracellular and extracellular space (J_i, J_e) can be described with Ohm's law:

$$J_i = -\boldsymbol{G_i}\nabla V_i \tag{21}$$

$$J_e = -\boldsymbol{G_e}\nabla V_e \tag{22}$$

Considering the conservation of charge, intracellular and extracellular current densities must balance out, as described by Vigmond (2020, p. 7-6), resulting in:

$$\nabla \cdot J_i = -I_m * \beta \tag{23}$$

$$\nabla \cdot J_e = I_m * \beta \tag{24}$$

Considering also that $V_m = V_i - V_e$, Equations (8) and (21) to (24) yield the bidomain equations (Clayton et al., 2011; Sepulveda et al., 1989):

$$\nabla \cdot \boldsymbol{G_i}(\nabla V_m + \nabla V_e) = \beta \left(C_m \frac{\partial V_m}{\partial t} + I_{ion} \right) \tag{25}$$

$$\nabla \cdot \left((\boldsymbol{G_i} + \boldsymbol{G_e})\nabla V_e\right) = -\nabla \cdot (\boldsymbol{G_i}\nabla V_m) \quad (26)$$

Equations (25) and (26) can be simplified when assuming that the intracellular and extracellular conductivities are proportional ($\boldsymbol{G_e} = \lambda \boldsymbol{G_i}$) and by introducing the diffusivity tensor $\boldsymbol{D} = \frac{\lambda}{1+\lambda}\frac{1}{\beta C_m}\boldsymbol{G_i}$, as summarised by Clayton et al. (2011) and Vigmond (2020, p.7-12). Also considering the application of a transmural stimulus (I_{stim}) yields the monodomain equation:

$$\frac{\partial V_m}{\partial t} = \nabla \cdot (\boldsymbol{D}\nabla V_m) - \frac{I_{ion} - I_{stim}}{C_m} \quad (27)$$

While the bidomain model is essential in simulating extracellular current injection, such as during defibrillation (Trayanova, 2006), monodomain and bidomain equations have been shown by Potse et al. (2006) to produce near identical results otherwise. The main advantage of the monodomain model is its significantly reduced computational cost, as it contains only a single partial differential equation. Other models of wavefront propagation include the Eikonal model, which can be used to efficiently compute activation times, the phenomenological FitzHugh-Nagumo model, or graph-based alternatives (FitzHugh, 1961; Nagumo et al., 1962; Wallman et al., 2012). Due to the discussed advantages, particularly the faster computational run time, I chose the monodomain equation for this work.

4.4 Computational model solvers for 3D tissue simulations

The monodomain and bidomain models in (25) to (27) are partial differential equations and hence cannot easily be solved analytically. To efficiently approximate solutions, the PDEs are turned into linear systems of equations through spatial discretisation methods,

such as the Finite Volume Method (FVM), the Finite Element Method (FEM), or the Finite Differences Method (FDM), as summarised by Clayton et al. (2011). The FVM uses the divergence theorem to convert the PDE's volume integrals into surface integrals and calculates them as fluxes on each volume's surface, as summarised by Shukla et al. (2011). In the FEM, the spatial domain is divided into small sub-spaces, inside of which solutions are derived using an interpolation function, and, finally, the FDM approximates the PDEs with equal distance across the mesh using difference quotients, as discussed by Clayton et al. (2011) and Vigmond & Plank (2019, pp. 14-16). In contrast to the FEM and FVM, the FDM struggles to reproduce curved surfaces smoothly and may not be suitable for unstructured meshes or mechanical simulations (Vigmond & Plank, 2019, p. 15). Geometrical representation of the elements should also be considered; cubic elements are easier to derive straight from imaging data and reduce computational cost, but tetrahedral meshes produce a more accurate curvature (Clayton et al., 2011).

To discretise the system in time, one of the most common methods is the forward Euler method. To approximate a y at time $t + h$, it uses the slope at time t, resulting in the following equation, where $f(t, y) = \frac{dy}{dt}$:

$$y^{t+h} = y^t + h * f(t, y) \tag{28}$$

Another method, which has been widely used for solving stiff cellular models is the Rush-Larsen method, which, compared to the Euler method, improves stability and may even speed up computational run time because it can use coarser time steps (Rush & Larsen, 1978). It is utilised for gating variables w_i; by introducing $a_{w_i}(V_m) = -\frac{1}{\tau_{w_i}(V_m)}$ and $b_{w_i}(V_m) = \frac{w_{i_\infty}(V_m)}{\tau_{w_i}(V_m)}$, Equation (17) can be written as:

$$\frac{dw_i}{dt} = a_{w_i}(V_m)w_i + b_{w_i}(V_m) \tag{29}$$

Considering the above, if V_m is constant over the time interval h, w_i^{t+h} can be determined as (Garcia-Molla et al., 2014; Rush & Larsen, 1978):

$$w_i^{t+h} = e^{h*a_{w_i}(V_m)}\left(w_i^t + \frac{b_{w_i}(V_m)}{a_{w_i}(V_m)}\right) - \frac{b_{w_i}(V_m)}{a_{w_i}(V_m)} \tag{30}$$

The above methods can be combined to efficiently solve a system of ODEs, where the Rush-Larsen method is used for gating variables and the forward Euler method for any other variables, as demonstrated by Garcia-Molla et al. (2014).

The accuracy of the numerical methods outlined in this section depends on the chosen resolution, both in space and in time. For very small step sizes, the solution may be more accurate, but computational cost will be higher. Due to the morphology of the AP, the optimal step size varies. Specifically, during the upstroke, where the membrane potential increases rapidly over a few milliseconds, small steps are needed. During the plateau and resting phase, voltage changes are small, and a coarser step may suffice. To overcome this issue, adaptive methods have been developed, where the step size at each iteration is determined using a given error tolerance, which can be approximated as described in Garcia-Molla et al. (2014). While adaptivity has been mostly applied to discretising time, it has also been suggested for spatial discretisation (Cherry et al., 2000). If a fixed temporal and spatial resolution are chosen, convergence analyses should be carried out to evaluate the error in APD, conduction velocity (CV), and activation times (Niederer et al., 2011).

Different computational software has been developed to approximate the solutions of the ODE and PDE models for cardiac electrophysiology described in this chapter. The 'Cancer, Heart and Soft-Tissue Environment' (CHASTE) was developed in 2009 and implements the FEM (Pitt-Francis et al., 2009). Also using the FEM, openCarp was developed a couple of years later and allows for monodomain as well as bidomain simulations (Plank et al., 2021). Another computational solver is Alya, which is often consulted for electromechanical simulations (Santiago et al., 2018).

Recently, the GPU-enabled high performance model solver MonoAlg3D was developed, which uses the monodomain equation, allows for time as well as space adaptivity, and employs the FVM (Berg et al., 2023; Sachetto Oliveira et al., 2018). Due to its fast performance and open-source nature, MonoAlg3D was chosen for the presented work and hence is explained in more detail below. Firstly, MonoAlg3D uses operator splitting to divide the monodomain equation into a nonlinear system of ODEs and a single parabolic linear PDE, where $\boldsymbol{\eta}$ is a vector of state variables and $\boldsymbol{\sigma}$ denotes the monodomain conductivity tensor (Sachetto Oliveira et al., 2018):

$$\frac{\partial V_m}{\partial t} = \frac{1}{C_m}(-I_{ion}(V_m, \boldsymbol{\eta}) + I_{stim}) \tag{31}$$

$$\frac{\partial \boldsymbol{\eta}}{\partial t} = \boldsymbol{f}(V_m, \boldsymbol{\eta}) \tag{32}$$

$$\beta C_m \frac{\partial V_m}{\partial t} = \nabla \cdot (\boldsymbol{\sigma} \nabla V_m) \tag{33}$$

To discretise the ODEs in time, the forward Euler and Rush-Larsen methods can be used as described in Equations (28) and (30). To discretise the PDE in time and in space, a

first-order Euler scheme and the FVM are employed, respectively. Particularly, a backwards Euler scheme is established through (Sachetto Oliveira et al., 2018):

$$\frac{\partial V_m}{\partial t} = \frac{V_m^{t_{n+1}} - V_m^{t_n}}{\Delta t} \tag{34}$$

The FVM is applied through integrating and applying the divergence theorem to Equation (33) and gives the following equation, where $\boldsymbol{n}$ is a vector normal to the surface and $J = -\boldsymbol{\sigma}\nabla V_m$ (Sachetto Oliveira et al., 2018):

$$\beta C_m \int_{\Omega} \frac{\partial V_m}{\partial t} dv = -\int_{\partial\Omega} J \cdot \boldsymbol{n}\, ds \tag{35}$$

The solver uses uniform cubic meshes; hence J can be computed as the sum of flows on the six faces of each element, where the conductivity values are calculated as the harmonic mean at the surfaces (Sachetto Oliveira et al., 2018). MonoAlg3D makes use of the parallel computing platform CUDA, which allows it to access the GPU and pass variables back and forth from the CPU. CUDA breaks the GPU down into grids, which are composed of blocks, which are made of threads. This way, MonoAlg3D can pass, e.g. each cell's cellular model to a thread to compute all membrane potentials in parallel. Finally, MonoAlg3D is open source and can easily be customised because of its module-like architecture. The solver can be downloaded from GitHub, which also includes an open discussion forum for users to ask questions and report bugs (https://github.com/rsachetto/MonoAlg3D_C/).

4.5 Modelling and simulation to augment clinical trials and risk predictions

As described in this chapter, computational models of cardiac electrophysiology are based on biological, physical, and chemical knowledge and therefore closely mirror the

mechanisms in the real human heart. They hence allow to simulate the heart's physiological as well as pathophysiological behaviour under different conditions. For example, the same heart can be investigated before and after a heart attack to identify mechanisms behind disease-related arrhythmias and suggest how treatments can be made more effective and safer (Viceconti, Emili, et al., 2021). Furthermore, clinical trials allow for only one therapy to be applied to a patient at a time, whilst *in silico* trials enable investigating hundreds of treatments in thousands of patients in parallel to identify optimal targets as well as safety risks (Pappalardo et al., 2019). Such computational trials further allow for systematically controlling environmental parameters, pausing and rewinding the simulations to investigate the behaviour even at single cell level, and accurately comparing outcomes under different conditions.

In silico trials often use the population of models approach, in which model parameters (such as ion channel conductances) are varied around their baseline value to capture the variability in our population, as done by Britton et al. (2013). As summarised by Sarkar et al. (2012), variability occurs at the ionic level because of differences in ion channel expression, at the single cell level visible through different AP phenotypes, at the organ level through changes in ECG and heart rate, and during clinical treatment, where different therapies can have different effects on different patients. To address this intersubject variability, model parameters can be varied randomly or using more advanced methods such as Latin Hypercube sampling or sequential Monte Carlo sampling, as compared by Drovandi et al. (2016). Next, the models are calibrated against experimental biomarkers to ensure they are physiological (Britton et al., 2013). The resulting population of models can represent experimentally observed intersubject and intrasubject variability and offer quantitative comparison of simulated and experimental

predictions, as discussed by Muszkiewicz et al. (2016). For example, a population of ventricular cell models was used to identify arrhythmia mechanisms and anti-arrhythmic drugs in hypertrophic cardiomyopathy by Passini et al. (2016). Studies such as this have motivated large scale *in silico* drug trials, which have been used also by companies and shown to reproduce drug effects in human more accurately than some animal models (Passini et al., 2017, 2021). Intersubject variability has also been modelled at organ-level, e.g. in simulation studies investigating mechanisms of atrial fibrillation (Dasí et al., 2024; Elliott et al., 2020; Sánchez et al., 2013).

While *in silico* trials often aim to conduct modelling and simulation in large cohorts, other studies have focused on building 'digital twins', i.e. patient-specific models, such as demonstrated in a recent study on familial cardiomyopathies by Filipovic et al. (2022). Digital twins are built straight from patient data to virtually re-create a patient's heart. For this, imaging data such as cardiovascular magnetic resonance images are used, which allow for reconstructing the patient's torso and heart geometry (Banerjee et al., 2021; H. J. Smith et al., 2022). The resulting 3D geometries can be processed to achieve the desired resolution. As conductivity between cardiomyocytes is anisotropic, CV varies along the muscle fibres and sheets. To reproduce this computationally, fibre, sheet, and sheet normal directions are prescribed using rule-based methods (J. D. Bayer et al., 2012; Doste et al., 2019; Streeter et al., 1969). Conductivities in each direction can either be derived by calibrating against experimentally observed CVs (Caldwell et al., 2009; Taggart et al., 2000) or be inferred to reproduce the patient's QRS complex (Camps et al., 2021); the latter method may also infer the root nodes of the Purkinje system, which are crucial in reproducing the patient's cardiac activation sequence. Recently, these methods have been extended to reconstruct full Purkinje trees, their CV, and the delay at each root node

(Álvarez-Barrientos et al., 2025; Camps et al., 2024). Also incorporated into the patient's biventricular geometry are electrophysiological gradients transmurally (Boukens et al., 2015; Okada et al., 2011), from apex to base (Chauhan et al., 2006; Colli Franzone et al., 2008), and between the LV and RV (Arteyeva, 2020).

Modelling and simulation can also be used to investigate underlying causes for ECG characteristics on a multiscale level. For example, simulation studies have examined the effect of torso and heart anatomy on the ECG signal and concluded that the position of the heart within the torso as well as its anatomy are key in modulating ECG morphology (Mincholé et al., 2019; Nguyên et al., 2015). Personalised cardiac models have also been created to represent disease phenotypes and their effects on the subjects' ECGs (Lyon et al., 2019; Potse et al., 2014). A limitation of many 3D simulation studies is the absence of the cardiac conduction system, particularly in human, as stressed by Deo et al. (2009). Computational work by Dux-Santoy et al. (2011) has further highlighted the relevance of the Purkinje network in modelling and simulation by showing differences in the effects of drug-induced I_{Kr} block.

As outlined by Niederer et al. (2019), 3D simulations have been used extensively to investigate mechanisms behind cardiac arrhythmias under different disease conditions. A recent simulation study investigated arrhythmogenicity of size, transmurality, and location of the ischemic zone in a human biventricular model (Martinez-Navarro et al., 2019). Martinez-Navarro et al. (2019) concluded that vulnerable windows (VWs), the time span during which arrhythmias may occur, were largest for transmural ischemia and were further impacted by ischemia size and location. The same group published a further 3D simulation study a year later, which investigated the impact of sodium current availability

on arrhythmic risk in acute ischemia (Martinez-Navarro et al., 2021). Another computational study by Deng et al. (2016) focused on infarction rather than ischemia and demonstrated that arrhythmic risk in post-MI models with preserved LVEF can be correctly predicted from 3D simulations. Lopez-Perez et al. (2019) created a personalised biventricular model capturing the patient's anatomy and scar geometry to investigate the effects of variability in electrophysiological and structural remodelling on VT inducibility. They established credibility of their results using patient-specific ECG data and in their study found that APD heterogeneities in the border zone as well as reduced CV are the main drivers of VT susceptibility (Lopez-Perez et al., 2019). *In silico* models have also been developed to capture the progression of MI (Wang et al., 2021; Zhou et al., 2021, 2024) as well as MI-related cell death, wall thinning, and ventricular dilation (Sáez & Kuhl, 2015). Further methods and examples of computational modelling and simulation of MI can be drawn from Connolly & Bishop (2016) and Mangion et al. (2018).

Recent studies further focused on modelling and simulating hPSC-CMs including under diseased conditions (Kernik et al., 2020; Paci et al., 2017) and drug action (Paci et al., 2021; Tveito et al., 2018). Over the last few years, 3D modelling and simulation has also been used to assess the safety of regenerative cell therapy. Based on experimental observations, one study modelled tissue slabs with human adult cardiomyocytes coupled to increasing numbers of mesenchymal stem cells to investigate arrhythmogenicity (Mayourian et al., 2016). Mayourian et al. (2017) later extended their work to determine the impact of paracrine signalling and heterocellular coupling on contractility and arrhythmic risk. Other studies developed models to represent cardiac tissue with multiple cell types, such as atrial-like and ventricular-like hPSC-CMs (Bowler

et al., 2019), or investigated the change in arrhythmic risk of hPSC-CMs under I_{CaL} block (Dasí et al., 2021).

Recently, a series of different cell therapy scenarios were modelled at organ level; J. K. Yu et al. (2019) found that an increase in junctional conductance enabled the hPSC-CMs' spontaneous APs to spread in the adult ventricular tissue and that cells injected proximal to the infarct resulted in ectopic propagation for all but very small density and clustering parameters. Finally, the study showed that 90° anisotropic hPSC-CM patches may be less pro-arrhythmic than 0° and 45° anisotropic and isotropic patches and that engraftment of hPSC-CMs onto Purkinje fibres can cause bundle branch block for a sufficiently large junctional conductance (J. K. Yu et al., 2019). The same group published two further *in silico* studies of cell therapy, where they investigated the effects of poor gap junctional coupling and circumferential distribution of sodium channels on formation and propagation of ectopic beats (J. K. Yu, Liang, Weinberg, et al., 2022) as well as the impact of graft location, size, alignment, and conductivity on arrhythmic burden in two human-based biventricular post-MI models (J. K. Yu, Liang, Franceschi, et al., 2022). In the latter, they concluded that re-entry dominates over the propagation of spontaneous beats as an arrhythmia mechanism and further found re-entry burden to depend mostly on location, surface-to-volume ratio, thickness, and conductivity of the transplanted patch (J. K. Yu, Liang, Franceschi, et al., 2022). The role of hPSC-CM patch conductivity has also been highlighted by Rosales et al. (2024), who simulated a range of scaffolds with varying pore shapes and sizes to optimise cell sheet designs. Fassina et al. (2022) demonstrated that besides patch conductivity, transmurality of the infarct scar is crucial in determining arrhythmogenicity and that targeting I_{NaF} and I_{K1} may improve the therapy's safety. Another 3D simulation study compared the arrhythmic risk before and after cell therapy in two

personalised post-MI models focussing on the role of isthmuses in the scar core as well as the delivered cells' APD (Fassina et al., 2023). Whilst these studies have focused on the re-entrant risk of cell therapy, Gibbs et al. (2023) investigated the risk of spontaneous hPSC-CM beats and pointed out that slow as well as fast host-graft coupling and improved conductivity within the scar may reduce automaticity.

Overall, modelling and simulation carries clear benefits for non-invasive, personalised, and cost-effective risk prediction and offers an ethical alternative to animal models. However, as discussed by Cluitmans et al. (2024), so far only few have been integrated into clinical practice with promising simulations, such as on atrial and ventricular ablation as well as sudden cardiac arrest, still waiting to be incorporated.

4.6 Verification, validation, and uncertainty quantification principles

Increasing computational power and resources led to a surge in *in silico* trials. Different contexts of use warrant different methods, complexity, and simulation protocols, thereby resulting in a multitude of modelling and simulation frameworks (Viceconti, Emili, et al., 2021). The reported methodological detail and testing between these studies differ and call for uniform standards, acceptance criteria, and risk assessments (Musuamba et al., 2021). For example, descriptions of patient demographics have been shown to vary between *in silico* studies, with some omitting them completely, as discussed by Rodero et al. (2023). To demonstrate the credibility of existing and new tools, verification, validation, and uncertainty criteria have been established, also considering the risk model decisions can carry (Viceconti, Pappalardo, et al., 2021).

Verification refers to the correct functioning of the software, including implementation of the underlying mathematical equations. For this, benchmark tests and comparisons to

previous implementations, such as in single cell solvers and across different platforms, can be executed. Additionally, test-driven development can ensure stability as the software evolves. Making code open source enhances its availability and encourages users to contribute to finding bugs for different use cases.

Validation assesses whether models and simulations behave physiologically. To demonstrate a system is suitable to simulate a given biophysiological scenario, calibration and validation data are usually kept distinct. For example, a model may be calibrated to a healthy patient, with experimentally reported disease changes implemented on top, and the resulting model compared against biomarkers from diseased patients. Validation techniques should be carried out not only on the modelling and simulation outputs, but also on the input data used to inform the framework.

Finally, uncertainty quantification evaluates which parameters in the model are variable or unknown in the real world, by how much they may change, and how fluctuations would affect the model output. Sensitivity analyses are commonly employed here, in which a given parameter is varied around its baseline value and the impact on the model quantified, for example through measuring changes in APD. Uncertainty quantification is key in understanding the unknowns and their effects in a system but can also give insights into model mechanisms, which may have real world implications. For example, a sensitivity analysis would show both, *in silico* and *in vivo* human ventricular cardiomyocytes highly sensitive to changes in I_{Kr} because it is important in repolarising not only virtual but also real cardiomyocytes.

Overall and as shown in Figure 6, to establish robustness of a computational modelling and simulation framework, verification, validation, and uncertainty quantification (VVUQ)

should be considered at every stage, from data analysis over model design to output evaluation.

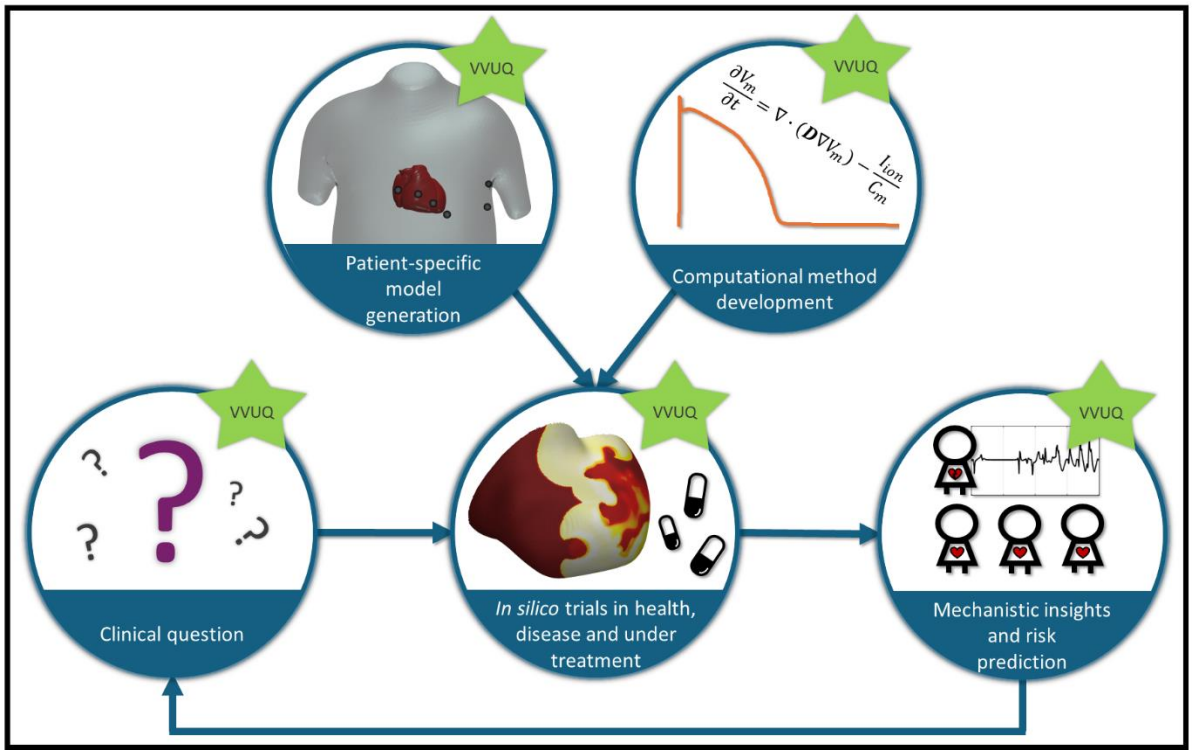


Figure 6. In silico trials pipeline including clinical motivation, patient-specific model generation, computational method development, simulation study execution, mechanistic insights, and risk predictions. Consideration of verification, validation, and uncertainty quantification (VVUQ) criteria is indicated throughout. Four chamber mesh from Rodero et al. (2021) and biventricular and torso mesh from Mincholé et al. (2019).

5 Human ventricular electrophysiological modelling and simulation of ischemic heart disease for risk stratification and treatment optimisation

To address this project's aim in investigating arrhythmia mechanisms in the human ventricles during ischemia and infarction, I integrated, calibrated, and evaluated state-of-the-art multiscale human ventricular electrophysiological modelling and simulation tools. In the following sections, I will first describe how human ventricular electrophysiology was modelled and simulated from cellular to organ level and how variability in electrophysiological and structural remodelling following ischemic heart disease was introduced. Next, I present simulation protocols to investigate arrhythmia inducibility, sustainability, and complexity in ischemic heart disease and treatment. Finally, I demonstrate credibility of this framework to investigate the questions at hand through verification, validation, and uncertainty quantification.

5.1 Multiscale modelling and simulation of healthy human ventricular electrophysiology

In this first section, I describe how electrophysiological activity in the healthy human ventricles was modelled and simulated, from the cellular AP over tissue propagation and biventricular activation to the ECG.

5.1.1 Modelling human ventricular and Purkinje cellular electrophysiology

To simulate cellular APs of human ventricular cardiomyocytes, I used the state-of-the-art ToR-ORd model (Tomek et al., 2019), specifically the latest published model version with dynamic intracellular Cl^- concentrations (in addition to the default dynamic intracellular Ca^{2+}, Na^+ and K^+ concentrations) because it has been shown to improve model stability

over time (Tomek et al., 2020). I chose the human ventricular ToR-ORd model not only because it is one of the latest models, benefitting from model development experience and knowledge gained over the last decades, but also because its biophysiological detail allows for accurately capturing the repolarisation abnormalities and drug response of human cardiomyocytes (Passini et al., 2017). Similarly, I selected the state-of-the-art Trovato2020 model to represent the AP of human Purkinje cells because it has shown powerful in accurately predicting drug-induced effects (Trovato et al., 2020, 2022).

5.1.2 Simulating electrical propagation in the human ventricles

As shown in Figure 7, I used a patient-specific biventricular hexahedral mesh with an edge length of 300 µm, which was previously constructed by Mincholé et al. (2019) from MRI data of a healthy patient. I then incorporated transmurally varying fibre, sheet, and normal orientations, which were derived with a rule-based method by Doste et al. (2019). I then calibrated conductivities in fibre direction to obtain a CV of 65 cm/s as clinically reported (Taggart et al., 2000).

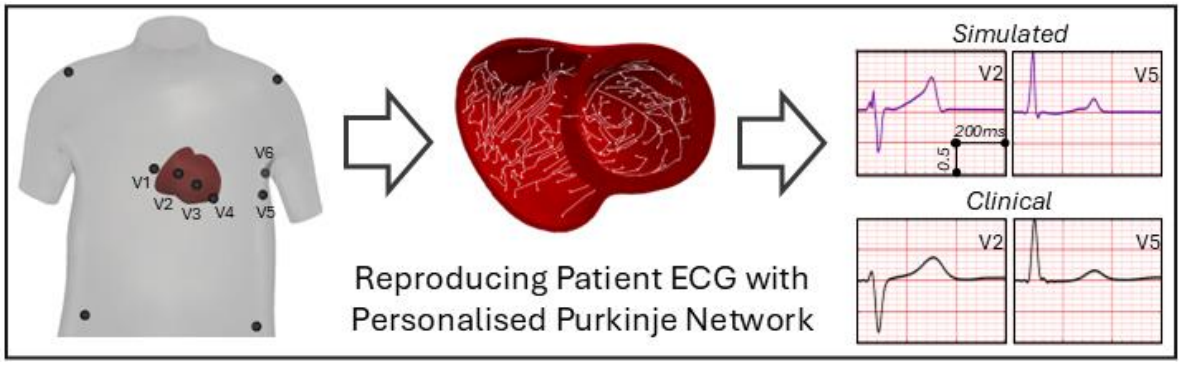


Figure 7. Left: Torso and biventricular geometry derived from a female patient (Mincholé et al., 2019). Middle: Inferred Purkinje conduction network (Camps et al., 2024). Right: Using the inferred Purkinje conduction network and CVs, the patient's ECG (Mincholé et al., 2019) was reproduced in the simulations. Caption modified and figure cropped but otherwise unmodified from Riebel et al. (2024) under CC BY license (https://creativecommons.org/licenses/by/4.0/).

Next, I calibrated conductivities to achieve personalised sheet (38 cm/s) and normal CVs (47 cm/s), which were derived by Camps et al. (2024) through an ECG-based inference algorithm. I further used a Purkinje network, which was also created by Camps et al.

(2024) to reproduce the same patient's ECG, whose biventricular geometry was used; CV in the Purkinje network was calibrated to 200 cm/s, as observed in isolated human hearts (Durrer et al., 1970). I show resulting biventricular activation and repolarisation times in Figure 8 A and compare clinical and simulated ECGs in Figure 8 B.

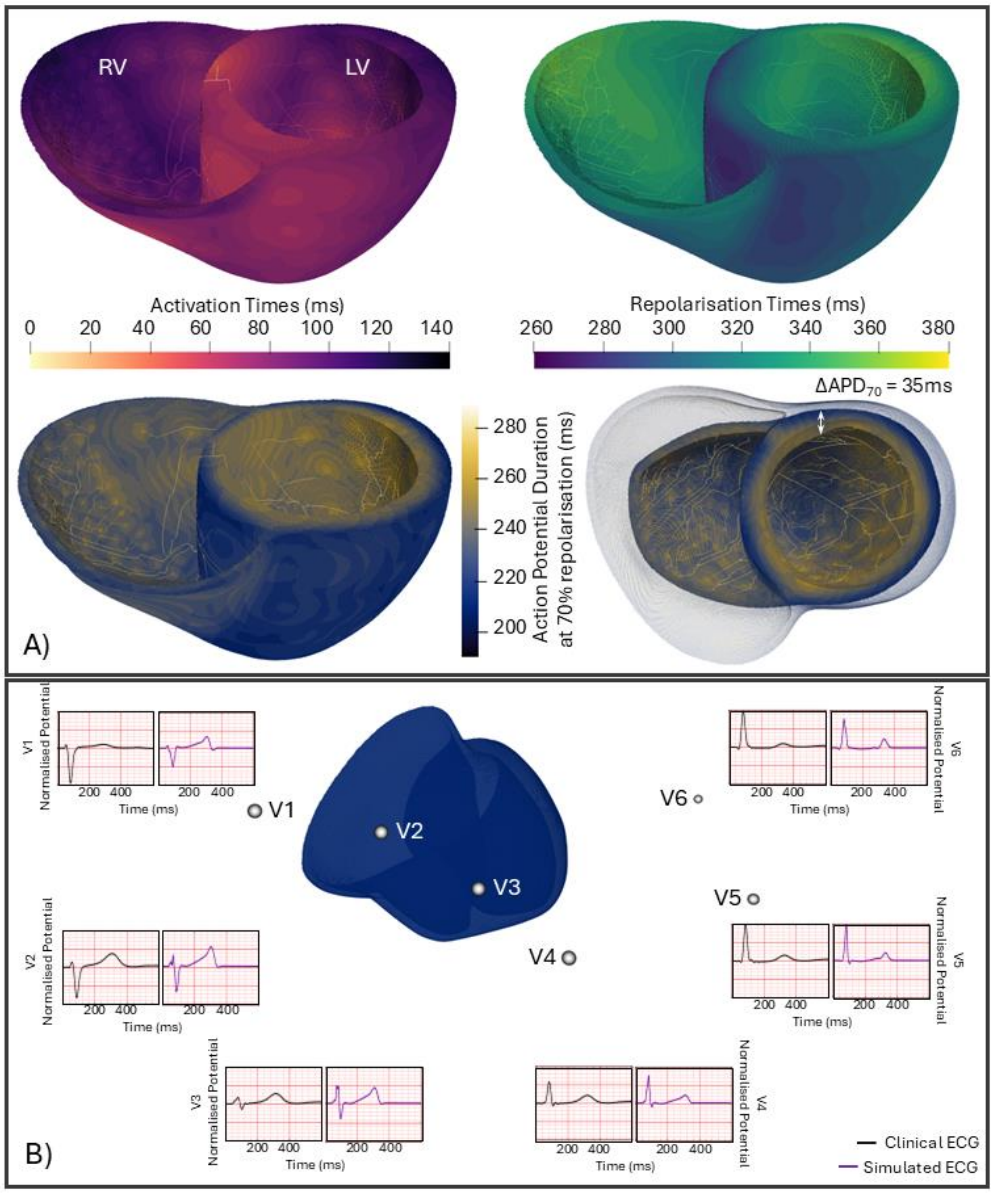


Figure 8. Electrical activation in the healthy biventricular model. A) top left: activation time map, top right: repolarisation time map, and bottom: AP duration at 70% repolarisation. B) ECG electrodes and clinical (solid black traces, Mincholé et al. (2019)) versus simulated (solid purple traces) ECGs. Caption modified and labels A) and B) were added but otherwise the figure is unmodified and was obtained from the supplementary material of Riebel et al. (2024) under CC BY license (https://creativecommons.org/licenses/by/4.0/).

To capture electrophysiological heterogeneity across the ventricles, I applied established cellular scaling factors, as summarised in Table 2, to produce an apicobasal gradient of

10 ms and a transmural gradient of 35 ms (Boukens et al., 2015; Franz et al., 1987; Mincholé et al., 2019; Okada et al., 2011; Szentadrassy et al., 2005; Tomek et al., 2019), as shown in the bottom of Figure 8 A.

Table 2. Scaling factors for ionic current conductances and time constants resulting in a transmural (endocardial vs epicardial) gradient of 35 ms and an apicobasal gradient of 10 ms as computationally established in Mincholé et al. (2019), Okada et al. (2011), and Tomek et al. (2019).

Model Parameter	Epicardial Cells	Apicobasal Gradient
G_{NaL}	$* 0.6$	
P_{NaK}	$* 0.9$	
G_{to}	$* 2.0$	
$delta_{epi}$	$= 1 - \frac{0.95}{1+e^{\frac{V_m+70}{5}}}$	
G_{Kr}	$* 1.3$	
G_{Ks}	$* 1.4$	$* gradient\ between$ $0.2\ (base)\ and\ 5.0\ (apex)$
G_{K1}	$* 1.2$	
G_{Kb}	$* 0.6$	
G_{NaCa}	$* 1.1$	
P_{Ca}	$* 1.2$	
J_{upnp}	$* 1.3$	
J_{upp}	$* 1.3$	
$cmdn_{max}$	$* 1.3$	

5.2 Modelling functional and structural changes in ischemic heart disease

As I described in Section 3.1, ischemia denotes an insufficient blood, oxygen, and nutrient supply to the cardiac tissue. As a response, cardiomyocytes undergo electrophysiological and structural remodelling. To investigate arrhythmic risk in ischemic heart disease and treatment, I incorporated electrophysiological remodelling at different stages of ischemia and infarction. Specifically, in the following sections, I will detail the modelling and simulation choices from single cell to the ventricles to capture I_{KATP} activation in early ischemia as well as remodelling in acute, healing, and chronic MI.

5.2.1 Modelling electrophysiological changes induced by ischemia and infarction

As previously mentioned, insufficient nutrient supply during ischemia leads to the affected myocardium to become hypoxic. During hypoxia, low oxygen levels cause a reduced availability of ATP, which in turn results in I_{KATP} channels of human cardiomyocytes to open. I introduced a well-established formulation of I_{KATP} (Dutta et al., 2017; Ferrero et al., 1996; Martinez-Navarro et al., 2019, 2024; Michailova et al., 2005; Shaw & Rudy, 1997) into the cellular ToR-ORd model of human ventricular cardiomyocytes, which depends on the membrane potential (V_m), the Nernst Potential for potassium (E_K), the channel conductance (G_{KATP}), a scaling factor for the fraction of open I_{KATP} channels (f_{KATP}), the extracellular K^+ concentration (K_e), the intracellular ATP concentration (ATP_i), and the sensitivity of I_{KATP} channels to ATP (K_{ATP}):

$$I_{KATP} = G_{KATP} * (V_m - E_K) * \left(\frac{[K_e]}{[K_{e,normal}]}\right)^{0.24} * \left(\frac{1}{1 + \left(\frac{[ATP_i]}{K_{ATP}}\right)^2}\right) * f_{KATP} \quad (36)$$

In healthy conditions, f_{KATP} was 0 and no I_{KATP} was flowing. To simulate hypoxia in myocardial ischemia, I set ATP_i to 2.0, G_{KATP} to 4.4, K_{ATP} to 0.25, and varied f_{KATP} between 0.05 and 0.1. These values were calibrated by others in previous work to achieve a physiological AP shortening in line with experimental observations (Dutta et al., 2017; Ferrero et al., 1996; Martinez-Navarro et al., 2019; Shaw & Rudy, 1997). In line with updates made in the human ventricular cardiomyocyte ToR-ORd model used here (Tomek et al., 2019, 2020), I set $K_{e,normal}$ to 5.0 rather than to the frequently used value of 5.4.

Reduced wash out and hyperkalaemia may prevail in the post-ischemic myocardium; accordingly, to simulate acute MI, I increased K_e in the infarct centre to 8.5 mM, as done

by Wang et al. (2021). To simulate scarring and cell death that starts to occur in the acute and healing infarct, I incorporated further ion channel remodelling as established in previous work by Zhou et al. (2024) and Wang et al. (2021), which used experimental evidence as summarised in Table 3. These included reduced Na^+, K^+, and Ca^{2+} currents as suggested experimentally (Aggarwal & Boyden, 1995; Hegyi et al., 2018; M. Jiang et al., 2000; Lue & Boyden, 1992; Pu & Boyden, 1997; Valdivia et al., 2005).

Table 3. Scaling factors to model injury (IZ), border (BZ), and remote zones (RZ) during ischemia as well as acute, healing, and chronic MI, as established in Wang et al. (2021) and Zhou et al. (2024). Supporting data can be found in [1]Hund et al. (2008), [2]Lue & Boyden (1992), [3]M. Jiang et al. (2000), [4]Maier et al. (2003), [5]Pu & Boyden (1997), [6]Aggarwal & Boyden (1995), [7]Ringenberg et al. (2014), [8]Valdivia et al. (2005), [9]Hegyi et al. (2018), [10]M. T. Jiang et al. (2002), [11]Høydal et al. (2018), and [12]Hoch et al. (1999). G_s: conductance of ion channel s, K_o: extracellular K^+ concentration, f_{KATP}: scaling factor for the fraction of open I_{KATP} channels, P_s: permeability to ion species s, J_{up}: total Ca^{2+} uptake through SERCA, tau_{relp}: time constant of Ca^{2+}/calmodulin-dependent protein kinase II (CaMK)-induced Ca^{2+} release, aCaMK: CaMK autophosphorylation rate. Caption modified and table reordered and extended with I_{KATP} remodelling but otherwise unmodified from the supplementary material of Riebel et al. (2024) under CC BY license (https://creativecommons.org/licenses/by/4.0/).

Model Para-	Ischemia	Acute Infarction		Healing Infarction		Chronic Infarction		
meter	IZ	IZ	BZ	IZ	BZ	IZ	BZ	RZ
V_m						$= -60^{7}$		
G_{Na}		$* 0.575$	$* 0.575$	$* 0.4^{1,5}$	$* 0.4^{1,5}$		$* 0.43^{8}$	$* 0.43^{8}$
G_{NaL}							$* 1.275^{9}$	$* 1.413^{9}$
K_o		$= 8.5$						
G_{to}		$* 0^{1,2}$	$* 0^{1,2}$	$* 0^{1,2}$	$* 0^{1,2}$			
G_{Kr}		$* 0.375^{3}$	$* 0.7$	$* 0.375^{3}$	$* 0.7$		$* 0.89^{9}$	$* 0.87^{9}$
G_{K1}		$* 0.6^{1}$	$* 0.6^{1}$	$* 0.6^{1}$	$* 0.6^{1}$		$* 0.76^{9}$	
f_{KATP}	$= \{0.05 \mid 0.1\}$							
G_{KCa}							$* 2^{9}$	$* 2^{9}$
P_{Ca}		$* 0.7$	$* 0.7$	$* 0.64^{1,6}$	$* 0.64^{1,6}$		$* 0.7^{9}$	
P_{Cab}		$* 1.33^{1}$	$* 1.33^{1}$	$* 1.33^{1}$	$* 1.33^{1}$			
J_{up}							$* 0.4^{10,11}$	$* 0.4^{10,11}$
tau_{relp}		$* 6^{4}$	$* 6^{4}$	$* 6^{4}$	$* 6^{4}$		$* 6^{4}$	$* 6^{4}$
aCaMK		$* 1.5^{1}$	$* 1.5^{1}$	$* 1.5^{1}$	$* 1.5^{1}$		$* 1.5^{12}$	$* 1.5^{12}$
G_{ClCa}							$* 1.25^{9}$	$* 1.25^{9}$

Finally, once the affected tissue has turned into a scar, very few, if any, viable cardiomyocytes remain. Instead, the chronic infarct core is now largely composed of collagen and fibroblasts, as discussed by Rog-Zielinska et al. (2016). As fibroblasts have been shown to produce AP-like fluctuations when coupled to cardiomyocytes (Camelliti

et al., 2005; Klesen et al., 2018; Kohl, 2003; Yue et al., 2011), I modelled chronic infarct scars as conducting but electrically non-active as done in previous studies; specifically, the starting membrane potential of scarred cardiomyocytes was set to -60 mV and only changed through terms of diffusivity (Connolly & Bishop, 2016; Ringenberg et al., 2014).

Additionally, the loss of viable myocardium results in adverse remodelling also in the remote zone, which compensates for the loss of contractility and increased stiffness of the scar. This has been shown to involve an upregulation of the Ca^{2+}-activated potassium (I_{KCa}) and chloride (I_{ClCa}) channels, as described experimentally (Hegyi et al., 2018). As I_{KCa} is not present in the human ventricular cardiomyocyte ToR-ORd model by default, it was included, together with a 10% down-regulation of the background K^+ current's (I_{Kb}) conductance to compensate for the added potassium current, by Zhou et al. (2024) and used here. Specifically, I_{KCa} was calculated as follows, using the channel's conductance (G_{KCa}), the fraction of I_{KCa} channels in the junctional subspace ($f_{IKCa,ss}$), the membrane potential (V_m), the Nernst potential for K^+ (E_K), and the Ca^{2+} concentrations in the subspace as well as the free intracellular space (Zhou et al., 2024):

$$I_{KCa} = G_{KCa} * (V_m - E_K) * (f_{IKCa,ss} * \frac{[Ca_{ss}]^{3.5}}{[Ca_{ss}]^{3.5}+0.000605^{3.5}} + (1 - f_{IKCa,ss}) * \frac{[Ca_i]^{3.5}}{[Ca_i]^{3.5}+0.000605^{3.5}}) \quad (37)$$

I show the resulting simulated AP traces of ischemia as well as acute, healing, and chronic infarction of human ventricular cardiomyocytes in Figure 9 B.

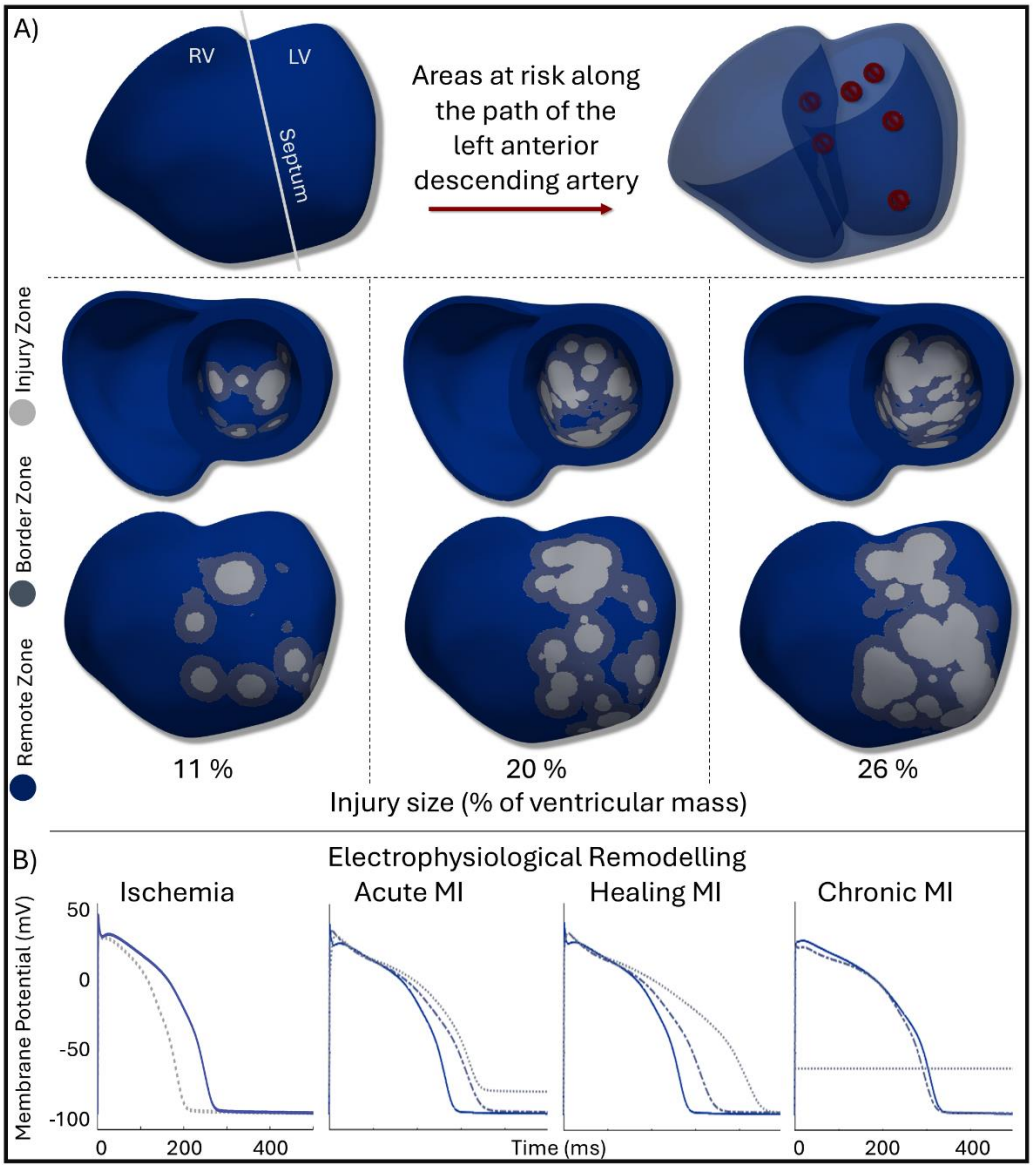


Figure 9. Modelling and simulating ischemic heart disease. A) Landmarks to model occlusion of the left anterior descending artery and example injuries created with the algorithm from Cardone-Noott et al. (2014) and Y. R. Hill et al. (2016). B) APs in ischemia (focus on I_{KATP}-activation) as well as acute, healing, and chronic MI. Note that when simulating ischemia, the border zone was considered healthy. For the shown ischemic AP, f_{KATP} was set to 0.1.

5.2.2 Creating physiological geometries of ischemic heart disease injury

For this work, I introduced a range of post-occlusion injury geometries and sizes into a healthy biventricular geometry to study associated pro-arrhythmic effects. The pro-arrhythmic role of isthmuses through the scar core has been highlighted in a comparative computational study by Connolly & Bishop (2016). Accordingly, to model complex physiological scars, I employed an established algorithm by Cardone-Noott et al. (2014) and Y. R. Hill et al. (2016) to create non-uniform transmural post-occlusion injuries and

surrounding border zones. The algorithm works as follows: the user defines contact points that represent the path of the occluded artery along the myocardium. Here, to model LAD occlusion (Brinkman et al., 1994), I selected six landmarks: two in the septum, three in the anterior wall, and one in the apex, as shown in Figure 9 A. Next, the algorithm randomly selects as many post-occlusion injury cores as desired, with respect to the defined contact points. Finally, the distance of each mesh element to the post-occlusion injury cores is calculated using Dijkstra's algorithm, and elements are tagged as injury or border zone if below a user-specified cut-off distance (Cardone-Noott et al., 2014; Y. R. Hill et al., 2016). To create a cohort of transmural ischemic heart disease injuries, I varied the number of cores between 50 and 300 and calibrated the resulting LAD-occlusion injury population to cover clinically reported LV infarct masses between 10% and 30% (Garg et al., 2017; Reindl et al., 2020; Spath et al., 2021). I further calibrated the post-occlusion injury zone threshold and, where used, border zone threshold to 0.13 and 0.18, respectively, to reproduce clinically observed infarct and border zone ratios (Tülümen et al., 2021). The algorithm also includes a scaling factor of 1.2 for the cutoff distance to favour apical mesh elements (Cardone-Noott et al., 2014; Y. R. Hill et al., 2016); this accounts for the spreading and branching of the LAD towards the apex, facilitating apical involvement in anterior scars as highlighted clinically (Ørn et al., 2007). The ischemic heart disease injury geometries I created here are all transmural and resemble occlusion of the proximal LAD. Their different sizes may clinically relate to the timing of reperfusion but could also capture overlapping injuries after re-infarction. For each research question and based on the desired scar complexity and size, I chose a set of LAD-occlusion injury geometries from the cohort, some examples of which are shown in Figure 9 A.

5.2.3 Structural remodelling of the ventricles after myocardial infarction

Infarction causes necrosis and fibrosis and therefore pronounced structural changes of the affected area, as summarised by Holmes et al. (2005). Specifically, and as mentioned in Section 5.2.1, because fibroblasts do not produce an AP but mere AP-like voltage fluctuations, their ability to propagate the heartbeat is reduced. Additionally, collagen deposits within the scar further insulate electrical propagation (Holmes et al., 2005). In line with experimental reports, I calibrated conductivity tensors within the infarct cores and border zone to achieve a 70% reduced CV in healing MI (Aronis et al., 2020; Jamil-Copley et al., 2015). I also used the calibrated conductivity tensor in the central and border zone of acute and chronic infarction, but not in early ischemia, as structural damage may not occur immediately. Due to further ionic remodelling, particularly reduced Na^+ channel conductance, CVs varied across stages of ischemic heart disease from early ischemia to chronic infarction, as shown in Table 4.

Table 4. CV (cm/s) for different stages and areas of ischemic heart disease injury (all calibrated in a fully endocardial tissue slab). For the ischemic stage, the f_{KATP} parameter was set to 0.1. Remote zone and ischemic injury zone conductivity tensor: (2.60, 1.05, 1.60) mS/cm, injury zone and border zone conductivity tensor during infarction: (0.60, 0.35, 0.45) mS/cm. F: fibre, S: sheet (transmural), N: sheet normal direction.

	CVs (cm/s)								
	Remote Zone			Border Zone			Injury Zone		
	F	S	N	F	S	N	F	S	N
Ischemia	65	38	47	-	-	-	64	37	47
Acute Infarction	65	38	47	22	14	17	15	10	12
Healing Infarction	65	38	47	19	12	15	19	12	15
Chronic Infarction	49	27	34	19	12	15	9	7	8

5.3 Modelling and simulation of therapies for ischemic heart disease

The human myocardium does not sufficiently regenerate and hence the damage caused by ischemic heart disease is largely irreversible. Novel treatment strategies include the injection of stem cells and hPSC-CMs to revitalise the scarred myocardium. However, immaturity and heterogeneity amongst the injected cells may be pro-arrhythmic and

drugs to mitigate such safety concerns are needed. The following sections will outline the modelling and simulation tools I employed or developed to simulate cell therapy and drug application for arrhythmia investigations.

5.3.1 Simulating regenerative cell therapy

5.3.1.1 Cellular models of stem cell derived cardiomyocytes

To simulate ventricular-like hPSC-CMs, I used the Paci2020 model by Paci et al. (2020). Furthermore, as pro-arrhythmic heterogeneity within the delivered cell population is a frequent concern in pre-clinical studies (Selvakumar et al., 2024), I constructed an atrial-like and a nodal-like hPSC-CM phenotype from the baseline model. For this, I created a population of 10,000 Paci2020 models by scaling key ion channel conductances, specifically those of I_{NaF}, I_{NaL}, I_{to}, I_{Kr}, I_{Ks}, I_{K1}, I_{CaL}, I_{NaCa}, I_{NaK}, I_{up}, I_{rel}, I_{leak}, and I_f, with a random value between 0 and 5. To calibrate the resulting models, I consulted atrial-like and nodal-like AP biomarkers from the same experimental dataset that was used to construct the baseline ventricular-like hPSC-CM Paci2020 model (Ma et al., 2011). From the hPSC-CM population, I selected the two models most closely resembling the experimental atrial-like and nodal-like phenotype; AP traces are depicted in Figure 10 and a comparison of biomarkers and ionic current conductance scaling factors for the different cell types is shown in Table 5 and Table 6, respectively.

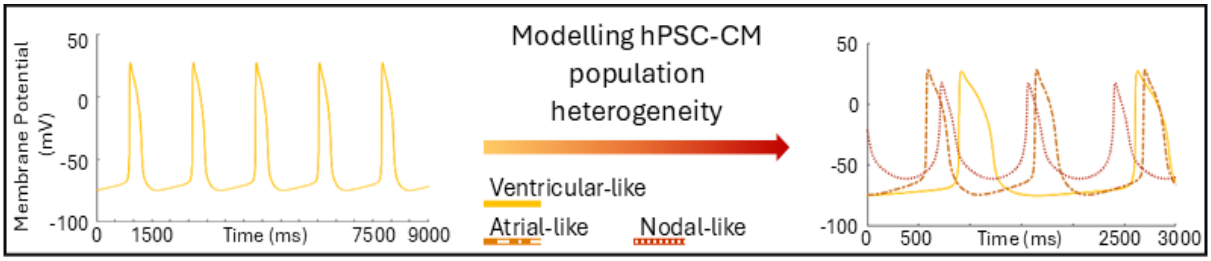


Figure 10. hPSC-CM APs of the ventricular-like (solid yellow traces left and right), atrial-like (dashed orange traces right), and nodal-like (dotted red traces right) phenotype. Note, the nodal-like hPSC-CMs exhibit the most depolarised diastolic membrane potential, fastest beating, and shortest APD.

Table 5. Experimental (from [1]Ma et al. (2011)) and simulated (using Paci et al. (2020)) spontaneous AP biomarkers of the ventricular-like, atrial-like, and nodal-like hPSC-CMs. $V_{m,peak}$: peak membrane voltage, Interval: spontaneous beating interval. Caption extended and values in the table rounded but otherwise unmodified from the supplementary material of Riebel et al. (2024) under CC BY license (https://creativecommons.org/licenses/by/4.0/).

	MDP (mV)		dV/dt_{max} (V/s)		$V_{m,peak}$ (mV)		APD_{90} (mV)		Interval (s)	
	Exp.[1]	Sim.	Exp.[1]	Sim.	Exp.[1]	Sim.	Exp.[1]	Sim.	Exp.[1]	Sim.
Ventr.	-75.6	-74.9	27.8	20.5	28.3	27.1	415	402	1.7	1.7
Atrial	-73.5	-74.2	26.2	8.9	26.7	28.0	286	269	1.2	1.1
Nodal	-60.1	-61.1	5.5	4.3	19.5	17.4	255	271	1.0	0.9

Table 6. Ionic current scaling factors to simulate ventricular-like, atrial-like, and nodal-like phenotypes of the stem cell-derived cardiomyocyte Paci2020 model (Paci et al., 2020). G_s: conductance of ion channel s, k_{NaCa}: scaling factor for I_{NaCa}, p_{NaK}: maximum I_{NaK}, $V_{max,up}$: maximum I_{up}, V_{leak}: maximum I_{leak}. Caption extended but table unmodified and obtained from the supplementary material of Riebel et al. (2024) under CC BY license (https://creativecommons.org/licenses/by/4.0/).

Scaled Parameters	Scaling Factor		
	Ventricular-like	Atrial-like	Nodal-like
G_{NaF}	1.00	0.57	1.17
G_{NaLmax}	1.00	3.48	1.84
G_{to}	1.00	3.15	2.28
G_{Kr}	1.00	4.21	3.15
G_{Ks}	1.00	0.63	0.57
G_{K1}	1.00	0.35	0.01
G_{CaL}	1.00	1.75	0.95
k_{NaCa}	1.00	1.54	1.18
p_{NaK}	1.00	1.17	0.95
V_{maxup}	1.00	2.96	0.05
G_f	1.00	1.17	1.25
$G_{irelmax}$	1.00	0.09	1.20
V_{leak}	1.00	0.11	2.91

5.3.1.2 Modelling cell delivery into the ventricles

As I discussed in Section 3.5.1, delivery of stem cells and hPSC-CMs after MI has been achieved through transplantation of *in vitro* grown cell sheets during open-heart surgery as well as intramyocardial injection, commonly using a catheter. Here, to model spatial distribution of delivered cells, I created an algorithm that allows for modelling both, cell sheet transplantation as well as cell injection. This algorithm, summarised in Algorithm 1, starts from a user defined set of delivery locations. The user is further able to set area-dependent probabilities of where delivered cells engraft, i.e. the chance to settle in the

endocardium, subendocardium, or epicardium of the remote zone, healthy zone, and infarcted area. These parameters allow for incorporating experimental observations, such as the engraftment transmurality (e.g. injection in the endocardium versus epicardium), migration, and retention (e.g. if paracrine signals in the infarct promote cell survival). Next, for each mesh element it is decided whether it is replaced by an hPSC-CM. This decision is made using a uniformly distributed random number, which is scaled depending on the distance to the closest delivery location and a user-defined clustering and cutoff factor. The former favours hPSC-CMs to be introduced close to the delivery locations whilst the latter restricts the size of the hPSC-CM areas to a set radius around the delivery points.

Algorithm 1. Modelling cell delivery into the ventricles

User defines mesh and delivery locations

User defines clustering scaling factor and cutoff distance

User defines area-dependent probabilities, i.e. chance for delivered cells to settle in the endocardium, subendocardium, and epicardium of the remote zone, border zone and infarct zone

User defines probability for the delivered cell to be ventricular-like, atrial-like, or nodal-like

for *each mesh element within the LV* **do**

Calculate distance to each delivery location and select minimum

Scale distance as: $\frac{cutoff\ distance - min(distance)}{\frac{cutoff\ distance}{clustering\ scaling\ factor}}$

Choose a uniformly distributed random number between 0 and 100

if *random number* < *scaled distance* * *local probability* **do**

Draw another random number using the heterogeneity-dependent probabilities to decide on the delivered cell's cell type

Tag element as ventricular-like, atrial-like, or nodal-like hPSC-CM

else do

Do nothing – element stays native adult ventricular cardiomyocyte

Algorithm 1. Pseudo-algorithm to model spatial distribution of delivered hPSC-CMs in the infarcted ventricles, as described in Riebel et al. (2024).

To achieve physiological spatial hPSC-CM distributions, as shown in Figure 11, I calibrated the local probabilities, scaling factor, and cutoff distance against pre-clinical data of cell therapy in non-human primate myocardial tissue slices and in the injured pig heart from Poch et al. (2022). Specifically, the referenced paper shows that delivered cells were more likely to settle in the infarct than in the border zone (Poch et al., 2022, Figure 3h), how, from their subendocardial injection point, the cells migrate towards the endocardium and epicardium (Poch et al., 2022, Figure 6g), and the overall ratio of injected cells to native adult ventricular cardiomyocytes in the infarct core (Poch et al., 2022, Figure 6g). After calibration, this resulted in 28.4, 22.1 and 23.4% of the small, medium, and large infarct, respectively, being replaced by hPSC-CMs in my simulations.

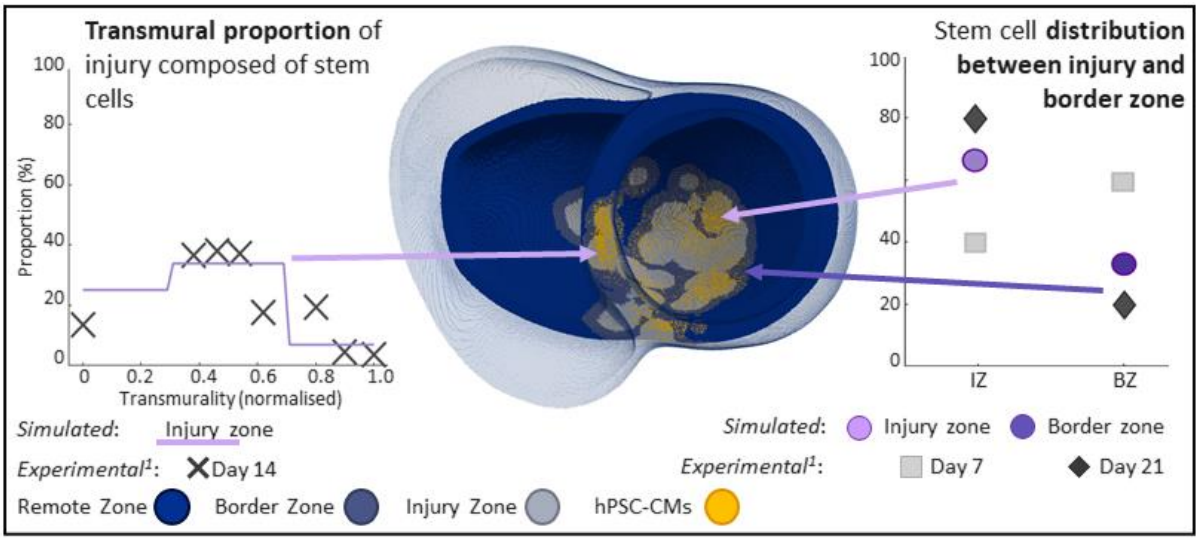


Figure 11. Modelling and simulating spatial distribution of cell therapy and comparing in silico distributions with [1]experimental data from Poch et al. (2022, Figures 3h and 6g and related supplementary data). Note, stem cell distribution between injury and border zone (right graph) refers to out of all hPSC-CMs, how many locate in the border zone versus the infarct zone.

Furthermore, to investigate the arrhythmogenic implications of delivered cell population heterogeneity, I created a homogeneous, moderately heterogeneous, and severely heterogeneous hPSC-CM population with a ratio of 100:0:0%, 80:10:10%, and 50:25:25% of ventricular-like, atrial-like, and nodal-like cells, respectively (see 5.3.1.1 for AP details). Resulting calibrated parameters for Algorithm 1 are shown in Table 7.

Table 7. Calibrated parameters for the spatial stem cell-derived cardiomyocyte distribution algorithm. Ratio between endocardium, subendocardium, and epicardium was set to 30:40:30 in the biventricular geometry.

Clustering scaling factor	3
Cutoff distance	16,500 µm

Area-dependent probabilities (%):			
	Endocardium	Subendocardium	Epicardium
Remote Zone	0	0	0
Border Zone	9	16	4
Infarct Zone	21	36	11

Heterogeneity-dependent probabilities (%):			
	Ventricular-like	Atrial-like	Nodal-like
100:0:0 population	100	0	0
80:10:10 population	80	10	10
50:25:25 population	50	25	25

Finally, with a conductivity tensor of (0.2, 0.2, 0.2) mS/cm, I calibrated ventricular-like hPSC-CM CV to 10 cm/s, as reported in pre-clinical studies (Hansen et al., 2018). Due to cellular differences, this resulted in CVs of 8 and 6 cm/s in the atrial-like and nodal-like hPSC-CMs, respectively. At the interface between hPSC-CMs and adult ventricular cardiomyocytes, conductivities were calculated as the harmonic mean (Sachetto Oliveira et al., 2018).

5.3.2 Simulating ionic current agonists and antagonists

Many therapeutic actions, such as drug application, block or enhance ionic currents. First, to simulate the application of a drug at dose D, I used the simple pore block model, as described in Brennan et al. (2009). It derives the conductance g_x of a blocked ion channel x using the half maximal inhibitory concentration $IC_{50,x}$ and the Hill coefficient h, as shown below (A. V. Hill, 1910; Passini et al., 2017).

$$g_x = g_{x,control} * \frac{1}{1 + \left(\frac{[D]}{[IC_{50,x}]}\right)^h} \quad (38)$$

Next and similarly to the above, I simulated long term up- or downregulation of ionic currents, such as in different cell cultures or after gene editing, by scaling the affected ion channel's conductance. In the 3D modelling and simulation framework, ionic current agonists or antagonists could be applied either globally to all cells in the biventricular mesh or localised to a specific cell type, such as the injected hPSC-CMs.

In this thesis, I investigated ionic targets mainly for the purpose of reducing arrhythmia burden. However, many therapeutic interventions also impact the heart's calcium dynamics and, therefore, its contractile capabilities. Maintaining the heart's pumping function is especially crucial in post-MI patients, who often develop heart failure, including heart failure with reduced EF. In the case of cell therapy, therapy safety is considered the primary endpoint but needs to be balanced against the cells' efficacy, for which they were injected in the first place. Here, to identify ionic targets that reduce arrhythmic risk whilst considering the effects on hPSC-CM contractility, I defined a 'Safety-Efficacy' score. Safety and efficacy criteria may vary across different application scenarios, but in this work were defined as target APD_{90} (to reduce pro-arrhythmic repolarisation gradients) and as target CaT amplitude (a surrogate to maximise mechanical function), respectively. Using weights w_{safety} and $w_{efficacy}$ to prioritise safety or efficacy, I calculated the Safety-Efficacy score (SE score) as:

$$SE\ score\ = \frac{w_s * \left(1 - \frac{\left|APD_{90,target} - APD_{90}\right|}{APD_{90,target}}\right) + w_e * \left(1 - \frac{\left|CaT_{Amp,target} - CaT_{Amp}\right|}{CaT_{Amp,target}}\right)}{w_s + w_e} \quad (39)$$

While also suitable to compare different drugs, in this work, I consulted the Safety-Efficacy score to identify the optimal degree of ionic current up- or downregulation to design hPSC-CMs with reduced arrhythmogenicity.

5.4 Simulation protocols

The following sections outline the cellular and 3D simulation protocols I consulted or constructed, particularly those to induce and quantify arrhythmic risk.

5.4.1 Simulating sinus rhythm

To reach steady state, I paced the human ventricular cardiomyocyte ToR-ORd model at 1 Hz for 500 s, with the conditions after the last beat saved and fed into the biventricular model. For the Purkinje model, published steady-state conditions after 1,000 s were used (Camps et al., 2024; Trovato et al., 2020). Where investigated, I obtained steady state conditions of the hPSC-CMs Paci2020 model after 1,000 s of spontaneous activity. I used spontaneous rather than paced conditions for two reasons: 1) coupling in the ventricles was modelled as impaired, with a reduced conductivity tensor, and hence full pacing of the hPSC-CMs could not be assumed and 2) for some of the simulated hPSC-CM phenotypes, spontaneous activity overrode the paced activity in single cell, thereby leading to a lack of steady state under paced conditions.

From the respective single cell steady state conditions, I paced the biventricular models at 1 Hz for three beats. As established by Camps et al. (2024), I applied pacing with a stimulus strength of -40 A/F for 2 ms at a time at the top 25 mesh elements of the bundle of His, each with an edge length of 100 µm.

5.4.2 Stimulation protocol to assess arrhythmic burden

As mentioned in Section 3.3, re-entrant arrhythmias require a substrate as well as a trigger. Re-entrant substrates are commonly provided through repolarisation gradients, which lead to the unidirectional conduction block of a stimulus. In this work, substrates

for unidirectional conduction block were provided by different remodelling conditions in ischemia and infarction as well as effects of treatment, particularly, delivered hPSC-CMs, as described in Section 5.2 and 5.3.1. In the following paragraphs, I will focus on the stimulation protocols I employed or designed to induce and assess ventricular arrhythmias.

First, I consulted the widely used S1-S2 stimulus protocol. Here, the S1 stimulus refers to the last sinus beat, followed by an ectopic S2 beat, originating within the myocardium rather than the bundle of His. These ectopic stimuli are representative of triggered activity, commonly observed in ischemic heart disease and as described in Section 3.3.1. I applied S2 beats with a strength of -100 A/F for 2 ms at a time and investigated different S1-S2 intervals. To obtain an initial estimate of pro-arrhythmic S1-S2 intervals, I calculated the shortest effective AP refractoriness as this is the first time point at which an ectopic beat may propagate in the tissue. In 3D, the refractoriness varied across the tissue, depending on the time of activation during sinus rhythm and the underlying cellular properties. If the beat did propagate at the initially estimated stimulus time, I reduced the S1-S2 interval until no propagation occurred. I also increased the estimated S1-S2 interval – to achieve an S1-S2 interval range of at least 100 ms and until any re-entrant arrhythmias disappeared. In some cases, especially during chronic MI, the repolarisation time difference between the healthy and infarcted tissue was quite large and I had to investigate more S1-S2 intervals. Once both the LAD-occlusion injury and the healthy tissue have fully repolarised, re-entrant arrhythmias are less likely to occur as conduction block is eliminated. It should be noted that re-entrant arrhythmias may also be inducible through fast pacing (El-Sherif et al., 1984), however, I did not investigate this here. I paired the different S1-S2 intervals with different ectopic stimulus locations from

within the border zone. Specifically, I selected 15 subendocardial locations, distributed across the border zone, i.e. the circumference, of the ischemic heart disease injury, as shown in Figure 12.

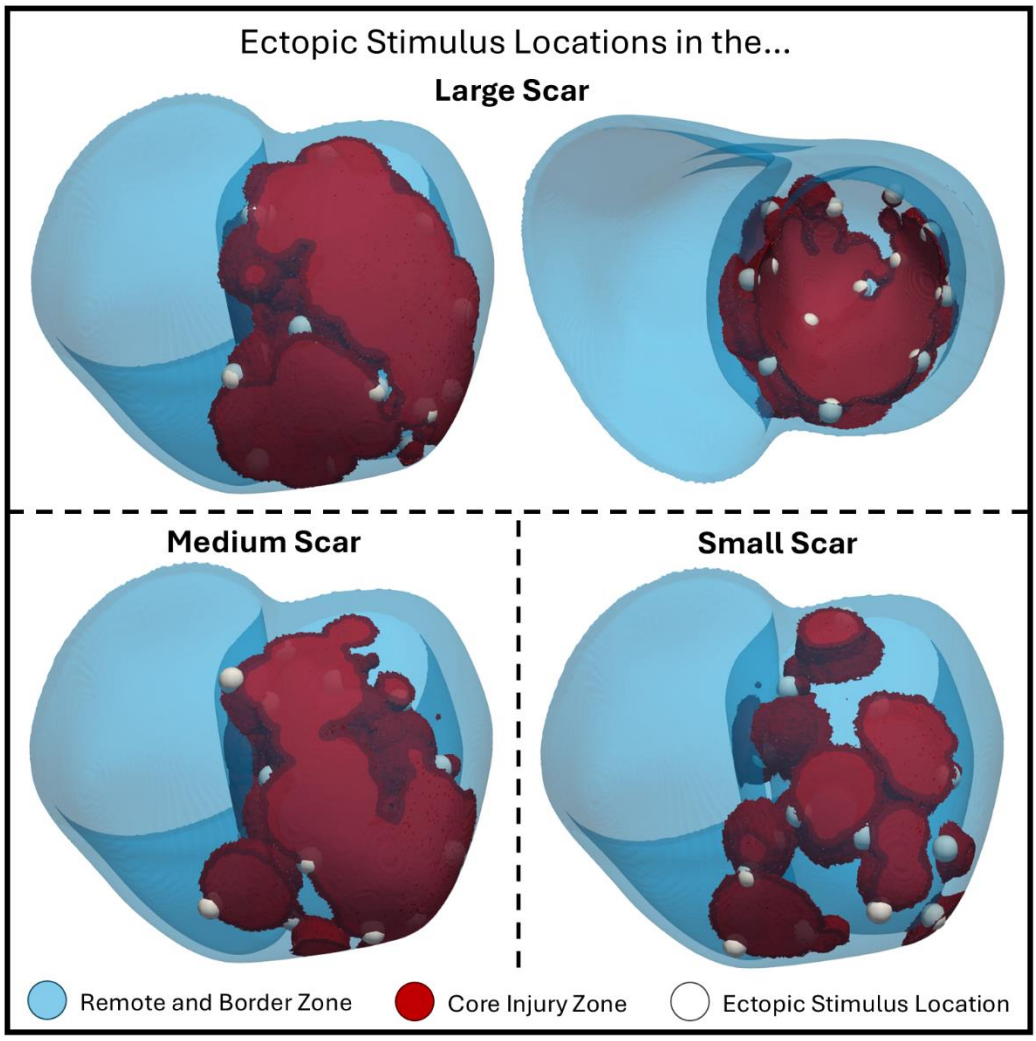


Figure 12. 15 ectopic stimulus locations selected in the subendocardial border zone of three different transmural injury geometries. Note that dark red shading does not indicate the border zone (which is visualised together with the remote zone in blue), but part of the scar that is transmural and hence overshadowed by some of the blue.

Where I investigated hPSC-CM delivery, a second arrhythmia induction protocol was employed. The ectopic S2 beat from within the myocardium was provided by the hPSC-CMs' spontaneous activity rather than an applied stimulus. As this spontaneous beat occurred intrinsically, I did not investigate different ectopic beat locations or S1-S2 intervals. Instead, I ceased sinus pacing after the three initial steady state beats to observe whether spontaneous hPSC-CM beats would emerge and activate the ventricles.

Depending on the hPSC-CMs' beating rate, the ventricular tissue may have already completely depolarised when the spontaneous hPSC-CM beat occurred. Hence, I investigated unidirectional conduction block and subsequent arrhythmogenicity of a following sinus beat (i.e. an S1-S2-S1 pattern). For this, after the initial three 1 Hz steady state beats, I slowed down sinus pacing to varying heart rates.

5.5 Simulation tools and software

I obtained single cell simulations and steady states using the published MatLab code of the respective cellular models. As discussed in the previous chapter, a range of software to simulate 3D electrophysiological propagation in the human heart is available. To facilitate my research's aim to conduct simulations in multiscale human biventricular models of disease and treatment, constraints for my choice of software were 1) allow for fast simulations, 2) be easily customisable to a range of disease conditions and treatments, and 3) enable open-source distribution of the resulting framework. These motivated my choice for the open-source GPU monodomain solver MonoAlg3D (Sachetto Oliveira et al., 2018). Recently, Berg et al. (2023) and Camps et al. (2024) integrated modelling and simulation of Purkinje networks into MonoAlg3D through adding an additional current to both the Purkinje network ($I_{PMJ,P}$) and the endocardial tissue ($I_{PMJ,T}$) side of each Purkinje-myocyte junction (PMJ) to represent their electrical coupling:

$$I_{PMJ,P} = \sum_{i=1}^{N_{T:PMJ}} \frac{(V_{m,T_i} - V_{m,P})}{R_{PMJ}} \quad (40)$$

$$I_{PMJ,T} = \sum_{i=1}^{N_{T:PMJ}} \frac{(V_{m,P} - V_{m,T_i})}{R_{PMJ}} \quad (41)$$

Here, R_{PMJ} denotes the resistance at the PMJ, $N_{T:PMJ}$ the number of mesh elements coupled to the PMJ, V_{m,T_i} the membrane potential in each coupled mesh element, and $V_{m,P}$ the membrane potential of the Purkinje element at the PMJ. By setting $R_{PMJ} = 500\ k\Omega$ and $N_{T:PMJ} = 60$, as done in Camps et al. (2024), the conduction delay in the anterograde (Purkinje to myocardium) as well as the retrograde (myocardium to Purkinje) direction was calibrated to 2 and 1 ms, respectively, similar to experimental recordings (Joyner & Overholt, 1985; Wiedmann et al., 1996).

General input parameters for MonoAlg3D which have not been discussed in previous sections are shown in Table 8 and, unless stated otherwise in Section 5.6 below, were obtained from the original publication (Sachetto Oliveira et al., 2018) or the extension of MonoAlg3D to include the Purkinje network (Camps et al., 2024).

Table 8. General input parameters for MonoAlg3D (Camps et al., 2024; Sachetto Oliveira et al., 2018).

dt_{pde}	0.01 ms
Space adaptivity	false
Output format	ensight
ECG $sigma_b$	20

	ToR-ORd	Trovato2020	Paci2020
dt_{ode}	0.01	0.01	0.01
Absolute tolerance	1e-12	1e-16	1e-12
Use GPU	True	False	True
Time adaptivity	False	False	False
Linear system solver gradient	GPU biconjugate	GPU conjugate	GPU biconjugate
Linear system solver tolerance	1e-12	1e-16	1e-12

Finally, MonoAlg3D simulates the ECG using the pseudo-bidomain approach, in which the extracellular potential V_e can be derived using the distance vector between source and field points $\boldsymbol{r}$, the membrane surface to volume ratio β, and the bath conductivity σ_b, as derived in Bishop & Plank (2011):

$$V_e = \frac{1}{4\pi\sigma_b}\int_{\Omega}\frac{\beta I_m}{||\boldsymbol{r}||}d\Omega \quad (42)$$

Using state-of-the-art supercomputers, such as Piz Daint (Cray XC50 multiprocessor and NVIDIA Tesla P100 GPUs) at the Swiss National Supercomputing Centre, simulating one second of electrical activity in a 3D adult biventricular mesh with an edge length of 300 μm and ~3,960,000 mesh elements took approximately five hours. Simulations were faster in the small, paediatric-like ventricles (due to a decrease in the number of mesh elements to ~2,030,000), for high numbers of hPSC-CMs (as the Paci2020 model contains less state variables), chronic infarction (due to the absence of APs in the scar core), and when the print rate of output files was reduced (e.g. when simulating steady state, where less detailed visual inspection was necessary).

5.5.1 Custom 3D model solver functions

To adapt MonoAlg3D for the purpose of this work, I created some new functions. Firstly, to reduce the size of the mesh file, which contained just under 3,960,000 elements in the adult geometry, I encoded cell types in the mesh file and decoded them in the domain function of MonoAlg3D as described in Table 9.

Table 9. Cell type encoding in the mesh files for MonoAlg3D.

	Endocardial	Midmyocardial	Epicardial
Remote Zone	1	2	3
Border Zone	7	8	9
LAD-Occlusion Injury Zone	4	5	6

	Ventricular-like	Atrial-like	Nodal-like
hPSC-CM	10	11	12

Furthermore, I assigned four fields to each myocardial volume within the MonoAlg3D grid to encode the elements' cell type, transmurality, area, and apicobasal scaling, as shown

in Table 10. I used these fields in MonoAlg3D's models and assembly matrix functions to assign each element the correct cell model, conductivities, and cell model starting states. I did not apply the above to the Purkinje cells because they already had an extensive functionality implemented in MonoAlg3D and did not require further customisation (Camps et al., 2024).

Table 10. Grid element fields for myocardial cells (excluding Purkinje elements). IS_HPSCCM: describes whether this cell is a hPSC-CM, LAYER: encodes location of the cell within the ventricular wall, INJURY_ZONE: LAD-Occlusion injury cores, and APICOBASAL: stores the scaling factor to include apicobasal repolarisation gradients.

Field	Data type	Possible values
IS_HPSCCM	Integer	0: adult ventricular cell 1: ventricular-like hPSC-CM 2: atrial-like hPSC-CM 3: nodal-like hPSC-CM
LAYER	Integer	1: endocardial 2: midmyocardial 3: epicardial 4: irrelevant, cell is hPSC-CM
INJURY_ZONE	Integer	0: remote zone 1: central injury zone 2: border zone 3: irrelevant, cell is hPSC-CM
APICOBASAL	Float	Between 0 and 1 (irrelevant but fixed to 0.5 for hPSC-CMs) and to be normalised to between 0.2 and 5.0 in the cell model

Lastly, I created an extra data function that allowed the user to scale ionic current conductances and concentrations in each cell's cellular model. Extra data included parameters for each of the channels that were remodelled in the remote zone, border zone, and LAD-occlusion injury zone and across the progression of ischemic heart disease from early ischemia to infarction, as listed in Table 3. Extra data also contained global scaling factors, which were applied to all myocardial elements during drug action. In total this amounted to 45 customisable extra data parameters.

5.6 Verification, validation, and uncertainty quantification

To demonstrate the framework's accurate functioning and predictive capabilities to study ischemic heart disease arrhythmias and treatments, I considered verification, validation, and uncertainty quantification principles throughout this work (Musuamba et al., 2021; Viceconti, Pappalardo, et al., 2021).

Software verification was carried out through benchmark tests in the original publications (Paci et al., 2020; Sachetto Oliveira et al., 2018; Tomek et al., 2019; Trovato et al., 2020) and I further compared cellular AP traces and biventricular activation time maps to previous work (Wang et al., 2021). I also established my correct transfer of single cell models into MonoAlg3D's C code by comparing AP traces in MatLab and in a single 3D volume in MonoAlg3D.

The use of experimental and clinical data throughout ensured the modelling and simulation techniques used are suitable to investigate the function of the human ventricles in health and during ischemic heart disease. In support, previous studies demonstrated the power of the utilised cellular models to predict the response in human cells, particularly under drug block (Paci et al., 2021; Passini et al., 2017; Trovato et al., 2022). Furthermore, the used ionic remodelling following ischemic heart disease has been shown to reproduce clinical ECG biomarkers of patients during ischemia and MI (Martinez-Navarro et al., 2019; Wang et al., 2021; Zhou et al., 2024). I performed further comparison to clinical ECG data, particularly across different scar geometries and across the progression of ischemic heart disease, as presented in the relevant results sections.

Finally, I quantified uncertainty through a range of sensitivity analyses. First, I addressed uncertainty in the cellular models' extracellular concentrations, as the human ventricular

cardiomyocyte ToR-ORd model, the Purkinje cell Trovato2020 model, and the ventricular-like hPSC-CM Paci2020 model all contain slightly different non-dynamic extracellular concentrations. Specifically, the extracellular K^+ and Na^+ concentrations in baseline conditions in the ToR-ORd, Trovato2020, and Paci2020 models are 5.0 and 140 mM, 5.4 and 140 mM, and 5.4 and 151 mM, respectively. I did not change these concentrations when the models were introduced into 3D because concentrations as well as AP biomarkers are variable in space and over time. Additionally, maintaining the concentrations as in the original model publications enabled direct comparison between the AP phenotypes to previous works. To assess the impact of concentration uncertainty, I measured the effect of changing the concentrations in Paci2020 to the ToR-ORd values. Depending on the cell type-specific model, the difference in APD_{90} was less than 20 ms, which is within the ranges of experimentally observed AP variability (Ma et al., 2011).

Moving on to verification, validation, and uncertainty in 3D; I carried out convergence analysis for the CV, PDE and ODE time steps, and mesh resolution, as shown in Figure 13 A and B. For this, I constructed a tissue slab with dimensions 20 x 7 x 3 mm and stimulated it in a 1.5 x 1.5 x 1.5 mm corner, in line with established benchmark tests for cardiac solvers (Niederer et al., 2011). Based on these results, I chose a time step of 0.01 ms and a mesh resolution of 300 µm to give a CV error below 10%. As depicted in Figure 13 C, I balanced this against the run time, which increased exponentially for fine mesh resolutions, particularly below 250 µm. Finer time steps also resulted in an increased run time, however the effects were smaller and rather linear (Figure 13D).

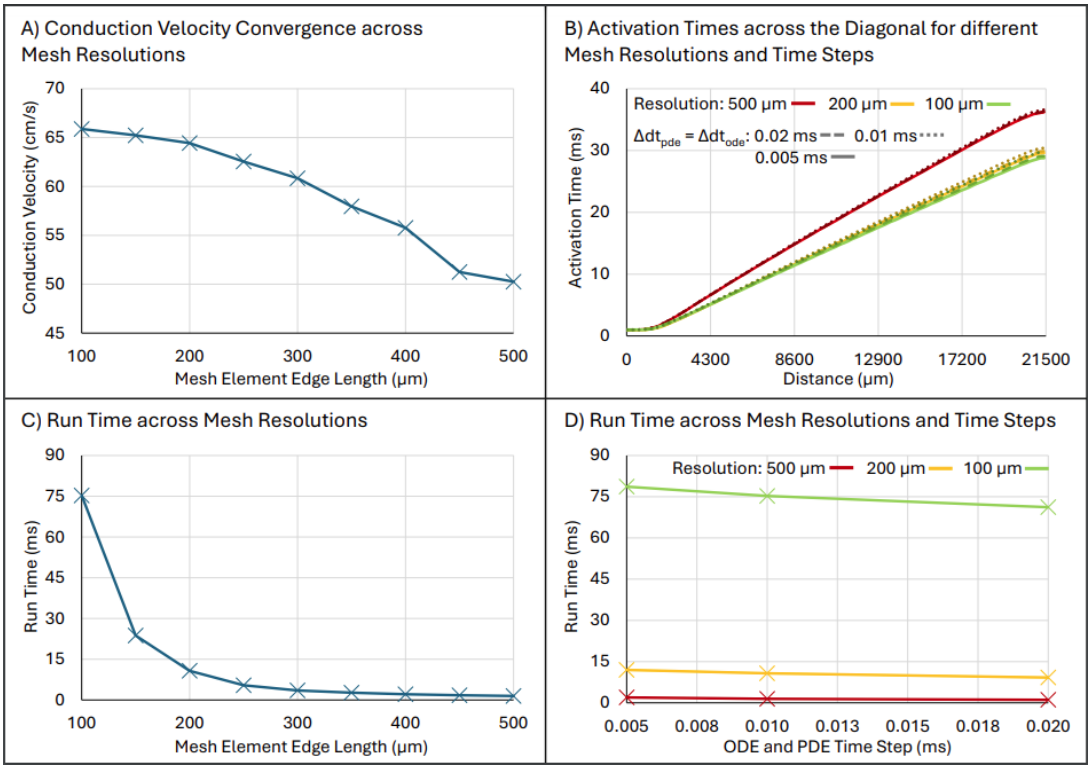


Figure 13. Convergence and run time analyses for different mesh resolutions and time steps as suggested in Niederer et al. (2011).

The effect of the randomness introduced during the hPSC-CM spatial allocation (see Algorithm 1) was addressed by comparing the ECG signals of three different meshes created with the algorithm; as shown in Figure 14, these were virtually identical.

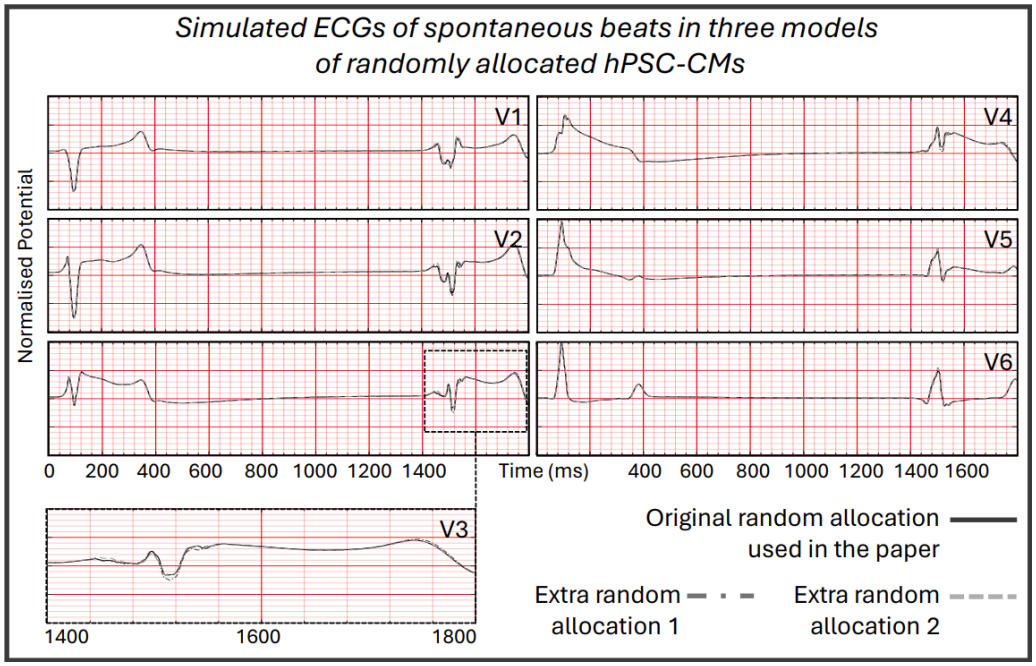


Figure 14. ECG traces to quantify the uncertainty introduced in the random stem cell spatial distribution algorithm shown in Algorithm 1. Note, the traces almost completely overlap. Caption modified but figure unmodified and obtained from the supplementary material of Riebel et al. (2024) under CC BY license (https://creativecommons.org/licenses/by/4.0/).

Uncertainty in experimental and clinical values used for calibration was addressed by investigating the effects of enabled versus disabled retrograde Purkinje propagation and +/- 20% hPSC-CM CV (see Figure 15 and Figure 16). Again, resulting ECGs were nearly indistinguishable.

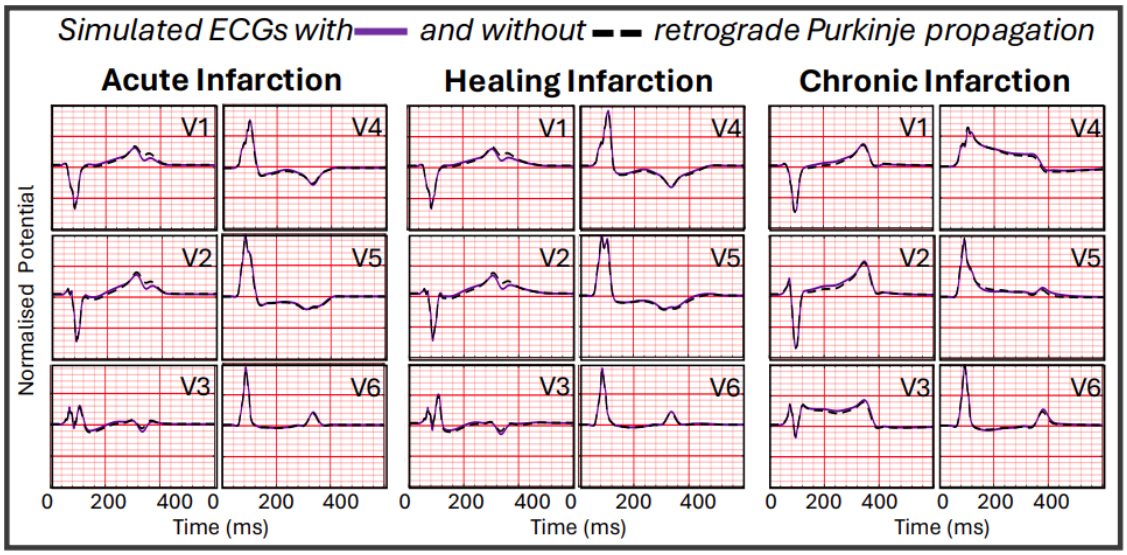


Figure 15. ECG traces with (solid purple line) and without (dashed black line) retrograde Purkinje propagation, which may be impaired following infarction. Note, the traces almost completely overlap. Caption modified but figure unmodified from the supplementary material of Riebel et al. (2024) under CC BY license (https://creativecommons.org/licenses/by/4.0/).

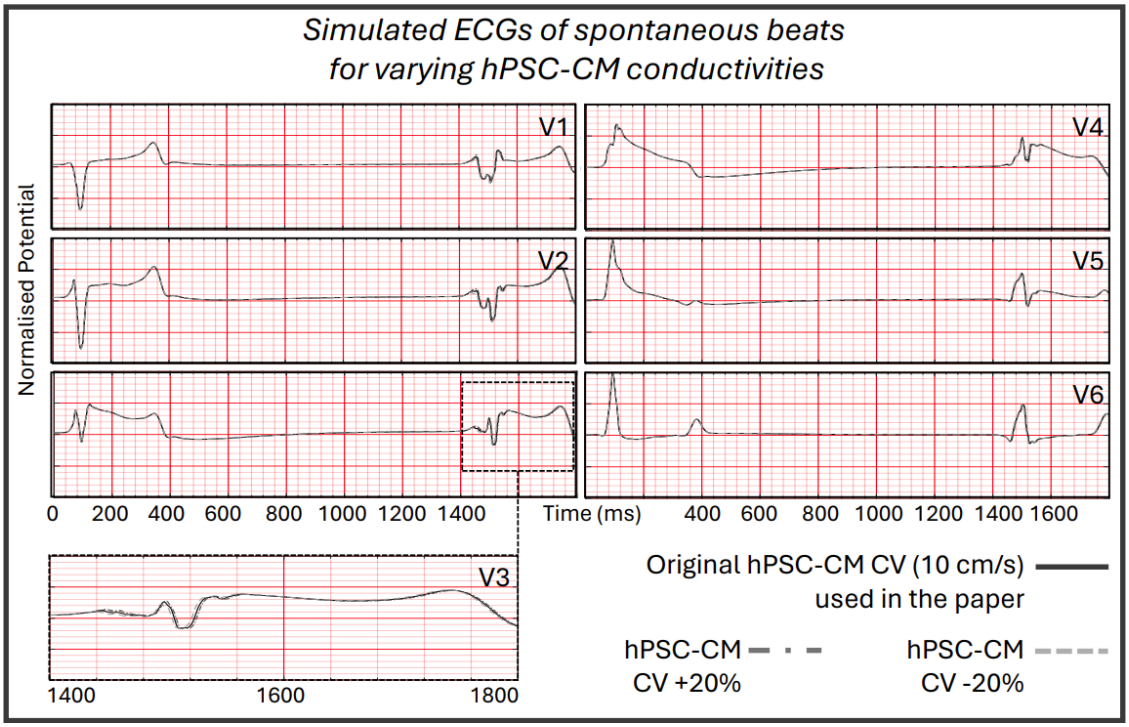


Figure 16. ECG traces to assess uncertainty in hPSC-CM CV. Note, the traces almost completely overlap. Caption modified but figure unmodified and obtained from the supplementary material of Riebel et al. (2024) under CC BY license (https://creativecommons.org/licenses/by/4.0/).

6 Identifying arrhythmic risk markers in small ischemic ventricles to aid clinical risk prediction in paediatric patients

In this chapter, I applied multiscale human ventricular electrophysiological modelling and simulation of ischemic heart disease to elucidate cardiac disease mechanisms aimed to augment clinical risk stratification. Specifically, I studied ischemia-induced arrhythmias, with a focus on I_{KATP}-activation, in small ventricles to aid mechanistic understanding in paediatric patients. To determine pro-arrhythmic risk markers, I investigated the effects of variability in severity of ischemia-induced electrophysiological remodelling and size of the ischemic region. I further studied how AP restitution curve steepness may promote VF rather than VT-like arrhythmias.

6.1 Introduction

As described in Section 3.1, ischemia can be the result of narrowed or blocked coronary arteries, or an otherwise caused mismatch in oxygen demand and output (Thygesen et al., 2019). This occurs not only due to atherosclerotic plaque build-up and rupture in older patients but may also be due to vascular and microvascular dysfunctions, which include structural and functional abnormalities, such as tortuosity of coronary vessels (Del Buono et al., 2021). These may lead to acute hypoperfusion, VF, and ultimately sudden cardiac death. Acute hypoperfusion can cause ischemia and therefore hypoxia and lower ATP availability in the myocardium, which has been linked to an activation of I_{KATP} (Moréna et al., 1980; Nichols, 2016; Noma, 1983; Picard et al., 1999; Weiss et al., 1992).

Due to its detail and systematic control over individual parameters, modelling and simulation brings the unique potential to systematically investigate the precise

mechanisms underlying arrhythmogenesis of ischemia. Human-based simulations are particularly useful where clinical studies are limited, e.g. due to small patient cohorts, ethical concerns, or translational and longitudinal constraints (Bellanti & Della Pasqua, 2011; Fernandez de Canete et al., 2014; Lennie et al., 2022). This is the case in children with chromosomal abnormalities, such as Williams-Beuren syndrome. The disease is rare, affecting 1 in 7,500 (Kozel et al., 2021; Strømme et al., 2002), but commonly leads to congenital heart disease and increased mortality (Salzillo et al., 2024; Twite et al., 2019). Particularly, Williams-Beuren syndrome may involve deletion of elastin genes, which may result in vascular dysfunction (Ewart et al., 1993; D. Y. Li et al., 1997). Cardiovascular complications, also including VF, are amongst the most common causes of death in Williams-Beuren patients, especially under anaesthesia (Bird et al., 1996; Cathey et al., 2024; Hornik et al., 2015; Levin & Kozel, 2017). The pro-arrhythmic contribution of myocardial ischemia and infarction in sudden deaths of Williams-Beuren patients has also been highlighted (Collins, 2013; Conway et al., 1990; Pober et al., 2008; Terhune et al., 1985), with an emphasis on I_{KATP} activation (Levin et al., 2025).

In this chapter, I investigated the re-entrant mechanisms of ischemia driven by congenital heart diseases in small, paediatric-like ventricles using the human electrophysiological modelling and simulation framework, described in Chapter 5. Particularly, my aim for this study was to 1) establish the pro-arrhythmic implications of the ischemic area's size, the severity of I_{KATP} activation, and AP restitution curve steepness and 2) identify the role of these factors to enable VF rather than VT-like arrhythmias in children with rare congenital heart diseases.

6.2 Methods

In the following sections, I summarise the main components of human ventricular electrophysiological modelling and simulation with Purkinje, as described in Chapter 5, and introduce any relevant adaptations.

6.2.1 Simulating ischemia in two action potential phenotypes

As outlined in Section 5.2.1, I modelled ischemia with a focus on the opening of I_{KATP} channels as previously established (Dutta et al., 2017; Ferrero et al., 1996; Martinez-Navarro et al., 2019; Michailova et al., 2005; Shaw & Rudy, 1997). I varied f_{KATP} from 0 (healthy control) over 0.05 to 0.1, resulting in a shortening of the APD by about 40 and 70 ms, respectively, as shown in Figure 17 A.

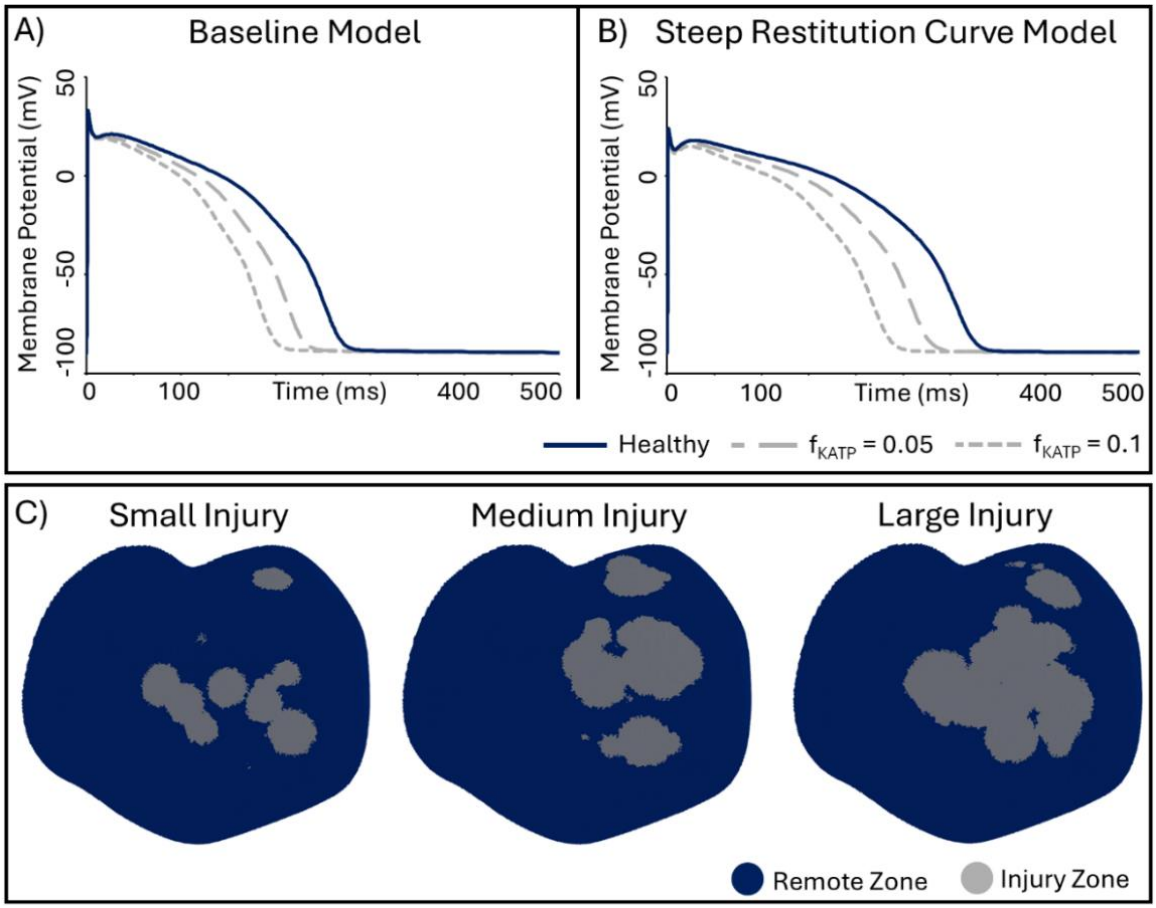


Figure 17. Modelling and simulating I_{KATP}-activation in ischemia. A) ToR-ORd model in health (solid blue line) and ischemia (dashed grey line). B) Steep restitution curve ToR-ORd model from Martinez-Navarro et al. (2024) in health and ischemia. C) Ischemic injuries were created with Cardone-Noott et al. (2014) and Y. R. Hill et al. (2016).

The link between ischemia and VF has long been known experimentally, clinically, and computationally (Bardou et al., 1995; Bradley et al., 2011; Kaplinsky et al., 1979; Luqman et al., 2007; Pogwizd & Corr, 1990). In a recent paper, Martinez-Navarro et al. (2024) created a steep-restitution human ventricular cardiomyocyte ToR-ORd model using the scaling factors shown in Table 11, which I used here, as shown in Figure 17 B, to investigate the effect of AP phenotype on arrhythmia morphology. Note, as chronic infarction was not investigated here, I did not include I_{KCa} in the cellular model of this study.

Table 11. Scalings to create a steep restitution curve ToR-ORd model (Martinez-Navarro et al., 2024). G_s: conductance of ion channel s, P_s: permeability to ion species s, J_{up}/J_{rel}: total Ca^{2+} uptake/release through SERCA, tau_h/tau_j: time constants for inactivation of I_{Na}, tau_{hL}: time constant for inactivation of I_{NaL}, tau_{ff}/tau_{fs}: time constants for inactivation of I_{CaL}, $beta_i$: I_{Kr} inactivation.

Model parameter	Scaling factor	Model parameter	Scaling factor
G_{NaF}	1.3924	G_{K1}	0.7497
tau_h	0.5031	G_{Kb}	0.9069
tau_j		P_{Ca}	0.5956
G_{NaL}	1.3914	tau_{ff}	1.9010
tau_{hL}	0.6590	tau_{fs}	
P_{Nab}	1.3113	P_{Cab}	1.3574
G_{NaCa}	0.9089	G_{pCa}	1.1021
P_{NaK}	1.2763	J_{up}	1.3674
G_{to}	1.4755	J_{rel}	0.6196
G_{Kr}	1.1341	G_{ClCa}	0.7447
$beta_i$	0.3525	G_{Clb}	0.6777
G_{Ks}	0.8178		

Restitution curve, which relates the APD_{90} against the diastolic interval, i.e. the time between the cell's relaxation and following excitation, are known to be crucial for VF susceptability (Garfinkel et al., 2000). A steep restitution curve means that a cell's APD changes more drastically under changing heart rates. Accordingly, a heterogeneous substrate is created, which allows rotors with different wavelengths to meander. Restitution curve steepness has been shown to generally increase with increasing APD at sinus heart rates (Shattock et al., 2017), which agrees with the increase in APD of the two cellular models used here (see Figure 17 A and B).

To obtain steady-state conditions, I paced the healthy and ischemic cellular models for 100 and 500 s, respectively, and then introduced them into the biventricular model. As shown in Figure 18, compared to the baseline AP model, the steep restitution model produced a longer QT interval in 3D, as expected due to its longer APD. To investigate the effect of ventricular size on the ECG, I scaled the healthy adult patient's biventricular geometry, described in Section 5.1.2, and torso by 0.7, 0.8, and 0.9. I also scaled the Purkinje network but maintained myocardial and Purkinje CVs.

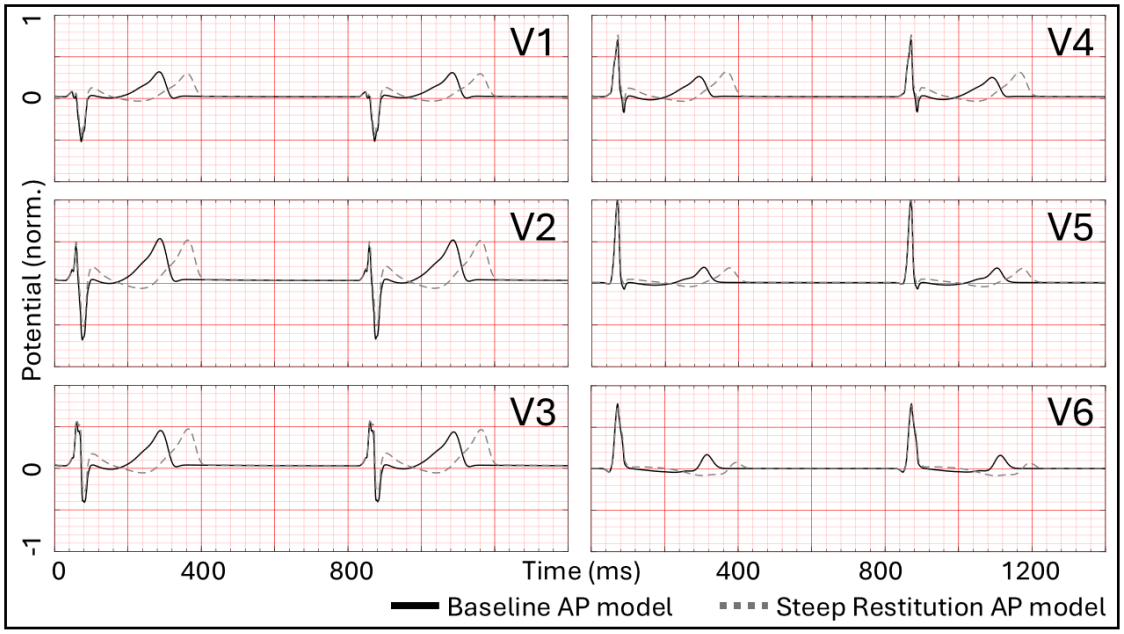


Figure 18. ECGs in a healthy adult ventricular geometry scaled by 0.8 for the baseline and steep-restitution human cardiomyocyte ToR-ORd model (Martinez-Navarro et al., 2024; Tomek et al., 2019).

Using an established algorithm (Cardone-Noott et al., 2014; Y. R. Hill et al., 2016) as outlined in Section 5.2.2, I created three transmural ischemic regions without border zones in the healthy ventricles, as shown in Figure 17 C. These made up 5.2%, 7.8%, and 11.3% of the ventricular volume and will be referred to as the small, medium, and large ischemic regions throughout this chapter.

6.2.2 Simulation and arrhythmia induction protocols

I designed and conducted simulations as described in Section 5.4. Briefly, I simulated three sinus beats to reach steady state in 3D. I increased the sinus pacing rate to 1.25 Hz, i.e. 75 bpm, to be representative of physiological heartrates in children. I chose a relatively slow paediatric heartrate, particularly for young children, as arrhythmias in congenital heart diseases in children, such as Williams-Beuren syndrome are often observed during anaesthesia (Levin & Kozel, 2017). To induce re-entry, I delivered three S1-S2 stimuli at twelve different intervals (from 140 to 360 ms after the last sinus beat) and from 15 different subendocardial locations spread across the edges of the ischemic core. As shown in Figure 12, I varied these locations for each ischemic injury; for the healthy control, I used the stimulus locations of the large ischemic area. Afterwards, I observed simulations for two seconds to assess whether arrhythmias occurred.

This resulted in 1260 biventricular simulations ((healthy control + healthy control with steep restitution cellular model + large ischemic region with f_{katp} = 0.05 + large ischemic region with f_{katp} = 0.1 + three sizes of ischemic regions with steep restitution cellular model and f_{KATP} = 0.1) * 15 stimulus locations * twelve S1-S2 intervals).

6.3 Results

6.3.1 The effect of growing ventricular size on the electrocardiogram

As discussed in Chapter 2.1, the size of the human heart changes as we grow up. For this work, I first assessed how ventricular size effects the ECG. Specifically, whether small ventricular size would explain typical paediatric ECG phenomena, such as shorter QRS intervals and prominent R waves in lead V1. As shown in Figure 19 A and C, scaling the

adult geometry by 0.9, 0.8, and 0.7 produced LV masses of 86, 61, and 44 g, respectively, consistent with ages of approximately 13, 9, and 5 years old (Khoury et al., 2009).

Next, I compared simulated ECG biomarkers with clinical data from children of the same age group (Saarel et al., 2018), as shown in Figure 19 B to F. Downscaling the ventricles caused faster biventricular activation and resulted in QRS shortening, as highlighted in Figure 19 D. Similarly, I observed a reduction of the QT interval with decreasing ventricular size in the baseline and steep restitution curve AP model (see Figure 19 F); as expected, the latter produced longer QT intervals than the baseline model. Whilst within reported ranges, the QT interval from the large to the small ventricular geometry did not shorten as steeply as I expected from clinical data (Saarel et al., 2018). Although my simulations reproduced a general increase of the R wave amplitude for smaller ventricles (see Figure 19 E), they did not capture prominent R-waves in lead V1 (see Figure 19 B) (Rijnbeek et al., 2001; Saarel et al., 2018). They also did not capture inverted T-waves in leads V1 to V3, as often seen in children until adolescence (Saarel et al., 2018).

In summary, my simulations showed that smaller ventricular size in children explains some but not all the typical paediatric ECG features. Nevertheless, because pathway length is a crucial determinant of re-entrant arrhythmia, ventricular size may impact rotor formation and wave breakup. Hence, to investigate ventricular arrhythmias in children, for the rest of this study, I chose to conduct simulations in the mesh scaled by 0.8, representative of the ventricles of an approximately 9-year-old.

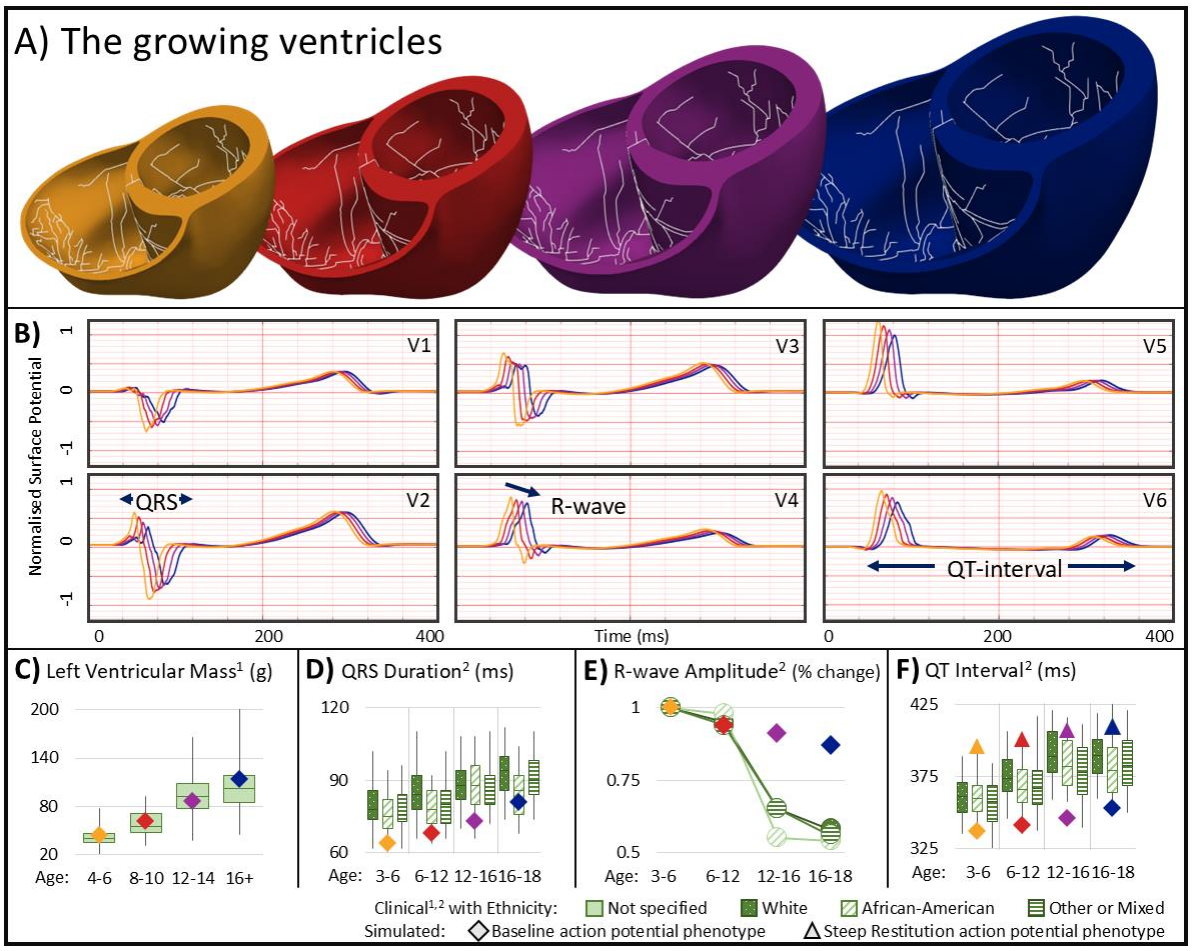


Figure 19. Effects of ventricular size on the ECG. A) An adult female geometry with unknown ethnicity (blue) was scaled by 0.9 (purple), 0.8 (red), and 0.7 (yellow) to produce ECGs (B) and LV masses (calculated as in (Khoury et al., 2009)) (C). Simulated ECG features (colourful squares), specifically QRS duration measured in lead V2 (D), R-wave amplitude measured in lead V4 (E), and Fridericia corrected QT interval duration measured in lead V6 (F), were compared to clinical data (green traces) from healthy female children[1,2] with age given in years. Note that in E), clinical (mean) and simulated R-wave amplitudes were normalised with the maximum clinical mean and simulated R-wave amplitude (i.e. at age 3-6), respectively, to show percentual change. Clinical data was obtained from [1]Khoury et al. (2009, Table 2) and [2]Saarel et al. (2018, Supplementary Tables 12, 18A, and 34).

6.3.2 Arrhythmic risk increases with increasing ischemia severity

First, I assessed arrhythmic risk in the healthy control ventricles. No arrhythmias occurred when using the baseline nor the steep restitution curve AP model. Next, to assess how severity of ischemia modulates arrhythmic risk, I investigated moderate and severe ischemia, i.e. setting f_{KATP} to 0.05 and 0.1, respectively, in the large ischemic injury and the baseline AP model. As shown in the top of Figure 20, the VW increased from 40 to 280 ms under moderate and severe ischemia, respectively.

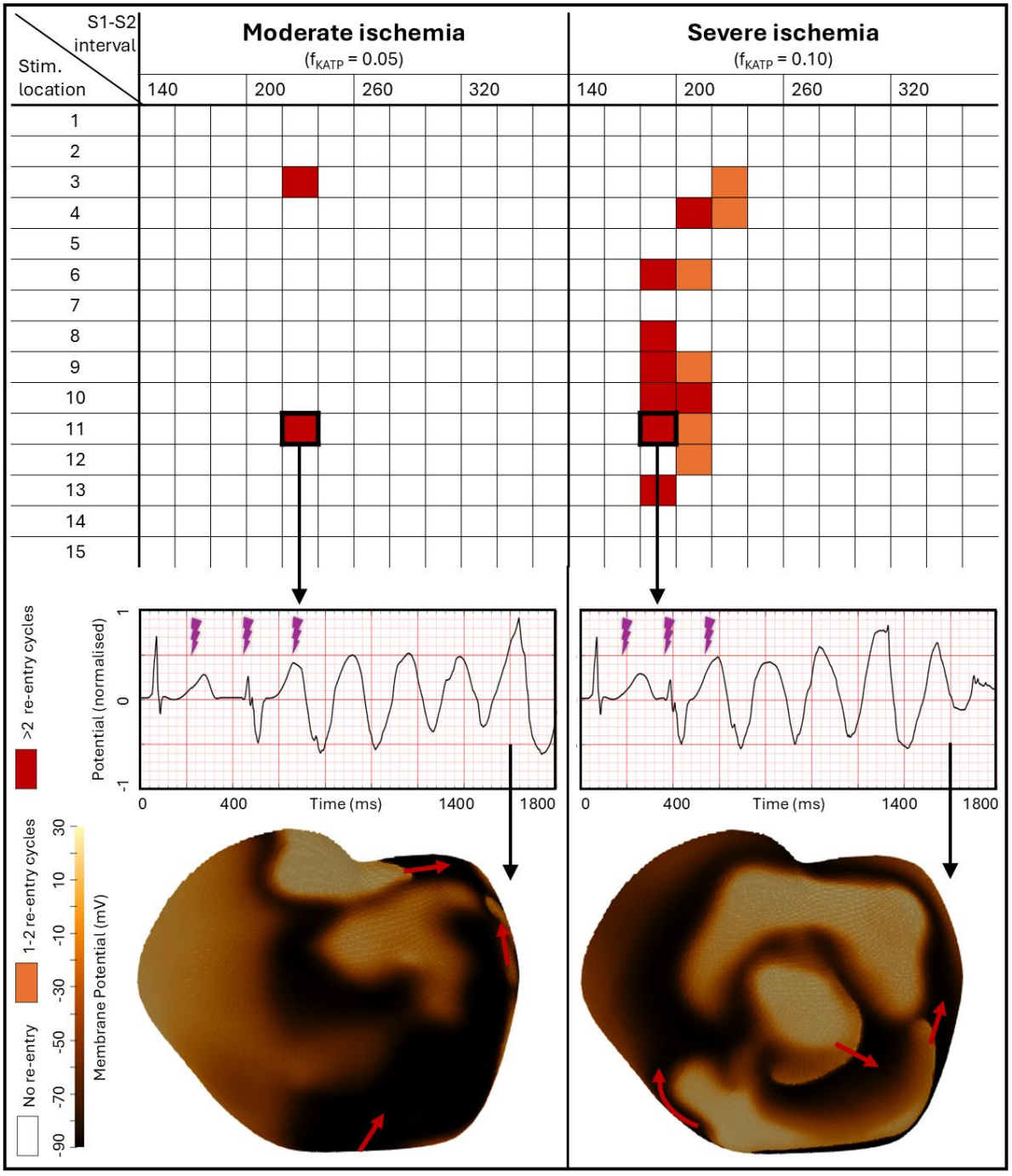


Figure 20. VWs in a large ischemic injury with moderate (left column) or severe (right column) ischemia. Ectopic stimulus locations were ordered from most anterior-basal to most inferior-apical. In the middle, ECG traces of lead V4 for a respective arrhythmia are shown; note, that the first beat at 0 ms is a sinus beat, applied at the bundle of His. Purple bolts indicate the three ectopic stimuli, applied on the edge of the ischemic core. Below that, membrane potentials of the anterior wall at 1600 s after the last sinus beat are shown to highlight rotor complexity.

As I show in the ECGs and biventricular electrical propagation snapshots in Figure 20, arrhythmias followed a VT-typical saw-tooth morphology. The sinus beat shown at the start of these ECGs also highlighted that the T-wave became wider with increasing f_{KATP}. This was due to the APDs in the ischemic cores shortening as ischemia severity increased.

Accordingly, repolarisation across the ventricles became more heterogeneous and provided a more arrhythmogenic substrate, as highlighted by the increase in observed arrhythmias. Ectopic stimuli, which I delivered at the edges of the ischemic region, could not excite the healthy tissue and instead travelled through the injury. They were then able to either exit the ischemic cores at the opposite end or excite PMJs within the endocardial ischemic zone.

Both re-entries under moderate ischemia occurred for stimuli within the septum. Under severe ischemia, arrhythmias were induced by anterior or septal stimuli, with neither of the two most basal nor the two most apical stimuli causing re-entry. This may be related to the geometry of the ischemic region, which was most prominent on the anterior septum, but also to the ventricular activation sequence. The septum gets activated very early, so septal stimuli exploit the ventricles' natural repolarisation gradient. In detail, the healthy repolarisation gradient follows cardiac activation from the septum across the ventricular walls to the base. Therefore, a non-sinus stimulus at the septum may encounter a refractory base. Contrarily, apical and basal stimuli that propagated through the ischemic cores met healthy, already repolarised tissue on the anterior and septal walls, which could be re-excited, therefore hindering rotos to form.

As depicted in the ECGs in Figure 20, not all three applied ectopic stimuli (purple bolts) were able to propagate. In the two cases I show in the middle of Figure 20, the first ectopic stimulus did not propagate, as highlighted by the lack of excitation and flat ECG following the sinus T-wave. Instead, the second one excited the ischemic region and met unidirectional conduction block in the healthy tissue. In some cases, the third stimulus propagated as well and was essential in eliciting re-entry.

6.3.3 Steep-restitution action potentials facilitate ventricular fibrillation-like arrhythmias

Next, as shown in Figure 21, my simulation results identified that a steep restitution curve AP model caused an increased VW (1,540 ms) compared to the baseline AP model (280 ms). Whilst the baseline model showed arrhythmias following ectopic stimuli at nine out of 15 investigated locations, the steep restitution model produced at least three re-entries for all of them. Furthermore, the VW started earlier and closed later for the steep restitution model (160 to 320 S1-S2 interval) than for the baseline model (180 to 220 ms). The wider VWs were due to increased repolarisation gradients, as ischemia in the baseline AP model caused less APD shortening (by 70 ms) than in the steep restitution AP model (90 ms, see Figure 17). This can be seen in the first (sinus) beat of the simulated ECGs in Figure 21, where the steep restitution model produced wider T-waves with a flatter peak, highlighting the prolonged repolarisation.

Arrhythmia susceptibility as well as sustainability increased with steeper restitution; the percentage of re-entries lasting for more than two cycles rose from 57% in the baseline model to 86% in the steep-restitution model. Of note, some simulations (e.g. for S1-S2 interval of 160 ms at stimulus location 2 in the large scar with the steep-restitution model) produced ECGs with a non-sustained re-entry pattern; however, this was caused by the stimulus meandering in the injury core without re-entering into the rest of the ventricles. As I show in the ECG traces and snapshots of biventricular electrophysiological activity in the bottom of Figure 21, arrhythmias in the baseline model resembled a saw-tooth, VT-typical morphology, whereas the arrhythmias in the steep restitution model were more prone to wave breakup, meandering rotors, and a VF-like pattern.

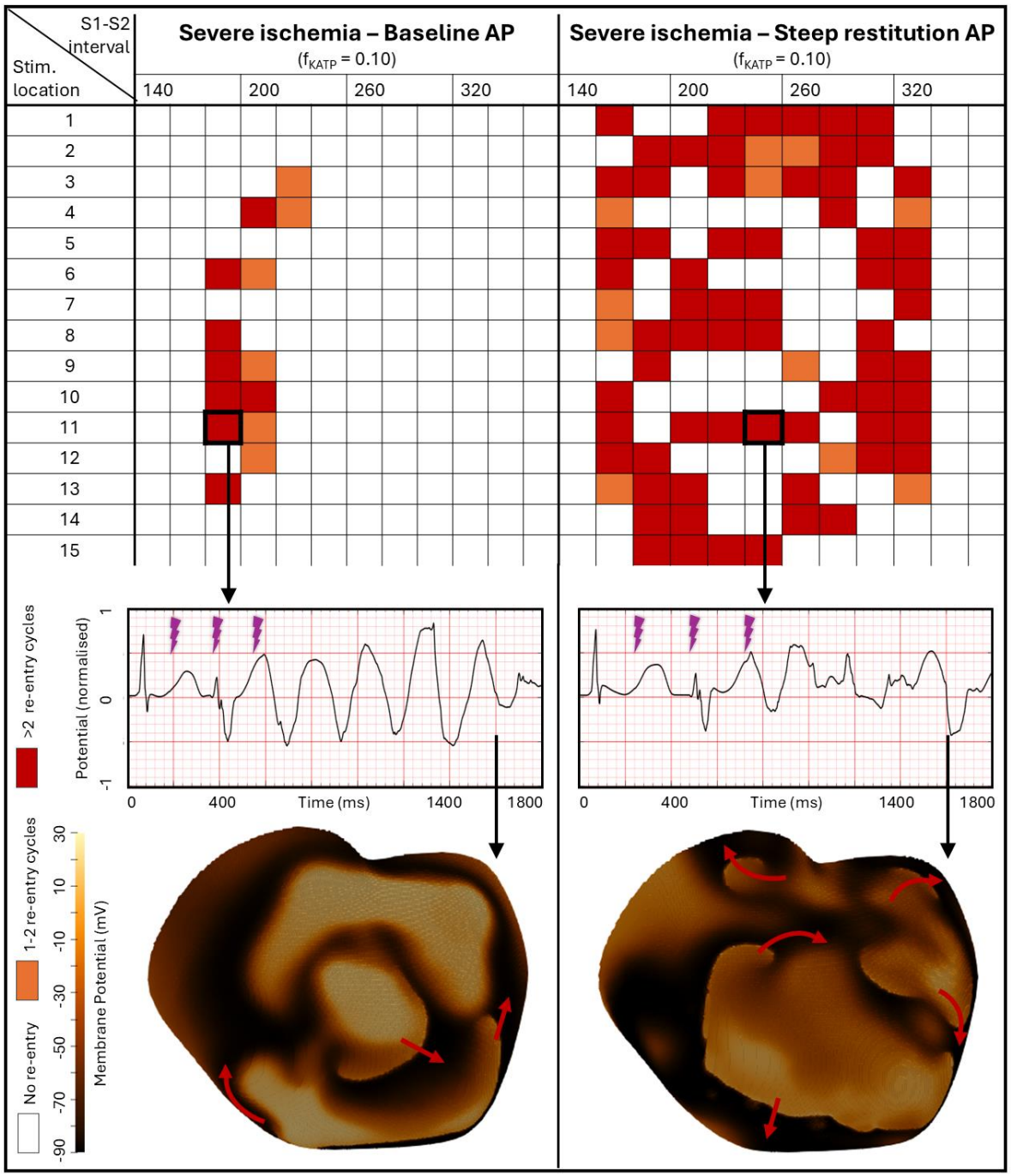


Figure 21. VWs in a large ischemic injury with severe ischemia using two different AP phenotypes – baseline (left column) and with a steep restitution curve (right column). Ectopic stimulus locations were ordered from most anterior-basal to most inferior-apical. In the middle, ECG traces of lead V4 for a respective arrhythmia are shown; note, that the first beat at 0 ms is a sinus beat, applied at the bundle of His. Purple bolts indicate the three ectopic stimuli, applied on the edge of the ischemic zone. Below that, membrane potentials of the anterior wall at 1600 s after the last sinus beat are shown to highlight rotor complexity.

6.3.4 Arrhythmic risk is substantially reduced in small but only slightly in medium-sized ischemic regions

Finally, my simulations show that a 54% decrease in ischemic area caused a 48% decrease of arrhythmic risk (see Figure 22). Specifically, the VWs in the large, medium,

and small severely ischemic regions were 1,540, 1,360, and 800 ms, respectively, all using the steep restitution model. Interestingly, whilst the size of the ischemic region decreased almost uniformly by 31% (from large to medium) and 33% (from medium to small), VWs shortened non-uniformly by 12% and 41%, respectively. I carried out a closer investigation of the arrhythmic patterns, which suggested that this is due to the small ischemic injury consisting of smaller more individual cores, whereas the medium and large cases both contained a larger central ischemic core. This large core allowed for longer paths, which, due to the large repolarisation time differences between the healthy tissue and the ischemic myocardium, were necessary to allow for re-entry.

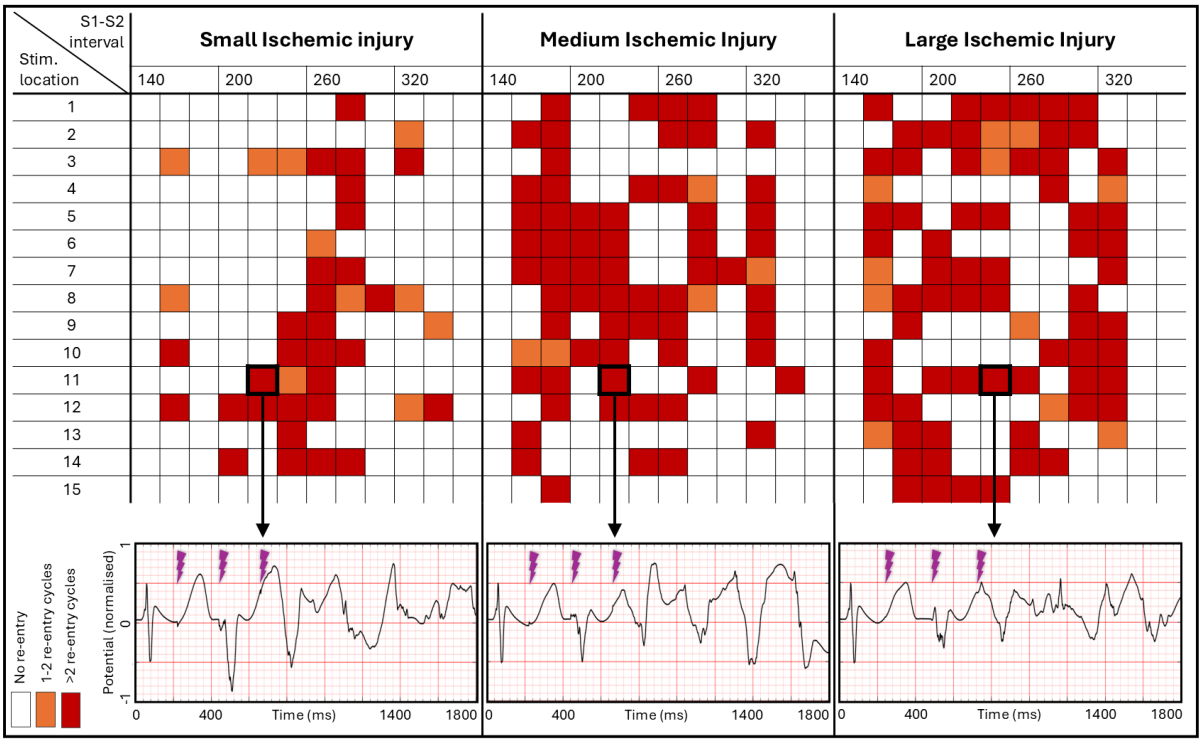


Figure 22. VWs in the severely ischemic small (left column), medium (middle column), and large (right column) injury, all in the steep restitution model. Ectopic stimulus locations were ordered from anterior-basal to inferior-apical. Below that, ECG traces of lead V2 for one respective arrhythmia are shown. Note that the first beat at 0 ms is a sinus beat, applied at the bundle of His. Purple bolts indicate the three ectopic stimuli, applied on the edge of the ischemic zone.

The overall increase of arrhythmic risk with increasing ischemic area is due to the source-sink mismatch (Weiss, 1997). Smaller ischemic regions provide a smaller current source, especially in the isolated spread-out ischemic cores. The surrounding tissue, which acts

as a current sink, prolongs the ischemic cells' APD in the border zone, thereby reducing repolarisation gradients. Furthermore, small ischemic areas may struggle to re-excite the large surrounding tissue sink and may require stronger re-entrant currents.

As I show in the ECGs of Figure 22, all three geometries of ischemia produced arrhythmias with chaotic, VF-typical patterns. Arrhythmia sustainability was not related to size of the ischemic region, with a similar percentage of re-entries lasting for more than two cycles in the large (86%), medium (93%), and small (73%) ischemic injury.

6.4 Discussion

In summary, in this chapter, I designed, conducted, and analysed multiscale human ventricular electrophysiological simulations, which demonstrated that ischemia, known to contribute to ventricular arrhythmias in the adult ventricles (Bardou et al., 1995; Bradley et al., 2011; Kaplinsky et al., 1979; Luqman et al., 2007; Martinez-Navarro et al., 2019; Pogwizd & Corr, 1990), can facilitate VF-like arrhythmias also in smaller, paediatric-like ventricles. My investigations identified that small ventricular size in children explains some but not all the typical paediatric ECG features. I further showed that re-entry susceptibility was modulated mainly by severity of ischemia-induced electrophysiological remodelling and the restitution curve steepness of the underlying AP phenotype; the latter also determined whether resulting arrhythmias were more VT or VF-like.

Firstly, my simulations showed that small ventricular size in children explains some but not all the typical paediatric ECG features. Specifically, whilst, in smaller ventricles, my simulations captured shorter QRS and QT interval durations, they did not produce inverted T-waves in leads V1 to V3 or prominent R-waves in lead V1. This suggests that

there are factors other than ventricular size contributing to the paediatric ECG. One possibility is that the LV and RV grow at different rates which would not be captured by scaling both uniformly, as I have done here. In fact, the RV is responsible for about 2/3rd of the blood supply before birth, when the ventricles pump blood in parallel rather than in sequence (Freed, 2006). In the first two days after birth, the RV has been recorded to quickly adapt to its new function by decreasing in volume (Clark et al., 2002). Clinical data further suggests that whilst the LV grows rapidly over the first few weeks (Joyce et al., 2004), LV and RV mass increase at a similar rate after (Krupickova et al., 2021; van der Ven et al., 2020). Hence, different growth rates of the LV and RV in the investigated age groups may be unlikely. Instead, it may be more plausible, that the ventricles change shape, especially with regards to neighbouring organs, which may grow and restrict growth in a certain direction. Another possibility is that the heart moves within the torso and hence the relative distance to the ECG leads changes. Indeed, studies have shown that from three years old, the apex beat moves from the 4th to the 5th intercoastal space (Antia et al., 1978), supporting that hypothesis.

Next, my results showed that ischemia in a small biventricular geometry with a LV mass matching that of a 9-year-old, can facilitate re-entrant arrhythmias. Previous computational studies have also scaled an adult geometry to study the foetal heart and used this set up to investigate the effects of global ischemia on the foetal ECG (Pérez et al., 2024; Uv et al., 2025). Children are highly unlikely to experience ischemic injury or sudden cardiac death (Gajewski & Saul, 2010) and hence, even though critical for risk prediction and treatment development, the arrhythmia mechanisms in small hearts during ischemia are poorly understood. Several studies have highlighted the importance of heart size in arrhythmia susceptibility and maintenance (Aras et al., 2018; Garrey, 1914;

Hartley et al., 2021). Specifically, the 'critical mass' theory denotes that fibrillatory patterns are only possible in sufficiently large myocardial volumes (Garrey, 1914). As described in Section 3.3, this is due to a sufficiently long path being required for a wavefront to re-enter (Connolly & Bishop, 2016; Janse et al., 1980). Computational studies have shown that whilst fibrillation may be inducible in smaller tissues, it may terminate quickly (Qu, 2006). The critical mass theory is commonly brought up when discussing transferability of small animal studies (Chong et al., 2014; Vaidya et al., 1999) but may also be relevant to paediatric arrhythmias. The results I presented here demonstrate that fibrillation-like arrhythmias are indeed possible in small ventricles and that their VWs are comparable in duration with similar studies conducted in adult human ventricles (Martinez-Navarro et al., 2019, 2024). To increase comparability, future work should directly compare the re-entrant risk in small and adult sized ventricles, using the same arrhythmia induction protocols. Future studies may also investigate faster sinus pacing; to account for ventricular arrhythmias in children with rare congenital heart diseases (caused for example by Williams-Beuren syndrome) commonly being observed during anaesthesia, the heartrate I investigated here was slow for a 9-year-old.

I further identified that severity of the ischemia-induced electrophysiological remodelling, particularly activation of I_{KATP}, may have a stronger effect on arrhythmia susceptibility than area-at-risk. However, this will also depend on the geometry of the ischemic area. Clinically, the size of the affected area may depend on the affected vessel and how much of the myocardium it supplies with blood, whilst ischemia severity may be more impacted by how long the oxygen is reduced for. Both may further be subject to the patient's physiology, particularly how the vessels are distributed and if alternative, nearby vessels may allow for some limited blood flow.

Here, I investigated the pro-arrhythmic role of I_{KATP} specifically, however, during ischemia, hypoxia commonly occurs together with acidosis and hyperkalaemia, and hence future work may study a combination of these, especially with regards to hyperkalaemia-induced elevated MDP (Kodama et al., 1984). Effects of hypoxia on other ion channels, such as decreased I_{NaK} (Cross et al., 1995; Winston et al., 1990) and I_{up} (Ronkainen et al., 2011), may also be investigated. Several *in silico* studies have investigated the arrhythmic risk during ischemia including hyperkalaemia and acidosis (Alday et al., 2016; Martinez-Navarro et al., 2019, 2021; Ramirez et al., 2014). For example, Ramirez et al. (2014) showed how ischemia and associated conduction abnormalities can result in re-entry involving also the Purkinje network, and Martinez-Navarro et al. (2019) established that transmural ischemia, especially in the septo-apical region, can favour re-entry occurrence.

Finally, the results I presented showed that a steep restitution curve model was more prone to arrhythmias with VF-like chaotic morphology compared to a baseline AP model. Steep restitution curves have long been known to impact the formation of rotors and VF (Garfinkel et al., 2000; Martinez-Navarro et al., 2024); however, their interaction with I_{KATP} particularly and whether they could favour VF in smaller hearts has not yet been investigated. Furthermore, my results suggest that QT interval, which is modulated by the APD which in turn is a main determinant of restitution steepness (Shattock et al., 2017), may be a crucial indicator of arrhythmic risk. Establishing non-invasive risk markers is especially crucial in vulnerable patients, including children with rare chromosomal abnormalities or anomalous coronary arteries.

6.5 Conclusions

To conclude, in this chapter I presented how multiscale human ventricular electrophysiological modelling and simulation can be employed to study re-entrant arrhythmia mechanisms of ischemia in small, paediatric-like ventricles. Specifically, my simulations showed that arrhythmic risk was mainly modulated by severity of the ischemia-induced electrophysiological remodelling and the steepness of AP restitution. The latter also determined the morphology of the arrhythmias, with the steeper restitution curve model favouring VF-like ECG patterns of arrhythmias over a VT-like morphology. This work is a first step towards investigating arrhythmias in children which are difficult to study clinically and urgently require novel tools to augment clinical risk prediction in rare paediatric syndromes.

7 Uncovering arrhythmia mechanisms of regenerative cell therapy in the infarcted adult human ventricles

In this chapter, I demonstrate how I used multiscale human ventricular electrophysiological modelling and simulation, as described in Chapter 5, to assess pro-arrhythmic safety concerns of new treatments for ischemic heart disease before they are deployed clinically. Specifically, I conducted simulations of cell therapy in the infarcted human ventricles to identify post-delivery arrhythmia mechanisms and the effects of variability in scar size, infarct stage, and injected cell population heterogeneity. My results showed a multitude of re-entrant pathways, including through the Purkinje network, and highlighted that re-entrant arrhythmias post cell injection may occur with or without the cells spontaneously beating.

We recently published parts of this chapter, not including Section 7.3.2, in Riebel et al. (2024), Scientific Reports with DOI: 10.1038/s41598-024-67951-5.

7.1 Introduction

As I outlined in Chapter 3, myocardial damage after prolonged ischemia is irreversible. Cell therapy is a promising new treatment, hoped to restore the heart's function after MI and in heart failure patients. Pre-clinical testing and early clinical trials are ongoing to determine the therapy's safety and feasibility (Bayes-Genis et al., 2024; Y.-C. Cheng et al., 2023; Kawamura et al., 2023; Lou et al., 2023; Petrosyan et al., 2022; Poch et al., 2022; Querdel et al., 2021; Yamada et al., 2024). However, it remains a challenge to manufacture pure cell cultures at large doses, which are required in the clinic (Ban et al., 2017; B. Jiang et al., 2020; Selvakumar et al., 2024). Furthermore, the optimal delivery

method still needs to be decided on; cells may be injected intramyocardially using a catheter or stitched onto the epicardial surface as cell patches during open heart surgery (Dib et al., 2011). Additionally, whilst cell therapy is targeted towards and tested in patients with chronic MI and a prognosis of heart failure, re-infarction cannot be ruled out and early injection may be beneficial in terms of cell retention, proliferation, and overall increase efficacy (Xu et al., 2019; J. Yu et al., 2022). Such variabilities in the delivery methodology – including culture heterogeneity, cell dosage, transplantation location, and delivery time – may have crucial arrhythmogenic implications, which need to be addressed before clinical deployment.

Indeed, preclinical studies in animal models have shown that arrhythmic events do occur after cell delivery (Chong et al., 2014; Liu et al., 2018; Romagnuolo et al., 2019; Selvakumar et al., 2024). Whilst it has been suggested that the arrhythmias are largely caused by the delivered cells' spontaneous activity (Chong et al., 2014; Marchiano et al., 2023; Romagnuolo et al., 2019), the exact mechanisms remain unknown. It is further unclear how such arrhythmogenicity would translate into human and whether there could be additional arrhythmogenic pathways that may not be captured in animal models. Arrhythmia vulnerability may also depend on the patient substrate, as has been shown in post-MI patients (Chung, 2023; Sharma et al., 2022). Differences such as infarct size and scar complexity are crucial factors to determine the pathlength and wavefront speed required for re-entries to occur (Connolly & Bishop, 2016) and may also impact the cells' spontaneous beating.

My focus for this study was to mechanistically investigate the arrhythmogenic potential of injected cells to 1) provide re-entrant substrates by introducing APD and conduction

heterogeneities into the human ventricles and 2) produce re-entrant triggers through spontaneous beating activity. For the first part, I assessed the re-entrant risk in three chronic MI geometries before and after cell delivery and following an ectopic stimulus arising from the infarct border zone, rather than from the injected cells. For the second part, I investigated spontaneous beating in the three infarct geometries across acute, healing, and chronic MI and for three levels of injected cell population heterogeneity.

7.2 Methods

In the following sections, I summarise the main components of the human ventricular electrophysiological modelling and simulation framework, as described in Chapter 5, and introduce any adaptations relevant for this study.

7.2.1 Modelling and simulating cell delivery into the infarcted human ventricles

I simulated electrophysiological activity of the human ventricles from cellular over biventricular to ECG level, as described in Chapter 5 and summarised in Figure 23 A. To model MI, I created a cohort of post-MI injury geometries using an established algorithm (Cardone-Noott et al., 2014; Y. R. Hill et al., 2016), as described in Chapter 5.2.2, from which I selected three scar geometries that captured clinical ranges of scar size (see Figure 23 B). I then included remodelling in acute, healing, and chronic MI using experimentally reported changes in ion channel conductances and time constants, as established by Wang et al. (2021) and Zhou et al. (2024) and summarised in Table 3. Further, I incorporated post-MI structural remodelling by reducing conductivities in the infarct and border zone, resulting in CVs as shown in Table 4.

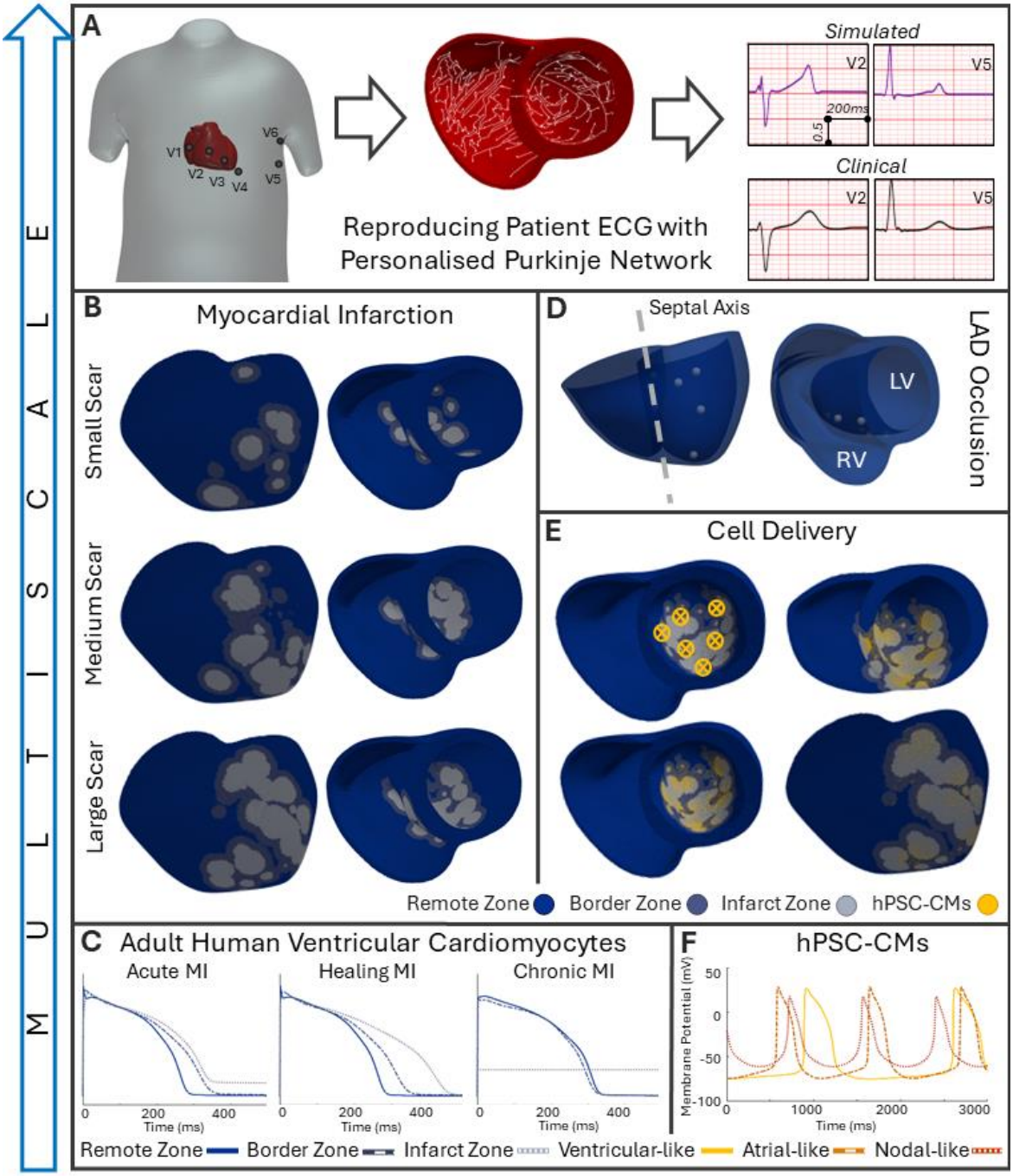


Figure 23. Summary of modelling and simulating cell therapy in myocardial infarction of the human ventricles. A) Healthy human biventricular anatomy (four chamber mesh from Rodero et al. (2021), biventricular mesh from Mincholé et al. (2019)) with an inferred Purkinje network calibrated to the clinical ECG (Camps et al., 2024). B) Three myocardial infarct scars with remote, border, and core infarct zone. C) AP traces of remodelled cardiomyocytes in acute, healing, and chronic infarction. D) Left anterior descending artery occlusion points to create myocardial infarction scars. E) Simulated cell injection locations from the basal (bottom left), anterior (bottom right), and transmural (top right) view. F) Simulated APs of ventricular-like, atrial-like, and nodal-like hPSC-CMs. Caption modified and heart geometry in the left of A) changed for illustration purposes but otherwise unmodified from Riebel et al. (2024) under CC BY license (https://creativecommons.org/licenses/by/4.0/).

Informed by pre-clinical data (Poch et al., 2022), I introduced hPSC-CMs into the infarcted ventricles as described in Section 5.3.1. For this, from the ventricular-like hPSC-CM Paci2020 model (Paci et al., 2020), I derived an atrial-like and nodal-like phenotype

(see Table 6). Using these, I varied injected hPSC-CM population heterogeneity in 3D from 100:0:0% (fully ventricular-like) over 80:10:10% (10% atrial-like and nodal-like cells) to 50:25:25% (25% atrial-like and nodal-like cells).

7.2.2 Simulation and arrhythmia quantification protocol

To reach steady state, I started biventricular simulations with three sinus beats at 1 Hz paced from the bundle of His (further detail in Section 5.4.1).

I then designed and used two different arrhythmia induction protocols to investigate the arrhythmogenic potential of hPSC-CMs with or without them beating spontaneously. To quantify the arrhythmic risk of hPSC-CMs as a re-entrant substrate without involvement of spontaneous hPSC-CM activity, I applied ectopic beats at varying S1-S2 intervals and across 15 locations within the infarct border zone, as described in Section 5.4.1. I repeated this protocol in all three post-MI scar geometries and before and after cell delivery. Next, to quantify the arrhythmogenicity of spontaneous hPSC-CM beats, I first observed the ectopic beating rate of the three hPSC-CM populations with increasing heterogeneity over two seconds under the absence of sinus beating. Where spontaneous beating occurred, I assessed subsequent re-entrant arrhythmia risk by applying proceeding sinus beats at varying heart rates between 32 and 37 bpm. To assess the role of the Purkinje system in spreading the spontaneous beat across the ventricles, I carried out the above protocol twice, once with healthy Purkinje-myocyte coupling and once with disabled retrograde Purkinje-myocyte coupling.

This resulted in approximately 1,450 simulations including: 990 cases to determine re-entry vulnerability in the absence of spontaneous beats (3 scar sizes x 11 S1-S2 intervals x 15 ectopic stimulus locations x 2 cases, pre- and post-injection), 27 cases to assess

spontaneous beating risk (3 scar sizes x 3 infarct stages x 3 heterogeneity levels), and 414 cases to quantify re-entry risk after spontaneous beats (3 scar sizes x 3 infarct stages x 23 heart rates x 2 Purkinje-myocyte couplings). For both arrhythmia induction protocols, I qualified arrhythmic burden as the VW, the time span during which re-entries were inducible.

7.3 Results

7.3.1 Establishing credibility - simulations produce physiological electrocardiograms in acute, healing, and chronic myocardial infarction

My simulations showed that in all three scar sizes, acute and healing MI produced very similar ECGs, as shown in Figure 24 A and B. Small differences were visible in the ST-segment in lead V3 and the QT interval across all leads. Even though the Na^{2+} current further decreased from acute to healing MI, biventricular activation times (also depicted in Figure 24) were almost identical due to similar CVs. The return to normal extracellular K^{+} levels from acute to healing MI caused an increased APD within the infarct (as shown in Figure 23 C) and ultimately increased repolarisation times. Remodelling in chronic MI produced a distinct ECG phenotype with an increased ST-segment elevation in leads V2 to V5 and normalised T-waves in leads V3 to V5. This was caused by the further reduced CV and the lack of electrical excitability within the infarct, which prolonged activation and repolarisation, as displayed in Figure 24 C.

Trust in utilising human ventricular electrophysiological modelling and simulation to investigate MI is supported by the use of largely human-based experimental and clinical data to inform models from cellular to biventricular level (see Chapter 5, particularly section 5.6). To further establish credibility, I compared simulated ECG traces in acute,

healing, and chronic MI to clinical ECGs of patients with anterior and antero-septal infarcts from the PTB diagnostic databank (Bousseljot et al., 1995; Goldberger et al., 2000). Specifically, I compared simulated post-MI ECGs, shown in Figure 25 A, with recordings from one patient one day, one week, and three months post-MI, shown in Figure 25 B.

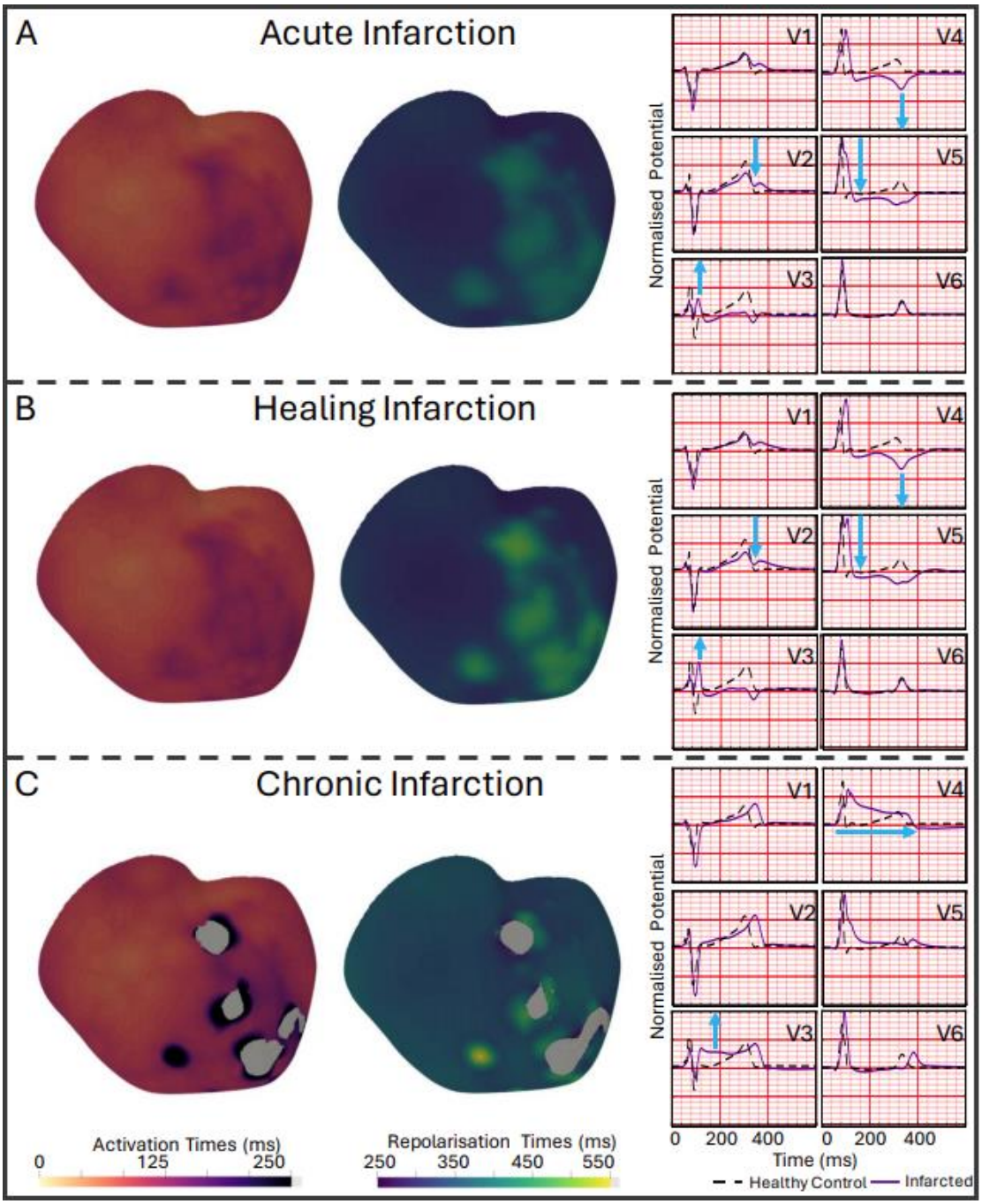


Figure 24. Activation (left) and repolarisation (right) time maps as well as ECG signals in healthy (dotted black line) and post-MI (solid purple line) conditions of A) acute, B) healing, and C) chronic myocardial infarction. Caption modified but figure unchanged from the supplementary material of Riebel et al. (2024) under CC BY license (https://creativecommons.org/licenses/by/4.0/).

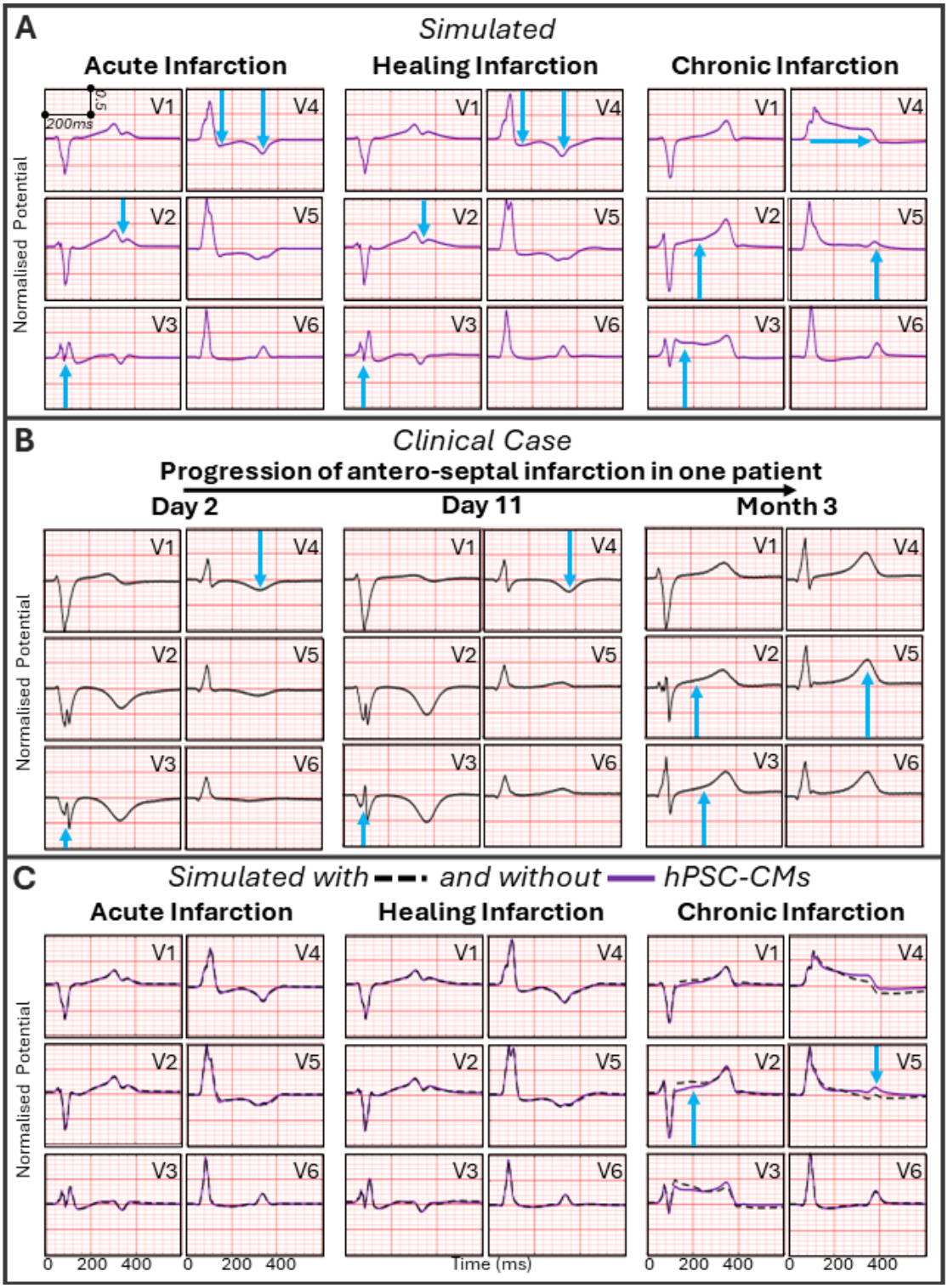


Figure 25. Comparison of simulated (A) and clinical ECGs (B) in acute, healing, and chronic infarction and following cell delivery (C). Clinical ECGs were obtained from patient 033 at 1, 10, and 89 days after anteroseptal infarction from the PTB diagnostic ECG database, https://physionet.org/content/ptbdb/1.0.0/ (Bousseljot et al., 1995; Goldberger et al., 2000). Key changes compared to the healthy control are highlighted with blue arrows. Corresponding simulations were carried out in the medium scar and, where applicable, with high injected cell heterogeneity (50:25:25% ventricular:atrial:nodal-like cells, respectively). Caption slightly modified but figure unchanged and obtained from Riebel et al. (2024) under CC BY license (https://creativecommons.org/licenses/by/4.0/).

As shown in Figure 25 B, my simulations during acute and healing MI agreed with clinical records and showed fragmented QRS complexes in lead V3 as well as inverted T-waves in

leads V3 to V5. In chronic MI, persistent ST-segment elevation in leads V2 and V3 and T-wave normalisation in leads V2 to V5 were visible in the clinical and simulated traces. Following cell injection, ECG signals changed only marginally. As I display in Figure 25 C, in acute and healing MI, ECGs pre and post cell delivery were almost indistinguishable because of a similarly reduced conductivity and increased APD in the injected cells and the infarct centre. In chronic MI, cell delivery increased electrical excitability and conductivity within the unexcitable scar, and, accordingly, changes were visible in the ST-segment and T-wave amplitude.

7.3.2 Injected cells increase arrhythmia vulnerability by enabling re-entrant wavefront conduction through scar cores

After comparison with clinical post-MI data, I investigated whether ventricular-like only hPSC-CM populations would increase arrhythmia susceptibility in chronic MI and how this may be modulated by variability in scar size and the location of ectopy arising within the infarct border zone rather than the hPSC-CMs. As shown in Figure 26, re-entry susceptibility increased from before to after cell injection in all three investigated scar sizes.

Pre-delivery (top row in Figure 26), I found no re-entries in the small scar and three re-entries, two non-sustained and one sustained, in both the medium and large scar. Due to the three scars' different geometries, I varied locations of the ectopic stimuli for each scar size; to allow for comparability, I ordered the stimulus locations shown in Figure 26 from antero-basal to inferior-apical. It is of note that all three scars spread across the apex, and, hence, depending on the scar size, 35% to 45% of ectopic stimulus locations (stimulus 8-10 onwards in Figure 26), were close to the apex. In contrast, only 20% to 25%

(up to stimulus 3-4 in Figure 26) were close to the base. All other stimuli were delivered anteriorly or in the septum. In the medium scar, one of the pre-cell-delivery re-entries occurred for an anterior-septal stimulus close to the base, while the other two showed after an inferior-lateral stimulus towards the apex. All three re-entries in the large scar happened for apical stimuli.

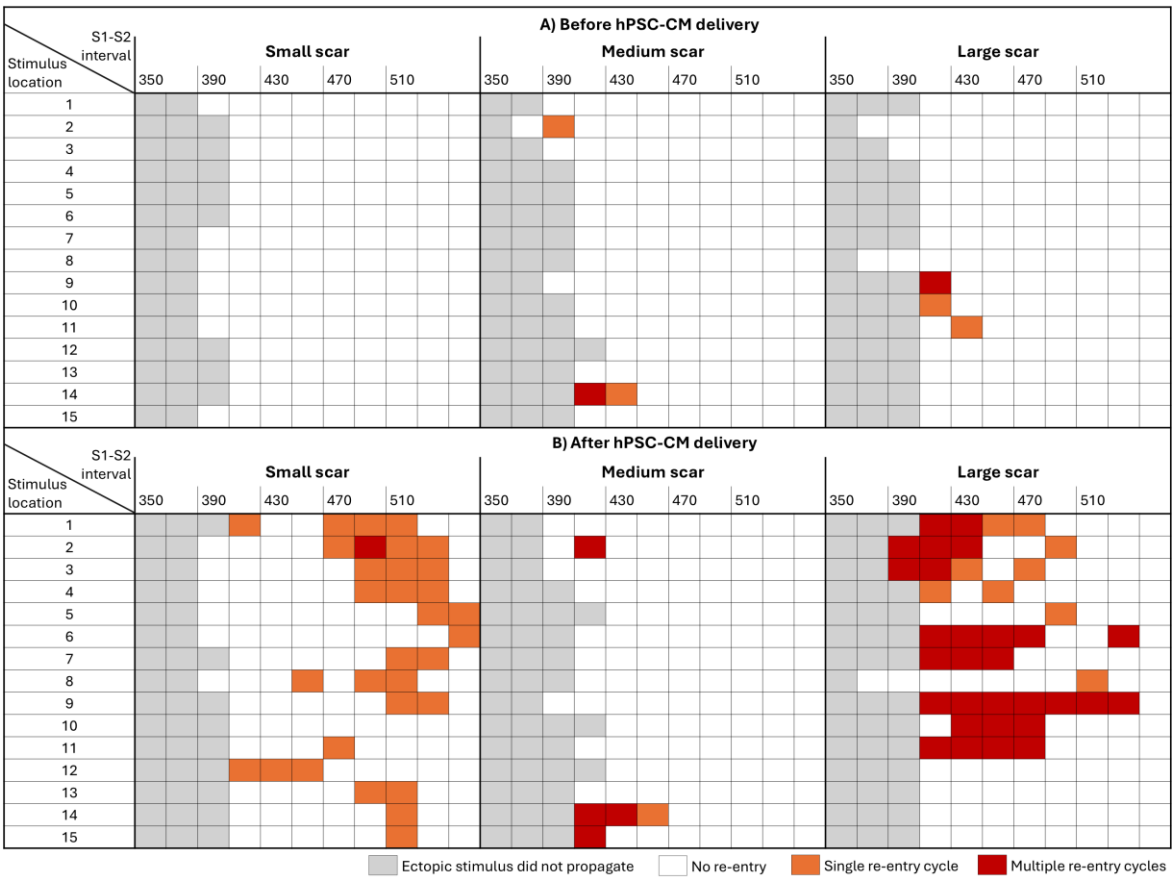


Figure 26. VWs in the small, medium, and large chronic scar; A) pre cell injection, B) post cell injection (ventricular-like only hPSC-CM population). Ectopic stimulus locations were ordered from anterior-basal to inferior-apical. Grey shading indicates that the ectopic stimulus did not propagate into the tissue at all. No shading indicates that the ectopic beat activated the ventricles, but no arrhythmias were observed. Orange and red shades indicate re-entries with a single or multiple cycles, respectively. Note, S1-S2 intervals of 570 ms were investigated in the small scar with no further arrhythmias observed.

After cell delivery, VWs increased from 0 to 640 ms in the small scar, from 60 to 100 ms in the medium scar, and from 60 to 760 ms in the large scar. While the VW post-delivery was larger in the small than in the medium scar, it should be noted that all but one re-entry in the small scar lasted for a single re-entrant cycle, whilst 80% of re-entries in the medium scar sustained for at least two cycles. Upon closer investigation, I discovered that all but

one re-entry in the small scar occurred through a PMJ. Of those, 90% happened through the same PMJ, within a large scar core on the anterior wall (which is clearly visible in Figure 27). The remaining 10% of re-entries involving the Purkinje system occurred through a second PMJ, also within a scar core on the anterior wall, this time close to the basal septum (also visible in Figure 27 as the most basal scar core). The only re-entry in the small scar that lasted for more than one cycle, involved both of those PMJs. The patchy scar geometry of the small scar with its isolated scar core islands provided a perfect substrate for the classical figure-of-eight re-entry pattern. In fact, the most proarrhythmic scar core on the anterior wall was indeed shaped like an eight. The ectopic stimuli propagated through the tissue and met unidirectional conduction block at one side of the scar core, which was still refractory due to the long APD of delivered hPSC-CMs. The wavefront then propagated around the core in a symmetrical motion and finally re-entered through the opposite side. Instead of exiting through the stimulus site, the re-entry occurred through re-activation of the PMJ within the scar core.

Conversely, the medium and large scar contained less individual scar islands; many of the epicardial and endocardial scar cores visible in Figure 27 were connected through the subendocardium. Due to this, classical figure-of-eight re-entries were hindered in the larger scars. In the medium scar before cell delivery, the re-entry following a septal-basal stimulus occurred through an anterior PMJ within the scar. For the other two, the apical stimulus re-entered through tissue in between the more isolated epicardial scar cores on the apex. After cell delivery, re-entries in the medium scar were very similar to before cell delivery and, again, occurred either through an anterior PMJ within the scar or through the epicardial cluster of scar islands on the apex.

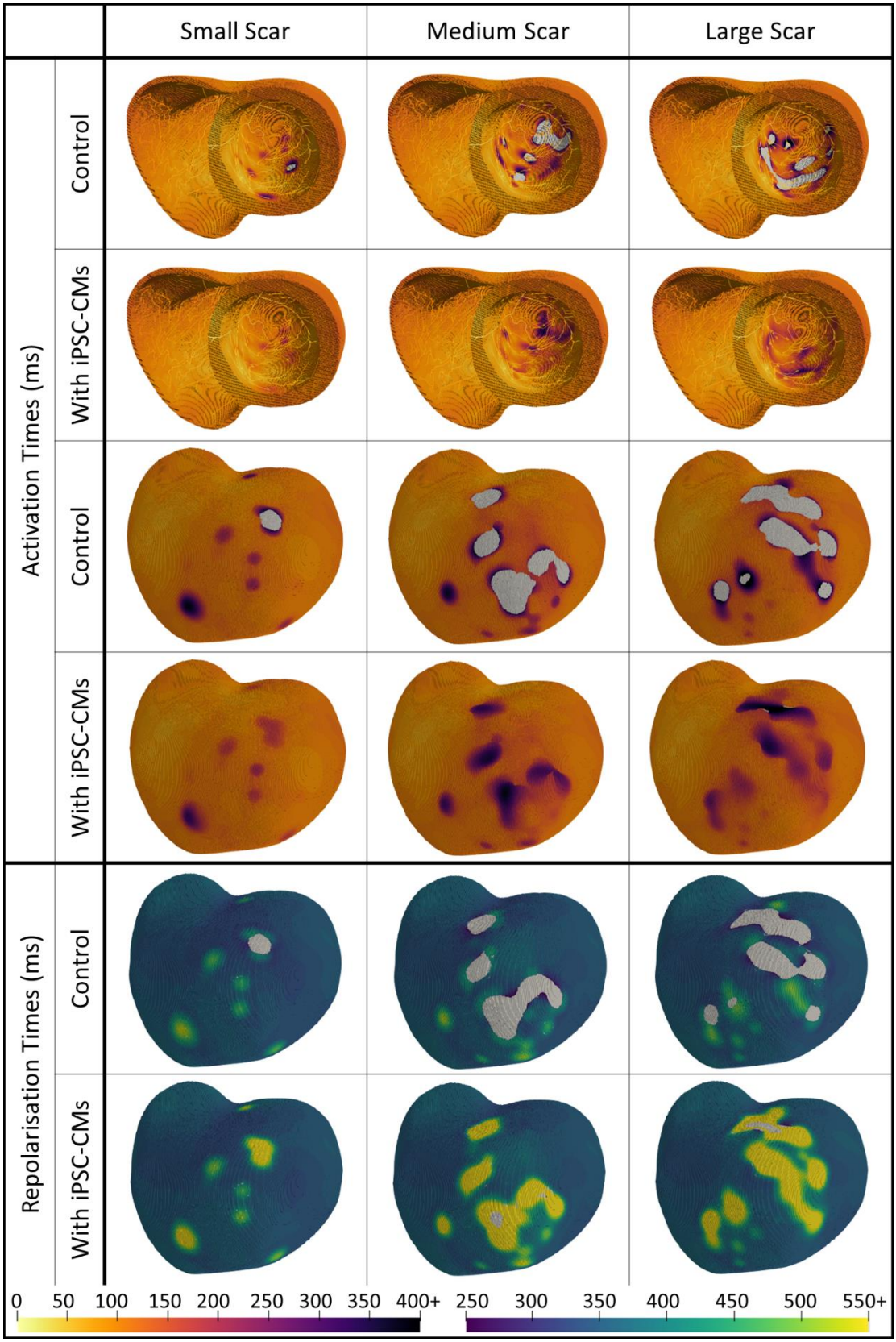


Figure 27. Activation (top) and repolarisation (bottom) time maps before and after simulated hPSC-CM delivery in the small, medium, and large chronic scar. Grey shading indicates activation / repolarisation failure.

In the large scar pre cell delivery, none of the re-entries occurred through a PMJ. Instead, they all followed apical stimuli which – like in the medium scar – re-entered through a

cluster of scar core islands on the apex. Contrary to the medium scar, re-entry risk in the large scar increased substantially after cell injection. As I show in Figure 27, the large scar contained many narrow passages between scar cores. After cell delivery into the infarct, the previously unexcitable scar cores now became refractory (due to the hPSC-CMs' long APD). Wavefronts travelling through the narrow passages met conduction block but could eventually re-enter from the other side. Wavefronts were also observed to re-enter transmurally through subendocardial areas where hPSC-CMs had been injected.

For all scars, it was apparent how even after cell delivery, the Purkinje network failed to excite the scar cores. Instead, where excitable at all, the scar was activated by the wavefront travelling through the myocardium. Even though the delivered cells increased excitability of the scar, their connectivity was much lower than that of the adult ventricular tissue with a CV like that of the unexcitable scar core, therefore, hindering activation through the Purkinje network.

To summarise, hPSC-CM delivery caused unexcitable scar cores to become excitable, but, due to their increased APD, they facilitated conduction block and enabled re-entrant wavefronts, particularly between and around islands of scar cores. How much arrhythmia susceptibility increased depended on the scar geometry, particularly on the amount of scar core islands, availability of passages through the scar, and PMJ distribution in the infarcted area.

7.3.3 Slow heart rates, chronic myocardial infarction, and heterogeneous injected cell populations facilitate spontaneous beats in the ventricles

Next, I investigated the risk of spontaneous beats emerging from the injected cells. Specifically, I assessed how cell population heterogeneity, infarct progression from acute

over healing to chronic MI, and the three infarct geometries modulate spontaneous beats of injected cells and subsequent arrhythmic risk.

Firstly, my results showed that homogeneous ventricular-only populations did not beat spontaneously in any of the three scar geometries and that at least 10% of each atrial-like and nodal-like cells was necessary for cells to autonomously depolarise in the ventricles (see Figure 28 A). Whilst I expected from the cellular investigations that heterogeneous populations with a higher ratio of more quickly beating atrial-like and nodal-like cells would beat faster, I did not expect that the ventricular-like only population would not beat at all. Upon closer examination, I identified an increase of upstroke velocity from 0.8 to 2.6 mV/ms in the medium scar after injection of the 80:10:10% and 50:25:25% hPSC-CM population, respectively. An increase in upstroke velocity signals an increased strength of the injected cells as an ionic current source against the surrounding quiescent adult tissue. Hence, my results suggest that injected ventricular-like cells did not provide a sufficiently rapid upstroke to excite neighbouring cells and were instead suppressed by the surrounding tissue.

Next, my simulations showed that whilst the 50:25:25% population beat in all considered scar geometries and infarct stages, the 80:10:10% population only produced spontaneous beats during chronic MI. This was caused by the chronic scar core (modelled with a membrane potential of -60 mV and changing only through diffusivity), which, compared to the stable adult tissue (MDP of -90 mV), provided an already depolarised sink. Similarly, although the differences in beating intervals were very small, the 50:25:25% populations depolarised fastest in acute and chronic MI. While in acute MI the infarct centre is excitable, its resting potential is elevated due to hyperkalaemia,

which, again, promotes quicker spontaneous depolarisation. As shown in Figure 28 B, whilst spontaneous depolarisation occurred slightly sooner in chronic MI because of the severely impaired conductivity within the scar, the spontaneous beat propagated faster in acute MI.

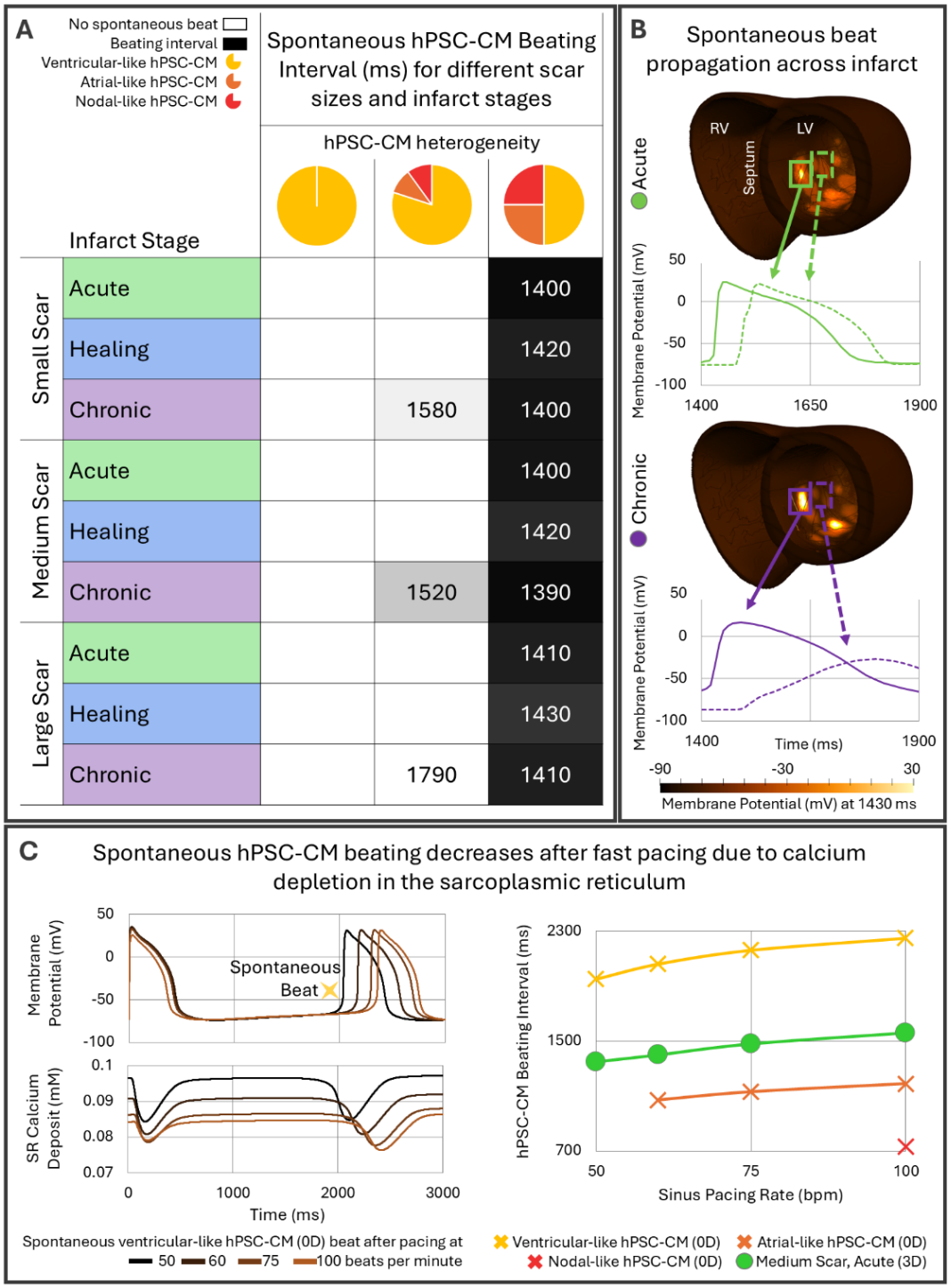


Figure 28. Mechanisms of spontaneous beats after cell delivery. A) Spontaneous beating interval of injected cells with different proportions of ventricular-like, atrial-like, and nodal-like cells within the cell population. Darker shades indicate shorter intervals, i.e. faster beating. B) APs following spontaneous depolarisation in the infarct centre (solid

line) and border zone (dotted line) during acute (green traces) and chronic (purple traces) MI. C, left) Spontaneous beating of ventricular-like cells following different preceding sinus pacing rates with the last sinus beat and following autonomous depolarisation shown. Right: spontaneous beating intervals in the ventricular-like, atrial-like, and nodal-like cellular models (marked with crosses) as well as in the biventricular model with a medium sized scar during acute infarction (green circles). Caption changed but figure unmodified from Riebel et al. (2024) under CC BY license (https://creativecommons.org/licenses/by/4.0/).

Additionally, I observed that for the 80:10:10% and 50:25:25% populations, spontaneous beating was fastest in the medium scar. As I determined above, spontaneous beating was encouraged by a depolarised MDP of the surrounding tissue. Due to the source-sink mismatch, in larger scars the depolarised acute and chronic infarct provided a stronger current source against the border and remote zone. As shown in Figure 29, this resulted in an elevated resting potential within the scar, suggesting that spontaneous beating was fastest in large scars. Contrarily, in smaller scars, where the infarct provides a weaker sink, the increased APD of the remodelled tissue was shortened by the healthy tissue's quicker repolarisation (see Figure 29). This enabled the injected cells to depolarise sooner after the last sinus beat. These two mechanisms may counteract each other and explain why spontaneous beating was fastest in the medium scar.

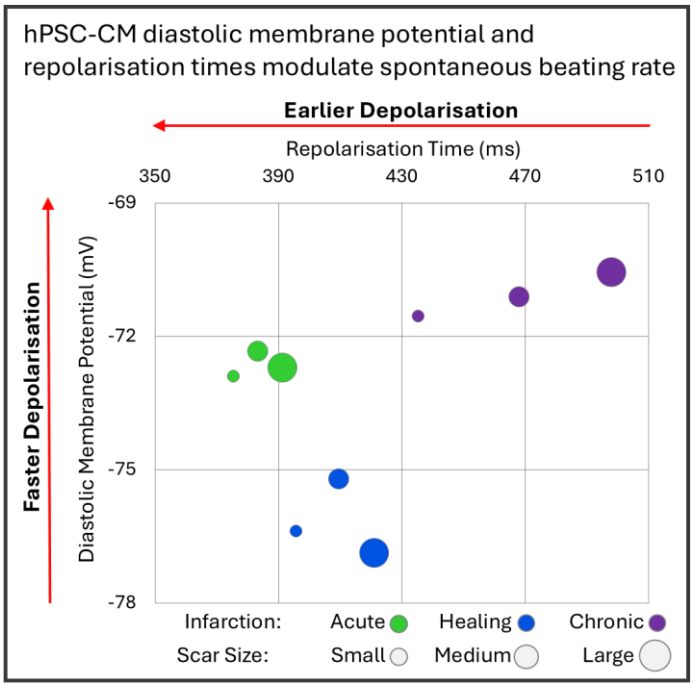


Figure 29. Mechanisms that shorten hPSC-CM beating intervals across infarct stages and sizes: most depolarised MDP versus average repolarisation time following sinus pacing in hPSC-CMs in the infarct centre. Red arrows indicate the direction of increased spontaneous beating. Figure and caption unmodified and obtained from the supplementary material of Riebel et al. (2024) under CC BY license (https://creativecommons.org/licenses/by/4.0/).

Finally, my simulations showed that the spontaneous beating became faster for slower preceding sinus pacing. Specifically, as shown in Figure 28 C, ventricular-like only hPSC-CMs depolarised quicker after pacing with 50 bpm than 100 bpm. I also observed this in the atrial-like hPSC-CMs; however, I could not analyse the effects of slow pacing in nodal-like cells, due to their very rapid beating. Slower sinus pacing also sped up spontaneous beating in the biventricular simulations (see right of Figure 28 C). Closer examination of ionic currents, as summarised in Figure 30, showed that fast pacing caused an accumulation of intracellular Ca^{2+}, similarly to adult cardiomyocytes (Vassalle & Lin, 2004). However, the available time for I_{up} to restore the SR-Ca^{2+} deposit was reduced under fast pacing and in turn less Ca^{2+} could be released into the intracellular space through I_{rel}, therefore lowering the CaT peak. This also led to reduced I_{NaF}, I_{NaL}, and I_{NaCa} peaks (see Figure 30). Similar observations have been made experimentally, where hPSC-CMs showed a reduced contractile amplitude under fast pacing (Hinata et al., 2022).

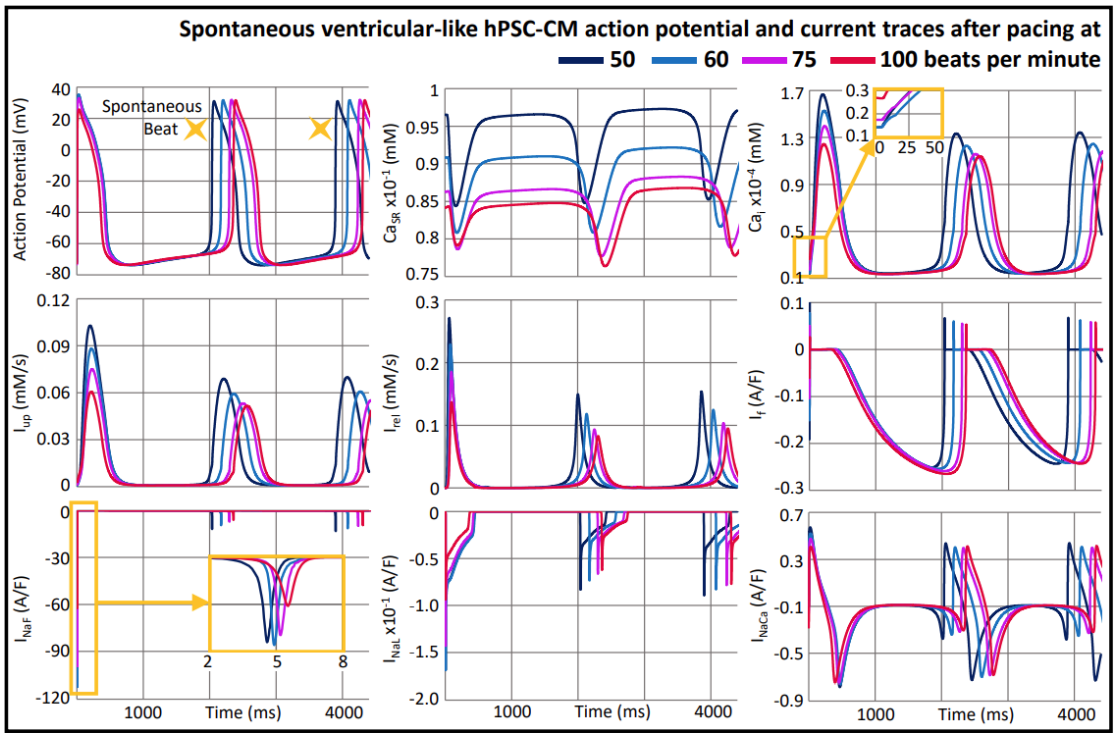


Figure 30. AP and ionic current traces for the ventricular-like hPSC-CM phenotype; shown is the last of 1,000 sinus beats at 50 (dark blue), 60 (light blue), 75 (purple), or 100 (red) bpm pacing followed by two spontaneous beats. Figure and caption unmodified and obtained from the supplementary material of Riebel et al. (2024) under CC BY license (https://creativecommons.org/licenses/by/4.0/).

7.3.4 Impaired Purkinje-myocyte coupling increases re-entrant arrhythmia susceptibility following spontaneous stem cell beats

As I presented in Section 7.3.3, heterogeneous injected cell populations produced spontaneous beats in the infarcted ventricles, especially during chronic infarction and under slow sinus heart rates. However, as spontaneous beating was slow (every 1.4 s), it did not meet any conduction block in the ventricles, which had already completely recovered from the previous beat (see Figure 31), and did not lead to re-entrant arrhythmias. Instead, and as shown in the left panel of Figure 31, proceeding sinus beats collided with myocardium still refractory from the spontaneous beat and induced re-entries in the large acute and chronic infarcts. This occurred under heart rates of around 33 bpm and with re-entries travelling through PMJs within the anteroseptal scar core.

Because the Purkinje network has been shown to be impaired following MI (Sayers et al., 2025), I investigated the re-entrant risk with 1) healthy Purkinje-myocyte coupling as described above and 2) impaired retrograde Purkinje-myocyte coupling. As shown in the right panel of Figure 31, the VW increased from 20 to 900 ms under healthy and impaired Purkinje network conditions, respectively. Where the PMJs were coupled healthily, the spontaneous beat, which emerged from the stem cells within the scar core, was rapidly spread across the ventricles once it reached the nearest PMJ. An impaired Purkinje coupling meant the spontaneous beat could not excite the Purkinje network and instead had to travel out of and around the infarct zone to reach the rest of the myocardium. This meant that the following sinus beat wavefront, which originated from the bundle of His rather than from within the scar core, met heterogeneous refractory tissue, unidirectional conduction block and could re-enter through the scar cores. Furthermore, healthy PMJ

coupling led to the Purkinje network being refractory and non-excitable for heart rates above 34 bpm (grey rectangles in Figure 31 B).

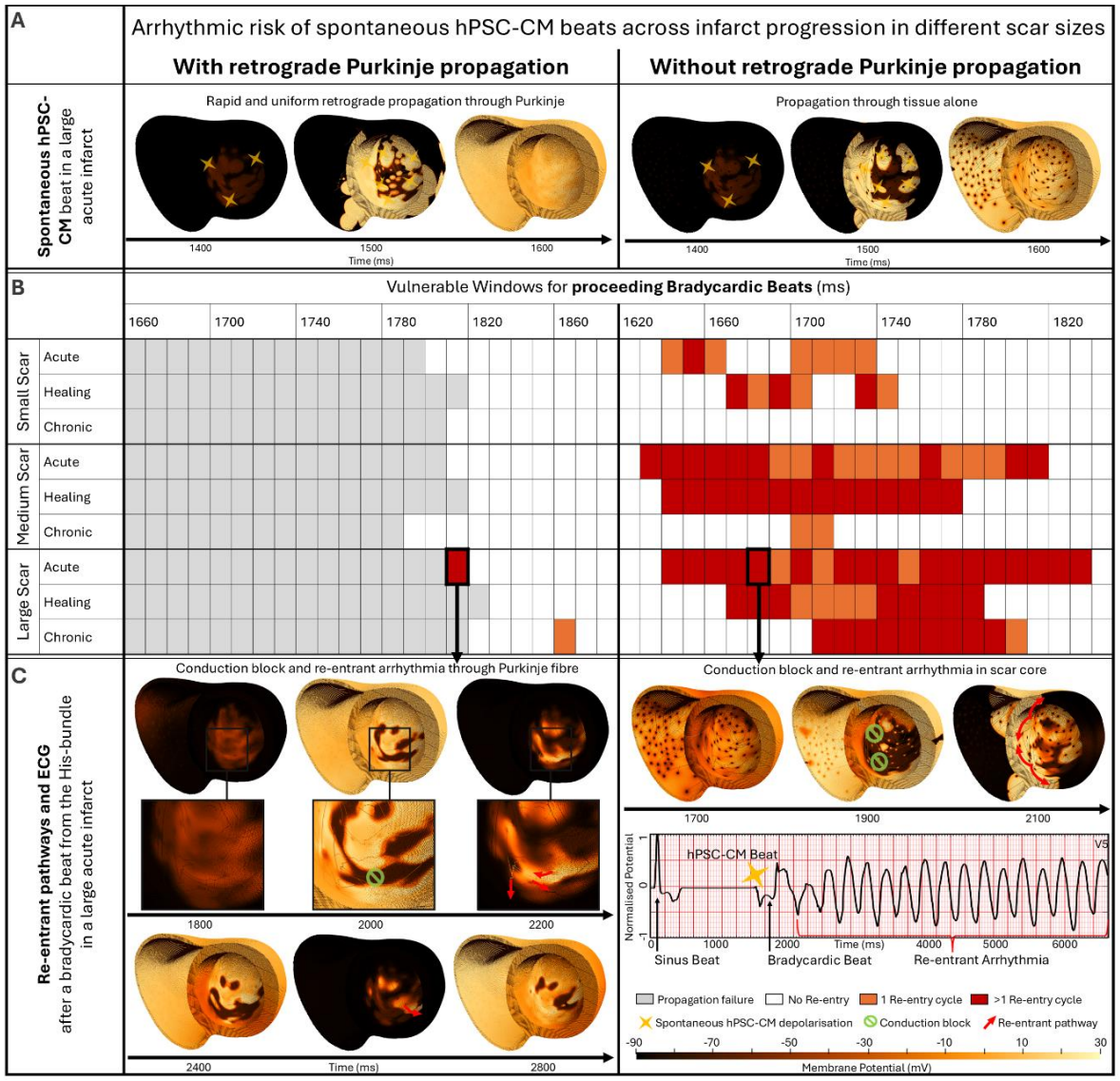


Figure 31. Depolarisation of the ventricles through spontaneous hPSC-CM beats and subsequent arrhythmia inducibility and sustainability. A) Emergence of spontaneous hPSC-CM beats in the large scar during the acute stage with (left) and without (right) retrograde Purkinje propagation. B) Vulnerable windows in small, medium, and large scars across acute, healing, and chronic MI with and without retrograde propagation through the Purkinje network. C) Propagation of electrical excitation following a proceeding bradycardic beat in the large scar during acute MI with and without retrograde Purkinje propagation. The dark spots in the scenarios with retrograde Purkinje propagation disabled indicate the PMJs, showing that current could not flow from the myocardial tissue into the PMJs. Figure and caption unmodified and obtained from Riebel et al. (2024) under CC BY license (https://creativecommons.org/licenses/by/4.0/).

Re-entrant risk for impaired PMJ coupling increased with increasing scar size; the VW in the small, medium, and large scar was 130, 350, and 420 ms, respectively. Furthermore, re-entrant susceptibility was largest in acute MI and lowest in chronic MI; VWs of all infarct sizes combined were 460, 320, and 120 ms during acute, healing, and chronic MI,

respectively. Additionally, most re-entries in chronic MI were more organised and involved a single rotor location. As I summarise in Figure 32, 78%, and 75% of re-entries in acute and healing MI involved rotors in two or more locations simultaneously.

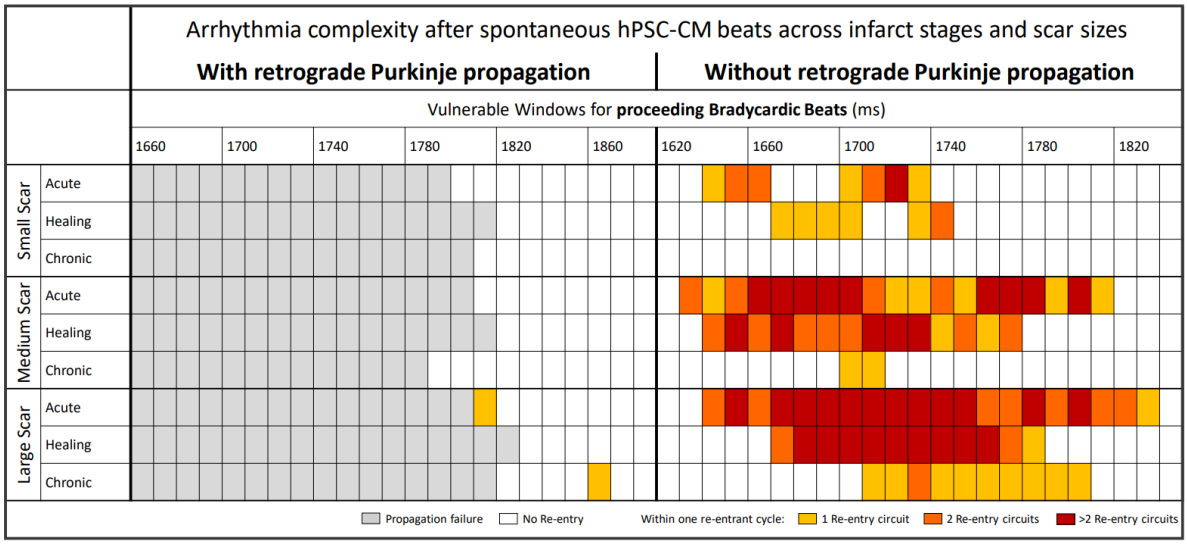


Figure 32. Arrhythmia complexity across all infarct stages and scar sizes and with and without retrograde Purkinje propagation enabled; measured as the number of re-entrant circuit locations within the first re-entrant cycle. Figure and caption unmodified from the supplementary material of Riebel et al. (2024) under CC BY license (https://creativecommons.org/licenses/by/4.0/).

7.4 Discussion

In this chapter, I applied multiscale human ventricular electrophysiological modelling and simulation of MI, as described in Chapter 5, to identify how injected cells, with or without beating spontaneously, can act as a substrate for re-entrant arrhythmias.

Firstly, I showed how cell delivery increases re-entrant risk in chronic MI, without the need for the delivered cells to beat spontaneously. Instead, re-entrant triggers were provided by ectopic stimuli from within the post-MI border zone, as observed experimentally and attributed to electrophysiological remodelling and an increased risk of alternans and repolarisation abnormalities (Amoni et al., 2021; Chou et al., 2007). While a previous *in silico* study showed that delivery of cell patches could increase or decrease arrhythmic risk, depending on the patient substrate and delivery location (J. K. Yu, Liang, Franceschi, et al., 2022), all three scars I investigated here showed an increase in re-entrant

susceptibility from before to after cell delivery. In my study, how much the re-entrant risk increased was subject to the scar morphology and the distribution of PMJs within the scar cores. Specifically, the small and large scar I investigated here allowed for significantly more re-entries than the medium scar. However, 90% of re-entries in the small scar were facilitated through the same PMJ, which was located in a scar core with a particularly pro-arrhythmic shape. As the scars I modelled here were aimed to provide physiological infarct anatomies, they were complex, asymmetrical, and involved non-uniform isthmuses through the scar cores. The role of isthmuses within the scar has been highlighted in several *in silico* studies as crucial in determining the arrhythmic risk (Campos et al., 2018; Connolly & Bishop, 2016; Myklebust et al., 2024; Ringenberg et al., 2014). In my simulations, whilst re-entry inducibility depended more on scar geometry rather than scar size, arrhythmia sustainability did increase with increasing scar size.

In the second part of this study, I determined that cell population heterogeneity is crucial to enable spontaneous beating, which is encouraged in chronic MI and by slow sinus heart rates. Whilst ventricular-like only cell populations did not spontaneously depolarise the ventricles, 10% of atrial-like and nodal-like cells each was sufficient to elicit automaticity. Cell culture purity has been linked to arrhythmias experimentally (Selvakumar et al., 2024). As exact purification and reproducibility of maturation protocols at large scale is challenging (Ban et al., 2017; B. Jiang et al., 2020), their arrhythmogenic implications need to be thoroughly investigated. Whilst the aim for regeneration of the ventricles is to inject ventricular-like hPSC-CMs, experimental studies have reported large variability in AP morphology and spontaneous beating rate (Doss et al., 2012; He et al., 2003). Hence, some cell lines may be more accurately represented

with the atrial-like or nodal-like cell type I used here and warrant arrhythmia investigations into fully atrial-like and nodal-like populations.

Whilst other *in silico* studies have established that spontaneous beating is increased for high hPSC-CM clustering, density, and delivery proximal to the infarct (J. K. Yu et al., 2019), here I chose to model the spatial distribution of delivered cells based on pre-clinical observations (Poch et al., 2022). Although I kept the relative number of delivered cells constant across the three scar geometries, their absolute number varied due to differences in scar volume. This resulted in a large number of injected cells to cluster in the thick anterior septal infarct core of the medium scar, which, according to J. K. Yu et al. (2019), may influence arrhythmogenicity. Further modelling and simulation studies showed that the coupling of injected cells is also crucial in modulating the burden of spontaneous beats, which Gibbs et al. (2023) concluded was highest for some but incomplete coupling. Others found that delivered cells with a CV of around 80% lower than that of adult myocardium, as I modelled here, may promote arrhythmic events (Fassina et al., 2023).

Next in this chapter, I identified that infarct stage has a more crucial effect on spontaneous beating rate than infarct size. Even though cell therapy has so far been explored as a treatment for patients with heart failure or chronic MI, reinfarction at the time of delivery cannot be ruled out. Furthermore, optimal delivery methodology is yet to be determined and could show treatment early after infarction as beneficial. Hence, investigation of arrhythmogenicity across the progression of MI is crucial and, in the future, should be extended to the non-automaticity-involved re-entries I examined in part one of this study.

Whilst in my simulations re-entry susceptibility following ectopic stimuli from the border zone showed no clear association with scar size, re-entry susceptibility after spontaneous beating of injected cells showed a clear increase in VWs from the small to the large scar. This difference may be due to the arrhythmia induction protocol. In the first part of this study, I applied a single ectopic beat in the border zone and hence the re-entrant wavefront heterogeneously activated the ventricles. In the second part of this work, I applied the re-entry-triggering sinus beat at the top of the bundle of His. Even though the ventricles were still non-uniformly refractory from the preceding spontaneous beat of injected cells, this following sinus beat propagated more uniformly and may have hence prevented the figure-of-eight re-entries I observed so frequently in the small chronic scar during part one of this study.

Finally, I investigated the pro-arrhythmic role of the Purkinje network post-MI and cell delivery. My simulations showed that the rapid activation through the Purkinje network abolished some re-entrant pathways, whilst also creating new ones, which is supported by other *in silico* studies (Deo et al., 2009; Jian et al., 2022). Overall, the arrhythmic risk after spontaneous hPSC-CM beats was reduced for healthy Purkinje coupling. However, as here Purkinje coupling was homogeneously impaired across the ventricles, future studies may focus on the arrhythmogenic implications of remodelled PMJs specifically within the scar.

7.5 Conclusions

In this chapter, I employed multiscale human electrophysiological modelling and simulation of the infarcted ventricles and established how cell delivery can cause re-entrant arrhythmias, with or without the injected cells beating spontaneously. Specifically,

I determined that in the absence of injected cells beating spontaneously, the re-entrant risk was higher after than before cell delivery and highest for the large scar. Next, I showed that spontaneous beating occurred for heterogeneous injected cell populations only and was encouraged by chronic infarction and slow sinus heart rates. Finally, my simulations identified that following sinus beats may meet unidirectional conduction block, due to the previous automaticity of injected cells, and induce re-entrant arrhythmias, which were promoted in larger scars, acute MI, and for impaired Purkinje-myocyte coupling.

8 Designing anti-arrhythmic treatments to mitigate safety concerns of cell injection in the chronically infarcted human ventricles

In this chapter, I applied multiscale human ventricular electrophysiological modelling and simulation, as described in Chapter 5, to identify anti-arrhythmic targets and design and optimise post-MI treatments. Specifically, automaticity-induced VT after cell injection is a common pre-clinical concern that hinders clinical application of regenerative cell therapy for the human heart. Hence, I investigated experimentally observed slow and rapid beating cells and ionic targets to suppress their automaticity. Based on the results of Chapter 7, I combined these with ionic targets that inhibit the mechanisms through which injected cells can act as a substrate for re-entrant arrhythmias. The result was a combination of ionic targets, that mitigates safety concerns of cell therapy, whilst also aiming to maintain calcium transients, which are crucial for therapy efficacy.

8.1 Introduction

As I discussed in Section 3.5, whilst cell therapy has shown promise to improve the heart's mechanical function after MI (Foo et al., 2018; Querdel et al., 2021; Zimmermann et al., 2006), VT arrhythmias have been observed during pre-clinical testing. Different studies identified these arrhythmias as transient, occurring within the first three weeks after cell delivery (Chong et al., 2014; Liu et al., 2018; Romagnuolo et al., 2019). Using electrical mapping, it has furthermore been shown that the origin of such arrhythmias appears to be within the areas in which the cells where injected (Liu et al., 2018; Romagnuolo et al., 2019). Hence, it is believed that, due to their immaturity, the delivered cells produce spontaneous beats at fast frequencies in the ventricles.

The underlying mechanisms behind the surge in arrhythmias was unclear, until a recent experimental study measured the gene expression of I_f, I_{CaT}, I_{K1}, I_{NaF}, I_{CaL}, I_{NaCa}, I_{Kr}, I_{to}, and I_{Ks} at varying time points from zero to 84 days after cell injection into murine models (Marchiano et al., 2023). The results of Marchiano et al. (2023) suggest that during the first weeks, an increase in SLC8A1 (encoding I_{NaCa}), may encourage an increased spontaneous beating rate. They further indicate that after week four, a reduction in HCN4 (responsible for I_f) and an increase in KCNJ2 (encoding I_{K1}), amongst others, may reduce the spontaneous beating (Marchiano et al., 2023). Marchiano et al. (2023) proceeded to target the identified currents to create an improved cell line that would abolish arrhythmic concerns; they showed that a combination of HCN4, CACNA1H (encoding I_{CaT}), and SLC8A1 knock-out as well as an overexpression of KCNJ2 was necessary to stop spontaneous beating. Whilst knock-out of I_f and upregulation of I_{K1} are in line with the cells' natural maturation towards an adult phenotype (Goversen et al., 2018), I_{NaCa} is crucial, at least in adult cardiomyocytes. I_{NaCa} and I_{CaT} knock-out may substantially intervene in the cells' functioning and pave the way for new arrhythmias. Furthermore, as shown in the supplementary materials of Marchiano et al. (2023), their proposed modifications appear to cause intracellular Ca^{2+} accumulation and a reduced CaT amplitude. This may impact the cells' contractile capabilities, for which they were injected in the first place.

Whilst the main safety concern is the cells' automaticity, their potential to further facilitate re-entrant arrhythmias should also be considered. Indeed, as I established in Chapter 7, the re-entrant risk in three human biventricular models of chronic infarction increased after cell delivery. Hence, novel ionic targets to reduce arrhythmic burden through the cells' automaticity as well as their immature AP characteristics are needed.

Furthermore, throughout the last years, a range of suitable cell types all with different maturation and differentiation protocols has been put forward. Since all these cell lines present with a different electrophysiological phenotype, different anti-arrhythmic strategies may be required and efficient new tools to identify and calibrate such anti-arrhythmic targets are needed.

After in the previous chapter I identified how injected cells can provide a substrate for re-entries, here I utilise human ventricular electrophysiological modelling and simulation, as described in Chapter 5, to also establish the cells' potential to facilitate automaticity-induced VT arrhythmias and to identify novel strategies that mitigate both, spontaneous ectopy and re-entrant induced, arrhythmic pathways. For this, I designed, conducted, and analysed simulation studies to identify and optimise anti-arrhythmic targets after cell delivery, whilst also aiming to maintain the cells' contractile capacities (using their CaTs as a surrogate).

8.2 Methods

In the following sections, I summarise how I adapted the human ventricular electrophysiological modelling and simulation framework, described in Chapter 5, for this study. Unless described otherwise below, cell injection in the chronically infarcted human ventricles was modelled and simulated as described in Sections 5.3.1 and 7.2.

8.2.1 Experimentally informed *in silico* maturation of injected cells

In the following, I will refer to the baseline ventricular-like hPSC-CM Paci2020 model (Paci et al., 2020) as D0 hPSC-CMs. To reproduce the cells' *in vivo* maturation 14 days after injection (from here on called D14 hPSC-CMs), I scaled I_f, I_{K1}, I_{to}, I_{Ks}, I_{Kr}, I_{NaF}, I_{NaCa}, and I_{CaL}, as shown in Table 12, based on *in vivo* gene expression data at 14 days after cell injection

from Marchiano et al. (2023). It should be noted that gene expression may not relate to ionic current expression in a 1:1 fashion. The exact degree of up- or downregulation would need to be determined experimentally through measuring the ionic currents and may further vary between cell types. Here, to relate gene expression to ionic current expression in a systematic way, I estimated relative change in gene expression from Marchiano et al., (2023, Figure 1F) and multiplied it by 0.25 to give the scaling of each channel's conductance. I scaled down the conductance multiplier because some of the relative gene expression changes reached values of over eight, which would have impacted the model too extremely to produce physiological APs. I establish credibility of this approach in the following results section.

Table 12. Ionic current conductances, scaled to produce D14 (Marchiano et al., 2023, Figure 1F), rapid beating, and I_{NaCa}-KO (Marchiano et al., 2023) hPSC-CMs. To create rapid beating D14 hPSC-CMs, the product of both scalings was applied. G_s: conductance of ion channel s, k_{NaCa}: scaling factor for I_{NaCa}, $V_{max,up}$: maximum I_{up}. Empty cells represent no scaling, i.e. a scaling factor of 1.

Model Parameter	D14	Rapid	I_{NaCa}-KO
G_f	1.25	2.50	0.00
G_{K1}	1.25		1.50
G_{to}	1.50		
G_{Ks}	2.00		
G_{Kr}	1.75		
G_{NaF}	2.50		
k_{NaCa}	2.00	2.50	0.00
G_{CaL}	3.00		
$V_{max,up}$		2.50	

Whilst the D0 and D14 models beat every 1,700 and 1,300 ms, respectively, much shorter beating intervals, down to 850 ms, have been reported in the literature (Doss et al., 2012; He et al., 2003). To investigate such faster beating hPSC-CMs, I created a rapid beating phenotype by scaling conductances of I_f, I_{NaCa}, and I_{up} by 2.5. I combined this rapid phenotype with the scaling factors at D0 and D14 to produce rapid D0 and rapid D14 hPSC-CMs, which beat every 1,150 and 910 ms, respectively. APs of D0, D14, and rapid

D14 hPSC-CMs are shown in Figure 33, and a comparison of AP biomarkers is provided in Table 13.

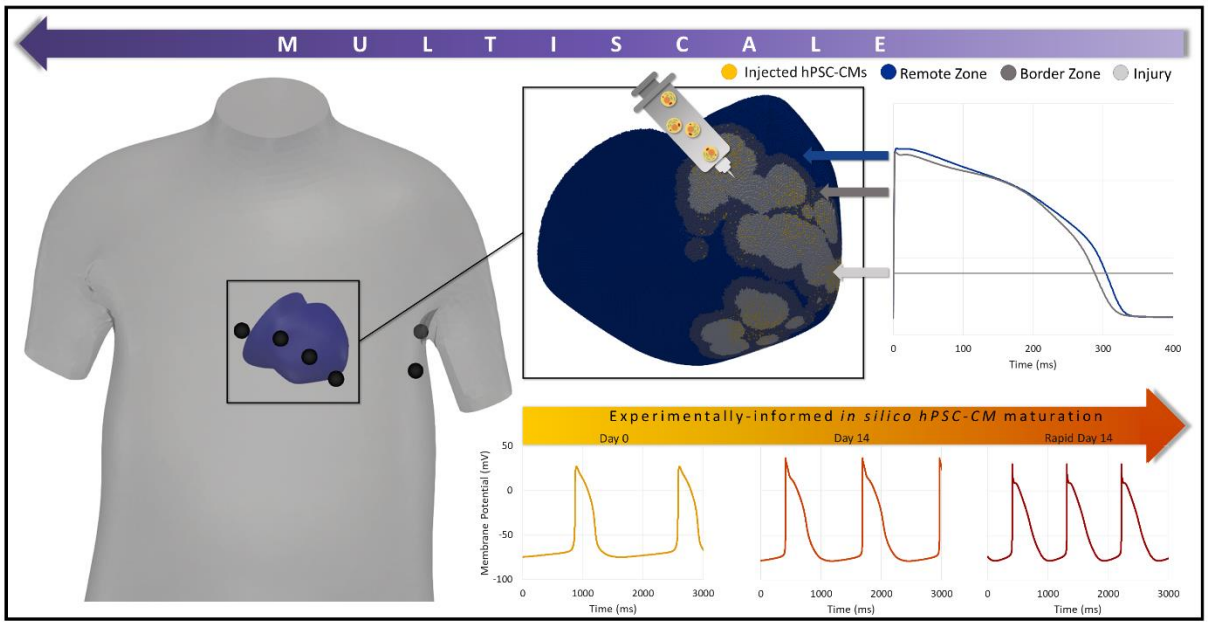


Figure 33. Pipeline to simulate injection of D0, D14, and rapid D14 hPSC-CMs in the chronically infarcted human ventricles.

Table 13. AP biomarkers of the D0, rapid D0, D14, and rapid D14 hPSC-CM phenotypes. DDR: average diastolic depolarisation rate, $V_{m,peak}$: peak membrane voltage, Interval: spontaneous beating interval.

	DDR (V/s)	MDP (mV)	dV/dt_{max} (V/s)	$V_{m,peak}$ (mV)	APD_{90} (mV)	Interval (s)
D0	0.01	-74.87	20.54	27.14	402.42	1.71
Rapid D0	0.02	-74.90	26.49	18.76	424.27	1.15
D14	0.02	-78.79	172.26	36.53	446.31	1.28
Rapid D14	0.03	-78.57	168.01	29.94	414.57	0.91

For comparison, I modelled and simulated ionic current changes proposed by Marchiano et al. (2023) as shown in Table 12 and in the following refer to them as I_{NaCa}-KO hPSC-CMs. As I_{CaT} is not present in the ventricular-like Paci2020 model, I did not include its knock-out, as suggested by Marchiano et al. (2023), in this simulation study. Furthermore, the exact effect of KCNJ2 upregulation on actual I_{K1} is difficult to estimate and will vary between cells. Hence, as Marchiano et al. (2023) reported I_{K1} upregulation alone to be insufficient to suppress spontaneous beating and the D0 model does cease beating for I_{K1} upregulation alone with a scaling above 1.6 (i.e. 1.65), I chose a factor of 1.5.

8.2.2 Identifying anti-arrhythmic targets and optimising Ca^{2+} transients of injected cells

To identify ionic targets, I carried out a single cell sensitivity analysis in the spontaneous Paci2020 model, similarly to a sensitivity analysis we performed of paced hPSC-CMs in a previous study (Riebel et al., 2021). Here, I analysed the sensitivity of five AP biomarkers, namely MDP, dV/dt_{max}, peak membrane potential ($V_{m,peak}$), APD_{90}, and beating interval, to 25% up- and downregulation of key ionic current conductances. I computed relative sensitivities as in Romero et al. (2009), which varied between -1 (strong negative correlation) and 1 (strong positive correlation).

From the sensitivity analysis results, I identified promising ionic targets. As spontaneous depolarisation in hPSC-CMs occurs via I_f as well as the cells' intrinsic Ca^{2+}-clock (Kim et al., 2015; Maltsev & Lakatta, 2012), suppression of a single ionic current may not be sufficient. Considering this and that in this work I aim to also reduce re-entrant inducibility, a combination of anti-arrhythmic strategies may be required. Accordingly, to identify optimal ionic target combinations, I created populations of hPSC-CM models. For this, I investigated all combinations of ionic current conductances within a set of discrete scaling factors. Specifically, to determine the optimal combination of I_{Kr}, I_{K1}, and I_{NaK} scaling, I created a population of cellular D0 and D14 models by upregulating the conductance of I_{Kr} (G_{Kr}) between 1 and 5 in 0.5 steps and the conductance of I_{K1} (G_{K1}) as well as maximum I_{NaK} (p_{NaK}) between 1 and 3 in 0.25 steps. These models also contained full I_f block, which I did not vary and hence is not specifically pointed out in the following. Next, I computed APD_{90} and CaT amplitude in the resulting 1,458 models (exploring all combinations of G_{Kr}, G_{K1}, and p_{NaK} scalings, i.e. 9 x 9 x 9) of D0 and D14 hPSC-CMs.

To determine the optimal ionic targets and their combinations, I considered three main acceptance criteria. Firstly, spontaneous hPSC-CM beats needed to be suppressed. Secondly, re-entrant arrhythmia inducibility should be reduced. Thirdly, hPSC-CM mechanical efficacy may be maximised. I only considered the second aim if the first was satisfied and the third only if the second was met. I accepted the first criterion if and only if hPSC-CMs did not beat spontaneously in the single cell model as well as the biventricular setting. Furthermore, hPSC-CMs had to be 'pacable', meaning I only considered them further if an AP of at least 100 ms with a peak above 0 mV was produced under 1 Hz pacing and no EADs, DADs, or spontaneous depolarisations were visible in the last 15 beats.

As I concluded in Chapter 7, increased APD was the main determinant behind the increased re-entrant arrhythmia vulnerability after compared to before cell injection. Hence, for the second criterion, to estimate biventricular re-entry inducibility from the cellular population of models, I selected a target APD_{90} to reduce biventricular repolarisation gradients. As a starting point, I set this desired APD_{90} to 330 ms (~3/4 of the baseline Paci2020 model under the stimulation protocol described below). For the third criterion, I used CaT as a surrogate to measure mechanical efficacy in the human electrophysiological models and simulations. Whilst the occurrence of spontaneous beating in my simulations was a clear binary event – either the cells beat spontaneously, or they do not – a reduction of the VW and maximisation of CaT is more subjective. Hence for the third criterion, I introduced the Safety-Efficacy score, which prioritised hPSC-CMs with the desired APD_{90} but also considered the cells' CaT, as described in detail in Chapter 5.3.2 and Equation (39). To prioritise safety over efficacy, I set the weighting factors w_s and w_e to 1.5 and 1, respectively.

From the resulting ionic target combinations, I selected the most promising one with the highest Safety-Efficacy score and investigated it in 3D. For this, I plugged the shortlisted model into the biventricular framework, whilst maintaining the previously introduced spatial hPSC-CM distribution to allow for comparability between simulations. Hence, to clarify, I only changed ionic currents in the hPSC-CMs, not in the adult ventricular or scarred tissue. This mimics experimental gene editing protocols, which would target the hPSC-CMs specifically and before injection.

8.2.3 Simulation and arrhythmia quantification protocol

Where I created a cellular population of hPSC-CM models to calculate Safety-Efficacy scores, I left each model within the population to beat spontaneously for 1,000 s. Afterwards, if spontaneous activity ceased, I simulated three paced beats and calculated the APD_{90} as well as the CaT from the last AP. At the start of all biventricular simulations, I applied three 1 Hz beats at the bundle of His to reach steady state (further detail in Section 5.4.1).

To test whether ionic targets and their combinations were suitable to suppress spontaneous beating, I then simulated two seconds without pacing. If spontaneous beating did occur, I simulated a full ten seconds under 1 Hz pacing to observe whether the spontaneous beats would also arise under physiological sinus pacing. Next, to test whether shortlisted hPSC-CM models reduced the re-entry risk, I applied ectopic beats at varying S1-S2 intervals across 15 locations across the infarct border zone, as described in Section 5.4.2.

This resulted in 1,500 single cell simulations and 350 biventricular simulations, the latter included: 10 simulations of testing quiescence in D0, D14, rapid D0, and rapid D14 hPSC-

CMs before and after ionic targets were addressed and 330 simulations to test re-entry risk (2 shortlisted hPSC-CM models x 11 S1-S2 intervals x 15 ectopic stimulus locations). I quantified re-entry burden as the VW, the time span during which arrhythmias were inducible.

8.3 Results

8.3.1 Establishing credibility – simulations of cell therapy in the infarcted ventricles capture experimentally observed surge in tachycardia arrhythmias

To demonstrate that human ventricular electrophysiological modelling and simulation as described in chapter 5 is suitable to investigate ionic targets that suppress automaticity of cells injected into the infarcted human ventricles, I simulated arrhythmic risk at D0 and D14 after cell delivery. The spontaneous beating interval in single cell D0 and D14 hPSC-CMs shortened from 1,710 to 1,280 ms, respectively. This qualitatively captures experimentally reported increasing hPSC-CM automaticity and provides confidence in the D0 and D14 models, i.e. the inference of *in silico* ionic current expression from the experimentally reported gene expression data from Marchiano et al. (2023), as described in Section 8.2.1.

In the infarcted biventricular models, the D0 hPSC-CM model did not beat spontaneously, in line with Chapter 7.3.3, where I showed that ventricular-like only hPSC-CM populations do not produce spontaneous beats in 3D. The D14 model however caused spontaneous depolarisation of the ventricles every 1,425 ms. The emergence of spontaneous beats may not be caused by the cellular beating rate alone but also by the diastolic depolarisation rate (DDR), the rate at which the hPSC-CM membrane potential rises from the MDP to the point of upstroke. Here, as shown in Table 13, the average DDR was 0.01

and 0.02 V/s in the D0 and D14 models, respectively, suggesting an increased beating strength in the D14 hPSC-CMs.

The rapidly beating D0 and D14 hPSC-CM cellular models beat every 1,150 and 910 ms, respectively. In the chronically infarcted ventricles, the rapid D0 model produced ectopic beats every 1,300 ms and hence was suppressed by 1 Hz sinus beating. However, simulation of the rapid D14 hPSC-CMs did elicit VT arrhythmias in all three infarcted biventricular models, as shown in Figure 34. Detailed analysis of the simulation outputs showed that VT was induced by a mix of automaticity and re-entrant patterns, highlighted in Figure 34 as purple and orange stars, respectively.

As I show in Figure 34, especially during the first 3,000 ms, the spontaneous beating occurred more frequently in the medium and large than in the small scar. This may seem counterintuitive considering the findings I presented in Section 7.3.3, i.e. that spontaneous depolarisation is fastest in the medium and slowest in the large scar. Here, upon closer investigation, the first hPSC-CM depolarised at around 750 ms in all three scars. Compared to the heterogeneous population I used in Chapter 7 (containing 50% ventricular-like, 25% atrial-like, and 25% nodal-like hPSC-CMs), the rapid D14 hPSC-CMs population beat faster. Hence, when the rapid D14 hPSC-CMs started to depolarise, not all of the scar tissue had repolarised, therefore raising the hPSC-CMs' MDP. In line with Section 7.3.3, this enabled faster spontaneous beating, especially in the larger scars, which provided a stronger current source. This explains the reduced difference in hPSC-CM depolarisation times. Furthermore, whilst in Chapter 7 the injected hPSC-CM population was heterogeneous with the faster beating atrial-like and nodal-like cells having to excite not only the adult ventricular tissue but also the ventricular-like hPSC-

CMs, the population investigated here contained only rapid D14 hPSC-CMs. Hence, the dampening effect of non-conducting large scars described in Chapter 7 may have less of an impact on the timing of spontaneous beats here.

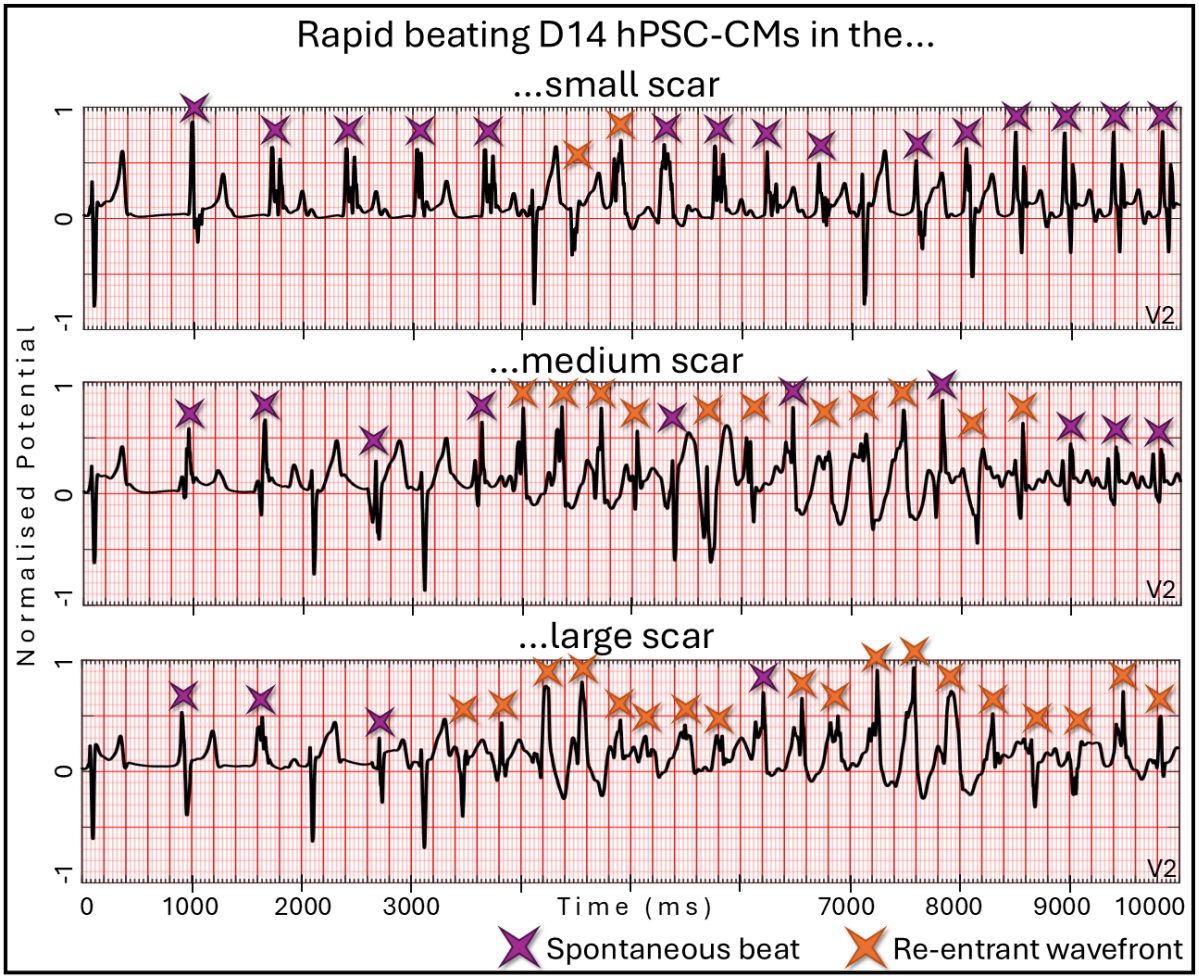


Figure 34. Simulated ECGs after rapid D14 hPSC-CM delivery into a biventricular model with a small (top), medium (middle), and large (bottom panel) chronic MI scar. Spontaneous beating (purple stars) and re-entrant wavefronts (orange stars) are indicated; beats with no indication are sinus beats applied at 1 Hz from the bundle of His.

Overall, the frequency of arrhythmic wavefronts decreased with decreasing scar size, namely from 22 over 21 to 17 non-sinus activations during 10,000 ms in the large, medium, and small scar, respectively. Furthermore, contribution of spontaneous beats to the VT arrhythmia, as shown in Figure 34, increased with decreasing scar size. Specifically, spontaneous depolarisations accounted for 18% (4 out of 22), 48% (10 out of 21) and 88% (15 out of 17) of arrhythmic waves in the large, medium, and small scar, respectively. However, in the medium and large scar, several of the marked re-entrant arrhythmias

coincided with spontaneous depolarisation, which was visibly imminent. In the medium and small scar, the arrhythmias appeared to reach a steady state towards the end of the simulation. The last 1,500 ms in both were comprised of spontaneous hPSC-CM-induced VT with a consistent morphology. The spontaneous beating increased throughout the simulations to intervals of up 420 ms (or approximately 140 bpm), similar to experimental observations of heart rates of approximately 150 bpm (Marchiano et al., 2023).

8.3.2 Targeting the Na^+-K^+ pump to suppress spontaneous beating

To investigate alternative ionic targets for ectopy suppression, I carried out a sensitivity analysis of the spontaneously beating D0 hPSC-CM model. As highlighted in Figure 35, this showed that the current influencing the spontaneous beating most is I_{NaK}. Specifically, both, reducing p_{NaK} below 0.75-fold or increasing it above 1.25-fold, abolished any automaticity. I hypothesise that the high model sensitivity to I_{NaK} is due to: 1) the effect of I_{NaK} on intracellular Na^+ concentration (e.g., reduced p_{NaK} causes intracellular Na^+ accumulation) and therefore the reverse mode of I_{NaCa} (Bueno-Orovio et al., 2014), which modulates the Ca^{2+}-clock (further detail below), and 2) I_{NaK}'s role as an outward current during the resting phase (Britton et al., 2017), therefore hindering spontaneous depolarisation.

	MDP	dV/dt_{max}	V_{peak}	APD_{90}	F
G_{NaF}		0.99			0.15
G_{NaL}					
G_{to}					
G_{Kr}	0.15	-0.10	-0.29	-0.90	0.24
G_{Ks}					
G_{K1}	1.00	0.40	-0.41	-0.74	
G_{CaL}	-0.12	0.84	0.89	1.00	0.21
G_{NaCa}	0.13		-0.26	0.24	0.37
G_{NaK}	-0.17	-1.00	1.00	0.25	-1.00
G_{up}		0.67	0.15	0.11	0.51
G_f	-0.11	-0.46	-0.20	-0.29	0.35

Figure 35. Relative sensitivities computed from the biomarker changes observed in non-paced simulated hPSC-CMs when scaling current conductances between 0.75 and 1.25. Darker shades of green or red correspond to a larger positive or negative relative sensitivity, respectively. Values below +/-0.1 are not shown. F: spontaneous beating frequency.

The sensitivity analysis further confirmed I_{K1} as the main contributor to a stable MDP and, therefore, sufficient G_{K1} upregulation may prevent spontaneous depolarisation. In hPSC-CMs, spontaneous activity is triggered by I_f in combination with Ca^{2+} release from the SR; together with I_{NaCa}, these cause spontaneous depolarisation of the membrane potential (Bogdanov et al., 2001; Koivumäki et al., 2018; Paci et al., 2020). In the paced hPSC-CM model (a sensitivity analysis of which is presented in (Riebel et al., 2021)), I_{NaCa} is a stable net inward current during rest, where it pumps one Ca^{2+} ion out of the cell in exchange for three Na^+ ions entering the cell. Similarly to human adult ventricular cardiomyocytes and as described in 2.2, following the upstroke, I_{NaCa} reverses its function until the plateau phase, during which it reverses again. In the unpaced hPSC-CM model, due to the absence of a regular stimulus, the Ca^{2+} release of the SR is prolonged. This causes an increase of Ca^{2+} in the main cytosolic pool and leads to a larger net inward I_{NaCa}, which encourages the spontaneous depolarisation of the cell membrane (see Figure 36). The crucial role of Ca^{2+} release from the SR in the spontaneous upstroke also explains the

strong dependence of the beating frequency on I_{up} and on I_{CaL}. I_{up} is created by Ca^{2+} being pumped from the main cytosolic pool into the SR, without which the SR's Ca^{2+} deposit would not be sufficiently restored. Similarly, inhibiting I_{CaL} causes fewer Ca^{2+} available inside the cell and, therefore, a strong I_{CaL} block results in the spontaneous activity to cease.

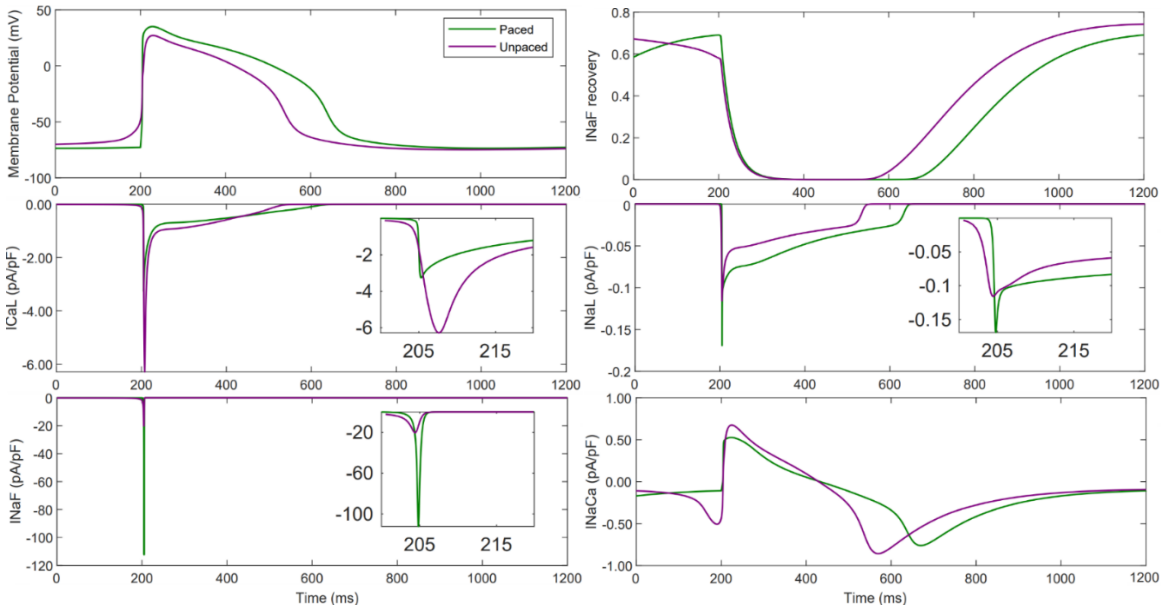


Figure 36. AP and ionic current traces for the ventricular-like hPSC-CM Paci2020 model under paced (green) and unpaced (purple) conditions.

Based on these sensitivity analysis results, while I_{NaCa}, I_{up}, and I_f may all be promising to suppress spontaneous beating, I_{NaK} had the strongest effects and hence I chose to investigate it further. In the D14 hPSC-CMs, I observed that a 15% p_{NaK} reduction was sufficient for the ectopic beats to stop. However, whilst not beating spontaneously, the model also showed a diminished paced AP, shown in Figure 37 A. Reduced p_{NaK} also caused an accumulation of intracellular Ca^{2+} and a lower CaT peak, as shown in Figure 37 A, and may hence hinder efficacy if the cells are injected.

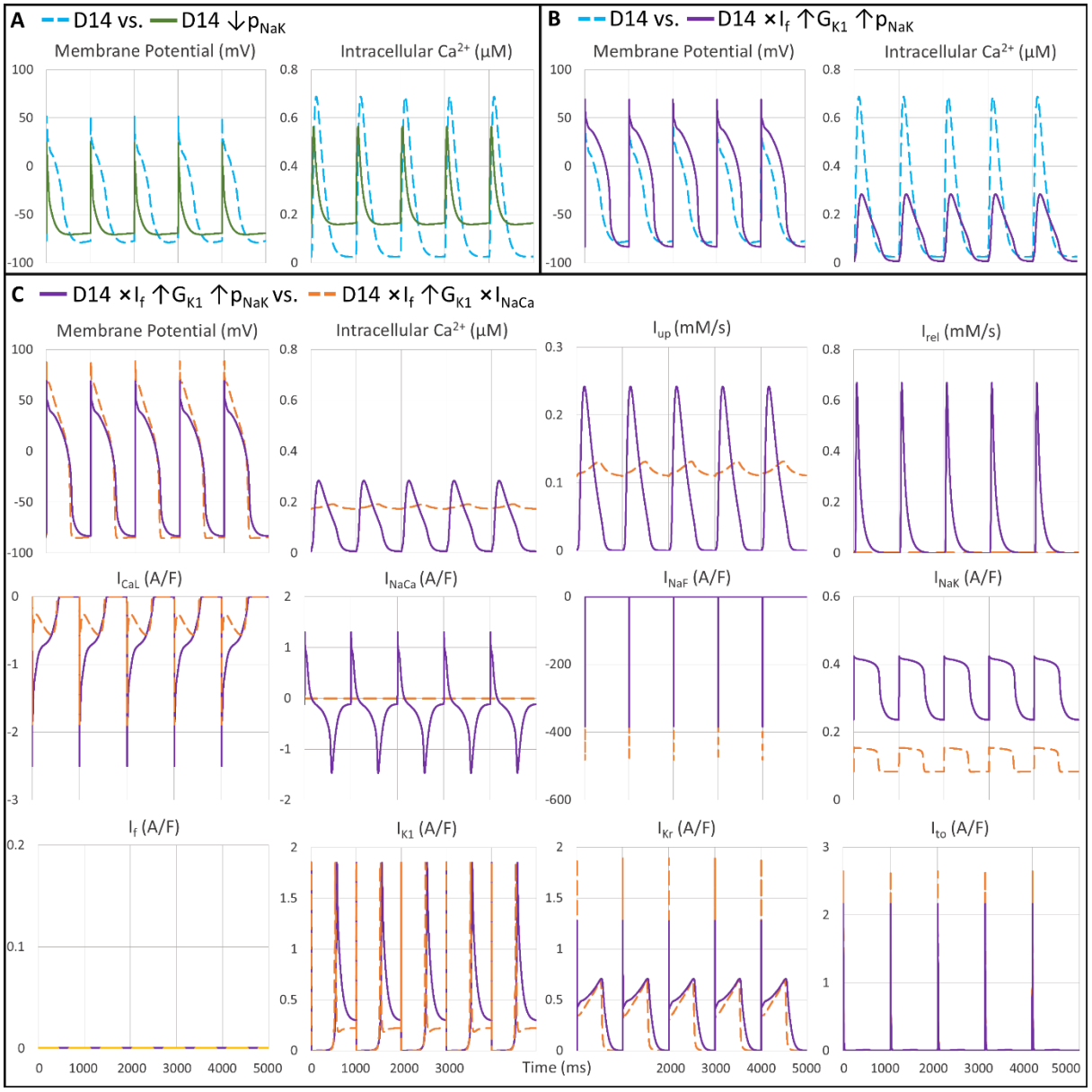


Figure 37. The effects of p_{NaK} modulation on AP. A) Paced APs of D14 hPSC-CMs before (blue dotted line) and after (green solid line) 0.85 reduction of p_{NaK}. B) Paced APs of D14 hPSC-CMs before (blue dotted line) and after (purple solid line) I_f knock-out as well as 50 and 40% G_{K1} and p_{NaK} increase, respectively. C) Paced APs and ionic current traces of D14 hPSC-CMs with full I_f block and 50% G_{K1} increase and with either 40% p_{NaK} enhancement identified here (purple solid line) or full I_{NaCa} block (orange dotted line, corresponding to the D14 I_{NaCa}-KO hPSC-CMs created based on Marchiano et al. (2023)). In silico hPSC-CMs were paced at 1 Hz for 1,000 s in A) and 2,000s in B) and C).

Accordingly, I focused on whether spontaneous beats in D0 as well as D14 hPSC-CMs could also be suppressed by p_{NaK} up- rather than downregulation. In contrast to D0 hPSC-CMs, even for p_{NaK} upregulation with a factor of 5, spontaneous activity of D14 hPSC-CMs continued. Hence, I combined p_{NaK} enhancement with 50% G_{K1} upregulation and I_f block; I_f and I_{K1} have been identified as suitable targets to improve maturity and reduce

spontaneous activity in several previous studies (Dark et al., 2023; Goversen et al., 2018; Maltsev & Lakatta, 2012; Marchiano et al., 2023; Riebel et al., 2021). Full I_f block paired with 40% and 50% upregulation of p_{NaK} and G_{K1}, respectively, stopped automaticity in D0 and D14 hPSC-CMs whilst allowing for physiological paced APs (see Figure 37 B). In the rapid hPSC-CMs, I had to increase p_{NaK} upregulation, together with 50% G_{K1} upregulation and I_f block, to 65% to abolish automaticity. Neither on their own nor combined, did 50% G_{K1} upregulation and I_f knock-out suffice in simulated D14 hPSC-CMs.

To evaluate the benefits of p_{NaK} upregulation versus I_{NaCa} knock-out, as proposed by Marchiano et al. (2023), I simulated full block of I_f and I_{NaCa} as well as upregulation of G_{K1} (see Table 12). Indeed, spontaneous beating was abolished, whilst pacing still produced APs (Figure 37 C), as suggested by Marchiano et al. (2023). However, my simulations also showed that under sinus pacing, intracellular Ca^{2+} accumulated and CaT peaks were substantially reduced. In contrast, the ionic targets I suggested here, which also upregulate G_{K1} and fully block I_f but replace I_{NaCa} knock-out with p_{NaK} upregulation, produced more physiological CaTs with an increased amplitude, as shown in Figure 37 C. Furthermore, I_{rel}, which was almost zero under I_{NaCa} block, showed physiological traces for p_{NaK} upregulation. In biventricular simulations, I confirmed the absence of ectopic activity at D14 for both p_{NaK} downregulation as well as p_{NaK} and G_{K1} enhancement plus I_f inhibition.

8.3.3 Ionic targes to suppress spontaneous beats, modulate pro-arrhythmic action potential duration, and maintain physiological Ca^{2+} transients

Whilst combining I_f block with G_{K1} and p_{NaK} enhancement successfully eliminated automaticity-induced arrhythmias, it also caused a substantially prolonged APD, as

shown in Figure 37 C (purple traces). If introduced into the adult ventricular tissue, increased hPSC-CM APD would not only result in an exacerbation of repolarisation gradients and, therefore, arrhythmogenic risk, but also cause dyssynchronous CaTs, which may hinder uniform contraction. Therefore, shorter hPSC-CM APDs more like in the human adult ventricular cardiomyocytes would be beneficial from a safety as well as efficacy standpoint.

Again, I consulted the sensitivity analysis summarised in Figure 35 to identify additional ionic targets that can shorten the APD. The most promising targets for this were I_{CaL}, I_{Kr}, and I_{K1}. Whilst, as outward currents, increased I_{Kr} and I_{K1} both cause an APD shortening, I_{CaL} shows an inverse relationship with APD: a 25% block reduced the paced cellular D0 model's APD_{90} by approximately 90 ms because of a shortened plateau phase. However, as my aim in this study was to maximise CaTs, I discarded I_{CaL} block. I_{K1} was already increased in the suggested ionic strategy, leaving I_{Kr} as a target to reduce APD. Furthermore, I_{Kr} has been highlighted promising to modulate hPSC-CM AP morphology towards an adult phenotype also in previous studies (Fassina et al., 2023; Riebel et al., 2021). In the paced cellular D0 model, doubling G_{Kr} resulted in a 115 ms shorter APD_{90}.

Next, I constructed a population of models with upregulated p_{NaK}, G_{K1}, and G_{Kr} as well as fully blocked I_f, as described in Section 8.2.2, and using a target APD_{90} of 330 ms. Using the resulting APD_{90} and CaT amplitudes, I calculated the Safety-Efficacy scores for D0 and D14 hPSC-CMs. As injected cells mature over time, D0 and D14 safety and efficacy should be considered together. Hence, I normalised the D0 and D14 Safety-Efficacy scores by the respective maximum Safety-Efficacy score and averaged it to create a combined D0 and D14 Safety-Efficacy score, shown in Figure 38.

	PNaK	1.5	1.75	2	2.25	2.5	2.75	3
GK1	GKr							
1	1		0.35	0.32	0.30	0.29	0.28	0.27
	1.5		0.57	0.54	0.53	0.51	0.50	0.50
	2		0.73	0.71	0.69	0.68	0.68	0.67
	2.5		0.86	0.84	0.83	0.81	0.81	0.80
	3		0.87	0.86	0.85	0.84	0.84	0.83
	3.5		0.85	0.84	0.84	0.83	0.82	0.82
	4		0.80	0.79	0.78	0.78	0.77	0.77
	4.5	0.77	0.75	0.74	0.73	0.73	0.72	0.72
	5	0.72	0.71	0.70	0.69	0.69	0.68	0.68
1.25	1	0.42	0.37	0.33	0.31	0.30	0.28	0.28
	1.5	0.62	0.58	0.55	0.53	0.52	0.51	0.50
	2		0.73	0.71	0.69	0.68	0.67	0.66
	2.5		0.86	0.83	0.82	0.81	0.80	0.80
	3		0.87	0.86	0.85	0.84	0.84	0.83
	3.5		0.86	0.84	0.83	0.83	0.83	0.82
	4		0.80	0.79	0.78	0.78	0.77	0.77
	4.5		0.75	0.74	0.74	0.73	0.73	0.73
	5		0.71	0.70	0.70	0.69	0.69	0.69
1.5	1	0.44	0.38	0.35	0.33	0.31	0.30	0.29
	1.5	0.64	0.59	0.55	0.53	0.52	0.51	0.50
	2	0.78	0.74	0.71	0.69	0.68	0.67	0.66
	2.5		0.86	0.84	0.82	0.81	0.80	0.79
	3		0.87	0.86	0.85	0.84	0.84	0.83
	3.5		0.86	0.84	0.84	0.83	0.83	0.82
	4			0.79	0.78	0.78	0.78	0.77
	4.5			0.75	0.74	0.73	0.73	0.73
	5			0.70	0.70	0.69	0.69	0.69
1.75	1	0.46	0.40	0.36	0.34	0.32	0.31	0.30
	1.5	0.65	0.59	0.56	0.54	0.53	0.51	0.51
	2	0.80	0.75	0.72	0.70	0.68	0.67	0.67
	2.5		0.86	0.84	0.82	0.81	0.80	0.79
	3			0.86	0.85	0.84	0.84	0.84
	3.5			0.84	0.84	0.83	0.83	0.83
	4				0.79	0.78	0.78	0.77
	4.5				0.74	0.74	0.73	0.73
	5				0.70	0.70	0.69	0.69
2	1	0.48	0.41	0.38	0.35	0.33	0.32	0.31
	1.5	0.66	0.61	0.57	0.55	0.53	0.52	0.51
	2		0.75	0.72	0.70	0.68	0.68	0.67
	2.5			0.84	0.82	0.81	0.80	0.79
	3				0.85	0.84	0.84	0.84
	3.5					0.83	0.83	0.83
	4					0.78	0.78	0.77
	4.5						0.73	0.73
	5							0.69
2.25	1	0.49	0.43	0.38	0.36	0.34	0.33	0.32
	1.5			0.58	0.56	0.54	0.53	0.52
	2					0.69	0.68	0.67
	2.5							
	3							
	3.5							
	4							
	4.5							
	5							
2.5	1							0.33
	1.5							
	2							
	2.5							
	3							
	3.5							
	4							
	4.5							
	5							

Figure 38. Safety-Efficacy score of hPSC-CMs with full I_f-block as well as G_{K1}, G_{Kr}, and p_{NaK} upregulation. A target APD_{90} of 330 ms was used to compute the safety component. Dark purple shading indicates a higher Safety-Efficacy score.

From the combined Safety-Efficacy score, I chose the ionic current combination with the highest Safety-Efficacy score. As shown in Figure 38, for a target APD_{90} of 330 ms, this resulted in the following model: I_f block plus 200%, 50%, and 75% upregulation (i.e. scaling factors of 3, 1.5, and 1.75) of G_{Kr}, G_{K1}, and p_{NaK}. To highlight, the combined Safety-Efficacy score aimed to optimise both, D0 and D14 hPSC-CMs at the same time. Hence,

although a target APD_{90} of 330 ms was set, due to the much longer APD at D14, the APD_{90} in D0 hPSC-CMs was 'only' 284 ms. I proceeded simulating cell injection of the optimised D0 hPSC-CMs in the biventricular model to investigate arrhythmic burden. As shown in Figure 39, the arrhythmic risk decreased only slightly, if at all (S1-S2 intervals beyond 550 ms were not investigated here).

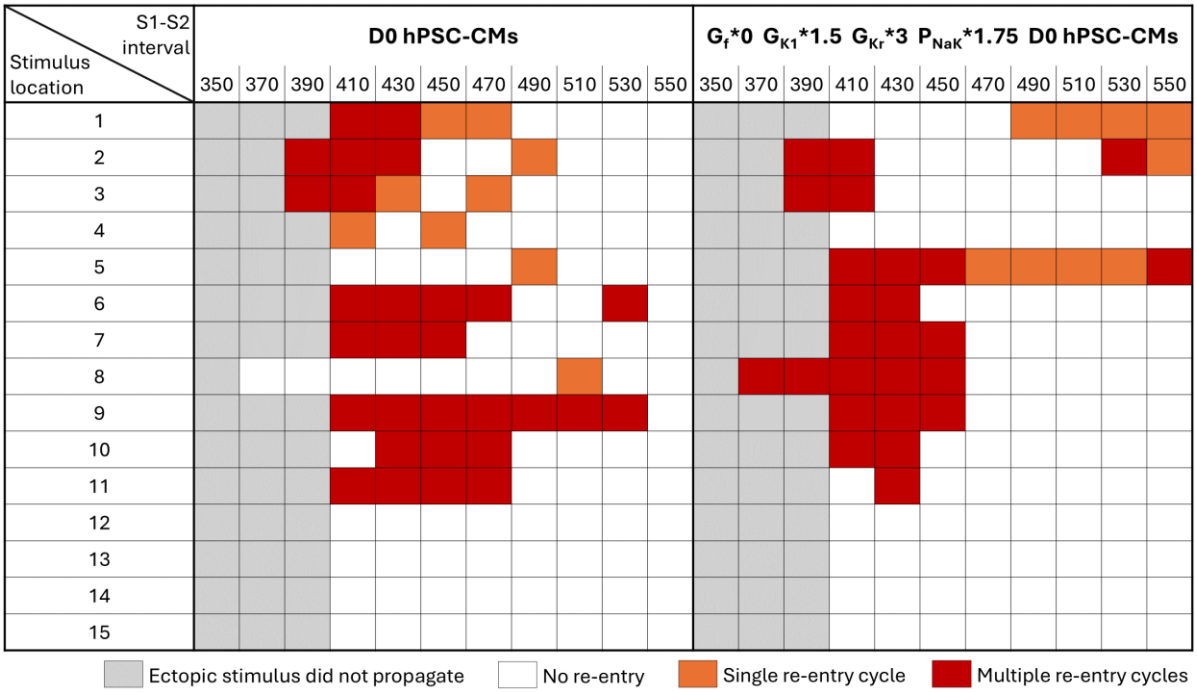


Figure 39. VWs for D0 (left) and modified (right) hPSC-CMs (APD_{90} of 284 ms) virtually injected into the human-based ventricles with a large chronic scar.

Upon closer investigation of simulation outputs, it was apparent that due to the slow conduction in the scar and hPSC-CMs, an hPSC-CM APD_{90} similar to that of adult human ventricular cardiomyocytes was not sufficient to enable homogeneous ventricular activation. Hence, these results suggested the need for a further shortening of the hPSC-CM APD beyond that of the adult ventricular cardiomyocytes. However, the APD should not become too short as it should still enable viable and synchronised CaTs. Therefore, I calculated the Safety-Efficacy score using a target hPSC-CM APD_{90} of 150 ms (~1/3 of the paced Paci2020 APD_{90}) next; the new combined D0 and D14 Safety-Efficacy scores are shown in Figure 40.

GK1	PNaK / GKr	1.5	1.75	2	2.25	2.5	2.75	3
1	1		0.28	0.25	0.23	0.22	0.21	0.20
	1.5		0.31	0.28	0.26	0.25	0.24	0.23
	2		0.33	0.30	0.29	0.28	0.27	0.26
	2.5		0.35	0.33	0.32	0.30	0.30	0.29
	3		0.41	0.38	0.37	0.35	0.34	0.34
	3.5		0.51	0.48	0.47	0.46	0.44	0.44
	4		0.64	0.61	0.60	0.59	0.58	0.57
	4.5	0.82	0.78	0.76	0.74	0.74	0.73	0.72
	5	0.94	0.90	0.88	0.87	0.86	0.85	0.85
1.25	1	0.33	0.28	0.25	0.23	0.21	0.20	0.20
	1.5	0.35	0.30	0.28	0.26	0.25	0.24	0.23
	2		0.33	0.30	0.29	0.27	0.27	0.26
	2.5		0.35	0.32	0.31	0.30	0.29	0.29
	3		0.40	0.37	0.35	0.34	0.33	0.32
	3.5		0.50	0.47	0.45	0.44	0.43	0.43
	4		0.63	0.60	0.58	0.57	0.56	0.56
	4.5		0.77	0.75	0.73	0.72	0.71	0.70
	5		0.89	0.87	0.85	0.85	0.83	0.83
1.5	1	0.33	0.28	0.25	0.23	0.21	0.20	0.19
	1.5	0.35	0.31	0.28	0.26	0.24	0.23	0.23
	2	0.37	0.33	0.30	0.29	0.27	0.26	0.26
	2.5		0.35	0.32	0.31	0.30	0.29	0.28
	3		0.40	0.37	0.35	0.33	0.33	0.31
	3.5		0.50	0.47	0.45	0.44	0.42	0.42
	4			0.60	0.58	0.56	0.55	0.54
	4.5			0.74	0.72	0.71	0.70	0.69
	5			0.86	0.84	0.83	0.83	0.82
1.75	1	0.34	0.28	0.25	0.23	0.21	0.20	0.19
	1.5	0.36	0.31	0.28	0.26	0.25	0.23	0.23
	2	0.38	0.33	0.30	0.29	0.27	0.26	0.26
	2.5		0.35	0.32	0.31	0.30	0.29	0.28
	3			0.37	0.35	0.33	0.32	0.31
	3.5			0.47	0.45	0.43	0.42	0.41
	4				0.57	0.56	0.55	0.54
	4.5				0.72	0.70	0.69	0.69
	5				0.84	0.83	0.82	0.82
2	1	0.34	0.29	0.25	0.23	0.21	0.20	0.19
	1.5	0.36	0.31	0.28	0.26	0.25	0.23	0.23
	2		0.33	0.31	0.29	0.27	0.26	0.26
	2.5			0.33	0.31	0.30	0.29	0.28
	3				0.35	0.33	0.32	0.31
	3.5					0.43	0.42	0.41
	4					0.56	0.54	0.53
	4.5						0.69	0.68
	5							0.81
2.25	1	0.35	0.29	0.25	0.23	0.22	0.20	0.20
	1.5			0.28	0.26	0.25	0.23	0.23
	2					0.27	0.26	0.26
	2.5							
	3							
	3.5							
	4							
	4.5							
	5							
2.5	1							0.20
	1.5							
	2							
	2.5							
	3							
	3.5							
	4							
	4.5							
	5							

Figure 40. Safety-Efficacy score of hPSC-CMs with full I_f-block as well as G_{K1}, G_{Kr}, and p_{NaK} upregulation. A target APD_{90} of 150 ms was used to compute the safety component. Dark purple shading indicates a higher Safety-Efficacy score.

Here, I found the highest Safety-Efficacy score for 400% and 50% G_{Kr} and p_{NaK} upregulation, respectively, without the need to target G_{K1}. However, this model showed small AP to AP variations ($V_{m,peak}$ differences of ~5 mV). Furthermore, different cell types may require more drastic ionic targets. Hence, to demonstrate anti-arrhythmic benefits of a combination targeting all three currents, I chose to further investigate the third best

model resulting in 400%, 25%, and 75% upscaling (i.e. scaling factors of 5, 1.25, and 1.75) of G_{Kr}, G_{K1}, and p_{NaK}, respectively. I then simulated injection of this version of optimised D0 hPSC-CMs (which had an APD_{90} of 169 ms) in the chronically infarcted ventricles to investigate arrhythmic risk. As depicted in Figure 41, the VW decreased from 760 to 340 ms using the D0 and new optimised D0 models, respectively. Whilst the arrhythmic burden was reduced compared to injecting the untreated D0 hPSC-CMs, it was still higher than the infarcted control scenario before hPSC-CM delivery (VW of 60 ms).

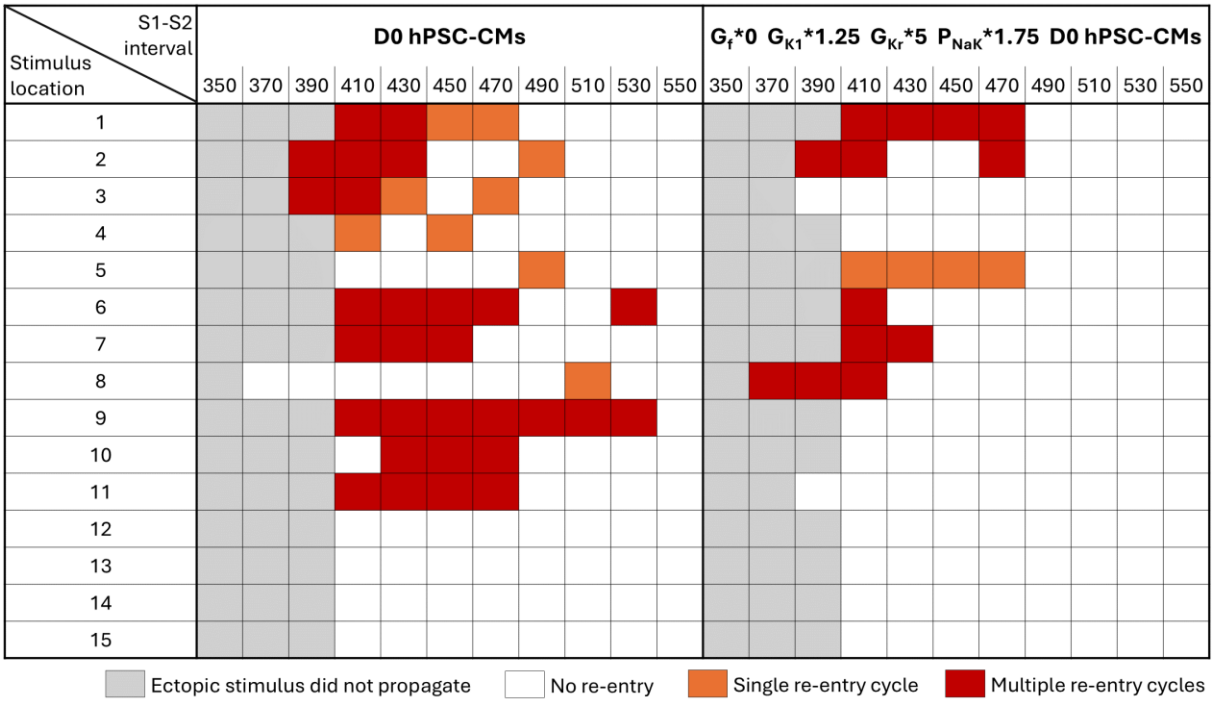


Figure 41. VWs for D0 (left) and optimised (right) hPSC-CMs (APD of 169 ms) virtually injected into the human-based ventricles with a large chronic scar.

In summary, my simulations suggest that, whilst spontaneous activity may be inhibited, completely abolishing re-entrant risk may be difficult to achieve. However, the optimised hPSC-CM model I propose, with an APD_{90} of 169 ms and with full I_f block as well as 400%, 25%, and 75% upregulation of G_{Kr}, G_{K1}, and p_{NaK}, may still half arrhythmic burden.

8.4 Discussion

In this chapter, I applied multiscale human ventricular electrophysiological modelling and simulation to mitigate safety concerns after regenerative cell therapy in the infarcted ventricles. Specifically, I showed that combining full I_f block with G_{K1}, G_{Kr}, and p_{NaK} upregulation can suppress spontaneous beating and lower re-entry susceptibility of injected cells. Importantly, in my simulations, I aimed to balance therapy safety with efficacy to ensure optimised *in silico* hPSC-CMs produced physiological CaTs.

Firstly, I showed that whilst injected cells do not produce arrhythmias at day zero after delivery, a fast-beating phenotype may facilitate rapid VT episodes (with rates of up to 140 bpm) two weeks after injection. Fast VT episodes after cell injection are frequently observed experimentally (Chong et al., 2014; Marchiano et al., 2023) but have been challenging to reproduce in modelling and simulation studies, which have reached spontaneous beating rates of around 115 bpm (Gibbs et al., 2023). The faster VT rate in my simulations was enabled by creating rapid beating injected cells (by upregulating I_{up}, I_f, and I_{NaCa}) and day 14 injected cells by incorporating recent experimental gene expression data of *in vivo* cell maturation by Marchiano et al. (2023). However, it should be noted, that gene expression may not directly translate to ionic current expression and may also be different for each ionic current. Furthermore, as specific electrophysiology and maturation of injected cells will depend on the cell line and differentiation protocol, variability between cells, whether *in silico* or experimental, are to be expected. I established credibility of inferring ionic scaling factors from the experimental gene expression data (Marchiano et al., 2023) to create the D14 phenotype by simulations reproducing experimentally observed surge in arrhythmias approximately two weeks

after injection (Chong et al., 2014; Romagnuolo et al., 2019; Selvakumar et al., 2024). Future studies may also investigate the arrhythmic burden beyond day 14, for which some gene expression data is available also in Marchiano et al. (2023).

Next, my simulations suggest that whilst spontaneous beating of injected cells can be inhibited, eliminating re-entrant burden may not be straightforward. As I identified in Chapter 7, whilst APD is the main contributing factor to re-entrant burden, hPSC-CM CV is a further denominator, which improves propagation in the post-MI scar but also enables pathways for the re-entrant wavefront to travel through the scar. Hence, reducing the injected cells' APD may need to be combined with increasing their conductivity. The role of electrophysiological as well as connective maturity in mitigating safety concerns has been highlighted also in other *in silico* studies (Fassina et al., 2023; Rosales et al., 2024; J. K. Yu, Liang, Franceschi, et al., 2022). Fassina et al. showed that I_{NaF} and I_{Kr} are promising targets to modulate the activation and repolarisation of delivered cells towards an adult phenotype, thereby reducing heterogeneous arrhythmogenic substrate (Fassina et al., 2022, 2023). Overexpression of I_{K1} has also been investigated in previous studies to stabilise the membrane potential of hPSC-CMs and make them more adult ventricular-like (Dark et al., 2023; Goversen et al., 2018; Verkerk & Wilders, 2023). Similarly, the role of I_f in the cells' spontaneous beating is a well-known fact, and it has further been established previously that inhibition of I_f alone is insufficient to suppress spontaneous hPSC-CM activity, due to an intrinsic calcium clock acting as a second depolarising mechanism, as discussed by Paci et al. (2020). The contribution of I_{NaCa} in the latter has also been discussed in the community (Kim et al., 2015). It should be noted that in the *in silico* D0 hPSC-CM model I used here, spontaneous beating is suppressed when individually knocking out I_f, upregulating G_{K1}, and up- or downregulating p_{NaK} sufficiently.

However, in most cases, the resulting cells did not produce physiological paced APs. Also, apart from G_{K1}, these ionic targets did not work on their own in the D14 (rather than D0) phenotype, warranting a combination of ionic targets. Whilst the hPSC-CM model I used here is quite sensitive to I_{K1}, it has been suggested in the literature that I_{K1} enhancement may be insufficient to suppress spontaneous activity in other phenotypes (Marchiano et al., 2023). Hence, whilst targeting the suggested ionic currents individually may suffice for some hPSC-CMs, my presented approach brought forward a robust combination of ionic targets that increases applicability to a range of cell types. Future studies could further investigate how AP variability amongst patients may modulate the arrhythmic risk, i.e. patients with a longer APD may not require the hPSC-CM AP to be shortened as much.

I further compared the ionic target combination I proposed here to state-of-the-art gene editing, recently developed to suppress spontaneous beating-induced arrhythmias after cell delivery by Marchiano et al. (2023). As mentioned above, this state-of-the-art method involves knocking out the genes encoding I_f, I_{CaT}, and I_{NaCa} as well as upregulating I_{K1} (Marchiano et al., 2023). As the hPSC-CM model I used here does not include I_{CaT}, I modelled the state-of-the-art approach by Marchiano et al. (2023) without I_{CaT} knock-out. However, I_{CaT}, whilst crucial in Purkinje and atrial cells (Shah et al., 2022), is not commonly expressed in adult ventricular cardiomyocytes and hence may also not be present in some experimentally cultured ventricular-like hPSC-CMs. Supporting this, I_f and I_{NaCa} block paired with I_{K1} upregulation was sufficient here to suppress spontaneous hPSC-CM beats.

Whilst my simulations showed a decrease of the CaT amplitude, it should be noted that I_{NaCa} downregulation, as suggested in the state-of-the-art gene editing approach by

Marchiano et al. (2023), is generally associated with an improved contractile strength because I_{NaCa} is a main cause for extraction of intracellular Ca^{2+} during rest (Ottolia et al., 2013). By reducing Ca^{2+} extrusion from the cell through I_{NaCa}, more Ca^{2+} is available to be pumped into the SR through I_{up} and to then be released during Ca^{2+}-induced Ca^{2+}-release as discussed by Ottolia et al. (2013). I_{NaCa} inhibitors have been explored particularly for heart failure patients, where I_{NaCa} may be increased (Hegyi et al., 2018) and I_{up} may be impaired (Høydal et al., 2018; M. T. Jiang et al., 2002). A recent study has shown a positive effect of I_{NaCa} downregulation also in hPSC-CMs – experimentally as well as *in silico* – although it should be noted that an adult ventricular-like computational cell model was used with some currents adapted to make it hPSC-CM-like (Ismaili et al., 2022). Whilst some I_{NaCa} block may be improving contraction, downregulation may also cause accumulation of diastolic intracellular Ca^{2+} which hinders cardiomyocyte relaxation. Additionally, it has been shown that I_{NaCa} inhibition reduces I_{CaL} (Henderson et al., 2004). Indeed, studies have shown that large scale I_{NaCa} knock-out results in reduced contractility, which may be attributed to an impaired excitation-contraction coupling (Henderson et al., 2004; Koushik et al., 2001; Reuter et al., 2003). Furthermore, hPSC-CMs may depend more critically on I_{NaCa} than adult ventricular cardiomyocytes, as highlighted by Koivumäki et al. (2018). Finally, I_{up} in hPSC-CMs is low, therefore reducing the availability of alternative Ca^{2+} extrusion mechanisms and overall loading of the SR Ca^{2+} deposit (Lee et al., 2011). Ca^{2+} overload for strong I_{NaCa} block was also observed in another *in silico* hPSC-CM model (Koivumäki et al., 2018, Figure 3 and caption).

I_{NaCa} has been reported to be closely linked to I_{NaK}; specifically, I_{NaK} maintains the Na^+ gradients that are crucial for I_{NaCa} to function (Shattock et al., 2015). Therefore, modulating I_{NaK} will also affect I_{NaCa} and the underlying mechanisms to making hPSC-CMs

quiescent may be linked. However, upregulating p_{NaK} by 50% may disturb hPSC-CM electrophysiology less than a full I_{NaCa} knock-out, as I highlighted throughout this chapter. Interestingly, amiodarone, which impacts I_{NaCa} as well as I_{NaK} (Gray et al., 1998; Watanabe & Kimura, 2000), has been shown to reduce pro-arrhythmia of regenerative cell delivery in pre-clinical studies (Nakamura et al., 2021). While I_{NaK} block has been linked to repolarisation abnormalities in adult human ventricular cardiomyocytes (Britton et al., 2017), less is known about I_{NaK} upregulation.

Finally, to enable my biophysically detailed investigations of arrhythmic risk in the infarcted human ventricles, I used fast and efficient electrophysiological modelling and simulation software. As mentioned, this did not allow me to directly measure mechanical function through EF or wall motion. Instead, I employed CaT amplitude as a surrogate to infer contractile strength. However, other Ca^{2+} dynamics may also inform mechanical efficacy, such as CaT duration or time to peak. Furthermore, uniform activation of the ventricles is another crucial biomarker, as prolonged or incomplete activation would imply dyssynchronous sarcomere contraction and relaxation and, therefore, inefficient pumping function.

8.5 Conclusions

The development of new therapies is time-consuming, and many are disregarded along the costly development process; in this chapter, I demonstrated how computational tools can be used to identify and mitigate arrhythmic concerns of new treatments to improve their safety and efficacy. Specifically, I derived a combination of ionic targets to suppress spontaneous beating and to reduce re-entrant susceptibility of cells injected into the chronically infarcted human ventricles. My simulations were able to reproduce the pre-

clinically observed surge in rapid VT arrhythmias approximately two weeks after cell delivery and with a rate of up to 140 bpm. In this work, I conclude that blocking I_f as well as upregulating G_{Kr}, G_{K1}, and p_{NaK} can inhibit automaticity of injected cells and cut arrhythmic burden post cell therapy in half.

9

Conclusions

The main contribution of my thesis project is the design, execution, and analysis of sophisticated multiscale human ventricular electrophysiological modelling and simulation studies to investigate arrhythmia mechanisms and treatments in ischemic heart disease. Throughout my thesis, I employed state-of-the-art modelling and simulation tools, established credibility of the framework through comparison with experimental and clinical data and designed and conducted simulation studies of arrhythmic risk.

First, in Chapter 6, I conducted multiscale human ventricular electrophysiological simulation studies to investigate arrhythmia mechanisms and risk markers in small, paediatric-like ventricles after ischemia. My simulations showed that ventricular size reproduces some clinically observed features of paediatric hearts, such as shorter QRS complexes and QT intervals, but is not sufficient to address others, such as dominant R-waves in leads V1-V2. Furthermore, my results determined that the underlying AP phenotype, particularly its restitution curve, is crucial in determining arrhythmia susceptibility and facilitating VF-like arrhythmia morphologies following I_{KATP} activation. Increased fraction of open I_{KATP} channels and, to a lesser extent, large ischemic areas further increased re-entry susceptibility.

In Chapter 7 and 8, I designed and conducted simulation studies to establish a range of pro-arrhythmic mechanisms following regenerative cell therapy in the infarcted human

ventricles. My simulations first demonstrated that re-entry risk increased after cell therapy in all three investigated scar sizes. Scar geometry, particularly with respect to the distribution of PMJs within the infarct core, was more determinant of arrhythmia susceptibility than scar size. However, increasing infarct size did increase re-entry sustainability. Next, my results showed how scar size, infarct stage, and delivered hPSC-CM population heterogeneity impact the risk of hPSC-CM-induced spontaneous beats. hPSC-CM automaticity occurred for heterogeneous populations only and was encouraged by depolarised infarcts, especially during chronic MI. In-depth analysis of simulation outputs identified that these spontaneous beats created a heterogeneous repolarisation and re-entry substrate across the ventricles, which enabled re-entrant arrhythmias under bradycardic sinus heart rates. The susceptibility of arrhythmias was increased in acute MI, large scars, and impaired Purkinje-myocyte coupling.

Finally, building on the arrhythmia mechanisms I identified in Chapter 7, in Chapter 8, I conducted multiscale human ventricular electrophysiological simulation studies to design anti-arrhythmic strategies that improve the safety of cell therapy in the infarcted human ventricles. Specifically, I established credibility of multiscale human ventricular electrophysiological modelling and simulation of ischemic heart disease to address the question at hand by reproducing experimentally observed surges in rapid VT arrhythmias, induced by the delivered cells' automaticity at approximately two weeks post injection. I further identified I_{NaK} as a novel target to suppress spontaneous hPSC-CM beats and showed that I_f block paired with p_{NaK}, G_{K1}, and G_{Kr} upregulation could further decrease re-entry susceptibility whilst allowing for a physiological CaT of injected cells.

9.1 Limitations and future directions

Even though the complex transmural scar geometries I chose for this work present a more realistic representation than uniform dense scars, commonly used in computational studies, they are not personalised. I imposed these scars in a healthy patient geometry, which hence lacks other structural post-MI remodelling such as hypertrophy. This further presents uncertainty with regards to the patient's artery distribution, which may cause post-LAD occlusion infarcts to be in different locations and with a different degree of septal or apical involvement across patients. Furthermore, whilst the complex scar representations I used enabled simulating physiological post-MI arrhythmias, they make straightforward comparison of scar size more difficult, e.g. two scars with the same volume may contain different numbers of isthmuses. Particularly, I identified PMJ distribution within the infarct as crucial in Chapter 7, highlighting the uncertainty of scar size, complexity, and location.

Not only scar geometry and ventricular size are variable amongst patients; wide physiological ranges of ECG and AP morphologies have been reported clinically and experimentally. These include AP and QT duration, but also CV, ionic current density, and drug response. To develop true digital twins, these variabilities need to be taken into consideration. While not addressing all these personalisation issues, my work takes a step forward by using a state-of-the-art pipeline that infers the conduction speeds and Purkinje network from the patient's ECG (Camps et al., 2024). Furthermore, simulating large cohorts, which may not be personalised but can capture the variability within our population, may be more impactful.

Most of the above limitations can be addressed by creating a much larger cohort of post-MI models to investigate disease mechanisms and treatments. Ideally, these would be derived straight from post-MI patient data. Although such data is still limited, resources like the UK biobank have substantially increased their availability (Sudlow et al., 2015). Whilst providing MRI and ECG data, information on the patients' AP characteristics is predominantly unavailable, as it would require extracting and analysing tissue samples. However, a recent computational study has developed a pipeline to infer detailed repolarisation gradients from the patient's ECG and allows for reproducing these in simulations by scaling the APD of different ventricular regions (Camps et al., 2025).

Further investigations should also include variability in the Purkinje network; as I describe throughout this thesis, position and distribution of the PMJs may be crucial in the initiation and sustainability of arrhythmias. Future studies may create a cohort of Purkinje networks for the same biventricular anatomy to further determine the effect of geometric Purkinje variability on arrhythmic burden; i.e. does only the path of re-entrant wavefronts change or is the overall VW impacted? Similarly, variability in heartrate should also be considered in future studies. In my investigations, I used relatively slow sinus rates of 60-75 bpm; however, MI may impact the autonomous nervous system and neurotransmission and ultimately may lead to increased arrhythmic burden and mortality (Herring et al., 2019; Vaseghi & Shivkumar, 2008).

While the electrophysiological and geometric models of ischemic heart disease and progression I investigated here matched clinical ECG records, they did not reproduce all expected or typical features of ischemia and infarction. Particularly, during ischemia, ST-segment elevation is one of the most prominent features in the ECG and has been

attributed to I_{KATP} activation (R. A. Li et al., 2000; Moréna et al., 1980). The lack of ST-segment elevation in ischemia in my simulations may be due to the lack of hyperkalaemia, which commonly occurs together with I_{KATP} activation and may be crucial in depolarising the MDP and further shortening the APD. I did however observe an increased T-wave amplitude and wider, symmetrical T-wave shape, which has been reported clinically as an ischemic feature that may precede ST-elevation (Thygesen et al., 2019). Similarly, I did not observe ST-elevation in acute infarction and again, whilst here I included hyperkalaemia (but not hypoxia), a combination of elevated K^+ concentration, I_{KATP}-activation, and even acidosis may be necessary. Conversely, I observed persistent ST-elevation in chronic MI, which was also present in the clinical chronic MI ECG I consulted. However, ST-elevation persisting into the chronic stages of MI is not commonly observed clinically and may be associated with LV aneurysms, although a link to, specifically, anterior MI (as modelled here) and extensive myocardial damage has also been suggested (Galiuto et al., 2007). A more typical post-MI feature are pathological Q-waves (Thygesen et al., 2019), which did not manifest in my simulations. One explanation for this may be the low CV (7-9 cm/s) I used for the chronic scars here. Clinical studies have observed CVs to be about two to three times lower in the infarct than the surrounding tissue (Aronis et al., 2020; Jamil-Copley et al., 2015). I used this data to calibrate the conductivities in healing MI and then maintained them across to chronic MI. However, due to the lack of electrical excitability, the same conductivities caused a much slower CV in chronic than in healing infarction. Hence, future work may investigate the effects of higher CV within the scar of approximately 20 cm/s; this may increase activation of the scar and eliminate the observed persistent ST-elevation.

The study I presented in Chapter 6 makes an important step towards extending modelling and simulation of the heart for paediatric patients. However, as discussed, this work needs further improvements to incorporate electrophysiological as well as anatomical differences as the ventricles develop. Future studies may use digital twinning pipelines to derive age-specific cardiac geometries straight from paediatric MRI. Such work may, however, be hindered by the availability of validation data in diseased and especially healthy children.

Regarding Chapter 7 and 8, substantial variability amongst hPSC-CMs has been reported experimentally; APD for instance has been reported to vary drastically between but even within hPSC-CM cultures and has been reported as both, shorter as well as longer than adult human ventricular cardiomyocyte APs (Doss et al., 2012; He et al., 2003; Ma et al., 2011). Whilst I constructed computational atrial-like, nodal-like, day 14, and rapid beating injected cells next to the baseline ventricular-like cells to include some AP variability, this does not cover the whole range of reported differences. Hence, depending on the utilised cell type, arrhythmia mechanisms – whether automaticity or re-entry-induced – may vary. Future studies may investigate this variability further by creating more populations of injected cells. Further work may also include the effect of immunosuppressants, which may be required after cell injection (Fang et al., 2020), on the risk of spontaneous beating and re-entrant arrhythmias.

A further limitation, which effects all three presented studies is the manual selection of ectopic stimulus locations. Whilst this might be similar to clinical selection of pacing points close to the scar, it introduces variability and some bias. Selecting ectopic stimulus locations in a large dense scar may be easily done through a deterministic

algorithm but is less straight forward in the complex and variable scars I used here. Future work should investigate solutions to this problem and might consult universal ventricular coordinates (J. Bayer et al., 2018) or the Virtual-heart Arrhythmia Risk Predictor (VARP) protocol (Arevalo et al., 2016).

Finally, whilst utilising state-of-the-art GPU technology (Sachetto Oliveira et al., 2018) enabled fast and efficient simulations, further opportunities for computational speed-up should be considered. Particularly, while I automated the creation of configuration files and job submission scripts, I manually analysed simulation outputs, which was time-consuming. Future efforts could be spent on utilising automated rotor analysis tools (Van Nieuwenhuyse et al., 2022) and ECG delineation software (Lyon et al., 2018).

Overall, the design, execution, and analysis of the sophisticated simulations I presented here demonstrate how multiscale human ventricular electrophysiological modelling and simulation can be used to conduct mechanistic studies of arrhythmias in ischemic heart disease to augment risk stratification as well as identify, test, and optimise new therapies.

REFERENCES

Aggarwal, R., & Boyden, P. A. (1995). Diminished Ca^{2+} and Ba^{2+} Currents in Myocytes Surviving in the Epicardial Border Zone of the 5-Day Infarcted Canine Heart. *Circulation Research*, *77*(6), 1180–1191. https://doi.org/10.1161/01.RES.77.6.1180

Ahmed, M. A., Burnham, J., Dwivedi, G., & AbuAsal, B. (2023). Achieving big with small: quantitative clinical pharmacology tools for drug development in pediatric rare diseases. *Journal of Pharmacokinetics and Pharmacodynamics*, *50*, 429–444. https://doi.org/10.1007/s10928-023-09863-x

Alberts, B., Johnson, A., Lewis, J., Raff, M., Roberts, K., & Walter, P. (2008). *Molecular Biology of The Cell* (5th ed.). Garland Science, Taylor & Francis Group.

Alday, E. A. P., Ni, H., Zhang, C., Colman, M. A., Gan, Z., & Zhang, H. (2016). Comparison of Electric- and Magnetic-Cardiograms Produced by Myocardial Ischemia in Models of the Human Ventricle and Torso. *PLoS ONE*, *11*(8), e0160999. https://doi.org/10.1371/journal.pone.0160999

Álvarez-Barrientos, F., Salinas-Camus, M., Pezzuto, S., & Sahli Costabal, F. (2025). Probabilistic learning of the Purkinje network from the electrocardiogram. *Medical Image Analysis*, *101*, 103460. https://doi.org/10.1016/j.media.2025.103460

Amoni, M., Claus, P., Dries, E., Nagaraju, C., De Buck, S., Vandenberk, B., Ingelaere, S., Vermoortele, D., Roderick, H. L., Sipido, K. R., & Willems, R. (2021). Discrete sites of frequent premature ventricular complexes cluster within the infarct border zone and coincide with high frequency of delayed afterdepolarizations under adrenergic stimulation. *Heart Rhythm*, *18*(11), 1976–1987. https://doi.org/10.1016/j.hrthm.2021.07.067

Antia, A. U., Maxwell, S. R., Gough, A., & Ayeni, O. (1978). Position of the apex beat in childhood. *Archives of Disease in Childhood*, *53*(7), 585–589. https://doi.org/10.1136/adc.53.7.585

Antman, E., Bassand, J.-P., Klein, W., Ohman, M., Lopez Sendon, J. L., Rydén, L., Simoons, M., & Tendera, M. (2000). Myocardial infarction redefined—a consensus document of The Joint European Society of Cardiology/American College of Cardiology committee for the redefinition of myocardial infarction. *Journal of the American College of Cardiology*, *36*(3), 959–969. https://doi.org/10.1016/S0735-1097(00)00804-4

Aras, K. K., Faye, N. R., Cathey, B., & Efimov, I. R. (2018). Critical Volume of Human Myocardium Necessary to Maintain Ventricular Fibrillation. *Circulation: Arrhythmia and Electrophysiology*, *11*(11). https://doi.org/10.1161/CIRCEP.118.006692

Arevalo, H. J., Vadakkumpadan, F., Guallar, E., Jebb, A., Malamas, P., Wu, K. C., & Trayanova, N. A. (2016). Arrhythmia risk stratification of patients after myocardial infarction using personalized heart models. *Nature Communications*, *7*, 11437. https://doi.org/10.1038/ncomms11437

Aronis, K. N., Ali, R. L., Prakosa, A., Ashikaga, H., Berger, R. D., Hakim, J. B., Liang, J., Tandri, H., Teng, F., Chrispin, J., & Trayanova, N. A. (2020). Accurate Conduction Velocity Maps and Their Association With Scar Distribution on Magnetic Resonance Imaging in Patients With Postinfarction Ventricular Tachycardias. *Circulation: Arrhythmia and Electrophysiology*, *13*(4). https://doi.org/10.1161/CIRCEP.119.007792

Arteyeva, N. V. (2020). Dispersion of ventricular repolarization: Temporal and spatial. *World Journal of Cardiology*, *12*(9), 437–449. https://doi.org/10.4330/wjc.v12.i9.437

Aslanidi, O. V., Dewey, R. S., Morgan, A. R., Boyett, M. R., & Zhang, H. (2008). Regional differences in rabbit atrial action potential properties: Mechanisms, consequences and pharmacological implications. *2008 30th Annual International Conference of the IEEE Engineering in Medicine and Biology Society*, 141–144. https://doi.org/10.1109/IEMBS.2008.4649110

Baker, P. F., Blaustein, M. P., Hodgkin, A. L., & Steinhardt, R. A. (1969). The influence of calcium on sodium efflux in squid axons. *The Journal of Physiology*, *200*(2), 431–458. https://doi.org/10.1113/jphysiol.1969.sp008702

Ban, K., Bae, S., & Yoon, Y. (2017). Current Strategies and Challenges for Purification of Cardiomyocytes Derived from Human Pluripotent Stem Cells. *Theranostics*, *7*(7), 2067–2077. https://doi.org/10.7150/thno.19427

Banerjee, A., Camps, J., Zacur, E., Andrews, C. M., Rudy, Y., Choudhury, R. P., Rodriguez, B., & Grau, V. (2021). A completely automated pipeline for 3D reconstruction of human heart from 2D cine magnetic resonance slices. *Philosophical Transactions of the Royal Society A: Mathematical, Physical and Engineering Sciences*, *379*(2212). https://doi.org/10.1098/rsta.2020.0257

Barbash, I. M., Chouraqui, P., Baron, J., Feinberg, M. S., Etzion, S., Tessone, A., Miller, L., Guetta, E., Zipori, D., Kedes, L. H., Kloner, R. A., & Leor, J. (2003). Systemic Delivery of Bone Marrow–Derived Mesenchymal Stem Cells to the Infarcted Myocardium. *Circulation*, *108*(7), 863–868. https://doi.org/10.1161/01.CIR.0000084828.50310.6A

Bardou, A. L., Auger, P. M., Achour, S., Dumee, P., Birkui, P. J., & Govaere, M.-C. (1995). Effect of myocardial infarction and ischemia on induction of cardiac reentries and ventricular fibrillation. *Acta Biotheoretica*, *43*, 363–372. https://doi.org/10.1007/BF00713559

Bartunek, J., Behfar, A., Dolatabadi, D., Vanderheyden, M., Ostojic, M., Dens, J., El Nakadi, B., Banovic, M., Beleslin, B., Vrolix, M., Legrand, V., Vrints, C., Vanoverschelde, J. L.,

Crespo-Diaz, R., Homsy, C., Tendera, M., Waldman, S., Wijns, W., & Terzic, A. (2013). Cardiopoietic Stem Cell Therapy in Heart Failure: The C-CURE (Cardiopoietic stem Cell therapy in heart failURE) Multicenter Randomized Trial With Lineage-Specified Biologics. *Journal of the American College of Cardiology*, *61*(23), 2329–2338. https://doi.org/10.1016/j.jacc.2013.02.071

Bartunek, J., Terzic, A., Davison, B. A., Behfar, A., Sanz-Ruiz, R., Wojakowski, W., Sherman, W., Heyndrickx, G. R., Metra, M., Filippatos, G. S., Waldman, S. A., Teerlink, J. R., Henry, T. D., Gersh, B. J., Hajjar, R., Tendera, M., Senger, S., Cotter, G., Povsic, T. J., … for the CHART Program. (2020). Cardiopoietic stem cell therapy in ischaemic heart failure: long-term clinical outcomes. *ESC Heart Failure*, *7*(6), 3345–3354. https://doi.org/10.1002/ehf2.13031

Bartunek, J., Terzic, A., Davison, B. A., Filippatos, G. S., Radovanovic, S., Beleslin, B., Merkely, B., Musialek, P., Wojakowski, W., Andreka, P., Horvath, I. G., Katz, A., Dolatabadi, D., El Nakadi, B., Arandjelovic, A., Edes, I., Seferovic, P. M., Obradovic, S., Vanderheyden, M., … for the CHART Program. (2017). Cardiopoietic cell therapy for advanced ischemic heart failure: results at 39 weeks of the prospective, randomized, double blind, sham-controlled CHART-1 clinical trial. *European Heart Journal*, *38*(9), 648–660. https://doi.org/10.1093/eurheartj/ehw543

Bayer, J. D., Blake, R. C., Plank, G., & Trayanova, N. A. (2012). A Novel Rule-Based Algorithm for Assigning Myocardial Fiber Orientation to Computational Heart Models. *Annals of Biomedical Engineering*, *40*, 2243–2254. https://doi.org/10.1007/s10439-012-0593-5

Bayer, J., Prassl, A. J., Pashaei, A., Gomez, J. F., Frontera, A., Neic, A., Plank, G., & Vigmond, E. J. (2018). Universal ventricular coordinates: A generic framework for describing position within the heart and transferring data. *Medical Image Analysis*, *45*, 83–93. https://doi.org/10.1016/j.media.2018.01.005

Bayes-Genis, A., Gastelurrutia, P., Monguió-Tortajada, M., Cámara, M. L., Prat-Vidal, C., Cediel, G., Rodríguez-Gómez, L., Teis, A., Revuelta-López, E., Ferrer-Curriu, G., Roura, S., Gálvez-Montón, C., Bisbal, F., Vives, J., Vilarrodona, A., Muñoz-Guijosa, C., & Querol, S. (2024). Implantation of a double allogeneic human engineered tissue graft on damaged heart: insights from the PERISCOPE phase I clinical trial. *EBioMedicine*, *102*, 105060. https://doi.org/10.1016/j.ebiom.2024.105060

Bellanti, F., & Della Pasqua, O. (2011). Modelling and simulation as research tools in paediatric drug development. *European Journal of Clinical Pharmacology*, *67*(Suppl 1), 75–86. https://doi.org/10.1007/s00228-010-0974-3

Berg, L. A., Rocha, B. M., Oliveira, R. S., Sebastian, R., Rodriguez, B., de Queiroz, R. A. B., Cherry, E. M., & Weber dos Santos, R. (2023). Enhanced optimization-based method

for the generation of patient-specific models of Purkinje networks. *Scientific Reports*, *13*, 11788. https://doi.org/10.1038/s41598-023-38653-1

Bergmann, O., Bhardwaj, R. D., Bernard, S., Zdunek, S., Barnabé-Heider, F., Walsh, S., Zupicich, J., Alkass, K., Buchholz, B. A., Druid, H., Jovinge, S., & Frisén, J. (2009). Evidence for Cardiomyocyte Renewal in Humans. *Science*, *324*(5923), 98–102. https://doi.org/10.1126/science.1164680

Bird, L. M., Billman, G. F., Lacro, R. V., Spicer, R. L., Jariwala, L. K., Hoyme, H. E., Zamora-Salinas, R., Morris, C., Viskochil, D., Frikke, M. J., & Jones, M. C. (1996). Sudden death in Williams syndrome: Report of ten cases. *The Journal of Pediatrics*, *129*(6), 926–931. https://doi.org/10.1016/S0022-3476(96)70042-2

Bishop, M. J., & Plank, G. (2011). Bidomain ECG Simulations Using an Augmented Monodomain Model for the Cardiac Source. *IEEE Transactions on Biomedical Engineering*, *58*(8), 2297–2307. https://doi.org/10.1109/TBME.2011.2148718

Boersma, E., Maas, A. C., Deckers, J. W., & Simoons, M. L. (1996). Early thrombolytic treatment in acute myocardial infarction: reappraisal of the golden hour. *The Lancet*, *348*(9030), 771–775. https://doi.org/10.1016/S0140-6736(96)02514-7

Bogdanov, K. Y., Vinogradova, T. M., & Lakatta, E. G. (2001). Sinoatrial Nodal Cell Ryanodine Receptor and Na^+ - Ca^{2+} Exchanger. *Circulation Research*, *88*(12), 1254–1258. https://doi.org/10.1161/hh1201.092095

Boukens, B. J., Sulkin, M. S., Gloschat, C. R., Ng, F. S., Vigmond, E. J., & Efimov, I. R. (2015). Transmural APD gradient synchronizes repolarization in the human left ventricular wall. *Cardiovascular Research*, *108*(1), 188–196. https://doi.org/10.1093/cvr/cvv202

Bousseljot, R., Kreiseler, D., & Schnabel, A. (1995). Nutzung der EKG-Signaldatenbank CARDIODAT der PTB über das Internet. *Biomedizinische Technik/Biomedical Engineering*, *40*, 317.

Bowler, L. A., Gavaghan, D. J., Mirams, G. R., & Whiteley, J. P. (2019). Representation of Multiple Cellular Phenotypes Within Tissue-Level Simulations of Cardiac Electrophysiology. *Bulletin of Mathematical Biology*, *81*, 7–38. https://doi.org/10.1007/s11538-018-0516-1

Boyden, P. A., & Pinto, J. M. (1994). Reduced calcium currents in subendocardial Purkinje myocytes that survive in the 24- and 48-hour infarcted heart. *Circulation*, *89*(6), 2747–2759. https://doi.org/10.1161/01.CIR.89.6.2747

Bradley, C. P., Clayton, R. H., Nash, M. P., Mourad, A., Hayward, M., Paterson, D. J., & Taggart, P. (2011). Human Ventricular Fibrillation During Global Ischemia and Reperfusion. *Circulation: Arrhythmia and Electrophysiology*, *4*(5), 684–691. https://doi.org/10.1161/CIRCEP.110.961284

Braunwald, E. (2018). Cell-Based Therapy in Cardiac Regeneration: An Overview. *Circulation Research*, *123*(2), 132–137. https://doi.org/10.1161/CIRCRESAHA.118.313484

Brennan, T., Fink, M., & Rodriguez, B. (2009). Multiscale modelling of drug-induced effects on cardiac electrophysiological activity. *European Journal of Pharmaceutical Sciences*, *36*(1), 62–77. https://doi.org/10.1016/j.ejps.2008.09.013

Brightman, M. W., & Reese, T. S. (1969). Junctions between intimately apposed cell membranes in the vertebrate brain. *The Journal of Cell Biology*, *40*(3), 648–677. https://doi.org/10.1083/jcb.40.3.648

Brinkman, A. M., Baker, P. B., Newman, W. P., Vigorito, R., & Friedman, M. H. (1994). Variability of human coronary artery geometry: An angiographic study of the left anterior descending arteries of 30 autopsy hearts. *Annals of Biomedical Engineering*, *22*, 34–44. https://doi.org/10.1007/BF02368220

British Heart Foundation. (2021). *Heart and Circulatory Disease Statistics 2021*. https://www.bhf.org.uk/what-we-do/our-research/heart-statistics/heart-statistics-publications/cardiovascular-disease-statistics-2021

British Heart Foundation. (2024a). *Heart and Circulatory Disease Statistics 2024*. https://www.bhf.org.uk/what-we-do/our-research/heart-statistics/heart-statistics-publications/cardiovascular-disease-statistics-2024

British Heart Foundation. (2024b). *UK Factsheet*. https://www.bhf.org.uk/-/media/files/for-professionals/research/heart-statistics/bhf-cvd-statistics-uk-factsheet.pdf

Britton, O. J., Bueno-Orovio, A., Van Ammel, K., Lu, H. R., Towart, R., Gallacher, D. J., & Rodriguez, B. (2013). Experimentally calibrated population of models predicts and explains intersubject variability in cardiac cellular electrophysiology. *Proceedings of the National Academy of Sciences*, *110*(23), E2098–E2105. https://doi.org/10.1073/pnas.1304382110

Britton, O. J., Bueno-Orovio, A., Virág, L., Varró, A., & Rodriguez, B. (2017). The Electrogenic Na^+/K^+ Pump Is a Key Determinant of Repolarization Abnormality Susceptibility in Human Ventricular Cardiomyocytes: A Population-Based Simulation Study. *Frontiers in Physiology*, *8*. https://doi.org/10.3389/fphys.2017.00278

Brown, H. F., DiFrancesco, D., & Noble, S. J. (1979). How does adrenaline accelerate the heart? *Nature*, *280*, 235–236. https://doi.org/10.1038/280235a0

Bu, L., Jiang, X., Martin-Puig, S., Caron, L., Zhu, S., Shao, Y., Roberts, D. J., Huang, P. L., Domian, I. J., & Chien, K. R. (2009). Human ISL1 heart progenitors generate diverse

multipotent cardiovascular cell lineages. *Nature*, *460*, 113–117. https://doi.org/10.1038/nature08191

Bueno-Orovio, A., Sánchez, C., Pueyo, E., & Rodriguez, B. (2014). Na/K pump regulation of cardiac repolarization: insights from a systems biology approach. *Pflügers Archiv - European Journal of Physiology*, *466*, 183–193. https://doi.org/10.1007/s00424-013-1293-1

Burdon-Sanderson, J., & Page, F. J. M. (1880). On the Time-Relations of the Excitatory Process in the Ventricle of the Heart of the Frog. *The Journal of Physiology*, *2*(5–6), 384–435. https://doi.org/10.1113/jphysiol.1880.sp000070

Burgess, D. C., Hunt, D., Li, L., Zannino, D., Williamson, E., Davis, T. M. E., Laakso, M., Kesaniemi, Y. A., Zhang, J., Sy, R. W., Lehto, S., Mann, S., & Keech, A. C. (2010). Incidence and predictors of silent myocardial infarction in type 2 diabetes and the effect of fenofibrate: an analysis from the Fenofibrate Intervention and Event Lowering in Diabetes (FIELD) study. *European Heart Journal*, *31*(1), 92–99. https://doi.org/10.1093/eurheartj/ehp377

Byrne, R. A., Rossello, X., Coughlan, J. J., Barbato, E., Berry, C., Chieffo, A., Claeys, M. J., Dan, G.-A., Dweck, M. R., Galbraith, M., Gilard, M., Hinterbuchner, L., Jankowska, E. A., Jüni, P., Kimura, T., Kunadian, V., Leosdottir, M., Lorusso, R., Pedretti, R. F. E., … ESC Scientific Document Group. (2023). 2023 ESC Guidelines for the management of acute coronary syndromes: Developed by the task force on the management of acute coronary syndromes of the European Society of Cardiology (ESC). *European Heart Journal*, *44*(38), 3720–3826. https://doi.org/10.1093/eurheartj/ehad191

Cahill, T. J., & Kharbanda, R. K. (2017). Heart failure after myocardial infarction in the era of primary percutaneous coronary intervention: Mechanisms, incidence and identification of patients at risk. *World Journal of Cardiology*, *9*(5), 407–415. https://doi.org/10.4330/wjc.v9.i5.407

Caldwell, B. J., Trew, M. L., Sands, G. B., Hooks, D. A., LeGrice, I. J., & Smaill, B. H. (2009). Three Distinct Directions of Intramural Activation Reveal Nonuniform Side-to-Side Electrical Coupling of Ventricular Myocytes. *Circulation: Arrhythmia and Electrophysiology*, *2*(4), 433–440. https://doi.org/10.1161/CIRCEP.108.830133

Camelliti, P., Borg, T., & Kohl, P. (2005). Structural and functional characterisation of cardiac fibroblasts. *Cardiovascular Research*, *65*(1), 40–51. https://doi.org/10.1016/j.cardiores.2004.08.020

Campbell, D. L., Rasmusson, R. L., Qu, Y., & Strauss, H. C. (1993). The calcium-independent transient outward potassium current in isolated ferret right ventricular myocytes. I. Basic characterization and kinetic analysis. *The Journal of General Physiology*, *101*(4), 571–601. https://doi.org/10.1085/jgp.101.4.571

Campos, F. O., Shiferaw, Y., Weber dos Santos, R., Plank, G., & Bishop, M. J. (2018). Microscopic Isthmuses and Fibrosis Within the Border Zone of Infarcted Hearts Promote Calcium-Mediated Ectopy and Conduction Block. *Frontiers in Physics*, *6*. https://doi.org/10.3389/fphy.2018.00057

Camps, J., Berg, L. A., Wang, Z. J., Sebastian, R., Riebel, L. L., Doste, R., Zhou, X., Sachetto, R., Coleman, J., Lawson, B., Grau, V., Burrage, K., Bueno-Orovio, A., Weber dos Santos, R., & Rodriguez, B. (2024). Digital twinning of the human ventricular activation sequence to Clinical 12-lead ECGs and magnetic resonance imaging using realistic Purkinje networks for in silico clinical trials. *Medical Image Analysis*, *94*, 103108. https://doi.org/10.1016/j.media.2024.103108

Camps, J., Lawson, B., Drovandi, C., Minchole, A., Wang, Z. J., Grau, V., Burrage, K., & Rodriguez, B. (2021). Inference of ventricular activation properties from non-invasive electrocardiography. *Medical Image Analysis*, *73*, 102143. https://doi.org/10.1016/j.media.2021.102143

Camps, J., Wang, Z. J., Doste, R., Berg, L. A., Holmes, M., Lawson, B., Tomek, J., Burrage, K., Bueno-Orovio, A., & Rodriguez, B. (2025). Harnessing 12-lead ECG and MRI data to personalise repolarisation profiles in cardiac digital twin models for enhanced virtual drug testing. *Medical Image Analysis*, *100*, 103361. https://doi.org/10.1016/j.media.2024.103361

Cardone-Noott, L., Bueno-Orovio, A., Minchole, A., Burrage, K., Wallman, M., Zemzemi, N., Dall'Armellina, E., & Rodriguez, B. (2014). A computational investigation into the effect of infarction on clinical human electrophysiology biomarkers. *2014 Computing in Cardiology (CinC)*, 673–676.

Carmona, F., Mata, K. M., Oliveira, M. S., & Ramos, S. D. (2013). Myocardial Ischemia in Congenital Heart Disease: A Review. In D. C. Gaze (Ed.), *Ischemic Heart Disease*. IntechOpen. https://doi.org/10.5772/53420

Carro, J., Rodríguez, J. F., Laguna, P., & Pueyo, E. (2011). A human ventricular cell model for investigation of cardiac arrhythmias under hyperkalaemic conditions. *Philosophical Transactions of the Royal Society A: Mathematical, Physical and Engineering Sciences*, *369*, 4205–4232. https://doi.org/10.1098/rsta.2011.0127

Cathey, B. M., Bellach, A., Troendle, J., Smith, K., Osgood, S., Raja, N., Kozel, B. A., & Levin, M. D. (2024). Increased heart rate fragmentation in those with Williams–Beuren syndrome suggests nonautonomic mechanistic contributors to sudden death risk. *American Journal of Physiology-Heart and Circulatory Physiology*, *327*(2), H521–H532. https://doi.org/10.1152/ajpheart.00601.2023

Cavero, I., Guillon, J.-M., & Holzgrefe, H. H. (2017). Reminiscing about Jan Evangelista Purkinje: a pioneer of modern experimental physiology. *Advances in Physiology Education*, *41*(4), 528–538. https://doi.org/10.1152/advan.00068.2017

Chauhan, V. S., Downar, E., Nanthakumar, K., Parker, J. D., Ross, H. J., Chan, W., & Picton, P. (2006). Increased ventricular repolarization heterogeneity in patients with ventricular arrhythmia vulnerability and cardiomyopathy: a human in vivo study. *American Journal of Physiology-Heart and Circulatory Physiology*, *290*(1), H79–H86. https://doi.org/10.1152/ajpheart.00648.2005

Chauveau, S., Anyukhovsky, E. P., Ben-Ari, M., Naor, S., Jiang, Y.-P., Danilo, P., Rahim, T., Burke, S., Qiu, X., Potapova, I. A., Doronin, S. V., Brink, P. R., Binah, O., Cohen, I. S., & Rosen, M. R. (2017). Induced Pluripotent Stem Cell–Derived Cardiomyocytes Provide In Vivo Biological Pacemaker Function. *Circulation: Arrhythmia and Electrophysiology*, *10*(5), e004508. https://doi.org/10.1161/CIRCEP.116.004508

Cheng, K., Li, T.-S., Malliaras, K., Davis, D. R., Zhang, Y., & Marbán, E. (2010). Magnetic Targeting Enhances Engraftment and Functional Benefit of Iron-Labeled Cardiosphere-Derived Cells in Myocardial Infarction. *Circulation Research*, *106*(10), 1570–1581. https://doi.org/10.1161/CIRCRESAHA.109.212589

Cheng, Y.-C., Hsieh, M. L., Lin, C.-J., Chang, C. M. C., Huang, C.-Y., Puntney, R., Wu Moy, A., Ting, C.-Y., Herr Chan, D. Z., Nicholson, M. W., Lin, P.-J., Chen, H.-C., Kim, G. C., Zhang, J., Coonen, J., Basu, P., Simmons, H. A., Liu, Y.-W., Hacker, T. A., … Hsieh, P. C. H. (2023). Combined Treatment of Human Induced Pluripotent Stem Cell–Derived Cardiomyocytes and Endothelial Cells Regenerate the Infarcted Heart in Mice and Non-Human Primates. *Circulation*, *148*(18), 1395–1409. https://doi.org/10.1161/CIRCULATIONAHA.122.061736

Cherry, E. M., Greenside, H. S., & Henriquez, C. S. (2000). A Space-Time Adaptive Method for Simulating Complex Cardiac Dynamics. *Physical Review Letters*, *84*(6), 1343–1346. https://doi.org/10.1103/PhysRevLett.84.1343

Chew, D. S., Wilton, S. B., Kavanagh, K., Vaid, H. M., Southern, D. A., Ellis, L., Howarth, A. G., White, J. A., & Exner, D. V. (2018). Fragmented QRS complexes after acute myocardial infarction are independently associated with unfavorable left ventricular remodeling. *Journal of Electrocardiology*, *51*(4), 607–612. https://doi.org/10.1016/j.jelectrocard.2018.04.004

Chong, J. J. H., Yang, X., Don, C. W., Minami, E., Liu, Y.-W., Weyers, J. J., Mahoney, W. M., Van Biber, B., Cook, S. M., Palpant, N. J., Gantz, J. A., Fugate, J. A., Muskheli, V., Gough, G. M., Vogel, K. W., Astley, C. A., Hotchkiss, C. E., Baldessari, A., Pabon, L., … Murry, C. E. (2014). Human embryonic-stem-cell-derived cardiomyocytes regenerate non-human primate hearts. *Nature*, *510*, 273–277. https://doi.org/10.1038/nature13233

Chou, C., Zhou, S., Hayashi, H., Nihei, M., Liu, Y., Wen, M., Yeh, S., Fishbein, M. C., Weiss, J. N., Lin, S., Wu, D., & Chen, P. (2007). Remodelling of action potential and intracellular calcium cycling dynamics during subacute myocardial infarction promotes ventricular arrhythmias in Langendorff-perfused rabbit hearts. *The Journal of Physiology*, *580*(3), 895–906. https://doi.org/10.1113/jphysiol.2006.120659

Chrysafides, S. M., Bordes, S. J., & Sharma, S. (2023). *Physiology, Resting Potential*. In: StatPearls [Internet]. Treasure Island (FL): StatPearls Publishing; Available from: https://www.ncbi.nlm.nih.gov/books/NBK538338/.

Chung, I. (2023). Incidence of arrhythmias post acute ST-elevation myocardial infarction (MI) in the modern era. *European Heart Journal: Acute Cardiovascular Care*, *12*(Supplement_1), zuad036.006. https://doi.org/10.1093/ehjacc/zuad036.006

Clark, S. J., Yoxall, C. W., & Subhedar, N. V. (2002). Measurement of right ventricular volume in healthy term and preterm neonates. *Archives of Disease in Childhood - Fetal and Neonatal Edition*, *87*(2), F89–F93. https://doi.org/10.1136/fn.87.2.F89

Clayton, R. H., Bernus, O., Cherry, E. M., Dierckx, H., Fenton, F. H., Mirabella, L., Panfilov, A. V., Sachse, F. B., Seemann, G., & Zhang, H. (2011). Models of cardiac tissue electrophysiology: Progress, challenges and open questions. *Progress in Biophysics and Molecular Biology*, *104*(1–3), 22–48. https://doi.org/10.1016/j.pbiomolbio.2010.05.008

Cluitmans, M. J. M., Plank, G., & Heijman, J. (2024). Digital twins for cardiac electrophysiology: state of the art and future challenges. *Herzschrittmachertherapie + Elektrophysiologie*, *35*, 118–123. https://doi.org/10.1007/s00399-024-01014-0

Cohen, M. I. (2019). Frequent premature ventricular beats in healthy children: when to ignore and when to treat? *Current Opinion in Cardiology*, *34*(1), 65–72. https://doi.org/10.1097/HCO.0000000000000581

Colli Franzone, P., Pavarino, L. F., Scacchi, S., & Taccardi, B. (2008). Modeling ventricular repolarization: Effects of transmural and apex-to-base heterogeneities in action potential durations. *Mathematical Biosciences*, *214*(1–2), 140–152. https://doi.org/10.1016/j.mbs.2008.06.006

Collins, R. T. (2013). Cardiovascular Disease in Williams Syndrome. *Circulation*, *127*(21), 2125–2134. https://doi.org/10.1161/CIRCULATIONAHA.112.000064

Connolly, A. J., & Bishop, M. J. (2016). Computational Representations of Myocardial Infarct Scars and Implications for Arrhythmogenesis. *Clinical Medicine Insights: Cardiology*, *10s1*. https://doi.org/10.4137/CMC.S39708

Conway, E. E., Noonan, J., Marion, R. W., & Steeg, C. N. (1990). Myocardial infarction leading to sudden death in the Williams syndrome: Report of three cases. *The*

Journal of Pediatrics, *117*(4), 593–595. https://doi.org/10.1016/S0022-3476(05)80696-1

Coronel, R., Wilms-Schopman, F. J., Opthof, T., van Capelle, F. J., & Janse, M. J. (1991). Injury current and gradients of diastolic stimulation threshold, TQ potential, and extracellular potassium concentration during acute regional ischemia in the isolated perfused pig heart. *Circulation Research*, *68*(5), 1241–1249. https://doi.org/10.1161/01.RES.68.5.1241

Cross, H. R., Radda, G. K., & Clarke, K. (1995). The role of Na+/K+ ATPase activity during low flow ischemia in preventing myocardial injury: A ^{31}P, ^{23}Na and ^{87}Rb NMR spectroscopic study. *Magnetic Resonance in Medicine*, *34*(5), 673–685. https://doi.org/10.1002/mrm.1910340505

Cyranoski, D. (2018). 'Reprogrammed' stem cells approved to mend human hearts for the first time. *Nature*, *557*, 619–620. https://doi.org/10.1038/d41586-018-05278-8

Cyranoski, D., Sipp, D., Mallik, S., & Rasko, J. E. J. (2023). Too little, too soon: Japan's experiment in regenerative medicine deregulation. *Cell Stem Cell*, *30*(7), 913–916. https://doi.org/10.1016/j.stem.2023.06.005

Dark, N., Cosson, M.-V., Tsansizi, L. I., Owen, T. J., Ferraro, E., Francis, A. J., Tsai, S., Bouissou, C., Weston, A., Collinson, L., Abi-Gerges, N., Miller, P. E., MacLeod, K. T., Ehler, E., Mitter, R., Harding, S. E., Smith, J. C., & Bernardo, A. S. (2023). Generation of left ventricle-like cardiomyocytes with improved structural, functional, and metabolic maturity from human pluripotent stem cells. *Cell Reports Methods*, *3*(4), 100456. https://doi.org/10.1016/j.crmeth.2023.100456

Dasí, A., Hernández-Romero, I., Gomez, J. F., Climent, A. M., Ferrero, J. M., & Trenor, B. (2021). Analysis of the response of human iPSC-derived cardiomyocyte tissue to I_{CaL} block. A combined in vitro and in silico approach. *Computers in Biology and Medicine*, *137*, 104796. https://doi.org/10.1016/j.compbiomed.2021.104796

Dasí, A., Nagel, C., Pope, M. T. B., Wijesurendra, R. S., Betts, T. R., Sachetto, R., Loewe, A., Bueno-Orovio, A., & Rodriguez, B. (2024). *In Silico* TRials guide optimal stratification of ATrIal FIbrillation patients to Catheter Ablation and pharmacological medicaTION: the i-STRATIFICATION study. *EP Europace*, *26*(6), euae150. https://doi.org/10.1093/europace/euae150

Davis, M. E., Hsieh, P. C. H., Grodzinsky, A. J., & Lee, R. T. (2005). Custom Design of the Cardiac Microenvironment With Biomaterials. *Circulation Research*, *97*(1), 8–15. https://doi.org/10.1161/01.RES.0000173376.39447.01

Del Buono, M. G., Montone, R. A., Camilli, M., Carbone, S., Narula, J., Lavie, C. J., Niccoli, G., & Crea, F. (2021). Coronary Microvascular Dysfunction Across the Spectrum of Cardiovascular Diseases: JACC State-of-the-Art Review. *Journal of the American*

College of Cardiology, *78*(13), 1352–1371. https://doi.org/10.1016/j.jacc.2021.07.042

Deng, D., Arevalo, H. J., Prakosa, A., Callans, D. J., & Trayanova, N. A. (2016). A feasibility study of arrhythmia risk prediction in patients with myocardial infarction and preserved ejection fraction. *EP Europace*, *18*(suppl_4), iv60–iv66. https://doi.org/10.1093/europace/euw351

Deo, M., Boyle, P., Plank, G., & Vigmond, E. (2009). Arrhythmogenic mechanisms of the Purkinje system during electric shocks: A modeling study. *Heart Rhythm*, *6*(12), 1782–1789. https://doi.org/10.1016/j.hrthm.2009.08.023

Devalla, H. D., & Passier, R. (2018). Cardiac differentiation of pluripotent stem cells and implications for modeling the heart in health and disease. *Science Translational Medicine*, *10*(435), eaah5457. https://doi.org/10.1126/scitranslmed.aah5457

Dib, N., Khawaja, H., Varner, S., McCarthy, M., & Campbell, A. (2011). Cell Therapy for Cardiovascular Disease: A Comparison of Methods of Delivery. *Journal of Cardiovascular Translational Research*, *4*, 177–181. https://doi.org/10.1007/s12265-010-9253-z

Dib, N., Menasche, P., Bartunek, J. J., Zeiher, A. M., Terzic, A., Chronos, N. A., Henry, T. D., Peters, N. S., Fernández-Avilés, F., Yacoub, M., Sanborn, T. A., DeMaria, A., Schatz, R. A., Taylor, D. A., Fuchs, S., Itescu, S., Miller, L. W., Dinsmore, J. H., Dangas, G. D., … Holmes, D. R. (2010). Recommendations for Successful Training on Methods of Delivery of Biologics for Cardiac Regeneration: A Report of the International Society for Cardiovascular Translational Research. *JACC: Cardiovascular Interventions*, *3*(3), 265–275. https://doi.org/10.1016/j.jcin.2009.12.013

DiFrancesco, D. (2010). The Role of the Funny Current in Pacemaker Activity. *Circulation Research*, *106*(3), 434–446. https://doi.org/10.1161/CIRCRESAHA.109.208041

Doss, M. X., Di Diego, J. M., Goodrow, R. J., Wu, Y., Cordeiro, J. M., Nesterenko, V. V., Barajas-Martínez, H., Hu, D., Urrutia, J., Desai, M., Treat, J. A., Sachinidis, A., & Antzelevitch, C. (2012). Maximum Diastolic Potential of Human Induced Pluripotent Stem Cell-Derived Cardiomyocytes Depends Critically on I_{Kr}. *PLoS ONE*, *7*(7), e40288. https://doi.org/10.1371/journal.pone.0040288

Doste, R., Soto-Iglesias, D., Bernardino, G., Alcaine, A., Sebastian, R., Giffard-Roisin, S., Sermesant, M., Berruezo, A., Sanchez-Quintana, D., & Camara, O. (2019). A rule-based method to model myocardial fiber orientation in cardiac biventricular geometries with outflow tracts. *International Journal for Numerical Methods in Biomedical Engineering*, *35*(4), e3185. https://doi.org/10.1002/cnm.3185

Drovandi, C. C., Cusimano, N., Psaltis, S., Lawson, B. A. J., Pettitt, A. N., Burrage, P., & Burrage, K. (2016). Sampling methods for exploring between-subject variability in

cardiac electrophysiology experiments. *Journal of The Royal Society Interface*, *13*(121). https://doi.org/10.1098/rsif.2016.0214

Durrer, D., Van Dam, R. Th., Freud, G. E., Janse, M. J., Meijler, F. L., & Arzbaecher, R. C. (1970). Total Excitation of the Isolated Human Heart. *Circulation*, *41*(6), 899–912. https://doi.org/10.1161/01.CIR.41.6.899

Dutta, S., Mincholé, A., Quinn, T. A., & Rodriguez, B. (2017). Electrophysiological properties of computational human ventricular cell action potential models under acute ischemic conditions. *Progress in Biophysics and Molecular Biology*, *129*, 40–52. https://doi.org/10.1016/j.pbiomolbio.2017.02.007

Dux-Santoy, L., Sebastian, R., Felix-Rodriguez, J., Ferrero, J. M., & Saiz, J. (2011). Interaction of Specialized Cardiac Conduction System With Antiarrhythmic Drugs: A Simulation Study. *IEEE Transactions on Biomedical Engineering*, *58*(12), 3475–3478. https://doi.org/10.1109/TBME.2011.2165213

Ebashi, S., & Endo, M. (1968). Calcium and muscle contraction. *Progress in Biophysics and Molecular Biology*, *18*, 123–183. https://doi.org/10.1016/0079-6107(68)90023-0

Ebashi, S., & Lipmann, F. (1962). Adenosine triphosphate-linked concentration of calcium ions in a particulate fraction of rabbit muscle. *The Journal of Cell Biology*, *14*(3), 389–400. https://doi.org/10.1083/jcb.14.3.389

Einthoven, W. (1895). Ueber die Form des menschlichen Electrocardiogramms. *Pflüger, Archiv Für Die Gesamte Physiologie Des Menschen Und Der Tiere*, *60*, 101–123. https://doi.org/10.1007/BF01662582

Elliott, J., Doessel, O., Loewe, A., Mainardi, L., Corino, V., & Rodriguez Matas, J. (2020). An In-silico Study Into The Impact of Electrophysiological Variability at the Cellular Level on the Reentry Patterns in Atrial Fibrillation. *2020 Computing in Cardiology (CinC)*. https://doi.org/10.22489/CinC.2020.436

El-Sherif, N., Mehra, R., Gough, W. B., & Zeiler, R. H. (1984). Reentrant ventricular arrhythmias in the late myocardial infarction period: II. Burst pacing versus multiple premature stimulation in the induction of reentry. *Journal of the American College of Cardiology*, *4*(2), 295–304. https://doi.org/10.1016/S0735-1097(84)80217-X

Ewart, A. K., Morris, C. A., Atkinson, D., Jin, W., Sternes, K., Spallone, P., Stock, A. D., Leppert, M., & Keating, M. T. (1993). Hemizygosity at the elastin locus in a developmental disorder, Williams syndrome. *Nature Genetics*, *5*, 11–16. https://doi.org/10.1038/ng0993-11

Fall, C. P., & Keizer, J. E. (2002). Voltage Gated Ionic Currents. In C. P. Fall, E. S. Marland, J. M. Wagner, & J. J. Tyson (Eds.), *Computational Cell Biology (Interdisciplinary Applied Mathematics, vol. 20)* (pp. 21–52). Springer-Verlag New York.

Fang, Y.-H., Wang, S. P. H., Chang, H.-Y., Yang, P.-J., Liu, P.-Y., & Liu, Y.-W. (2020). Immunogenicity in Stem Cell Therapy for Cardiac Regeneration. *Acta Cardiologica Sinica*, *36*(6), 588–594. https://doi.org/10.6515/ACS.202011_36(6).20200811A

Fassina, D., Costa, C. M., Longobardi, S., Karabelas, E., Plank, G., Harding, S. E., & Niederer, S. A. (2022). Modelling the interaction between stem cells derived cardiomyocytes patches and host myocardium to aid non-arrhythmic engineered heart tissue design. *PLoS Computational Biology*, *18*(4), e1010030. https://doi.org/10.1371/journal.pcbi.1010030

Fassina, D., M. Costa, C., Bishop, M., Plank, G., Whitaker, J., Harding, S. E., & Niederer, S. A. (2023). Assessing the arrhythmogenic risk of engineered heart tissue patches through in silico application on infarcted ventricle models. *Computers in Biology and Medicine*, *154*, 106550. https://doi.org/10.1016/j.compbiomed.2023.106550

Fatt, P., & Katz, B. (1953). The electrical properties of crustacean muscle fibres. *The Journal of Physiology*, *120*(1–2), 171–204. https://doi.org/10.1113/jphysiol.1953.sp004884

Feng, J., Yue, L., Wang, Z., & Nattel, S. (1998). Ionic Mechanisms of Regional Action Potential Heterogeneity in the Canine Right Atrium. *Circulation Research*, *83*(5), 541–551. https://doi.org/10.1161/01.RES.83.5.541

Feric, N. T., & Radisic, M. (2016). Maturing human pluripotent stem cell-derived cardiomyocytes in human engineered cardiac tissues. *Advanced Drug Delivery Reviews*, *96*, 110–134. https://doi.org/10.1016/j.addr.2015.04.019

Fernandez de Canete, J., Luque, J., Barbancho, J., & Munoz, V. (2014). Modelling of long-term and short-term mechanisms of arterial pressure control in the cardiovascular system: An object-oriented approach. *Computers in Biology and Medicine*, *47*, 104–112. https://doi.org/10.1016/j.compbiomed.2014.01.006

Ferraris, V. A. (2016). How do cells talk to each other?: Paracrine factors secreted by mesenchymal stromal cells. *The Journal of Thoracic and Cardiovascular Surgery*, *151*(3), 849–851. https://doi.org/10.1016/j.jtcvs.2015.11.035

Ferrero, J. M., Sáiz, J., Ferrero, J. M., & Thakor, N. V. (1996). Simulation of Action Potentials From Metabolically Impaired Cardiac Myocytes. *Circulation Research*, *79*(2), 208–221. https://doi.org/10.1161/01.RES.79.2.208

Filice, D., Dhahri, W., Solan, J. L., Lampe, P. D., Steele, E., Milani, N., Van Biber, B., Zhu, W.-Z., Valdman, T. S., Romagnuolo, R., Otero-Cruz, J. D., Hauch, K. D., Kay, M. W., Sarvazyan, N., & Laflamme, M. A. (2020). Optical mapping of human embryonic stem cell-derived cardiomyocyte graft electrical activity in injured hearts. *Stem Cell Research & Therapy*, *11*, 417. https://doi.org/10.1186/s13287-020-01919-w

Filipovic, N., Saveljic, I., Sustersic, T., Milosevic, M., Milicevic, B., Simic, V., Ivanovic, M., & Kojic, M. (2022). In Silico Clinical Trials for Cardiovascular Disease. *Journal of Visualized Experiments*, *183*, e63573. https://doi.org/10.3791/63573

Fink, M., & Noble, D. (2009). Markov models for ion channels: versatility versus identifiability and speed. *Philosophical Transactions of the Royal Society A: Mathematical, Physical and Engineering Sciences*, *367*, 2161–2179. https://doi.org/10.1098/rsta.2008.0301

Fink, M., Noble, P. J., & Noble, D. (2011). Ca^{2+}-induced delayed afterdepolarizations are triggered by dyadic subspace Ca^{2+} affirming that increasing SERCA reduces aftercontractions. *American Journal of Physiology-Heart and Circulatory Physiology*, *301*(3), H921–H935. https://doi.org/10.1152/ajpheart.01055.2010

FitzHugh, R. (1961). Impulses and Physiological States in Theoretical Models of Nerve Membrane. *Biophysical Journal*, *1*(6), 445–466. https://doi.org/10.1016/S0006-3495(61)86902-6

Flood, D., Lee, E. S., & Taylor, C. T. (2023). Intracellular energy production and distribution in hypoxia. *Journal of Biological Chemistry*, *299*(9), 105103. https://doi.org/10.1016/j.jbc.2023.105103

Folkmanaite, M., Zhou, X., Margara, F., Zaccolo, M., & Rodriguez, B. (2021). In Silico Human Induced Pluripotent Stem Cell Derived Cardiomyocyte Electro-Mechanical Modelling and Simulation. *2021 Computing in Cardiology (CinC)*. https://doi.org/10.23919/CinC53138.2021.9662938

Foo, K. S., Lehtinen, M. L., Leung, C. Y., Lian, X., Xu, J., Keung, W., Geng, L., Kolstad, T. R. S., Thams, S., Wong, A. O., Wong, N., Bylund, K., Zhou, C., He, X., Jin, S.-B., Clarke, J., Lendahl, U., Li, R. A., Louch, W. E., & Chien, K. R. (2018). Human $ISL1^{+}$ Ventricular Progenitors Self-Assemble into an In Vivo Functional Heart Patch and Preserve Cardiac Function Post Infarction. *Molecular Therapy*, *26*(7), 1644–1659. https://doi.org/10.1016/j.ymthe.2018.02.012

Forouzandehmehr, M., Cogno, N., Koivumäki, J., Hyttinen, J., & Paci, M. (2020). The Comparison Between Two Mathematical Contractile Elements Integrated into an hiPSC-CM In-silico Model. *2020 Computing in Cardiology (CinC)*. https://doi.org/10.22489/CinC.2020.055

Franz, M. R., Bargheer, K., Rafflenbeul, W., Haverich, A., & Lichtlen, P. R. (1987). Monophasic action potential mapping in human subjects with normal electrocardiograms: direct evidence for the genesis of the T wave. *Circulation*, *75*(2), 379–386. https://doi.org/10.1161/01.CIR.75.2.379

Freed, M. D. (2006). Fetal and Transitional Circulation. In J. F. Keane, J. E. Lock, & D. C. Fyler (Eds.), *Nadas' Pediatric Cardiology* (2nd ed., pp. 75–79). Saunders. https://doi.org/https://doi.org/10.1016/B978-1-4160-2390-6.50011-8

Friedman, P. L., Stewart, J. R., & Wit, A. L. (1973). Spontaneous and Induced Cardiac Arrhythmias in Subendocardial Purkinje Fibers Surviving Extensive Myocardial Infarction in Dogs. *Circulation Research*, *33*(5), 612–626. https://doi.org/10.1161/01.RES.33.5.612

Gajewski, K., & Saul, P. (2010). Sudden cardiac death in children and adolescents (excluding Sudden Infant Death Syndrome). *Annals of Pediatric Cardiology*, *3*(2), 107–112. https://doi.org/10.4103/0974-2069.74035

Galiuto, L., Barchetta, S., Paladini, S., Lanza, G., Rebuzzi, A. G., Marzilli, M., & Crea, F. (2007). Functional and structural correlates of persistent ST elevation after acute myocardial infarction successfully treated by percutaneous coronary intervention. *Heart*, *93*(11), 1376–1380. https://doi.org/10.1136/hrt.2006.105320

Garbern, J. C., & Lee, R. T. (2013). Cardiac Stem Cell Therapy and the Promise of Heart Regeneration. *Cell Stem Cell*, *12*(6), 689–698. https://doi.org/10.1016/j.stem.2013.05.008

Garcia-Molla, V. M., Liberos, A., Vidal, A., Guillem, M. S., Millet, J., Gonzalez, A., Martinez-Zaldivar, F. J., & Climent, A. M. (2014). Adaptive step ODE algorithms for the 3D simulation of electric heart activity with graphics processing units. *Computers in Biology and Medicine*, *44*, 15–26. https://doi.org/10.1016/j.compbiomed.2013.10.023

Garfinkel, A., Kim, Y.-H., Voroshilovsky, O., Qu, Z., Kil, J. R., Lee, M.-H., Karagueuzian, H. S., Weiss, J. N., & Chen, P.-S. (2000). Preventing ventricular fibrillation by flattening cardiac restitution. *Proceedings of the National Academy of Sciences*, *97*(11), 6061–6066. https://doi.org/10.1073/pnas.090492697

Garg, P., Broadbent, D. A., Swoboda, P. P., Foley, J. R. J., Fent, G. J., Musa, T. A., Ripley, D. P., Erhayiem, B., Dobson, L. E., McDiarmid, A. K., Haaf, P., Kidambi, A., van der Geest, R. J., Greenwood, J. P., & Plein, S. (2017). Acute Infarct Extracellular Volume Mapping to Quantify Myocardial Area at Risk and Chronic Infarct Size on Cardiovascular Magnetic Resonance Imaging. *Circulation: Cardiovascular Imaging*, *10*(7). https://doi.org/10.1161/CIRCIMAGING.117.006182

Garrey, W. E. (1914). The nature of fibrillary contraction of the heart - its relation to tissue mass and form. *American Journal of Physiology-Legacy Content*, *33*(3), 397–414. https://doi.org/10.1152/ajplegacy.1914.33.3.397

Garza, M. A., Wason, E. A., & Zhang, J. Q. (2015). Cardiac remodeling and physical training post myocardial infarction. *World Journal of Cardiology*, *7*(2), 52–64. https://doi.org/10.4330/wjc.v7.i2.52

Gerber, Y., Weston, S. A., Enriquez-Sarano, M., Manemann, S. M., Chamberlain, A. M., Jiang, R., & Roger, V. L. (2016). Atherosclerotic Burden and Heart Failure After Myocardial Infarction. *JAMA Cardiology*, *1*(2), 156–162. https://doi.org/10.1001/jamacardio.2016.0074

Ghuran, A. V, & Camm, A. J. (2001). Ischaemic heart disease presenting as arrhythmias. *British Medical Bulletin*, *59*(1), 193–210. https://doi.org/10.1093/bmb/59.1.193

Gibbs, C. E., Marchianó, S., Zhang, K., Yang, X., Murry, C. E., & Boyle, P. M. (2023). Graft-host coupling changes can lead to engraftment arrhythmia: A computational study. *The Journal of Physiology*, *601*(13), 2733–2749. https://doi.org/10.1113/JP284244

Goldberger, A. L., Amaral, L. A. N., Glass, L., Hausdorff, J. M., Ivanov, P. Ch., Mark, R. G., Mietus, J. E., Moody, G. B., Peng, C.-K., & Stanley, H. E. (2000). PhysioBank, PhysioToolkit, and PhysioNet: Components of a new research resource for complex physiologic signals. *Circulation*, *101*(23), e215–e220. https://doi.org/10.1161/01.CIR.101.23.e215

Goldman, D. E. (1943). Potential, Impedance, and Rectification in Membranes. *Journal of General Physiology*, *27*(1), 37–60. https://doi.org/10.1085/jgp.27.1.37

Goversen, B., van der Heyden, M. A. G., van Veen, T. A. B., & de Boer, T. P. (2018). The immature electrophysiological phenotype of iPSC-CMs still hampers in vitro drug screening: Special focus on I_{K1}. *Pharmacology & Therapeutics*, *183*, 127–136. https://doi.org/10.1016/j.pharmthera.2017.10.001

Grandi, E., Pasqualini, F. S., & Bers, D. M. (2010). A novel computational model of the human ventricular action potential and Ca transient. *Journal of Molecular and Cellular Cardiology*, *48*(1), 112–121. https://doi.org/10.1016/j.yjmcc.2009.09.019

Gray, D. F., Mihailidou, A. S., Hansen, P. S., Buhagiar, K. A., Bewick, N. L., Rasmussen, H. H., & Whalley, D. W. (1998). Amiodarone inhibits the Na^+-K^+ pump in rabbit cardiac myocytes after acute and chronic treatment. *The Journal of Pharmacology and Experimental Therapeutics*, *284*(1), 75–82. https://doi.org/https://doi.org/10.1016/S0022-3565(24)37204-0

Griffiths, E. J., Ocampo, C. J., Savage, J. S., Rutter, G. A., Hansford, R. G., Stern, M. D., & Silverman, H. S. (1998). Mitochondrial calcium transporting pathways during hypoxia and reoxygenation in single rat cardiomyocytes. *Cardiovascular Research*, *39*(2), 423–433. https://doi.org/10.1016/S0008-6363(98)00104-7

Grodzinsky, A., Goyal, A., Gosch, K., McCullough, P. A., Fonarow, G. C., Mebazaa, A., Masoudi, F. A., Spertus, J. A., Palmer, B. F., & Kosiborod, M. (2016). Prevalence and Prognosis of Hyperkalemia in Patients with Acute Myocardial Infarction. *The American Journal of Medicine*, *129*(8), 858–865. https://doi.org/10.1016/j.amjmed.2016.03.008

Grüntzig, A. (1978). Transluminal dilatation of coronary-artery stenosis. *The Lancet*, *311*(8058), 263. https://doi.org/10.1016/S0140-6736(78)90500-7

Haissaguerre, M., Vigmond, E., Stuyvers, B., Hocini, M., & Bernus, O. (2016). Ventricular arrhythmias and the His–Purkinje system. *Nature Reviews Cardiology*, *13*, 155–166. https://doi.org/10.1038/nrcardio.2015.193

Hansen, K. J., Laflamme, M. A., & Gaudette, G. R. (2018). Development of a Contractile Cardiac Fiber From Pluripotent Stem Cell Derived Cardiomyocytes. *Frontiers in Cardiovascular Medicine*, *5*. https://doi.org/10.3389/fcvm.2018.00052

Hanson, J., & Huxley, H. E. (1953). Structural Basis of the Cross-Striations in Muscle. *Nature*, *172*, 530–532. https://doi.org/10.1038/172530b0

Harris, A. S., Bisteni, A., Russell, R. A., Brigham, J. C., & Firestone, J. E. (1954). Excitatory Factors in Ventricular Tachycardia Resulting from Myocardial Ischemia. Potassium a Major Excitant. *Science*, *119*(3085), 200–203. https://doi.org/10.1126/science.119.3085.200

Hartley, A., Shalhoub, J., Ng, F. S., Krahn, A. D., Laksman, Z., Andrade, J. G., Deyell, M. W., Kanagaratnam, P., & Sikkel, M. B. (2021). Size matters in atrial fibrillation: the underestimated importance of reduction of contiguous electrical mass underlying the effectiveness of catheter ablation. *EP Europace*, *23*(11), 1698–1707. https://doi.org/10.1093/europace/euab078

Hasselbach, W., & Makinose, M. (1962). ATP and active transport. *Biochemical and Biophysical Research Communications*, *7*(2), 132–136. https://doi.org/10.1016/0006-291X(62)90161-4

He, J.-Q., Ma, Y., Lee, Y., Thomson, J. A., & Kamp, T. J. (2003). Human Embryonic Stem Cells Develop Into Multiple Types of Cardiac Myocytes. *Circulation Research*, *93*(1), 32–39. https://doi.org/10.1161/01.RES.0000080317.92718.99

Heerlein, K., Schulze, A., Hotz, L., Bärtsch, P., & Mairbäurl, H. (2005). Hypoxia Decreases Cellular ATP Demand and Inhibits Mitochondrial Respiration of A549 Cells. *American Journal of Respiratory Cell and Molecular Biology*, *32*(1), 44–51. https://doi.org/10.1165/rcmb.2004-0202OC

Hegyi, B., Bossuyt, J., Griffiths, L. G., Shimkunas, R., Coulibaly, Z., Jian, Z., Grimsrud, K. N., Sondergaard, C. S., Ginsburg, K. S., Chiamvimonvat, N., Belardinelli, L., Varró, A.,

Papp, J. G., Pollesello, P., Levijoki, J., Izu, L. T., Boyd, W. D., Bányász, T., Bers, D. M., & Chen-Izu, Y. (2018). Complex electrophysiological remodeling in postinfarction ischemic heart failure. *Proceedings of the National Academy of Sciences*, *115*(13), E3036–E3044. https://doi.org/10.1073/pnas.1718211115

Henderson, S. A., Goldhaber, J. I., So, J. M., Han, T., Motter, C., Ngo, A., Chantawansri, C., Ritter, M. R., Friedlander, M., Nicoll, D. A., Frank, J. S., Jordan, M. C., Roos, K. P., Ross, R. S., & Philipson, K. D. (2004). Functional Adult Myocardium in the Absence of Na^+-Ca^{2+} Exchange. *Circulation Research*, *95*(6), 604–611. https://doi.org/10.1161/01.RES.0000142316.08250.68

Herberts, C. A., Kwa, M. S., & Hermsen, H. P. (2011). Risk factors in the development of stem cell therapy. *Journal of Translational Medicine*, *9*, 29. https://doi.org/10.1186/1479-5876-9-29

Herring, N., Kalla, M., & Paterson, D. J. (2019). The autonomic nervous system and cardiac arrhythmias: current concepts and emerging therapies. *Nature Reviews Cardiology*, *16*, 707–726. https://doi.org/10.1038/s41569-019-0221-2

Herring, N., & Paterson, D. J. (2018). *Levick's Introduction to Cardiovascular Physiology* (6th ed.). CRC Press, Taylor & Francis Group. https://doi.org/10.1201/9781351107754

Hill, A. V. (1910). The possible effects of the aggregation of the molecules of haemoglobin on its dissociation curves. In Proceedings of the Physiological Society: January 22, 1910. *The Journal of Physiology*, *40*, 4–7. https://doi.org/10.1113/jphysiol.1910.sp001386

Hill, Y. R., Child, N., Hanson, B., Wallman, M., Coronel, R., Plank, G., Rinaldi, C. A., Gill, J., Smith, N. P., Taggart, P., & Bishop, M. J. (2016). Investigating a Novel Activation-Repolarisation Time Metric to Predict Localised Vulnerability to Reentry Using Computational Modelling. *PLoS ONE*, *11*(3), e0149342. https://doi.org/10.1371/journal.pone.0149342

Hinata, Y., Kagawa, Y., Kubo, H., Kato, E., Baba, A., Sasaki, D., Matsuura, K., Sawada, K., & Shimizu, T. (2022). Importance of beating rate control for the analysis of drug effects on contractility in human induced pluripotent stem cell-derived cardiomyocytes. *Journal of Pharmacological and Toxicological Methods*, *118*, 107228. https://doi.org/10.1016/j.vascn.2022.107228

Hoch, B., Meyer, R., Hetzer, R., Krause, E.-G., & Karczewski, P. (1999). Identification and Expression of δ-Isoforms of the Multifunctional Ca^{2+}/Calmodulin-Dependent Protein Kinase in Failing and Nonfailing Human Myocardium. *Circulation Research*, *84*(6), 713–721. https://doi.org/10.1161/01.RES.84.6.713

Hodgkin, A. L., & Huxley, A. F. (1952). A quantitative description of membrane current and its application to conduction and excitation in nerve. *The Journal of Physiology*, *117*(4), 500–544. https://doi.org/10.1113/jphysiol.1952.sp004764

Hodgkin, A. L., & Katz, B. (1949). The effect of sodium ions on the electrical activity of the giant axon of the squid. *The Journal of Physiology*, *108*(1), 37–77. https://doi.org/10.1113/jphysiol.1949.sp004310

Holmes, J. W., Borg, T. K., & Covell, J. W. (2005). Structure and Mechanics of Healing Myocardial Infarcts. *Annual Review of Biomedical Engineering*, *7*, 223–253. https://doi.org/10.1146/annurev.bioeng.7.060804.100453

Hong, K. U., Li, Q.-H., Guo, Y., Patton, N. S., Moktar, A., Bhatnagar, A., & Bolli, R. (2013). A highly sensitive and accurate method to quantify absolute numbers of c-kit+ cardiac stem cells following transplantation in mice. *Basic Research in Cardiology*, *108*, 346. https://doi.org/10.1007/s00395-013-0346-0

Hornik, C. P., Collins, R. T., Jaquiss, R. D. B., Jacobs, J. P., Jacobs, M. L., Pasquali, S. K., Wallace, A. S., & Hill, K. D. (2015). Adverse cardiac events in children with Williams syndrome undergoing cardiovascular surgery: An analysis of the Society of Thoracic Surgeons Congenital Heart Surgery Database. *The Journal of Thoracic and Cardiovascular Surgery*, *149*(6), 1516-1522.e1. https://doi.org/10.1016/j.jtcvs.2015.02.016

Høydal, M. A., Kirkeby-Garstad, I., Karevold, A., Wiseth, R., Haaverstad, R., Wahba, A., Stølen, T. L., Contu, R., Condorelli, G., Ellingsen, Ø., Smith, G. L., Kemi, O. J., & Wisløff, U. (2018). Human cardiomyocyte calcium handling and transverse tubules in mid-stage of post-myocardial-infarction heart failure. *ESC Heart Failure*, *5*(3), 332–342. https://doi.org/10.1002/ehf2.12271

Hund, T. J., Decker, K. F., Kanter, E., Mohler, P. J., Boyden, P. A., Schuessler, R. B., Yamada, K. A., & Rudy, Y. (2008). Role of activated CaMKII in abnormal calcium homeostasis and I_{Na} remodeling after myocardial infarction: Insights from mathematical modeling. *Journal of Molecular and Cellular Cardiology*, *45*(3), 420–428. https://doi.org/10.1016/j.yjmcc.2008.06.007

Huxley, A. F. (1957). Muscle Structure and Theories of Contraction. *Progress in Biophysics and Biophysical Chemistry*, *7*, 255–318. https://doi.org/10.1016/S0096-4174(18)30128-8

Huxley, H. E. (2004). Fifty years of muscle and the sliding filament hypothesis. *European Journal of Biochemistry*, *271*(8), 1403–1415. https://doi.org/10.1111/j.1432-1033.2004.04044.x

Iaquinta, M. R., Mazzoni, E., Bononi, I., Rotondo, J. C., Mazziotta, C., Montesi, M., Sprio, S., Tampieri, A., Tognon, M., & Martini, F. (2019). Adult Stem Cells for Bone

Regeneration and Repair. *Frontiers in Cell and Developmental Biology*, *7*. https://doi.org/10.3389/fcell.2019.00268

Ideker, R. E., Kong, W., & Pogwizd, S. (2009). Purkinje Fibers and Arrhythmias. *Pacing and Clinical Electrophysiology*, *32*(3), 283–285. https://doi.org/10.1111/j.1540-8159.2008.02232.x

Ismaili, D., Gurr, K., Horváth, A., Yuan, L., Lemoine, M. D., Schulz, C., Sani, J., Petersen, J., Reichenspurner, H., Kirchhof, P., Jespersen, T., Eschenhagen, T., Hansen, A., Koivumäki, J. T., & Christ, T. (2022). Regulation of APD and Force by the Na^+/Ca^{2+} Exchanger in Human-Induced Pluripotent Stem Cell-Derived Engineered Heart Tissue. *Cells*, *11*(15), 2424. https://doi.org/10.3390/cells11152424

Jamil-Copley, S., Vergara, P., Carbucicchio, C., Linton, N., Koa-Wing, M., Luther, V., Francis, D. P., Peters, N. S., Davies, D. W., Tondo, C., Della Bella, P., & Kanagaratnam, P. (2015). Application of Ripple Mapping to Visualize Slow Conduction Channels Within the Infarct-Related Left Ventricular Scar. *Circulation: Arrhythmia and Electrophysiology*, *8*(1), 76–86. https://doi.org/10.1161/CIRCEP.114.001827

Janse, M. J., van Capelle, F. J., Morsink, H., Kléber, A. G., Wilms-Schopman, F., Cardinal, R., d'Alnoncourt, C. N., & Durrer, D. (1980). Flow of "injury" current and patterns of excitation during early ventricular arrhythmias in acute regional myocardial ischemia in isolated porcine and canine hearts. Evidence for two different arrhythmogenic mechanisms. *Circulation Research*, *47*(2), 151–165. https://doi.org/10.1161/01.RES.47.2.151

Janse, M. J., & Wit, A. L. (1989). Electrophysiological mechanisms of ventricular arrhythmias resulting from myocardial ischemia and infarction. *Physiological Reviews*, *69*(4), 1049–1169. https://doi.org/10.1152/physrev.1989.69.4.1049

January, C. T., Chau, V., & Makielski, J. C. (1991). Triggered activity in the heart: cellular mechanisms of early after-depolarizations. *European Heart Journal*, *12*(suppl F), 4–9. https://doi.org/10.1093/eurheartj/12.suppl_F.4

Jawad, H., Ali, N. N., Lyon, A. R., Chen, Q. Z., Harding, S. E., & Boccaccini, A. R. (2007). Myocardial tissue engineering: a review. *Journal of Tissue Engineering and Regenerative Medicine*, *1*(5), 327–342. https://doi.org/10.1002/term.46

Jian, K., Li, C., Hancox, J. C., & Zhang, H. (2022). Pro-Arrhythmic Effects of Discontinuous Conduction at the Purkinje Fiber-Ventricle Junction Arising From Heart Failure-Induced Ionic Remodeling – Insights From Computational Modelling. *Frontiers in Physiology*, *13*. https://doi.org/10.3389/fphys.2022.877428

Jiang, B., Yan, L., Shamul, J. G., Hakun, M., & He, X. (2020). Stem Cell Therapy of Myocardial Infarction: A Promising Opportunity in Bioengineering. *Advanced Therapeutics*, *3*(3), 1900182. https://doi.org/10.1002/adtp.201900182

Jiang, M., Cabo, C., Yao, J.-A., Boyden, P. A., & Tseng, G.-N. (2000). Delayed rectifier K currents have reduced amplitudes and altered kinetics in myocytes from infarcted canine ventricle. *Cardiovascular Research*, *48*(1), 34–43. https://doi.org/10.1016/S0008-6363(00)00159-0

Jiang, M. T., Lokuta, A. J., Farrell, E. F., Wolff, M. R., Haworth, R. A., & Valdivia, H. H. (2002). Abnormal Ca^{2+} Release, but Normal Ryanodine Receptors, in Canine and Human Heart Failure. *Circulation Research*, *91*(11), 1015–1022. https://doi.org/10.1161/01.RES.0000043663.08689.05

Joyce, J. J., Dickson, P. I., Qi, N., Noble, J. E., Raj, J. U., & Baylen, B. G. (2004). Normal right and left ventricular mass development during early infancy. *The American Journal of Cardiology*, *93*(6), 797–801. https://doi.org/10.1016/j.amjcard.2003.11.063

Joyner, R. W., & Overholt, E. D. (1985). Effects of octanol on canine subendocardial Purkinje-to-ventricular transmission. *American Journal of Physiology-Heart and Circulatory Physiology*, *249*(6), H1228–H1231. https://doi.org/10.1152/ajpheart.1985.249.6.H1228

Kaplinsky, E., Ogawa, S., Balke, C. W., & Dreifus, L. S. (1979). Two periods of early ventricular arrhythmia in the canine acute myocardial infarction model. *Circulation*, *60*(2), 397–403. https://doi.org/10.1161/01.CIR.60.2.397

Kawamura, T., Ito, Y., Ito, E., Takeda, M., Mikami, T., Taguchi, T., Mochizuki-Oda, N., Sasai, M., Shimamoto, T., Nitta, Y., Yoshioka, D., Kawamura, M., Kawamura, A., Misumi, Y., Sakata, Y., Sawa, Y., & Miyagawa, S. (2023). Safety confirmation of induced pluripotent stem cell-derived cardiomyocyte patch transplantation for ischemic cardiomyopathy: first three case reports. *Frontiers in Cardiovascular Medicine*, *10*. https://doi.org/10.3389/fcvm.2023.1182209

Kelly, D. T. (1997). Disease burden of cardiovascular disease in the elderly. *Coronary Artery Disease*, *8*(10), 667–670. https://doi.org/10.1097/00019501-199710000-00010

Kernik, D. C., Morotti, S., Wu, H., Garg, P., Duff, H. J., Kurokawa, J., Jalife, J., Wu, J. C., Grandi, E., & Clancy, C. E. (2019). A computational model of induced pluripotent stem-cell derived cardiomyocytes incorporating experimental variability from multiple data sources. *The Journal of Physiology*, *597*(17), 4533–4564. https://doi.org/10.1113/JP277724

Kernik, D. C., Yang, P.-C., Kurokawa, J., Wu, J. C., & Clancy, C. E. (2020). A computational model of induced pluripotent stem-cell derived cardiomyocytes for high throughput risk stratification of KCNQ1 genetic variants. *PLoS Computational Biology*, *16*(8), e1008109. https://doi.org/10.1371/journal.pcbi.1008109

Khoury, P. R., Mitsnefes, M., Daniels, S. R., & Kimball, T. R. (2009). Age-Specific Reference Intervals for Indexed Left Ventricular Mass in Children. *Journal of the American Society of Echocardiography*, *22*(6), 709–714. https://doi.org/10.1016/j.echo.2009.03.003

Kim, J. J., Yang, L., Lin, B., Zhu, X., Sun, B., Kaplan, A. D., Bett, G. C. L., Rasmusson, R. L., London, B., & Salama, G. (2015). Mechanism of automaticity in cardiomyocytes derived from human induced pluripotent stem cells. *Journal of Molecular and Cellular Cardiology*, *81*, 81–93. https://doi.org/10.1016/j.yjmcc.2015.01.013

Klesen, A., Jakob, D., Emig, R., Kohl, P., Ravens, U., & Peyronnet, R. (2018). Cardiac fibroblasts. *Herzschrittmachertherapie + Elektrophysiologie*, *29*, 62–69. https://doi.org/10.1007/s00399-018-0553-3

Kodama, I., Wilde, A., Janse, M., Durrer, D., & Yamada, K. (1984). Combined effects of hypoxia, hyperkalemia and acidosis on membrane action potential and excitability of guinea-pig ventricular muscle. *Journal of Molecular and Cellular Cardiology*, *16*(3), 247–259. https://doi.org/10.1016/S0022-2828(84)80591-X

Kohl, P. (2003). Heterogeneous Cell Coupling in the Heart: An Electrophysiological Role for Fibroblasts. *Circulation Research*, *93*(5), 381–383. https://doi.org/10.1161/01.RES.0000091364.90121.0C

Koivumäki, J. T., Naumenko, N., Tuomainen, T., Takalo, J., Oksanen, M., Puttonen, K. A., Lehtonen, Š., Kuusisto, J., Laakso, M., Koistinaho, J., & Tavi, P. (2018). Structural Immaturity of Human iPSC-Derived Cardiomyocytes: In Silico Investigation of Effects on Function and Disease Modeling. *Frontiers in Physiology*, *9*. https://doi.org/10.3389/fphys.2018.00080

Koushik, S. V., Wang, J., Rogers, R., Moskophidis, D., Lambert, N. A., Creazzo, T. L., & Conway, S. J. (2001). Targeted inactivation of the sodium-calcium exchanger (Ncx1) results in the lack of a heartbeat and abnormal myofibrillar organization. *The FASEB Journal*, *15*(7), 1209–1211. https://doi.org/10.1096/fj.00-0696fje

Kozel, B. A., Barak, B., Kim, C. A., Mervis, C. B., Osborne, L. R., Porter, M., & Pober, B. R. (2021). Williams syndrome. *Nature Reviews Disease Primers*, *7*, 42. https://doi.org/10.1038/s41572-021-00276-z

Krogh-Madsen, T., & Christini, D. J. (2020). Quantitative description of cardiac action potentials. In T. Krogh-Madsen & D. J. Christini (Eds.), *Modeling and Simulating Cardiac Electrical Activity* (pp. 1.1-1.28). IOP Publishing. https://doi.org/10.1088/978-0-7503-2064-1ch1

Krupickova, S., Risch, J., Gati, S., Caliebe, A., Sarikouch, S., Beerbaum, P., Puricelli, F., Daubeney, P. E. F., Barth, C., Wage, R., Boroni Grazioli, S., Uebing, A., Pennell, D. J., & Voges, I. (2021). Cardiovascular magnetic resonance normal values in children for

biventricular wall thickness and mass. *Journal of Cardiovascular Magnetic Resonance*, *23*(1), 1. https://doi.org/10.1186/s12968-020-00692-2

Laflamme, M. A., Chen, K. Y., Naumova, A. V, Muskheli, V., Fugate, J. A., Dupras, S. K., Reinecke, H., Xu, C., Hassanipour, M., Police, S., O'Sullivan, C., Collins, L., Chen, Y., Minami, E., Gill, E. A., Ueno, S., Yuan, C., Gold, J., & Murry, C. E. (2007). Cardiomyocytes derived from human embryonic stem cells in pro-survival factors enhance function of infarcted rat hearts. *Nature Biotechnology*, *25*, 1015–1024. https://doi.org/10.1038/nbt1327

Land, S., Park-Holohan, S.-J., Smith, N. P., dos Remedios, C. G., Kentish, J. C., & Niederer, S. A. (2017). A model of cardiac contraction based on novel measurements of tension development in human cardiomyocytes. *Journal of Molecular and Cellular Cardiology*, *106*, 68–83. https://doi.org/10.1016/j.yjmcc.2017.03.008

Lee, Y.-K., Ng, K.-M., Lai, W.-H., Chan, Y.-C., Lau, Y.-M., Lian, Q., Tse, H.-F., & Siu, C.-W. (2011). Calcium Homeostasis in Human Induced Pluripotent Stem Cell-Derived Cardiomyocytes. *Stem Cell Reviews and Reports*, *7*, 976–986. https://doi.org/10.1007/s12015-011-9273-3

Lennie, J. L., Mondick, J. T., & Gastonguay, M. R. (2022). Bayesian modeling and simulation to inform rare disease drug development early decision-making: Application to Duchenne muscular dystrophy. *PLoS ONE*, *17*(4), e0247286. https://doi.org/10.1371/journal.pone.0247286

Levin, M. D. et al. (2025). Mechanisms of Sudden Cardiac Death in Williams Beuren Syndrome. *[Manuscript In Preparation]*.

Levin, M. D., & Kozel, B. A. (2017). General anesthesia risk in Williams Beuren syndrome patients in the current era. *Journal of the American College of Cardiology*, *69*(11), 598. https://doi.org/10.1016/S0735-1097(17)33987-6

Li, D. Y., Toland, A. E., Boak, B. B., Atkinson, D. L., Ensing, G. J., Morris, C. A., & Keating, M. T. (1997). Elastin point mutations cause an obstructive vascular disease, supravalvular aortic stenosis. *Human Molecular Genetics*, *6*(7), 1021–1028. https://doi.org/10.1093/hmg/6.7.1021

Li, R. A., Leppo, M., Miki, T., Seino, S., & Marbán, E. (2000). Molecular Basis of Electrocardiographic ST-Segment Elevation. *Circulation Research*, *87*(10), 837–839. https://doi.org/10.1161/01.RES.87.10.837

Linaro, D., & Giugliano, M. (2022). Markov Models of Ion Channels. In D. Jaeger & R. Jung (Eds.), *Encyclopedia of Computational Neuroscience* (pp. 1961–1972). Springer New York. https://doi.org/10.1007/978-1-0716-1006-0_131

Liu, Y.-W., Chen, B., Yang, X., Fugate, J. A., Kalucki, F. A., Futakuchi-Tsuchida, A., Couture, L., Vogel, K. W., Astley, C. A., Baldessari, A., Ogle, J., Don, C. W., Steinberg, Z. L., Seslar, S. P., Tuck, S. A., Tsuchida, H., Naumova, A. V, Dupras, S. K., Lyu, M. S., … Murry, C. E. (2018). Human embryonic stem cell–derived cardiomyocytes restore function in infarcted hearts of non-human primates. *Nature Biotechnology*, *36*, 597–605. https://doi.org/10.1038/nbt.4162

Lopez-Perez, A., Sebastian, R., Izquierdo, M., Ruiz, R., Bishop, M., & Ferrero, J. M. (2019). Personalized Cardiac Computational Models: From Clinical Data to Simulation of Infarct-Related Ventricular Tachycardia. *Frontiers in Physiology*, *10*. https://doi.org/10.3389/fphys.2019.00580

Lou, X., Tang, Y., Ye, L., Pretorius, D., Fast, V. G., Kahn-Krell, A. M., Zhang, J., Zhang, J., Qiao, A., Qin, G., Kamp, T., Thomson, J. A., & Zhang, J. (2023). Cardiac muscle patches containing four types of cardiac cells derived from human pluripotent stem cells improve recovery from cardiac injury in mice. *Cardiovascular Research*, *119*(4), 1062–1076. https://doi.org/10.1093/cvr/cvad004

Lu, L., Liu, M., Sun, R., Zheng, Y., & Zhang, P. (2015). Myocardial Infarction: Symptoms and Treatments. *Cell Biochemistry and Biophysics*, *72*, 865–867. https://doi.org/10.1007/s12013-015-0553-4

Lue, W. M., & Boyden, P. A. (1992). Abnormal electrical properties of myocytes from chronically infarcted canine heart. Alterations in Vmax and the transient outward current. *Circulation*, *85*(3), 1175–1188. https://doi.org/10.1161/01.CIR.85.3.1175

Luo, C. H., & Rudy, Y. (1991). A model of the ventricular cardiac action potential. Depolarization, repolarization, and their interaction. *Circulation Research*, *68*(6), 1501–1526. https://doi.org/10.1161/01.RES.68.6.1501

Luqman, N., Sung, R. J., Wang, C.-L., & Kuo, C.-T. (2007). Myocardial ischemia and ventricular fibrillation: Pathophysiology and clinical implications. *International Journal of Cardiology*, *119*(3), 283–290. https://doi.org/10.1016/j.ijcard.2006.09.016

Lyon, A., Mincholé, A., Bueno-Orovio, A., & Rodriguez, B. (2019). Improving the clinical understanding of hypertrophic cardiomyopathy by combining patient data, machine learning and computer simulations: A case study. *Morphologie*, *103*(343), 169–179. https://doi.org/10.1016/j.morpho.2019.09.001

Lyon, A., Mincholé, A., Martínez, J. P., Laguna, P., & Rodriguez, B. (2018). Computational techniques for ECG analysis and interpretation in light of their contribution to medical advances. *Journal of The Royal Society Interface*, *15*(138). https://doi.org/10.1098/rsif.2017.0821

Ma, J., Guo, L., Fiene, S. J., Anson, B. D., Thomson, J. A., Kamp, T. J., Kolaja, K. L., Swanson, B. J., & January, C. T. (2011). High purity human-induced pluripotent stem cell-

derived cardiomyocytes: electrophysiological properties of action potentials and ionic currents. *American Journal of Physiology-Heart and Circulatory Physiology*, *301*(5), H2006–H2017. https://doi.org/10.1152/ajpheart.00694.2011

Machiraju, P., & Greenway, S. C. (2019). Current methods for the maturation of induced pluripotent stem cell-derived cardiomyocytes. *World Journal of Stem Cells*, *11*(1), 33–43. https://doi.org/10.4252/wjsc.v11.i1.33

Maexa, R. (2022). Nernst-Planck Equation. In D. Jaeger & R. Jung (Eds.), *Encyclopedia of Computational Neuroscience* (pp. 2182–2187). Springer New York. https://doi.org/10.1007/978-1-0716-1006-0_233

Maier, L. S., Zhang, T., Chen, L., DeSantiago, J., Brown, J. H., & Bers, D. M. (2003). Transgenic CaMKIIδ_C Overexpression Uniquely Alters Cardiac Myocyte Ca^{2+} Handling. *Circulation Research*, *92*(8), 904–911. https://doi.org/10.1161/01.RES.0000069685.20258.F1

Mallapaty, S. (2020). Revealed: two men in China were first to receive pioneering stem-cell treatment for heart disease. *Nature*, *581*, 249–250. https://doi.org/10.1038/d41586-020-01285-w

Maltsev, V. A., & Lakatta, E. G. (2012). The funny current in the context of the coupled-clock pacemaker cell system. *Heart Rhythm*, *9*(2), 302–307. https://doi.org/10.1016/j.hrthm.2011.09.022

Mancuso, A., Barone, A., Cristiano, M. C., Cianflone, E., Fresta, M., & Paolino, D. (2020). Cardiac Stem Cell-Loaded Delivery Systems: A New Challenge for Myocardial Tissue Regeneration. *International Journal of Molecular Sciences*, *21*(20), 7701. https://doi.org/10.3390/ijms21207701

Mangion, K., Gao, H., Husmeier, D., Luo, X., & Berry, C. (2018). Advances in computational modelling for personalised medicine after myocardial infarction. *Heart*, *104*(7), 550–557. https://doi.org/10.1136/heartjnl-2017-311449

Marban, E., Robinson, S. W., & Wier, W. G. (1986). Mechanisms of arrhythmogenic delayed and early afterdepolarizations in ferret ventricular muscle. *Journal of Clinical Investigation*, *78*(5), 1185–1192. https://doi.org/10.1172/JCI112701

Marchiano, S., Nakamura, K., Reinecke, H., Neidig, L., Lai, M., Kadota, S., Perbellini, F., Yang, X., Klaiman, J. M., Blakely, L. P., Karbassi, E., Fields, P. A., Fenix, A. M., Beussman, K. M., Jayabalu, A., Kalucki, F. A., Potter, J. C., Futakuchi-Tsuchida, A., Weber, G. J., … Murry, C. E. (2023). Gene editing to prevent ventricular arrhythmias associated with cardiomyocyte cell therapy. *Cell Stem Cell*, *30*(4), 396-414.e9. https://doi.org/10.1016/j.stem.2023.03.010

Marcus, G. M. (2020). Evaluation and Management of Premature Ventricular Complexes. *Circulation*, *141*(17), 1404–1418. https://doi.org/10.1161/CIRCULATIONAHA.119.042434

Margara, F., Rodriguez, B., Toepfer, C. N., & Bueno-Orovio, A. (2021). Mavacamten Efficacy in Mutation-specific Hypertrophic Cardiomyopathy: an In-silico Approach to Inform Precision Medicine. *2021 Computing in Cardiology (CinC)*. https://doi.org/10.23919/CinC53138.2021.9662736

Margara, F., Wang, Z. J., Levrero-Florencio, F., Santiago, A., Vázquez, M., Bueno-Orovio, A., & Rodriguez, B. (2021). In-silico human electro-mechanical ventricular modelling and simulation for drug-induced pro-arrhythmia and inotropic risk assessment. *Progress in Biophysics and Molecular Biology*, *159*, 58–74. https://doi.org/10.1016/j.pbiomolbio.2020.06.007

Marrouche, N. F., Verma, A., Wazni, O., Schweikert, R., Martin, D. O., Saliba, W., Kilicaslan, F., Cummings, J., Burkhardt, J. D., Bhargava, M., Bash, D., Brachmann, J., Guenther, J., Hao, S., Beheiry, S., Rossillo, A., Raviele, A., Themistoclakis, S., & Natale, A. (2004). Mode of initiation and ablation of ventricular fibrillation storms in patients with ischemic cardiomyopathy. *Journal of the American College of Cardiology*, *43*(9), 1715–1720. https://doi.org/10.1016/j.jacc.2004.03.004

Martesanz, R. (2012). The Frontiers of Organ Transplantation and Cell Therapy. In C. Lopez-Larrea, A. Lopez-Vazquez, & B. Suarez-Alvarez (Eds.), *Stem Cell Transplantation (Advances in Experimental Medicine and Biology, vol. 741)* (pp. 1–12). Springer New York. https://doi.org/https://doi.org/10.1007/978-1-4614-2098-9_1

Martinez-Navarro, H., Bertrand, A., Doste, R., Smith, H., Tomek, J., Ristagno, G., Sachetto Oliveira, R., Weber dos Santos, R., Pandit, S. V, & Rodriguez, B. (2024). ECG analysis of ventricular fibrillation dynamics reflects ischaemic progression subject to variability in patient anatomy and electrode location. *Frontiers in Cardiovascular Medicine*, *11*. https://doi.org/https://doi.org/10.3389/fcvm.2024.1408822

Martinez-Navarro, H., Mincholé, A., Bueno-Orovio, A., & Rodriguez, B. (2019). High arrhythmic risk in antero-septal acute myocardial ischemia is explained by increased transmural reentry occurrence. *Scientific Reports*, *9*, 16803. https://doi.org/10.1038/s41598-019-53221-2

Martinez-Navarro, H., Zhou, X., Bueno-Orovio, A., & Rodriguez, B. (2021). Electrophysiological and anatomical factors determine arrhythmic risk in acute myocardial ischaemia and its modulation by sodium current availability. *Interface Focus*, *11*(1). https://doi.org/10.1098/rsfs.2019.0124

Mayourian, J., Cashman, T. J., Ceholski, D. K., Johnson, B. V., Sachs, D., Kaji, D. A., Sahoo, S., Hare, J. M., Hajjar, R. J., Sobie, E. A., & Costa, K. D. (2017). Experimental and

Computational Insight Into Human Mesenchymal Stem Cell Paracrine Signaling and Heterocellular Coupling Effects on Cardiac Contractility and Arrhythmogenicity. *Circulation Research*, *121*(4), 411–423. https://doi.org/10.1161/CIRCRESAHA.117.310796

Mayourian, J., Savizky, R. M., Sobie, E. A., & Costa, K. D. (2016). Modeling Electrophysiological Coupling and Fusion between Human Mesenchymal Stem Cells and Cardiomyocytes. *PLoS Computational Biology*, *12*(7), e1005014. https://doi.org/10.1371/journal.pcbi.1005014

Menasché, P., Vanneaux, V., Hagège, A., Bel, A., Cholley, B., Parouchev, A., Cacciapuoti, I., Al-Daccak, R., Benhamouda, N., Blons, H., Agbulut, O., Tosca, L., Trouvin, J.-H., Fabreguettes, J.-R., Bellamy, V., Charron, D., Tartour, E., Tachdjian, G., Desnos, M., & Larghero, J. (2018). Transplantation of Human Embryonic Stem Cell–Derived Cardiovascular Progenitors for Severe Ischemic Left Ventricular Dysfunction. *Journal of the American College of Cardiology*, *71*(4), 429–438. https://doi.org/10.1016/j.jacc.2017.11.047

Mendonca Costa, C., Neic, A., Kerfoot, E., Porter, B., Sieniewicz, B., Gould, J., Sidhu, B., Chen, Z., Plank, G., Rinaldi, C. A., Bishop, M. J., & Niederer, S. A. (2019). Pacing in proximity to scar during cardiac resynchronization therapy increases local dispersion of repolarization and susceptibility to ventricular arrhythmogenesis. *Heart Rhythm*, *16*(10), 1475–1483. https://doi.org/10.1016/j.hrthm.2019.03.027

Michailova, A., Saucerman, J., Ellen Belik, M., & McCulloch, A. D. (2005). Modeling Regulation of Cardiac K_{ATP} and L-type Ca^{2+} Currents by ATP, ADP, and Mg^{2+}. *Biophysical Journal*, *88*(3), 2234–2249. https://doi.org/10.1529/biophysj.104.046284

Mincholé, A., Zacur, E., Ariga, R., Grau, V., & Rodriguez, B. (2019). MRI-Based Computational Torso/Biventricular Multiscale Models to Investigate the Impact of Anatomical Variability on the ECG QRS Complex. *Frontiers in Physiology*, *10*. https://doi.org/10.3389/fphys.2019.01103

Mines, G. R. (1913). On dynamic equilibrium in the heart. *The Journal of Physiology*, *46*(4–5), 349–383. https://doi.org/10.1113/jphysiol.1913.sp001596

Moréna, H., Janse, M. J., Fiolet, J. W., Krieger, W. J., Crijns, H., & Durrer, D. (1980). Comparison of the effects of regional ischemia, hypoxia, hyperkalemia, and acidosis on intracellular and extracellular potentials and metabolism in the isolated porcine heart. *Circulation Research*, *46*(5), 634–646. https://doi.org/10.1161/01.RES.46.5.634

Mummery, C. L., Zhang, J., Ng, E. S., Elliott, D. A., Elefanty, A. G., & Kamp, T. J. (2012). Differentiation of Human Embryonic Stem Cells and Induced Pluripotent Stem Cells

to Cardiomyocytes. *Circulation Research*, *111*(3), 344–358. https://doi.org/10.1161/CIRCRESAHA.110.227512

Musuamba, F. T., Skottheim Rusten, I., Lesage, R., Russo, G., Bursi, R., Emili, L., Wangorsch, G., Manolis, E., Karlsson, K. E., Kulesza, A., Courcelles, E., Boissel, J., Rousseau, C. F., Voisin, E. M., Alessandrello, R., Curado, N., Dall'ara, E., Rodriguez, B., Pappalardo, F., & Geris, L. (2021). Scientific and regulatory evaluation of mechanistic in silico drug and disease models in drug development: Building model credibility. *CPT: Pharmacometrics & Systems Pharmacology*, *10*(8), 804–825. https://doi.org/10.1002/psp4.12669

Muszkiewicz, A., Britton, O. J., Gemmell, P., Passini, E., Sánchez, C., Zhou, X., Carusi, A., Quinn, T. A., Burrage, K., Bueno-Orovio, A., & Rodriguez, B. (2016). Variability in cardiac electrophysiology: Using experimentally-calibrated populations of models to move beyond the single virtual physiological human paradigm. *Progress in Biophysics and Molecular Biology*, *120*(1–3), 115–127. https://doi.org/10.1016/j.pbiomolbio.2015.12.002

Myklebust, L., Maleckar, M. M., & Arevalo, H. (2024). Fibrosis modeling choice affects morphology of ventricular arrhythmia in non-ischemic cardiomyopathy. *Frontiers in Physiology*, *15*. https://doi.org/10.3389/fphys.2024.1370795

Nable, J. V., & Brady, W. (2009). The evolution of electrocardiographic changes in ST-segment elevation myocardial infarction. *The American Journal of Emergency Medicine*, *27*(6), 734–746. https://doi.org/10.1016/j.ajem.2008.05.025

Nagumo, J., Arimoto, S., & Yoshizawa, S. (1962). An Active Pulse Transmission Line Simulating Nerve Axon. *Proceedings of the IRE*, *50*(10), 2061–2070. https://doi.org/10.1109/JRPROC.1962.288235

Nakamura, K., Neidig, L. E., Yang, X., Weber, G. J., El-Nachef, D., Tsuchida, H., Dupras, S., Kalucki, F. A., Jayabalu, A., Futakuchi-Tsuchida, A., Nakamura, D. S., Marchianò, S., Bertero, A., Robinson, M. R., Cain, K., Whittington, D., Tian, R., Reinecke, H., Pabon, L., … Murry, C. E. (2021). Pharmacologic therapy for engraftment arrhythmia induced by transplantation of human cardiomyocytes. *Stem Cell Reports*, *16*(10), 2473–2487. https://doi.org/10.1016/j.stemcr.2021.08.005

Nattel, S., Antzelevitch, C., & Noble, D. (2011). Resolving the M-cell debate: Why and how. *Heart Rhythm*, *8*(8), 1293–1295. https://doi.org/10.1016/j.hrthm.2011.06.002

Nayler, G. W., Poole-Wilson, P. A., & Williams, A. (1979). Hypoxia and calcium. *Journal of Molecular and Cellular Cardiology*, *11*(7), 683–706. https://doi.org/10.1016/0022-2828(79)90381-X

Negroni, J. A., Morotti, S., Lascano, E. C., Gomes, A. V., Grandi, E., Puglisi, J. L., & Bers, D. M. (2015). β-adrenergic effects on cardiac myofilaments and contraction in an

integrated rabbit ventricular myocyte model. *Journal of Molecular and Cellular Cardiology*, *81*, 162–175. https://doi.org/10.1016/j.yjmcc.2015.02.014

Nguyên, U. C., Potse, M., Regoli, F., Caputo, M. L., Conte, G., Murzilli, R., Muzzarelli, S., Moccetti, T., Caiani, E. G., Prinzen, F. W., Krause, R., & Auricchio, A. (2015). An in-silico analysis of the effect of heart position and orientation on the ECG morphology and vectorcardiogram parameters in patients with heart failure and intraventricular conduction defects. *Journal of Electrocardiology*, *48*(4), 617–625. https://doi.org/10.1016/j.jelectrocard.2015.05.004

Nichols, C. G. (2016). Adenosine Triphosphate-Sensitive Potassium Currents in Heart Disease and Cardioprotection. *Cardiac Electrophysiology Clinics*, *8*(2), 323–335. https://doi.org/10.1016/j.ccep.2016.01.005

Niederer, S. A., Kerfoot, E., Benson, A. P., Bernabeu, M. O., Bernus, O., Bradley, C., Cherry, E. M., Clayton, R., Fenton, F. H., Garny, A., Heidenreich, E., Land, S., Maleckar, M., Pathmanathan, P., Plank, G., Rodríguez, J. F., Roy, I., Sachse, F. B., Seemann, G., … Smith, N. P. (2011). Verification of cardiac tissue electrophysiology simulators using an N-version benchmark. *Philosophical Transactions of the Royal Society A: Mathematical, Physical and Engineering Sciences*, *369*, 4331–4351. https://doi.org/10.1098/rsta.2011.0139

Niederer, S. A., Lumens, J., & Trayanova, N. A. (2019). Computational models in cardiology. *Nature Reviews Cardiology*, *16*, 100–111. https://doi.org/10.1038/s41569-018-0104-y

Noble, D. (1960). Cardiac Action and Pacemaker Potentials based on the Hodgkin-Huxley Equations. *Nature*, *188*, 495–497. https://doi.org/10.1038/188495b0

Noble, D. (1962). A modification of the Hodgkin-Huxley equations applicable to Purkinje fibre action and pacemaker potentials. *The Journal of Physiology*, *160*(2), 317–352. https://doi.org/10.1113/jphysiol.1962.sp006849

Noble, D. (1965). Electrical properties of cardiac muscle attributable to inward going (anomalous) rectification. *Journal of Cellular and Comparative Physiology*, *66*(S2), 127–135. https://doi.org/10.1002/jcp.1030660520

Noble, D., & Tsien, R. W. (1969). Outward membrane currents activated in the plateau range of potentials in cardiac Purkinje fibres. *The Journal of Physiology*, *200*(1), 205–231. https://doi.org/10.1113/jphysiol.1969.sp008689

Noma, A. (1983). ATP-regulated K+ channels in cardiac muscle. *Nature*, *305*, 147–148. https://doi.org/10.1038/305147a0

O'Hara, T., Virág, L., Varró, A., & Rudy, Y. (2011). Simulation of the Undiseased Human Cardiac Ventricular Action Potential: Model Formulation and Experimental

Validation. *PLoS Computational Biology*, *7*(5), e1002061. https://doi.org/10.1371/journal.pcbi.1002061

Okada, J., Washio, T., Maehara, A., Momomura, S., Sugiura, S., & Hisada, T. (2011). Transmural and apicobasal gradients in repolarization contribute to T-wave genesis in human surface ECG. *American Journal of Physiology-Heart and Circulatory Physiology*, *301*(1), H200–H208. https://doi.org/10.1152/ajpheart.01241.2010

Oknińska, M., Mączewski, M., & Mackiewicz, U. (2022). Ventricular arrhythmias in acute myocardial ischaemia—Focus on the ageing and sex. *Ageing Research Reviews*, *81*, 101722. https://doi.org/10.1016/j.arr.2022.101722

Ørn, S., Manhenke, C., Anand, I. S., Squire, I., Nagel, E., Edvardsen, T., & Dickstein, K. (2007). Effect of Left Ventricular Scar Size, Location, and Transmurality on Left Ventricular Remodeling With Healed Myocardial Infarction. *The American Journal of Cardiology*, *99*(8), 1109–1114. https://doi.org/10.1016/j.amjcard.2006.11.059

Ottolia, M., Torres, N., Bridge, J. H. B., Philipson, K. D., & Goldhaber, J. I. (2013). Na/Ca exchange and contraction of the heart. *Journal of Molecular and Cellular Cardiology*, *61*, 28–33. https://doi.org/10.1016/j.yjmcc.2013.06.001

Paci, M., Hyttinen, J., Aalto-Setälä, K., & Severi, S. (2013). Computational Models of Ventricular- and Atrial-Like Human Induced Pluripotent Stem Cell Derived Cardiomyocytes. *Annals of Biomedical Engineering*, *41*, 2334–2348. https://doi.org/10.1007/s10439-013-0833-3

Paci, M., Koivumäki, J. T., Lu, H. R., Gallacher, D. J., Passini, E., & Rodriguez, B. (2021). Comparison of the Simulated Response of Three in Silico Human Stem Cell-Derived Cardiomyocytes Models and in Vitro Data Under 15 Drug Actions. *Frontiers in Pharmacology*, *12*. https://doi.org/10.3389/fphar.2021.604713

Paci, M., Passini, E., Klimas, A., Severi, S., Hyttinen, J., Rodriguez, B., & Entcheva, E. (2020). All-Optical Electrophysiology Refines Populations of In Silico Human iPSC-CMs for Drug Evaluation. *Biophysical Journal*, *118*(10), 2596–2611. https://doi.org/10.1016/j.bpj.2020.03.018

Paci, M., Passini, E., Severi, S., Hyttinen, J., & Rodriguez, B. (2017). Phenotypic variability in LQT3 human induced pluripotent stem cell-derived cardiomyocytes and their response to antiarrhythmic pharmacologic therapy: An in silico approach. *Heart Rhythm*, *14*(11), 1704–1712. https://doi.org/10.1016/j.hrthm.2017.07.026

Paci, M., Sartiani, L., Del Lungo, M., Jaconi, M., Mugelli, A., Cerbai, E., & Severi, S. (2012). Mathematical modelling of the action potential of human embryonic stem cell derived cardiomyocytes. *BioMedical Engineering OnLine*, *11*, 61. https://doi.org/10.1186/1475-925X-11-61

Pappalardo, F., Russo, G., Tshinanu, F. M., & Viceconti, M. (2019). In silico clinical trials: concepts and early adoptions. *Briefings in Bioinformatics*, *20*(5), 1699–1708. https://doi.org/10.1093/bib/bby043

Passini, E., Britton, O. J., Lu, H. R., Rohrbacher, J., Hermans, A. N., Gallacher, D. J., Greig, R. J. H., Bueno-Orovio, A., & Rodriguez, B. (2017). Human In Silico Drug Trials Demonstrate Higher Accuracy than Animal Models in Predicting Clinical Pro-Arrhythmic Cardiotoxicity. *Frontiers in Physiology*, *8*. https://doi.org/10.3389/fphys.2017.00668

Passini, E., Mincholé, A., Coppini, R., Cerbai, E., Rodriguez, B., Severi, S., & Bueno-Orovio, A. (2016). Mechanisms of pro-arrhythmic abnormalities in ventricular repolarisation and anti-arrhythmic therapies in human hypertrophic cardiomyopathy. *Journal of Molecular and Cellular Cardiology*, *96*, 72–81. https://doi.org/10.1016/j.yjmcc.2015.09.003

Passini, E., Zhou, X., Trovato, C., Britton, O. J., Bueno-Orovio, A., & Rodriguez, B. (2021). The virtual assay software for human in silico drug trials to augment drug cardiac testing. *Journal of Computational Science*, *52*, 101202. https://doi.org/10.1016/j.jocs.2020.101202

Paterson, D. J. (2013). Arrhythmia: 100 years on from George Ralph Mines. *The Journal of Physiology*, *591*(17), 4065–4066. https://doi.org/10.1113/jphysiol.2013.262386

Pérez, Á. J. B., Magoon, M. J., Sahota, M., Schicketanz, L., Uv, J. J., Boyle, P. M., & Arevalo, H. J. (2024). Non-Invasive Detection of Fetal Ischemia Through Electrocardiography. In K. J. McCabe (Ed.), *Computational Physiology. Simula SpringerBriefs on Computing* (Vol. 17, pp. 55–69). Springer. https://doi.org/10.1007/978-3-031-53145-3_4

Petrosyan, A., Martins, P. N., Solez, K., Uygun, B. E., Gorantla, V. S., & Orlando, G. (2022). Regenerative medicine applications: An overview of clinical trials. *Frontiers in Bioengineering and Biotechnology*, *10*. https://doi.org/10.3389/fbioe.2022.942750

Philipson, K. D., Longoni, S., & Ward, R. (1988). Purification of the cardiac Na^{+}-Ca^{2+} exchange protein. *Biochimica et Biophysica Acta (BBA) - Biomembranes*, *945*(2), 298–306. https://doi.org/10.1016/0005-2736(88)90492-0

Picard, S., Rouet, R., Ducouret, P., Puddu, P. E., Flais, F., Criniti, A., Monti, F., & Gérard, J. (1999). K_{ATP} channels and 'border zone' arrhythmias: role of the repolarization dispersion between normal and ischaemic ventricular regions. *British Journal of Pharmacology*, *127*(7), 1687–1695. https://doi.org/10.1038/sj.bjp.0702704

Pinto, J., & Boyden, P. A. (1999). Electrical remodeling in ischemia and infarction. *Cardiovascular Research*, *42*(2), 284–297. https://doi.org/10.1016/S0008-6363(99)00013-9

Pitt-Francis, J., Pathmanathan, P., Bernabeu, M. O., Bordas, R., Cooper, J., Fletcher, A. G., Mirams, G. R., Murray, P., Osborne, J. M., Walter, A., Chapman, S. J., Garny, A., van Leeuwen, I. M. M., Maini, P. K., Rodríguez, B., Waters, S. L., Whiteley, J. P., Byrne, H. M., & Gavaghan, D. J. (2009). Chaste: A test-driven approach to software development for biological modelling. *Computer Physics Communications*, *180*(12), 2452–2471. https://doi.org/10.1016/j.cpc.2009.07.019

Plank, G., Loewe, A., Neic, A., Augustin, C., Huang, Y.-L., Gsell, M. A. F., Karabelas, E., Nothstein, M., Prassl, A. J., Sánchez, J., Seemann, G., & Vigmond, E. J. (2021). The openCARP simulation environment for cardiac electrophysiology. *Computer Methods and Programs in Biomedicine*, *208*, 106223. https://doi.org/10.1016/j.cmpb.2021.106223

Pober, B. R., Johnson, M., & Urban, Z. (2008). Mechanisms and treatment of cardiovascular disease in Williams-Beuren syndrome. *Journal of Clinical Investigation*, *118*(5), 1606–1615. https://doi.org/10.1172/JCI35309

Poch, C. M., Foo, K. S., De Angelis, M. T., Jennbacken, K., Santamaria, G., Bähr, A., Wang, Q.-D., Reiter, F., Hornaschewitz, N., Zawada, D., Bozoglu, T., My, I., Meier, A., Dorn, T., Hege, S., Lehtinen, M. L., Tsoi, Y. L., Hovdal, D., Hyllner, J., … Laugwitz, K.-L. (2022). Migratory and anti-fibrotic programmes define the regenerative potential of human cardiac progenitors. *Nature Cell Biology*, *24*, 659–671. https://doi.org/10.1038/s41556-022-00899-8

Podolecki, T. S., Lenarczyk, R. K., Kowalczyk, J. P., Jedrzejczyk-Patej, E. K., Chodor, P. K., Mazurek, M. H., Francuz, P. J., Streb, W. A., Mitrega, K. A., & Kalarus, Z. F. (2018). Risk stratification for complex ventricular arrhythmia complicating ST-segment elevation myocardial infarction. *Coronary Artery Disease*, *29*(8), 681–686. https://doi.org/10.1097/MCA.0000000000000662

Pogwizd, S. M., & Corr, P. B. (1990). Mechanisms underlying the development of ventricular fibrillation during early myocardial ischemia. *Circulation Research*, *66*(3), 672–695. https://doi.org/10.1161/01.RES.66.3.672

Potse, M., Dube, B., Richer, J., Vinet, A., & Gulrajani, R. M. (2006). A Comparison of Monodomain and Bidomain Reaction-Diffusion Models for Action Potential Propagation in the Human Heart. *IEEE Transactions on Biomedical Engineering*, *53*(12), 2425–2435. https://doi.org/10.1109/TBME.2006.880875

Potse, M., Krause, D., Kroon, W., Murzilli, R., Muzzarelli, S., Regoli, F., Caiani, E., Prinzen, F. W., Krause, R., & Auricchio, A. (2014). Patient-specific modelling of cardiac electrophysiology in heart-failure patients. *EP Europace*, *16*(suppl 4), iv56–iv61. https://doi.org/10.1093/europace/euu257

Proudfit, W. L., Shirey, E. K., & Sones, F. M. (1966). Selective Cine Coronary Arteriography. *Circulation*, *33*(6), 901–910. https://doi.org/10.1161/01.CIR.33.6.901

Pu, J., & Boyden, P. A. (1997). Alterations of Na^+ Currents in Myocytes From Epicardial Border Zone of the Infarcted Heart: A Possible Ionic Mechanism for Reduced Excitability and Postrepolarization Refractoriness. *Circulation Research*, *81*(1), 110–119. https://doi.org/10.1161/01.RES.81.1.110

Qu, Z. (2006). Critical mass hypothesis revisited: role of dynamical wave stability in spontaneous termination of cardiac fibrillation. *American Journal of Physiology-Heart and Circulatory Physiology*, *290*(1), H255–H263. https://doi.org/10.1152/ajpheart.00668.2005

Querdel, E., Reinsch, M., Castro, L., Köse, D., Bähr, A., Reich, S., Geertz, B., Ulmer, B., Schulze, M., Lemoine, M. D., Krause, T., Lemme, M., Sani, J., Shibamiya, A., Stüdemann, T., Köhne, M., von Bibra, C., Hornaschewitz, N., Pecha, S., … Weinberger, F. (2021). Human Engineered Heart Tissue Patches Remuscularize the Injured Heart in a Dose-Dependent Manner. *Circulation*, *143*(20), 1991–2006. https://doi.org/10.1161/CIRCULATIONAHA.120.047904

Raab-Graham, K. F., Radeke, C. M., & Vandenberg, C. A. (1994). Molecular cloning and expression of a human heart inward rectifier potassium channel. *NeuroReport*, *5*(18), 2501–2505. https://doi.org/10.1097/00001756-199412000-00024

Raffel, O. C., & White, H. D. (2007). Acute Coronary Syndromes. In D. Sidebotham, A. Mckee, M. Gillham, & J. H. Levy (Eds.), *Cardiothoracic Critical Care* (pp. 257–277). Butterworth-Heinemann, Elsevier.

Ramirez, E., Saiz, J., Romero, L., Ferrero, J. M., & Trenor, B. (2014). In silico ischaemia-induced reentry at the Purkinje-ventricle interface. *EP Europace*, *16*(3), 444–451. https://doi.org/10.1093/europace/eut386

Reindl, M., Holzknecht, M., Tiller, C., Lechner, I., Schiestl, M., Simma, F., Pamminger, M., Henninger, B., Mayr, A., Klug, G., Bauer, A., Metzler, B., & Reinstadler, S. J. (2020). Impact of infarct location and size on clinical outcome after ST-elevation myocardial infarction treated by primary percutaneous coronary intervention. *International Journal of Cardiology*, *301*, 14–20. https://doi.org/10.1016/j.ijcard.2019.11.123

Reis, L. A., Chiu, L. L. Y., Feric, N., Fu, L., & Radisic, M. (2016). Biomaterials in myocardial tissue engineering. *Journal of Tissue Engineering and Regenerative Medicine*, *10*(1), 11–28. https://doi.org/10.1002/term.1944

Reuter, H., Henderson, S. A., Han, T., Mottino, G. A., Frank, J. S., Ross, R. S., Goldhaber, J. I., & Philipson, K. D. (2003). Cardiac excitation–contraction coupling in the absence of Na^+–Ca^{2+} exchange. *Cell Calcium*, *34*(1), 19–26. https://doi.org/10.1016/S0143-4160(03)00018-6

Ribatti, D. (2009). William Harvey and the discovery of the circulation of the blood. *Journal of Angiogenesis Research*, *1*(1), 3. https://doi.org/10.1186/2040-2384-1-3

Ribeiro, M. C., Tertoolen, L. G., Guadix, J. A., Bellin, M., Kosmidis, G., D'Aniello, C., Monshouwer-Kloots, J., Goumans, M.-J., Wang, Y., Feinberg, A. W., Mummery, C. L., & Passier, R. (2015). Functional maturation of human pluripotent stem cell derived cardiomyocytes in vitro – Correlation between contraction force and electrophysiology. *Biomaterials*, *51*, 138–150. https://doi.org/10.1016/j.biomaterials.2015.01.067

Rice, J. J., Wang, F., Bers, D. M., & de Tombe, P. P. (2008). Approximate Model of Cooperative Activation and Crossbridge Cycling in Cardiac Muscle Using Ordinary Differential Equations. *Biophysical Journal*, *95*(5), 2368–2390. https://doi.org/10.1529/biophysj.107.119487

Riebel, L. L., Passini, E., Margara, F., Paci, M., Biasetti, J., & Rodriguez, B. (2021). In Silico Identification of the Key Ionic Currents Modulating Human Pluripotent Stem Cell-Derived Cardiomyocytes Towards an Adult Phenotype. *2021 Computing in Cardiology (CinC)*. https://doi.org/10.23919/CinC53138.2021.9662683

Riebel, L. L., Wang, Z. J., Martinez-Navarro, H., Trovato, C., Camps, J., Berg, L. A., Zhou, X., Doste, R., Sachetto Oliveira, R., Weber dos Santos, R., Biasetti, J., & Rodriguez, B. (2024). In silico evaluation of cell therapy in acute versus chronic infarction: role of automaticity, heterogeneity and Purkinje in human. *Scientific Reports*, *14*, 21584. https://doi.org/10.1038/s41598-024-67951-5

Riegler, J., Gillich, A., Shen, Q., Gold, J. D., & Wu, J. C. (2014). Cardiac Tissue Slice Transplantation as a Model to Assess Tissue-Engineered Graft Thickness, Survival, and Function. *Circulation*, *130*(11_suppl_1), S77–S86. https://doi.org/10.1161/CIRCULATIONAHA.113.007920

Rijnbeek, P., Witsenburg, M., Schrama, E., Hess, J., & Kors, J. A. (2001). New normal limits for the paediatric electrocardiogram. *European Heart Journal*, *22*(8), 702–711. https://doi.org/10.1053/euhj.2000.2399

Ringenberg, J., Deo, M., Filgueiras-Rama, D., Pizarro, G., Ibañez, B., Peinado, R., Merino, J. L., Berenfeld, O., & Devabhaktuni, V. (2014). Effects of Fibrosis Morphology on Reentrant Ventricular Tachycardia Inducibility and Simulation Fidelity in Patient-Derived Models. *Clinical Medicine Insights: Cardiology*, *8s1*. https://doi.org/10.4137/CMC.S15712

Ringer, S. (1883). A further Contribution regarding the influence of the different Constituents of the Blood on the Contraction of the Heart. *The Journal of Physiology*, *4*(1), 29–42. https://doi.org/10.1113/jphysiol.1883.sp000120

Rodero, C., Baptiste, T. M. G., Barrows, R. K., Keramati, H., Sillett, C. P., Strocchi, M., Lamata, P., & Niederer, S. A. (2023). A systematic review of cardiac in-silico clinical trials. *Progress in Biomedical Engineering*, *5*, 032004. https://doi.org/10.1088/2516-1091/acdc71

Rodero, C., Strocchi, M., Marciniak, M., Longobardi, S., Whitaker, J., O'Neill, M. D., Gillette, K., Augustin, C., Plank, G., Vigmond, E. J., Lamata, P., & Niederer, S. A. (2021). Virtual cohort of adult healthy four-chamber heart meshes from CT images [Data set]. In *Linking statistical shape models and simulated function in the healthy adult human heart*. PLoS Computational Biology. https://doi.org/10.5281/zenodo.4590293

Rodríguez, B., Tice, B. M., Eason, J. C., Aguel, F., Ferrero, J. M., & Trayanova, N. (2004). Effect of acute global ischemia on the upper limit of vulnerability: a simulation study. *American Journal of Physiology-Heart and Circulatory Physiology*, *286*(6), H2078–H2088. https://doi.org/10.1152/ajpheart.01175.2003

Roger, V. L. (2013). Epidemiology of Heart Failure. *Circulation Research*, *113*(6), 646–659. https://doi.org/10.1161/CIRCRESAHA.113.300268

Rog-Zielinska, E. A., Norris, R. A., Kohl, P., & Markwald, R. (2016). The Living Scar – Cardiac Fibroblasts and the Injured Heart. *Trends in Molecular Medicine*, *22*(2), 99–114. https://doi.org/10.1016/j.molmed.2015.12.006

Romagnuolo, R., Masoudpour, H., Porta-Sánchez, A., Qiang, B., Barry, J., Laskary, A., Qi, X., Massé, S., Magtibay, K., Kawajiri, H., Wu, J., Valdman Sadikov, T., Rothberg, J., Panchalingam, K. M., Titus, E., Li, R.-K., Zandstra, P. W., Wright, G. A., Nanthakumar, K., … Laflamme, M. A. (2019). Human Embryonic Stem Cell-Derived Cardiomyocytes Regenerate the Infarcted Pig Heart but Induce Ventricular Tachyarrhythmias. *Stem Cell Reports*, *12*(5), 967–981. https://doi.org/10.1016/j.stemcr.2019.04.005

Romero, L., Pueyo, E., Fink, M., & Rodríguez, B. (2009). Impact of ionic current variability on human ventricular cellular electrophysiology. *American Journal of Physiology-Heart and Circulatory Physiology*, *297*(4), H1436–H1445. https://doi.org/10.1152/ajpheart.00263.2009

Ronkainen, V.-P., Skoumal, R., & Tavi, P. (2011). Hypoxia and HIF-1 suppress SERCA2a expression in embryonic cardiac myocytes through two interdependent hypoxia response elements. *Journal of Molecular and Cellular Cardiology*, *50*(6), 1008–1016. https://doi.org/10.1016/j.yjmcc.2011.02.017

Rosales, R. M., Mountris, K. A., Oliván-Viguera, A., Pérez-Zabalza, M., Cedillo-Servin, G., Iglesias-García, O., Hrynevich, A., Castilho, M., Malda, J., Prósper, F., Doblaré, M., Mazo, M. M., & Pueyo, E. (2024). Experimentally-guided in silico design of engineered heart tissues to improve cardiac electrical function after myocardial infarction.

Computers in Biology and Medicine, *171*, 108044. https://doi.org/10.1016/j.compbiomed.2024.108044

Rubenstein, D. S., & Lipsius, S. L. (1989). Mechanisms of automaticity in subsidiary pacemakers from cat right atrium. *Circulation Research*, *64*(4), 648–657. https://doi.org/10.1161/01.RES.64.4.648

Rush, S., & Larsen, H. (1978). A Practical Algorithm for Solving Dynamic Membrane Equations. *IEEE Transactions on Biomedical Engineering*, *BME-25*(4), 389–392. https://doi.org/10.1109/TBME.1978.326270

Russell, D. C., Lawrie, J. S., Riemersma, R. A., & Oliver, M. F. (1984). Mechanisms of phase 1a and 1b early ventricular arrhythmias during acute myocardial ischemia in the dog. *The American Journal of Cardiology*, *53*(2), 307–312. https://doi.org/10.1016/0002-9149(84)90444-2

Saarel, E. V., Granger, S., Kaltman, J. R., Minich, L. L., Tristani-Firouzi, M., Kim, J. J., Ash, K., Tsao, S. S., Berul, C. I., Stephenson, E. A., Gamboa, D. G., Trachtenberg, F., Fischbach, P., Vetter, V. L., Czosek, R. J., Johnson, T. R., Salerno, J. C., Cain, N. B., Pass, R. H., … for the Pediatric Heart Network Investigators. (2018). Electrocardiograms in Healthy North American Children in the Digital Age. *Circulation: Arrhythmia and Electrophysiology*, *11*(7). https://doi.org/10.1161/CIRCEP.117.005808

Sachetto Oliveira, R., Martins Rocha, B., Burgarelli, D., Meira, W., Constantinides, C., & Weber dos Santos, R. (2018). Performance evaluation of GPU parallelization, space-time adaptive algorithms, and their combination for simulating cardiac electrophysiology. *International Journal for Numerical Methods in Biomedical Engineering*, *34*(2), e2913. https://doi.org/10.1002/cnm.2913

Sáez, P., & Kuhl, E. (2015). Computational modeling of acute myocardial infarction. *Computer Methods in Biomechanics and Biomedical Engineering*, *19*(10), 1107–1115. https://doi.org/10.1080/10255842.2015.1105965

Salzillo, C., La Verde, M., Imparato, A., Molitierno, R., Lucà, S., Pagliuca, F., & Marzullo, A. (2024). Cardiovascular Diseases in Public Health: Chromosomal Abnormalities in Congenital Heart Disease Causing Sudden Cardiac Death in Children. *Medicina*, *60*(12), 1976. https://doi.org/10.3390/medicina60121976

Sampson, K. J., Iyer, V., Marks, A. R., & Kass, R. S. (2010). A computational model of Purkinje fibre single cell electrophysiology: implications for the long QT syndrome. *The Journal of Physiology*, *588*(14), 2643–2655. https://doi.org/10.1113/jphysiol.2010.187328

Sanchez, A., Schimmang, T., & Garcia-Sancho, J. (2012). Cell and Tissue Therapy in Regenerative Medicine. In C. Lopez-Larrea, A. Lopez-Vazquez, & B. Suarez-Alvarez

(Eds.), *Stem Cell Transplantation (Advances in Experimental Medicine and Biology, vol. 741)* (pp. 89–102). Springer New York. https://doi.org/https://doi.org/10.1007/978-1-4614-2098-9_7

Sánchez, C., Bueno-Orovio, A., Pueyo, E., & Rodriguez, B. (2013). Cell repolarization variability modulates atrial fibrillation dynamics in 3D virtual human atria. *2013 Computing in Cardiology (CinC)*, 911–914.

Santiago, A., Aguado-Sierra, J., Zavala-Aké, M., Doste-Beltran, R., Gómez, S., Arís, R., Cajas, J. C., Casoni, E., & Vázquez, M. (2018). Fully coupled fluid-electro-mechanical model of the human heart for supercomputers. *International Journal for Numerical Methods in Biomedical Engineering*, *34*(12), e3140. https://doi.org/10.1002/cnm.3140

Sarkar, A. X., Christini, D. J., & Sobie, E. A. (2012). Exploiting mathematical models to illuminate electrophysiological variability between individuals. *The Journal of Physiology*, *590*(11), 2555–2567. https://doi.org/10.1113/jphysiol.2011.223313

Sato, R., Noma, A., Kurachi, Y., & Irisawa, H. (1985). Effects of intracellular acidification on membrane currents in ventricular cells of the guinea pig. *Circulation Research*, *57*(4), 553–561. https://doi.org/10.1161/01.RES.57.4.553

Sayers, J. R., Martinez-Navarro, H., Sun, X., de Villiers, C., Sigal, S., Weinberger, M., Rodriguez, C. C., Riebel, L. L., Berg, L. A., Camps, J., Herring, N., Rodriguez, B., Sauka-Spengler, T., & Riley, P. R. (2025). Cardiac conduction system regeneration prevents arrhythmias after myocardial infarction. *Nature Cardiovascular Research*, *4*, 163–179. https://doi.org/10.1038/s44161-024-00586-x

Selvakumar, D., Clayton, Z. E., Prowse, A., Dingwall, S., Kim, S. K., Reyes, L., George, J., Shah, H., Chen, S., Leung, H. H. L., Hume, R. D., Tjahjadi, L., Igoor, S., Skelton, R. J. P., Hing, A., Paterson, H., Foster, S. L., Pearson, L., Wilkie, E., … Chong, J. J. H. (2024). Cellular heterogeneity of pluripotent stem cell-derived cardiomyocyte grafts is mechanistically linked to treatable arrhythmias. *Nature Cardiovascular Research*, *3*, 145–165. https://doi.org/10.1038/s44161-023-00419-3

Sepulveda, N. G., Roth, B. J., & Wikswo, J. P. (1989). Current injection into a two-dimensional anisotropic bidomain. *Biophysical Journal*, *55*(5), 987–999. https://doi.org/10.1016/S0006-3495(89)82897-8

Shah, K., Seeley, S., Schulz, C., Fisher, J., & Gururaja Rao, S. (2022). Calcium Channels in the Heart: Disease States and Drugs. *Cells*, *11*(6), 943. https://doi.org/10.3390/cells11060943

Sharma, R., Chowdhary, I., & Sharma, A. (2022). Arrhythmia and its risk factors post myocardial infarction: A prospective study. *Journal of Acute Disease*, *11*(1), 26–31. https://doi.org/10.4103/2221-6189.336578

Shattock, M. J., Ottolia, M., Bers, D. M., Blaustein, M. P., Boguslavskyi, A., Bossuyt, J., Bridge, J. H. B., Chen-Izu, Y., Clancy, C. E., Edwards, A., Goldhaber, J., Kaplan, J., Lingrel, J. B., Pavlovic, D., Philipson, K., Sipido, K. R., & Xie, Z. (2015). Na^+/Ca^{2+} exchange and Na^+/K^+-ATPase in the heart. *The Journal of Physiology*, *593*(6), 1361–1382. https://doi.org/10.1113/jphysiol.2014.282319

Shattock, M. J., Park, K. C., Yang, H.-Y., Lee, A. W. C., Niederer, S., MacLeod, K. T., & Winter, J. (2017). Restitution slope is principally determined by steady-state action potential duration. *Cardiovascular Research*, *113*(7), 817–828. https://doi.org/10.1093/cvr/cvx063

Shaw, R. M., & Rudy, Y. (1997). Electrophysiologic Effects of Acute Myocardial Ischemia. *Circulation Research*, *80*(1), 124–138. https://doi.org/10.1161/01.RES.80.1.124

Shen, A. C., & Jennings, R. B. (1972). Myocardial calcium and magnesium in acute ischemic injury. *The American Journal of Pathology*, *67*(3), 417–440.

Sherwood, L. (2001). *Human physiology: from cells to systems* (4th ed.). Brooks/Cole.

Shiba, Y., Gomibuchi, T., Seto, T., Wada, Y., Ichimura, H., Tanaka, Y., Ogasawara, T., Okada, K., Shiba, N., Sakamoto, K., Ido, D., Shiina, T., Ohkura, M., Nakai, J., Uno, N., Kazuki, Y., Oshimura, M., Minami, I., & Ikeda, U. (2016). Allogeneic transplantation of iPS cell-derived cardiomyocytes regenerates primate hearts. *Nature*, *538*, 388–391. https://doi.org/10.1038/nature19815

Shukla, A., Singh, A. K., & Singh, P. (2011). A Comparative Study of Finite Volume Method and Finite Difference Method for Convection-Diffusion Problem. *American Journal of Computational and Applied Mathematics*, *1*(2), 67–73. https://doi.org/10.5923/j.ajcam.20110102.13

Singam, N. S. V., Fine, C., & Fleg, J. L. (2020). Cardiac changes associated with vascular aging. *Clinical Cardiology*, *43*(2), 92–98. https://doi.org/10.1002/clc.23313

Skou, J. C. (1957). The influence of some cations on an adenosine triphosphatase from peripheral nerves. *Biochimica et Biophysica Acta*, *23*, 394–401. https://doi.org/10.1016/0006-3002(57)90343-8

Smith, G. D. (2002). Modeling the Stochastic Gating of Ion Channels. In C. P. Fall, E. S. Marland, J. M. Wagner, & J. J. Tyson (Eds.), *Computational Cell Biology (Interdisciplinary Applied Mathematics, vol. 20)* (pp. 285–319). Springer-Verlag New York.

Smith, H. J., Banerjee, A., Choudhury, R. P., & Grau, V. (2022). Automated Torso Contour Extraction from Clinical Cardiac MR Slices for 3D Torso Reconstruction. *2022 44th Annual International Conference of the IEEE Engineering in Medicine & Biology Society (EMBC)*, 3809–3813. https://doi.org/10.1109/EMBC48229.2022.9871643

Spath, N. B., Singh, T., Papanastasiou, G., Baker, A., Janiczek, R. J., McCann, G. P., Dweck, M. R., Kershaw, L., Newby, D. E., & Semple, S. (2021). Assessment of stunned and viable myocardium using manganese-enhanced MRI. *Open Heart*, *8*, e001646. https://doi.org/10.1136/openhrt-2021-001646

Srinivasan, N. T., Orini, M., Providencia, R., Dhinoja, M. B., Lowe, M. D., Ahsan, S. Y., Chow, A. W., Hunter, R. J., Schilling, R. J., Taggart, P., & Lambiase, P. D. (2019). Prolonged action potential duration and dynamic transmural action potential duration heterogeneity underlie vulnerability to ventricular tachycardia in patients undergoing ventricular tachycardia ablation. *EP Europace*, *21*(4), 616–625. https://doi.org/10.1093/europace/euy260

Stewart, P., Aslanidi, O. V., Noble, D., Noble, P. J., Boyett, M. R., & Zhang, H. (2009). Mathematical models of the electrical action potential of Purkinje fibre cells. *Philosophical Transactions of the Royal Society A: Mathematical, Physical and Engineering Sciences*, *367*, 2225–2255. https://doi.org/10.1098/rsta.2008.0283

Stone, P. H., Raabe, D. S., Jaffe, A. S., Gustafson, N., Muller, J. E., Turi, Z. G., Rutherford, J. D., Poole, W. K., Passamani, E., Willerson, J. T., Sobel, B. E., Robertson, T., Braunwald, E., & for the Milis Group. (1988). Prognostic significance of location and type of myocardial infarction: Independent adverse outcome associated with anterior location. *Journal of the American College of Cardiology*, *11*(3), 453–463. https://doi.org/10.1016/0735-1097(88)91517-3

Streeter, D. D., Spotnitz, H. M., Patel, D. P., Ross, J., & Sonnenblick, E. H. (1969). Fiber Orientation in the Canine Left Ventricle during Diastole and Systole. *Circulation Research*, *24*(3), 339–347. https://doi.org/10.1161/01.RES.24.3.339

Strocchi, M., Augustin, C. M., Gsell, M. A. F., Karabelas, E., Neic, A., Gillette, K., Razeghi, O., Prassl, A. J., Vigmond, E. J., Behar, J. M., Gould, J., Sidhu, B., Rinaldi, C. A., Bishop, M. J., Plank, G., & Niederer, S. A. (2020). A publicly available virtual cohort of four-chamber heart meshes for cardiac electro-mechanics simulations. *PLoS ONE*, *15*(6), e0235145. https://doi.org/10.1371/journal.pone.0235145

Strocchi, M., Gillette, K., Neic, A., Elliott, M. K., Wijesuriya, N., Mehta, V., Vigmond, E. J., Plank, G., Rinaldi, C. A., & Niederer, S. A. (2023). Effect of scar and His–Purkinje and myocardium conduction on response to conduction system pacing. *Journal of Cardiovascular Electrophysiology*, *34*(4), 984–993. https://doi.org/10.1111/jce.15847

Strømme, P., Bjømstad, P. G., & Ramstad, K. (2002). Prevalence Estimation of Williams Syndrome. *Journal of Child Neurology*, *17*(4), 269–271. https://doi.org/10.1177/088307380201700406

Stys, P. K., Waxman, S. G., & Ransom, B. R. (1995). Ion pumps and exchangers. In S. G. Waxman, J. D. Kocsis, & P. K. Stys (Eds.), *The Axon: Structure, Function and Pathophysiology* (pp. 296–310). Oxford University Press New York. https://doi.org/10.1093/acprof:oso/9780195082937.003.0015

Sudlow, C., Gallacher, J., Allen, N., Beral, V., Burton, P., Danesh, J., Downey, P., Elliott, P., Green, J., Landray, M., Liu, B., Matthews, P., Ong, G., Pell, J., Silman, A., Young, A., Sprosen, T., Peakman, T., & Collins, R. (2015). UK Biobank: An Open Access Resource for Identifying the Causes of a Wide Range of Complex Diseases of Middle and Old Age. *PLoS Medicine*, *12*(3), e1001779. https://doi.org/10.1371/journal.pmed.1001779

Sung, E., Prakosa, A., Aronis, K. N., Zhou, S., Zimmerman, S. L., Tandri, H., Nazarian, S., Berger, R. D., Chrispin, J., & Trayanova, N. A. (2020). Personalized Digital-Heart Technology for Ventricular Tachycardia Ablation Targeting in Hearts With Infiltrating Adiposity. *Circulation: Arrhythmia and Electrophysiology*, *13*(12), e008912. https://doi.org/10.1161/CIRCEP.120.008912

Sutton, M. G. St. J., & Sharpe, N. (2000). Left Ventricular Remodeling After Myocardial Infarction. *Circulation*, *101*(25), 2981–2988. https://doi.org/10.1161/01.CIR.101.25.2981

Szedlak, P., Steele, D. S., & Hopkins, P. M. (2023). Cardiac muscle physiology. *BJA Education*, *23*(9), 350–357. https://doi.org/10.1016/j.bjae.2023.05.004

Szentadrassy, N., Banyasz, T., Biro, T., Szabo, G., Toth, B., Magyar, J., Lazar, J., Varro, A., Kovacs, L., & Nanasi, P. (2005). Apico-basal inhomogeneity in distribution of ion channels in canine and human ventricular myocardium. *Cardiovascular Research*, *65*(4), 851–860. https://doi.org/10.1016/j.cardiores.2004.11.022

Szumowski, L., Sanders, P., Walczak, F., Hocini, M., Jaïs, P., Kepski, R., Szufladowicz, E., Urbanek, P., Derejko, P., Bodalski, R., & Haïssaguerre, M. (2004). Mapping and ablation of polymorphic ventricular tachycardia after myocardial infarction. *Journal of the American College of Cardiology*, *44*(8), 1700–1706. https://doi.org/10.1016/j.jacc.2004.08.034

Taggart, P., Sutton, P. M., Opthof, T., Coronel, R., Trimlett, R., Pugsley, W., & Kallis, P. (2000). Inhomogeneous Transmural Conduction During Early Ischaemia in Patients with Coronary Artery Disease. *Journal of Molecular and Cellular Cardiology*, *32*(4), 621–630. https://doi.org/10.1006/jmcc.2000.1105

Takahashi, M. (2010). Cardiac Ischemia in Pediatric Patients. *Pediatric Clinics of North America*, *57*(6), 1261–1280. https://doi.org/10.1016/j.pcl.2010.09.007

Ten Tusscher, K. H. W. J., Noble, D., Noble, P. J., & Panfilov, A. V. (2004). A model for human ventricular tissue. *American Journal of Physiology-Heart and Circulatory Physiology*, *286*(4), H1573–H1589. https://doi.org/10.1152/ajpheart.00794.2003

Ten Tusscher, K. H. W. J., & Panfilov, A. V. (2008). Modelling of the ventricular conduction system. *Progress in Biophysics and Molecular Biology*, *96*(1–3), 152–170. https://doi.org/10.1016/j.pbiomolbio.2007.07.026

Ten Tusscher, K. H. W. J., & Panfilov, A. V. (2006). Alternans and spiral breakup in a human ventricular tissue model. *American Journal of Physiology-Heart and Circulatory Physiology*, *291*(3), H1088–H1100. https://doi.org/10.1152/ajpheart.00109.2006

Terhune, P. E., Buchino, J. J., & Rees, A. H. (1985). Myocardial infarction associated with supravalvular aortic stenosis. *The Journal of Pediatrics*, *106*(2), 251–254. https://doi.org/10.1016/S0022-3476(85)80298-5

Terzic, A., & Behfar, A. (2014). Regenerative heart failure therapy headed for optimization. *European Heart Journal*, *35*(19), 1231–1234. https://doi.org/10.1093/eurheartj/ehu117

Thygesen, K., Alpert, J. S., Jaffe, A. S., Chaitman, B. R., Bax, J. J., Morrow, D. A., White, H. D., & ESC Scientific Document Group. (2019). Fourth universal definition of myocardial infarction (2018). *European Heart Journal*, *40*(3), 237–269. https://doi.org/10.1093/eurheartj/ehy462

Tomek, J., Bueno-Orovio, A., Passini, E., Zhou, X., Minchole, A., Britton, O., Bartolucci, C., Severi, S., Shrier, A., Virag, L., Varro, A., & Rodriguez, B. (2019). Development, calibration, and validation of a novel human ventricular myocyte model in health, disease, and drug block. *eLife*, *8*, e48890. https://doi.org/10.7554/eLife.48890

Tomek, J., Bueno-Orovio, A., & Rodriguez, B. (2020). ToR-ORd-dynCl: an update of the ToR-ORd model of human ventricular cardiomyocyte with dynamic intracellular chloride. *bioRxiv [Preprint]*. https://doi.org/10.1101/2020.06.01.127043

Trayanova, N. A. (2006). Defibrillation of the heart: insights into mechanisms from modelling studies. *Experimental Physiology*, *91*(2), 323–337. https://doi.org/10.1113/expphysiol.2005.030973

Trayanova, N. A., & Rice, J. J. (2011). Cardiac Electromechanical Models: From Cell to Organ. *Frontiers in Physiology*, *2*. https://doi.org/10.3389/fphys.2011.00043

Trovato, C., Mohr, M., Schmidt, F., Passini, E., & Rodriguez, B. (2022). Cross clinical-experimental-computational qualification of in silico drug trials on human cardiac purkinje cells for proarrhythmia risk prediction. *Frontiers in Toxicology*, *4*. https://doi.org/10.3389/ftox.2022.992650

Trovato, C., Passini, E., Nagy, N., Varró, A., Abi-Gerges, N., Severi, S., & Rodriguez, B. (2020). Human Purkinje in silico model enables mechanistic investigations into automaticity and pro-arrhythmic abnormalities. *Journal of Molecular and Cellular Cardiology*, *142*, 24–38. https://doi.org/10.1016/j.yjmcc.2020.04.001

Tülümen, E., Rudic, B., Ringlage, H., Hohneck, A., Röger, S., Liebe, V., Kuschyk, J., Overhoff, D., Budjan, J., Akin, I., Borggrefe, M., & Papavassiliu, T. (2021). Extent of peri-infarct scar on late gadolinium enhancement cardiac magnetic resonance imaging and outcome in patients with ischemic cardiomyopathy. *Heart Rhythm*, *18*(6), 954–961. https://doi.org/10.1016/j.hrthm.2021.01.023

Tveito, A., Jæger, K. H., Huebsch, N., Charrez, B., Edwards, A. G., Wall, S., & Healy, K. E. (2018). Inversion and computational maturation of drug response using human stem cell derived cardiomyocytes in microphysiological systems. *Scientific Reports*, *8*, 17626. https://doi.org/10.1038/s41598-018-35858-7

Twite, M. D., Stenquist, S., & Ing, R. J. (2019). Williams syndrome. *Pediatric Anesthesia*, *29*(5), 483–490. https://doi.org/10.1111/pan.13620

Ul Hassan, A., Hassan, G., & Rasool, Z. (2009). Role of stem cells in treatment of neurological disorder. *International Journal of Health Sciences (Qassim)*, *3*(2), 227–233.

Uv, J. J., Maleckar, M. M., & Arevalo, H. (2025). Impact of Vernix Caseosa Distribution on Non-Invasive Fetal ECG Morphology: A Computational Study. *IEEE Transactions on Biomedical Engineering*, *72*(3), 846–855. https://doi.org/10.1109/TBME.2024.3476379

Vaidya, D., Morley, G. E., Samie, F. H., & Jalife, J. (1999). Reentry and Fibrillation in the Mouse Heart. *Circulation Research*, *85*(2), 174–181. https://doi.org/10.1161/01.RES.85.2.174

Valdivia, C. R., Chu, W. W., Pu, J., Foell, J. D., Haworth, R. A., Wolff, M. R., Kamp, T. J., & Makielski, J. C. (2005). Increased late sodium current in myocytes from a canine heart failure model and from failing human heart. *Journal of Molecular and Cellular Cardiology*, *38*(3), 475–483. https://doi.org/10.1016/j.yjmcc.2004.12.012

Valensi, P., Lorgis, L., & Cottin, Y. (2011). Prevalence, incidence, predictive factors and prognosis of silent myocardial infarction: A review of the literature. *Archives of Cardiovascular Diseases*, *104*(3), 178–188. https://doi.org/10.1016/j.acvd.2010.11.013

van der Ven, J. P. G., Sadighy, Z., Valsangiacomo Buechel, E. R., Sarikouch, S., Robbers-Visser, D., Kellenberger, C. J., Kaiser, T., Beerbaum, P., Boersma, E., & Helbing, W. A. (2020). Multicentre reference values for cardiac magnetic resonance imaging derived ventricular size and function for children aged 0–18 years. *European Heart*

Journal - Cardiovascular Imaging, *21*(1), 102–113. https://doi.org/10.1093/ehjci/jez164

Van Nieuwenhuyse, E., Hendrickx, S., Abeele, R. Van den, Rajan, B., Lowie, L., Knecht, S., Duytschaever, M., & Vandersickel, N. (2022). DG-Mapping: a novel software package for the analysis of any type of reentry and focal activation of simulated, experimental or clinical data of cardiac arrhythmia. *Medical & Biological Engineering & Computing*, *60*, 1929–1945. https://doi.org/10.1007/s11517-022-02550-y

Vaseghi, M., & Shivkumar, K. (2008). The Role of the Autonomic Nervous System in Sudden Cardiac Death. *Progress in Cardiovascular Diseases*, *50*(6), 404–419. https://doi.org/10.1016/j.pcad.2008.01.003

Vassalle, M., & Lin, C.-I. (2004). Calcium overload and cardiac function. *Journal of Biomedical Science*, *11*, 542–565. https://doi.org/10.1007/BF02256119

Verkerk, A. O., & Wilders, R. (2023). Injection of I_{K1} through dynamic clamp can make all the difference in patch-clamp studies on hiPSC-derived cardiomyocytes. *Frontiers in Physiology*, *14*. https://doi.org/10.3389/fphys.2023.1326160

Viceconti, M., Emili, L., Afshari, P., Courcelles, E., Curreli, C., Famaey, N., Geris, L., Horner, M., Jori, M. C., Kulesza, A., Loewe, A., Neidlin, M., Reiterer, M., Rousseau, C. F., Russo, G., Sonntag, S. J., Voisin, E. M., & Pappalardo, F. (2021). Possible Contexts of Use for In Silico Trials Methodologies: A Consensus-Based Review. *IEEE Journal of Biomedical and Health Informatics*, *25*(10), 3977–3982. https://doi.org/10.1109/JBHI.2021.3090469

Viceconti, M., Pappalardo, F., Rodriguez, B., Horner, M., Bischoff, J., & Musuamba Tshinanu, F. (2021). In silico trials: Verification, validation and uncertainty quantification of predictive models used in the regulatory evaluation of biomedical products. *Methods*, *185*, 120–127. https://doi.org/10.1016/j.ymeth.2020.01.011

Vigmond, E. (2020). Tissue and organ scale modeling: coupled cells, wave propagation, simulated arrhythmia. In T. Krogh-Madsen & D. J. Christini (Eds.), *Modeling and Simulating Cardiac Electrical Activity* (pp. 7.1-7.23). IOP Publishing. https://doi.org/10.1088/978-0-7503-2064-1ch7

Vigmond, E., & Plank, G. (2019). Cardiac Modeling. In R. Narayan (Ed.), *Encyclopedia of Biomedical Engineering* (Vol. 3, pp. 1–20). Elsevier. https://doi.org/10.1016/B978-0-12-801238-3.99985-9

Vogel, B., Claessen, B. E., Arnold, S. V., Chan, D., Cohen, D. J., Giannitsis, E., Gibson, C. M., Goto, S., Katus, H. A., Kerneis, M., Kimura, T., Kunadian, V., Pinto, D. S., Shiomi, H., Spertus, J. A., Steg, P. G., & Mehran, R. (2019). ST-segment elevation myocardial infarction. *Nature Reviews Disease Primers*, *5*, 39. https://doi.org/10.1038/s41572-019-0090-3

Vozzi, C., Dupont, E., Coppen, S. R., Yeh, H.-I., & Severs, N. J. (1999). Chamber-related Differences in Connexin Expression in the Human Heart. *Journal of Molecular and Cellular Cardiology*, *31*(5), 991–1003. https://doi.org/10.1006/jmcc.1999.0937

Waller, A. D. (1887). A Demonstration on Man of Electromotive Changes accompanying the Heart's Beat. *The Journal of Physiology*, *8*(5), 229–234. https://doi.org/10.1113/jphysiol.1887.sp000257

Wallman, M., Smith, N. P., & Rodriguez, B. (2012). A Comparative Study of Graph-Based, Eikonal, and Monodomain Simulations for the Estimation of Cardiac Activation Times. *IEEE Transactions on Biomedical Engineering*, *59*(6), 1739–1748. https://doi.org/10.1109/TBME.2012.2193398

Wang, Z. J., Santiago, A., Zhou, X., Wang, L., Margara, F., Levrero-Florencio, F., Das, A., Kelly, C., Dall'Armellina, E., Vazquez, M., & Rodriguez, B. (2021). Human biventricular electromechanical simulations on the progression of electrocardiographic and mechanical abnormalities in post-myocardial infarction. *EP Europace*, *23*(Supplement_1), i143–i152. https://doi.org/10.1093/europace/euaa405

Warmke, J. W., & Ganetzky, B. (1994). A family of potassium channel genes related to eag in Drosophila and mammals. *Proceedings of the National Academy of Sciences*, *91*(8), 3438–3442. https://doi.org/10.1073/pnas.91.8.3438

Watanabe, Y., & Kimura, J. (2000). Inhibitory effect of amiodarone on Na^+/Ca^{2+} exchange current in guinea-pig cardiac myocytes. *British Journal of Pharmacology*, *131*(1), 80–84. https://doi.org/10.1038/sj.bjp.0703527

Weidmann, S. (1952). The electrical constants of Purkinje fibres. *The Journal of Physiology*, *118*(3), 348–360. https://doi.org/10.1113/jphysiol.1952.sp004799

Weiss, J. (1997). Ion Channels in Cardiac Muscle. In G. A. Langer (Ed.), *The Myocardium* (2nd ed., pp. 81–142). Academic Press. https://doi.org/10.1016/B978-012436570-4/50005-4

Weiss, J., & Shine, K. I. (1982). $[K^+]_o$ accumulation and electrophysiological alterations during early myocardial ischemia. *American Journal of Physiology-Heart and Circulatory Physiology*, *243*(2), H318–H327. https://doi.org/10.1152/ajpheart.1982.243.2.H318

Weiss, J., Venkatesh, N., & Lamp, S. T. (1992). ATP-sensitive K^+ channels and cellular K^+ loss in hypoxic and ischaemic mammalian ventricle. *The Journal of Physiology*, *447*(1), 649–673. https://doi.org/10.1113/jphysiol.1992.sp019022

Wickenden, A. D., Jegla, T. J., Kaprielian, R., & Backx, P. H. (1999). Regional contributions of Kv1.4, Kv4.2, and Kv4.3 to transient outward K^+ current in rat ventricle. *American*

Journal of Physiology-Heart and Circulatory Physiology, *276*(5), H1599–H1607. https://doi.org/10.1152/ajpheart.1999.276.5.H1599

Wickenden, A. D., Kaprielian, R., Kassiri, Z., Tsoporis, J. N., Tsushima, R., Fishman, G. I., & Backx, P. H. (1998). The role of action potential prolongation and altered intracellular calcium handling in the pathogenesis of heart failure. *Cardiovascular Research*, *37*(2), 312–323. https://doi.org/10.1016/S0008-6363(97)00256-3

Wiedmann, R. T., Tan, R. C., & Joyner, R. W. (1996). Discontinuous conduction at Purkinje-ventricular muscle junction. *American Journal of Physiology-Heart and Circulatory Physiology*, *271*(4), H1507–H1516. https://doi.org/10.1152/ajpheart.1996.271.4.H1507

Wiggers, C. J. (1921). Studies on the consecutive phases of the cardiac cycle. *American Journal of Physiology-Legacy Content*, *56*(3), 415–438. https://doi.org/10.1152/ajplegacy.1921.56.3.415

Wilkins, E., Wilson, L., Wickramasinghe, K., Bhatnagar, P., Leal, J., Luengo-Fernandez, R., Burns, R., Rayner, M., & Townsend, N. (2017). *European Cardiovascular Disease Statistics 2017*. European Heart Network, Brussels. https://ehnheart.org/wp-content/uploads/2023/07/CVD-Statistics.pdf

Wilson, F. N., Johnston, F. D., Macleod, A. G., & Barker, P. S. (1934). Electrocardiograms that represent the potential variations of a single electrode. *American Heart Journal*, *9*(4), 447–458. https://doi.org/10.1016/S0002-8703(34)90093-4

Winston, D. C., Spinale, F. G., Crawford, F. A., & Schulte, B. A. (1990). Immunocytochemical and enzyme histochemical localization of Na^+,K^+-ATPase in normal and ischemic porcine myocardium. *Journal of Molecular and Cellular Cardiology*, *22*(10), 1071–1082. https://doi.org/10.1016/0022-2828(90)90071-9

Wit, A. L., & Cranefield, P. F. (1978). Reentrant excitation as a cause of cardiac arrhythmias. *American Journal of Physiology-Heart and Circulatory Physiology*, *235*(1), H1–H17. https://doi.org/10.1152/ajpheart.1978.235.1.H1

World Health Organization. (2021). *Cardiovascular diseases (CVDs)*. https://www.who.int/en/news-room/fact-sheets/detail/cardiovascular-diseases-(cvds)

World Health Organization. (2024). *Ageing and health*. https://www.who.int/news-room/fact-sheets/detail/ageing-and-health

Xu, J., Xiong, Y.-Y., Li, Q., Hu, M.-J., Huang, P.-S., Xu, J.-Y., Tian, X.-Q., Jin, C., Liu, J.-D., Qian, L., & Yang, Y.-J. (2019). Optimization of Timing and Times for Administration of Atorvastatin-Pretreated Mesenchymal Stem Cells in a Preclinical Model of Acute

Myocardial Infarction. *Stem Cells Translational Medicine*, *8*(10), 1068–1083. https://doi.org/10.1002/sctm.19-0013

Yamada, S., Bartunek, J., Povsic, T. J., Cotter, G., Davison, B. A., Edwards, C., Behfar, A., Metra, M., Filippatos, G. S., Vanderheyden, M., Wijns, W., & Terzic, A. (2024). Cell Therapy Improves Quality-of-Life in Heart Failure: Outcomes From a Phase III Clinical Trial. *Stem Cells Translational Medicine*, *13*(2), 116–124. https://doi.org/10.1093/stcltm/szad078

Yang, X., Pabon, L., & Murry, C. E. (2014). Engineering Adolescence: Maturation of Human Pluripotent Stem Cell–Derived Cardiomyocytes. *Circulation Research*, *114*(3), 511–523. https://doi.org/10.1161/CIRCRESAHA.114.300558

Yatani, A., Brown, A. M., & Akaike, N. (1984). Effect of extracellular pH on sodium current in isolated, single rat ventricular cells. *The Journal of Membrane Biology*, *78*, 163–168. https://doi.org/10.1007/BF01869203

Yu, J. K., Franceschi, W., Huang, Q., Pashakhanloo, F., Boyle, P. M., & Trayanova, N. A. (2019). A comprehensive, multiscale framework for evaluation of arrhythmias arising from cell therapy in the whole post-myocardial infarcted heart. *Scientific Reports*, *9*, 9238. https://doi.org/10.1038/s41598-019-45684-0

Yu, J. K., Liang, J. A., Franceschi, W. H., Huang, Q., Pashakhanloo, F., Sung, E., Boyle, P. M., & Trayanova, N. A. (2022). Assessment of arrhythmia mechanism and burden of the infarcted ventricles following remuscularization with pluripotent stem cell-derived cardiomyocyte patches using patient-derived models. *Cardiovascular Research*, *118*(5), 1247–1261. https://doi.org/10.1093/cvr/cvab140

Yu, J. K., Liang, J. A., Weinberg, S. H., & Trayanova, N. A. (2022). Computational modeling of aberrant electrical activity following remuscularization with intramyocardially injected pluripotent stem cell-derived cardiomyocytes. *Journal of Molecular and Cellular Cardiology*, *162*, 97–109. https://doi.org/10.1016/j.yjmcc.2021.08.011

Yu, J., Zhang, R., Mao, Y., & Zhang, H. (2022). Efficacy and Safety of Mesenchymal Stem Cell Therapy in Patients with Acute Myocardial Infarction: A Systematic Review and Meta-analysis of Randomized Controlled Trials. *Current Stem Cell Research & Therapy*, *17*(8), 793–807. https://doi.org/10.2174/1574888X16666210816111031

Yue, L., Xie, J., & Nattel, S. (2011). Molecular determinants of cardiac fibroblast electrical function and therapeutic implications for atrial fibrillation. *Cardiovascular Research*, *89*(4), 744–753. https://doi.org/10.1093/cvr/cvq329

Zeng, J., & Rudy, Y. (1995). Early afterdepolarizations in cardiac myocytes: mechanism and rate dependence. *Biophysical Journal*, *68*(3), 949–964. https://doi.org/10.1016/S0006-3495(95)80271-7

Zeppenfeld, K., Tfelt-Hansen, J., de Riva, M., Winkel, B. G., Behr, E. R., Blom, N. A., Charron, P., Corrado, D., Dagres, N., de Chillou, C., Eckardt, L., Friede, T., Haugaa, K. H., Hocini, M., Lambiase, P. D., Marijon, E., Merino, J. L., Peichl, P., Priori, S. G., … ESC Scientific Document Group. (2022). 2022 ESC Guidelines for the management of patients with ventricular arrhythmias and the prevention of sudden cardiac death: Developed by the task force for the management of patients with ventricular arrhythmias and the prevention of sudden cardiac death of the European Society of Cardiology (ESC) Endorsed by the Association for European Paediatric and Congenital Cardiology (AEPC). *European Heart Journal*, *43*(40), 3997–4126. https://doi.org/10.1093/eurheartj/ehac262

Zhang, H., Xue, Y., Pan, T., Zhu, X., Chong, H., Xu, C., Fan, F., Cao, H., Zhang, B., Pan, J., Zhou, Q., Yang, G., Wang, J., & Wang, D.-J. (2022). Epicardial injection of allogeneic human-induced-pluripotent stem cell-derived cardiomyocytes in patients with advanced heart failure: protocol for a phase I/IIa dose-escalation clinical trial. *BMJ Open*, *12*(5), e056264. https://doi.org/10.1136/bmjopen-2021-056264

Zhou, X., Wang, Z. J., Camps, J., Tomek, J., Santiago, A., Quintanas, A., Vazquez, M., Vaseghi, M., & Rodriguez, B. (2024). Clinical phenotypes in acute and chronic infarction explained through human ventricular electromechanical modelling and simulations. *eLife*, *13*, RP93002. https://doi.org/https://doi.org/10.7554/eLife.93002.3

Zhou, X., Wang, Z., Tomek, J., Wang, L., & Rodriguez, B. (2021). Post myocardial infarction ionic remodelling promotes repolarisation dispersions and abnormalities in acute and chronic stages. *EP Europace*, *23*(Supplement_3), euab116.573. https://doi.org/10.1093/europace/euab116.573

Zijlstra, F., Patel, A., Jones, M., Grines, C., Ellis, S., Garcia, E., Grinfeld, L., Gibbons, R., Ribeiro, E., Ribichini, F., Granger, C., Akhras, F., Weaver, W., & Simes, R. (2002). Clinical characteristics and outcome of patients with early (<2h), intermediate (2–4h) and late (>4h) presentation treated by primary coronary angioplasty or thrombolytic therapy for acute myocardial infarction. *European Heart Journal*, *23*(7), 550–557. https://doi.org/10.1053/euhj.2001.2901

Zimmermann, W.-H., Melnychenko, I., Wasmeier, G., Didié, M., Naito, H., Nixdorff, U., Hess, A., Budinsky, L., Brune, K., Michaelis, B., Dhein, S., Schwoerer, A., Ehmke, H., & Eschenhagen, T. (2006). Engineered heart tissue grafts improve systolic and diastolic function in infarcted rat hearts. *Nature Medicine*, *12*, 452–458. https://doi.org/10.1038/nm1394